Design Conceptualization, Data Rate Studies and Physics Performance of the Silicon Tracking System at the Compressed Baryonic Matter Experiment

A Detector from its Embryonic State to Reality

Dissertation

zur Erlangung des Doktorgrades
der Naturwissenschaften

vorgelegt beim Fachbereich Physik
der Johann Wolfgang Goethe-Universität
in Frankfurt am Main

von
Mehulkumar J. Shiroya
aus Surat, Gujarat, India

Frankfurt am Main, 2025

D30

vom Fachbereich Physik

der Johann Wolfgang Goethe-Universität als Dissertation angenommen

Dekan: Prof. Dr. Marc Wagner

Gutachter: Prof. Dr. Alberica Toia

Prof. Dr. Christoph Blume

Betreuer: Dr. Volker Friese

Datum der Disputation: **27/04/2026**

Dedicated to...

...my family

Abstract

The Compressed Baryonic Matter (CBM) experiment at FAIR is designed to explore the phase diagram of nuclear matter in Quantum Chromodynamics (QCD) in the region of high net-baryon densities, using heavy-ion collisions at SIS-100 with a beam energy range of 2–12 AGeV/c. This regime, defined by baryochemical potential of $\mathcal{O}$(800–500) MeV and temperatures of $\mathcal{O}$(60–120) MeV, remains experimentally largely unexplored and is anticipated to contain the QCD Critical Point (CP). Operating in a free-streaming, triggerless mode at interaction rates up to 10 MHz, CBM enables the investigation of rare probes of strongly interacting matter with high statistical precision, including short-lived strange hadrons and hypernuclei, along with its other physics case studies, such as first-and second-order phase transitions, chiral symmetry and restoration, event-by-event net-proton and net-charge fluctuations, flow study, etc.

To investigate these physics cases in detail and with high precision, the CBM experiment requires a high-fidelity tracking system capable of reconstructing both primary and secondary particles and accurately determining their momenta. Therefore, CBM employs two detector subsystems: the Micro-Vertex Detector (MVD), which is used for reconstructing short-lived particles, and the Silicon Tracking System (STS), dedicated to efficiently reconstructing primary and secondary particle trajectories with excellent momentum resolution.

The STS detector consists of eight tracking stations, located downstream of the target between a range of 30-100 cm, housing a total of 876 double-sided, double-metal microstrip sensors of four variants, which are distinguished by their length. These sensors are systematically arranged at a different STS tracking station and provide a detector physics acceptance of $3^\circ < \eta < 25^\circ$. The STS detector is optimized to a low material budget, roughly (0.3 - 1.5% X_0 per station). It provides a momentum resolution of $\Delta p/p \leq 1.5\%$ for the primary particles below particle momentum 8 GeV/c and for secondary particles $\Delta p/p \leq 2\%$ up to the particle momentum 7 GeV/c. Also, the it provides a high tracking efficiency $\geq 97\%$ for the primary particles and $\geq 92\%$ for the secondary particles.

This thesis presents a comprehensive simulation-based study of the STS detector to provide a realistic, traceable description of its expected performance in the CBM experiment.

A central component of this work is the detailed implementation of the detector geometry, encompassing both the active sensor material and the intricate arrangement of passive structures, including support frames, cooling components, cabling, and readout infrastructure. The geometry model has been developed to ensure that the material budget, acceptance, and spatial configuration are reproduced with high fidelity.

A dedicated feasibility study was conducted to explore the potential of using tessellated geometries generated through a direct CAD-to-ROOT conversion workflow. This approach aims to preserve the exact mechanical shapes of complex components without resorting to simplified analytical volumes, thereby enabling a more precise assessment of scattering, energy loss, and secondary particle production in regions with intricate structures. The study, conducted on a prototype setup deployed within the mCBM experiment, provided an ideal test environment for evaluating the robustness, computational cost, and scalability of tessellated geometry in large-scale simulation campaigns. The experience gained from this prototype investigation provides valuable insights into the feasibility of integrating CAD-based models into future STS simulation frameworks.

Building on the detailed detector modelling, the simulation campaign developed in this thesis aims to reproduce the complete experimental environment as realistically as possible. Hadronic and beam–target interactions are generated with UrQMD and transported through the detector using GEANT4, with a primary focus on Au+Au collisions at beam momentum 12 AGeV/c. Additional studies are performed at lower energies to assess variations in background, acceptance, and multiplicity.

To reflect the triggerless, free-streaming operation of CBM, all events are digitized in a time-based mode, assuming the maximum expected interaction rate of 10 MHz. The digitizer features a realistic implementation of the STS response, including charge deposition, signal shaping, and cluster formation, and incorporates electronic noise to simulate real operating conditions.

On this realistically digitized data set, key performance metrics of the detector have been evaluated. These include the acceptance, hit and tracking efficiencies, spatial hit resolution, and momentum resolution across the relevant phase space. Furthermore, the expected data rates in the STS have been estimated to determine the bandwidth required for the readout system. These simulations have been cross-checked with measurements from the mCBM prototype, confirming the consistency of the predicted occupancies and data volumes.

The outcome of this thesis provides a baseline for the key performance parameters of the detector derived from realistic geometry and simulations, including all beam-target effects and noise. This work marks a key milestone for the STS, as it delivers the first performance evaluation within the full CBM setup.

Kurzfassung

Das *"Compressed Baryonic Matter"* (CBM)-Experiment an FAIR ist darauf ausgelegt, das Phasendiagramm der Kernmaterie in der *"Quantum Chromodynamics"* (QCD) im Bereich hoher Netto-Baryonendichten mithilfe von Schwerionenkollisionen am SIS-100-Beschleuniger in einem Strahlenergiebereich von $2-12$ AGeV/c zu untersuchen. Dieses Regime, charakterisiert durch ein baryochemisches Potenzial von $\mathcal{O}(800-500)$ MeV und Temperaturen von $\mathcal{O}(60-120)$ MeV, ist experimentell weitgehend unerforscht und wird als möglicher Bereich für den kritischen Punkt (CP) der QCD angesehen. Im triggerlosen Betriebsmodus bei Wechselwirkungsraten von bis zu 10 MHz ermöglicht CBM die Untersuchung seltener Sonden stark wechselwirkender Materie mit hoher statistischer Präzision, darunter kurzlebige Strange-Hadronen und Hyperkerne, sowie weiterer physikalischer Fragestellungen wie Phasenübergänge erster und zweiter Ordnung, chirale Symmetrie und deren Wiederherstellung, Ereignis-für-Ereignis- Fluktuationen von Netto-Protonen und Netto-Ladung, Flow-Studien usw.

Um diese physikalischen Fragestellungen im Detail und mit hoher Präzision zu untersuchen, benötigt das CBM-Experiment ein hochpräzises Trackingsystem, das sowohl primäre als auch sekundäre Teilchen rekonstruieren und ihre Impulse genau bestimmen kann. Daher verwendet CBM hierfür zwei Detektorsubsysteme: den Micro-Vertex Detector (MVD) zur Rekonstruktion kurzlebiger Teilchen und das Silicon Tracking System (STS), das der effizienten Rekonstruktion von primären und sekundären Teilchenspuren mit ausgezeichneter Impulsauflösung dient.

Der STS-Detektor besteht aus acht Tracking-Stationen, die sich in einem Bereich von 30 bis 100 cm hinter dem Target befinden und insgesamt 876 doppelseitige, doppelt metallisierte Mikrostreifensensoren in vier Varianten verwenden, die sich in ihrer Länge unterscheiden. Diese Sensoren sind auf einer anderen STS-Tracking-Station angeordnet und bieten eine Detektor-Akzeptanz von $3^{\circ} < \eta < 25^{\circ}$ Grad. Der STS-Detektor ist auf ein geringes Materialbudget optimiert, etwa (0,3 - 1,5% X_0 pro Station). Er bietet eine Impulsauflösung von $\Delta p/p \leq 1{,}5\%$ für die Primärteilchen unterhalb eines Teilchenimpulses von 8 GeV/c und für Sekundärteilchen $\Delta p/p \leq 2\%$ bis zu einem Teilchenimpuls

von 7 GeV/c. Außerdem bietet er eine hohe Tracking-Effizienz von $\geq 97\%$ für die Primärteilchen und $\geq 92\%$ für die Sekundärteilchen.

Eine dedizierte Machbarkeitsstudie wurde durchgeführt, um das Potenzial der Verwendung tessellierter Geometrien zu untersuchen, die durch einen direkten CAD-zu-ROOT– Konvertierungsworkflow erzeugt werden. Dieser Ansatz zielt darauf ab, die exakten mechanischen Formen komplexer Komponenten ohne Rückgriff auf vereinfachte analytische Volumina zu bewahren und somit eine präzisere Bewertung von Teilchenstreuung, Energieverlust und sekundärer Teilchenproduktion in Bereichen mit komplexen Detektorstrukturen zu ermöglichen. Die Studie, die an einem Prototypenaufbau im mCBM-Experiment durchgeführt wurde, bot eine ideale Testumgebung zur Bewertung der Robustheit, der Rechenkosten und der Skalierbarkeit tessellierter Geometrien in extensiven Simulationskampagnen. Die aus dieser Prototypenstudie gewonnenen Erfahrungen liefern wertvolle Einblicke in die Umsetzbarkeit der Integration CAD-basierter Modelle in zukünftige STS-Simulationsumgebungen.

Aufbauend auf der detaillierten Detektormodellierung zielt die in dieser Dissertation entwickelte Simulationskampagne darauf ab, die vollständige experimentelle Umgebung so realistisch wie möglich nachzubilden. Hadronische und Strahl-Target-Wechselwirkungen werden mit UrQMD generiert und mittels GEANT4 durch den Detektor transportiert, mit einem primären Fokus auf Au+Au-Kollisionen bei 12 AGeV/c. Zusätzliche Studien bei niedrigeren Energien werden durchgeführt, um Variationen in Hintergrund, Akzeptanz und Multiplizität zu bewerten.

Um den triggerlosen Betrieb von CBM mit freien Datenströmen in der Auslese widerzuspiegeln, werden alle Ereignisse in einem zeitbasierten Modus digitalisiert, wobei die maximal erwartete Wechselwirkungsrate von 10 MHz angenommen wird. Der Digitizer verfügt über eine realistische Implementierung der STS-Detektorantwort, einschließlich Ladungsdeposition, Signalformung und Clusterbildung, und berücksichtigt zusätzlich elektronisches Rauschen, um reale Betriebsbedingungen zu simulieren.

Auf Grundlage dieses realistisch digitalisierten Datensatzes wurden zentrale Leistungskennzahlen des Detektors ausgewertet. Dazu gehören die Akzeptanz, die Hit- und Trackingeffizienzen, die räumliche Trefferauflösung sowie die Impulsauflösung über den relevanten Phasenraum hinweg. Darüber hinaus wurden die erwarteten Datenraten im STS abgeschätzt, um die erforderliche Bandbreite für das Auslesesystem zu bestimmen. Diese Simulationen wurden anhand von Messungen des mCBM-Prototyps verifiziert, wodurch die Konsistenz der vorhergesagten Belegungen und Datenvolumina bestätigt werden konnte.

Das Ergebnis dieser Dissertation liefert eine Grundlage für die zentralen Leistungsparameter des Detektors, abgeleitet aus realistischer Geometrie und Simulationen, welche sämtliche Strahl–Target-Effekte sowie elektronisches Rauschen berücksichtigen. Diese Arbeit stellt einen wichtigen Meilenstein für das STS dar, da sie die erste Leistungsevaluierung innerhalb des vollständig implementierten CBM-Setups bereitstellt.

Zusammenfassung

Das Experiment *"Compressed Baryonic Matter"* (CBM) an der Facility for Antiproton and Ion Research (FAIR) zielt darauf ab, das QCD-Phasendiagramm bei hoher Netto-Baryonendichte zu untersuchen. Bei Strahlimpulsenergien von 2 bis 12 AGeV/c arbeitet CBM in Bereichen dichter Kernmaterie, die durch baryochemische Potenziale von $\mathcal{O}$(800–500)MeV und Temperaturen von $\mathcal{O}$(60–120)MeV gekennzeichnet sind. Das Physikprogramm umfasst die Messung seltener Sonden mit hoher Statistik, die Suche nach dem kritischen Punkt, Untersuchungen zu Phasenübergängen erster und zweiter Ordnung sowie zur Wiederherstellung der chiralen Symmetrie im angegebenen Phasenraum durch Differentialanalyse und Messungen von Dileptonspektren, kollektiven Fluss und Ereignis-für-Ereignis-Fluktuationen von Netto-Protonen und Netto-Ladung, wie in Kapitel **Chapter 1** ausführlich beschrieben.

Um diese Ziele zu erreichen, wird CBM mit einem kontinuierlichen (Schwer)ionenstrahl in einem triggerlosen und freilaufenden Datenerfassungsmodus mit Wechselwirkungsraten von bis zu $\mathcal{O}$(10MHz) betrieben. In diesem Modus werden die Detektorsignale kontinuierlich ausgelesen und die Online-Ereignisauswahl und -rekonstruktion in Echtzeit durchgeführt. Dieser innovative Ansatz ermöglicht die Detektion seltener Proben und kurzlebiger Teilchen mit hoher statistischer Präzision und liefert beispiellose Einblicke in die Eigenschaften stark wechselwirkender Materie bei hohen Baryonendichten.

Zwei sich ergänzende Tracking-Subsysteme sorgen für präzises Vertexing und Tracking im CBM-Experiment. Der Micro-Vertex-Detektor (MVD) basiert auf der Monolithic Active Pixel Sensor (MAPS) -Technologie mit dem "MIMOSIS"-Chip und ist für die hochpräzise Verfolgung und Vertex-Rekonstruktion kurzlebiger Teilchen optimiert. Nachgeschaltet zum MVD befindet sich das Silicon Tracking System (STS). Es ist das Hauptsystem zur Spurrekonstruktion für primäre und sekundäre geladene Teilchen und liefert Impulsmessungen in einem Dipolmagnetfeld.

Das STS befindet sich nach Konzeptualisierung und dem Bau von Prototypen nun im übergang von

seinem embryonalen Zustand zu seiner vollständigen physischen Realisierung, wobei die vollständige Montage des Detektors bis Ende 2027 erwartet wird. Es umfasst acht Tracking-Stationen innerhalb des Dipolmagneten, in denen insgesamt 876 doppelseitige Silizium- Mikrostreifensensoren in vier Varianten untergebracht sind, die auf leichten Tragkonstruktionen angeordnet sind (siehe siehe Abbildung Figure 2.3 und siehe Abbildung Figure 2.5). Er ist dafür ausgelegt, Tausende von geladenen Teilchenspuren pro Ereignis bei Kern-Kern-Kollisionen zu verarbeiten. Er spielt eine Schlüsselrolle als Tracking-System, das eine präzise Rekonstruktion des Impulses und der geladenen Teilchenspuren gewährleistet und gleichzeitig die höchsten Wechselwirkungsraten bewältigt, die für CBM bei FAIR vorgesehen sind. Um all diesen strengen Anforderungen gerecht zu werden, verfügt der STS-Detektor über ein geringes Materialbudget im aktiven physikalischen Akzeptanzbereich ($2{,}5^{\circ} < \eta < 25^{\circ}$, von der Targetposition aus), das grob etwa zwischen 0,3% und 1,5% pro Station liegt. Er hat eine Impulsauflösung ($\Delta p/p$) von $\approx \leq$ 1,5% für das Primärteilchen bis zu einem Teilchenimpuls von 8 GeV/c und für das sekundäre geladene Teilchen $\leq$ 2% bis zu einem Impulsbereich von 7 GeV/c, wie bereits in Kapitel **Chapter 2** erwähnt.

Detektorgeometrie

Ein zentraler Bestandteil dieser Arbeit ist die detaillierte Umsetzung der Detektorgeometrie, einschließlich des aktiven Sensormaterials und der komplexen Anordnung passiver Strukturen wie Stützrahmen, Kühlkomponenten, Verkabelung und Ausleseinfrastruktur. Das Geometriemodell wurde entwickelt, um sicherzustellen, dass das Materialbudget, die Akzeptanz und die räumliche Konfiguration mit hoher Genauigkeit reproduziert werden.

Darüber hinaus wurde ein alternativer Ansatz zur Konstruktion der Detektorsimulationsgeometrie untersucht, der eine direkte Konvertierung von CAD zu ROOT beinhaltet. Bei diesem Verfahren muss die STEP[1]-Datei aus dem CAD-System in ein für ROOT[2] lesbares Format konvertiert werden, in erster Linie in eine GDML[3]-Datei. Unter Verwendung des mSTS-Detektors als Testfall und unter Einsatz des CAD-zu-ROOT-Workflows wurde die mSTS-Geometrie erfolgreich konvertiert und durch Einlesen der GDML-Datei und Speichern im ROOT-Format vorbereitet. Sobald die Geometrie zusammengestellt ist, führen wir eine Simulation mit GEANT4, einer Ereignistransport-Engine, mit typischen von UrQMD-modellgenerierten Ereignissen durch, um die Laufzeitleistung der Simulation zu überprüfen und sie mit der einer mSTS-Geometrie zu vergleichen, die stattdessen

[1] Standard für den Austausch von Produktmodelldaten
[2] ROOT ist ein Software-Framework für die Hochenergiephysik
[3] Geometry Description Markup Language

aus primitiven Festkörpern aufgebaut ist.

Es wurde beobachtet, dass die Ereignislaufzeit im Fall einer tessellierten festkörperbasierten Geometrie im Vergleich zur primitiven festkörperbasierten Geometrie zunimmt, wie in Kapitel **Chapter 2**, Abschnitt **Section 2.4** erläutert. Darüber hinaus wurden auch die verschiedenen physikalischen Prozesse und die Sekundärteilchenproduktion simuliert und mit der Referenzgeometrie verglichen. Unsere Beobachtung aus dem Vergleich ist, dass beide Geometrievarianten fast denselben Trend ergeben, mit geringen bis keinen Unterschieden. Basierend auf dieser Studie kommen wir daher zu dem Schluss, dass die tessellierte, auf Volumenkörpern basierende Geometrie eine effiziente und zuverlässige Methode ist, um komplexe Detektorvolumenstrukturen und Hardware-Modifikationen zu integrieren und schnelle Tests zu ermöglichen. Für die Erstellung von Simulationsdaten in großem Maßstab ist jedoch eine vereinfachte Geometrie aus primitiven Volumenkörpern aufgrund des geringeren Rechenaufwands vorzuziehen. Daher ist es ein praktischer Ansatz, während der Entwurfs-, Optimierungs- und Validierungsphase des Detektors eine tessellierte, auf Volumenkörpern basierende Geometrie zu verwenden und dann, sobald der Entwurf des Detektors abgeschlossen ist, auf den vereinfachten Ansatz der Detektor-Geometrie umzusteigen.

Datenraten: Vergleich Datensimulation mit mCBM-Experiment

Wie bereits erwähnt erfolgt die Datenerfassung im Free-Streaming-Modus mit einer Wechselwirkungsrate von bis zu $\mathcal{O}(10\ \text{MHz})$, entsprechend den Anforderungen der STS-Detektoren. Daher muss das System vorab unter realen Experimentbedingungen getestet werden. Zu diesem Zweck wurden Prototypen aller Detektorsubsysteme im mCBM-Experiment an der GSI an deren Beschleunigeranlage SIS-18 getestet, um das Experiment unter realistischen Bedingungen mit einem Strahl zu testen. Das SIS-18 liefert einen Strahl verschiedener schwerer Kerne im Bereich von 1-2 AGeV/c. Die Tests sämtlicher Subdetektorsysteme, einschließlich der Elektronik-Hardware, des triggerlosen Datenaufnahmesystems, der Online-Rekonstruktion und der Ereignisauswahl-Software läuft seit 2018.

Das Mini-Silicon Tracking System (mSTS), ein kleiner Prototyp des gesamten STS, wird derzeit im Rahmen des mCBM-Experiments getestet. Es umfasst drei Tracking-Stationen, die mit zwölf Silizium-Mikrostreifensensoren unterschiedlicher Größe sowie der Datenausleseelektronik ausgestattet sind, die im endgültigen STS-Detektor für dessen Datenratenkapazität zum Einsatz kommen sollen. Die im Jahr 2024 gesammelten Daten wurden verwendet, um die Signal- und Rausch-Datenraten für jeden Sensor zu analysieren und einen Vergleich mit der in Kapitel **Chapter 3**

vorgestellten und diskutierten Simulation durchzuführen.

Die Datenerfassung im Jahr 2024 für den Lauf Id 2984 wurde mit einem Ni-Strahl bei 1,93 AGeV und einem Ni-Target mit einer Dicke von 0,4 cm durchgeführt. Die Strahlintensität, geschätzt durch den BMON-Detektor, der stromaufwärts des Targets platziert war, betrug$\sim$ 717 kHz. Die Strahlwechselwirkungswahrscheinlichkeit des Ni-Ionenstrahls mit dem Ni-Target der gegebenen Dicke betrug $\sim$10%.

Daher wurden simulierte Daten unter denselben Versuchsbedingungen erzeugt. Die Simulationsdaten umfassen Ni-Ni-Kollisionsereignisse, die mit UrQMD bei 1,93 AGeV/c erzeugt wurden, sowie Strahl-Hintergrundereignisse für δ-Elektronen, die mit Hilfe der GEANT4-Ereignistransport-Engine durch den Detektor transportiert wurden. Nach dem Ereignistransport bestand der nächste Schritt der Digitalisierung darin, die Detektorantwort im zeitbasierten Modus zu verarbeiten und die Diskriminator-Schwellenwerte für jeden Sensor so einzustellen, dass die Simulationsbedingungen die Experimenteinstellungen nachahmen. Die zeitbasierte Digitalisierung modelliert Detektorsignale durch Stichproben von Trefferquellen gemäß einer Poisson-Verteilung, die mit der angenommenen Wechselwirkungsrate übereinstimmt. Die Rice-Formel bestimmt die rauschbedingte Triggerrate und hängt von dem effektiven Rauschen (Equivalent Noise Charge - ENC), dem Diskriminatorschwellenwert sowie dem Baseline-Rauschen (Nullfrequenz) ab, die zur Erzeugung des Rauschens verwendet werden. Das Rauschen wird während der gesamten Zeitfensterphase der Digitalisierungsstufe mit einer konstanten Rate erzeugt.

Ein detaillierter, modulweiser Vergleich der Kanalraten zwischen Daten und Simulation wurde durchgeführt, indem die gemessenen mSTS-Daten in Off-Spill-Perioden – die nur elektronisches Rauschen enthalten – und In-Spill-Perioden, die Rauschen, hadronische und Strahl-Ziel-Wechselwirkungen umfassen, unterteilt wurden. Die Off-Spill-Daten wurden verwendet, um das simulierte Rauschen zu verifizieren. Während für die meisten Module die gemessenen Rauschraten mit dem simulierten Rauschband nach der Rice-Formel übereinstimmen, zeigen einige Sensoren eine Unter- oder über-schätzung, wahrscheinlich aufgrund von Schwellenwertdispersion oder temperaturabhängigen Schwankungen des Leckstroms, die den Rauschpegel verschieben. Der typische Dunkelratenbereich von 0,4 (Minimum) – 1,4 (maximal) kHz pro Kanal bestätigt, dass das Rauschen nur etwa 1% der verfügbaren Auslesebandbreite der Frontend-Elektronik einnimmt. Für den physikalischen Beitrag wurden die In-Spill- abzüglich der-Off-Spill-Daten mit Simulationen verglichen, die hadronische sowie die Strahl-Ziel-Wechselwirkungen beschreiben. In diesem hintergrundsubtrahierten Vergleich ist die übereinstimmung ausgezeichnet, da der Rauschbeitrag im Vergleich zu partikelinduzierten Treffern vernachlässigbar ist. Quantitativ beträgt die durchschnittliche

Rate pro Kanal für die n-Seite 2,23 kHz in den Daten gegenüber 2,01 kHz in der Simulation (10% Abweichung). Im Vergleich dazu beträgt sie für die p-Seite 2,92 kHz in den Daten gegenüber 2,03 kHz in der Simulation (30% Abweichung). Insgesamt zeigt die Studie, dass die Simulation die physikalischen Trefferraten mit hoher Genauigkeit reproduziert, während die verbleibenden Diskrepanzen hauptsächlich auf die Rauschmodellierung einiger weniger spezifischer Module beschränkt sind.

Datenraten: Erwartungen in STS @ CBM

In ähnlicher Weise wurde die Datenratenstudie für das vollstämdige Silizium-Tracking-System mittels Simulation durchgeführt und in Kapitel **Chapter 4** diskutiert. In diesem Fall haben wir die Ereignisse verwendet, die vom UrQMD-Modell für Au+Au-Kollisionen mit minimaler Verzerrung bei der höchsten für das CBM-Experiment vorgesehenen Strahlimpulsenergie (12 AGeV/c) generiert wurden. Wir haben auch den Strahlhintergrund für $\delta-$Elektronen-Ereignisse generiert, die mit Hilfe der GEANT4-Transport-Engine durch den Detektor transportiert wurden, wobei wir die Strahl-Target-Wechselwirkungswahrscheinlichkeit mit etwa $\sim$1% angenommen haben. Nach Abschluss des Ereignistransportschritts wurde die anschließende Digitalisierung der Detektorantwort im zeitbasierten Modus mit einer UrQMD-Ereignisrate von 10^7 Ereignissen/s und für den Strahlhintergrund mit 10^9 Ereignissen/s bei der höchsten Wechselwirkungsrate durchgeführt.

Während der Digitalisierungsphase haben wir die folgenden zwei Szenarien untersucht:

- **Erstens:** In diesem Fall haben wir den ENC- und den Diskriminatorschwellenwert 1000 e bzw. 4000 e (4σ) auf alle 876 Siliziumsensoren verwendet.
- **Zweitens:** In diesem Fall haben wir die ENC-Werte für jeden Sensor, der im STS-Detektor verwendet werden soll, auf der Grundlage der Eigenschaften des Moduls (Länge des Sensorstreifens und Länge des angeschlossenen Mikrokabels) und seines entsprechenden 4σ Diskriminatorschwellenwerts berechnet.

Die für jeden Fall ermittelte Datenrate pro Kanal wurde verglichen, um die Anzahl der für verschiedene Uplinks erforderlichen ASICs zu bestimmen.[4] Beim Vergleich der für die individuellen Einstellungen von ENC und Diskriminatorschwellenwert der Sensoren erhaltenen Rate pro Kanal haben wir festgestellt, dass ein kleiner Teil der ASICs im Vergleich zur globalen Einstellung mit ENC = 1000 e und Schwellenwert = 4000 e von der niedrigsten Bandbreite (einzelner Uplink)

[4] Die Ratenbänder sind $[0, 73)$, $[73, 146)$ und $[146, 367)$ kHits/s pro Kanal, was ASICs mit 1, 2 bzw. 5 Uplinks entspricht, basierend auf der nominalen Verbindungsbandbreite.

zu höheren Bandbreiten (zwei oder fünf Uplinks) gewechselt ist, wie in der Tabelle Table 4.6 dargestellt. Die Differenz zwischen der höchsten Gesamtrate pro Kanal, die für eine einzelne Einstellung beobachtet wurde, und der globalen Einstellung beträgt ca. 9% und ist auf eine kleine Anzahl von ASICs beschränkt. Dies deutet darauf hin, dass die im STS-Detektor zu erwartenden Signal- und Rauschraten innerhalb der vorgesehenen Auslesebandbreite und Rateneigenschaften bleiben.

Der STS-Detektor verwendet drei Arten von Front-End-Boards (FEBs), bezeichnet als FEB8, die sich durch die Anzahl der Uplinks unterscheiden: eins, zwei oder fünf. Der FEB-Typ wird auf der Grundlage der in diesem Modul erwarteten Rate zugewiesen.

Physikalische Leistung des STS

Schließlich diskutieren wir in Kapitel **Chapter 5** die physikalische Leistung des gesamten STS-Detektors und stellen wichtige Leistungsparameter wie Akzeptanz, Treffer- und Nachverfolgungseffizienz, räumliche Trefferauflösung und Impulsauflösung über den relevanten Phasenraum bereit.

Zunächst zeigen wir die Effizienz des STS-Detektors im Vergleich zur polaren Akzeptanz, was darauf hinweist, dass der STS als eigenständiger Detektor eine Effizienz von $\geq 95\%$ im Bereich von $5^{\circ} < \theta < 25^{\circ}$ aufweist. Zusätzlich wurde die Trefferrekonstruktionseffizienz für den gesamten STS-Detektor und für jeden Sensor in seiner jeweiligen Station bei verschiedenen Schwellenwert- und Totzeiteinstellungen bewertet. Wir haben beobachtet, dass die durchschnittliche Trefferrekonstruktionseffizienz für den gesamten STS mit einem ENC von 1000 e und einer Totzeit von 200 ns bei einem Diskriminatorschwellenwert von 2000 e bei $\sim$ 97,5% bleibt und bei einem Schwellenwert von 9000 e auf 94% sinkt. In ähnlicher Weise bleibt die Trefferrekonstruktionseffizienz bei einem ENC von 1000 e und einem Diskriminatorschwellenwert von 4000 e bei einer Totzeit von 200 ns bei etwa 97%, während sie bei einer Totzeit von 800 ns auf $\sim$ 95% sinkt.

Anschließend wurde die Effizienz der Spurrekonstruktion des STS-Detektors bewertet. Für alle Teilchen über $p \geq 1$ GeV/c wird eine Effizienz von 97% berechnet, während bei einer getrennten Bewertung für primäre und sekundäre Teilchen die berechnete Effizienz bei $\sim$ 98% bzw. $\sim$ 93% bleibt.

Darüber hinaus wird die Leistung der Clustercharakterisierung untersucht. Für Teilchen, die bei hadronischen Wechselwirkungen (UrQMD) entstehen, beträgt die typische Clustergröße 2, während für alle anderen Strahl-Target-Wechselwirkungen (typischerweise EM-Wechselwirkungen, die δ-

Elektronen erzeugen) die typische Clustergröße in der ersten STS-Station ~ 4 beträgt und in Richtung der der nachgeschalteten STS-Stationen auf ~ 3 abnimmt. Dies ist auf die $\delta-$Elektronen zurückzuführen, die im Magnetfeld stärker abgelenkt werden und die Detektorebene in einem höheren Einfallswinkel durchquert haben. Darüber hinaus haben wir auch die Beziehungen zwischen der Clustergröße und dem Neigungswinkel sowie zwischen der Clusterladung und anderen Faktoren diskutiert.

Darüber hinaus wird die räumliche Trefferauflösung des STS anhand von Treffer-Residuen untersucht, d. h. anhand der Differenz zwischen der Monte-Carlo-Position des Punktes und der Position des rekonstruierten Punktes. Das Ergebnis ist eine Auflösung von etwa 10μm, was mit dem Abstand von 58μm übereinstimmt.

Am Ende der Arbeit diskutieren wir das Potenzial des STS-Detektors für Anwendungen zur Teilchenidentifizierung. Dies würde die Flugzeitmessungen (TOF) mit dem TOF-detektor ergänzen, der im CBM-Experiment eine π/K-Trennung bis zu etwa 3,0 GeV/c und eine K/p-Trennung bis zu etwa 5,5 GeV/c ermöglicht. Unter Verwendung der Messung von $\langle dE/dx \rangle$ könnte der STS dazu beitragen, Teilchen mit dem gleichen m/Z-Verhältnis, insbesondere die Wasserstofffamilie $(d(^2H), t(^3H))$, bis zu einem Impuls von 2,5 GeV/c zu trennen. Dies ist äußerst nützlich für die Rekonstruktion von Hyperkernen.

Zusammenfassend liefert das Ergebnis dieser Arbeit eine Grundlage für die wichtigsten Leistungsparameter des Detektors, die aus realistischen Geometrien und Simulationen abgeleitet wurden, die alle Strahl-Ziel-Effekte und Störgeräusche berücksichtigen. Diese Arbeit stellt einen wichtigen Meilenstein für das STS dar, da sie die erste Leistungsbewertung innerhalb des vollständigen CBM-Aufbaus liefert.

Contents

Chapter 1

Introduction

The Standard Model (SM) of particle physics, a well-defined theoretical framework, describes three of the four fundamental forces: Electromagnetic, Strong, and Weak, except the Gravitational force. It classifies all known particles: six quarks, six leptons and their corresponding anti-particles, four gauge bosons, and scalar bosons as shown in Figure 1.1. However, the concept of gravitational force and its interaction is well beyond the SM. The hypothetical elementary particle known as the graviton is predicted to be the carrier of the gravitational force. If the Graviton exists, it must be massless, as a gravitational force has a long range and spin 2 boson, because the source of the gravitational field comes through the stress-energy-momentum tensor.

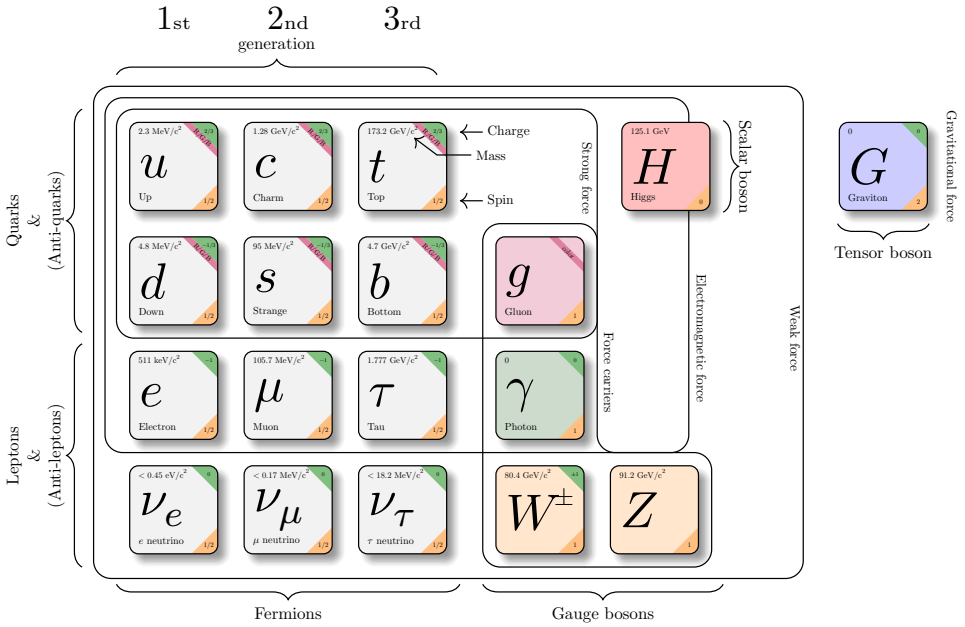

Figure 1.1: The standard model of particle physics with six quarks, six leptons, four gauge bosons, a Higgs boson, and a graviton. (Taken from: Source file [1], and modified)

The Standard Model (SM) classifies elementary particles into two distinct groups based on their spin: Fermions and Bosons. Fermions are particles with half-integer spin. They adhere to Fermi-Dirac statistics and follow the Pauli exclusion principle, which states that no two identical fermions can occupy the same quantum state simultaneously. On the other hand, Bosons are integer-spin particles, which obey Bose-Einstein statistics. Unlike the Fermions, multiple Bosons can occupy the same quantum states which allows a phenomena such as Bose-Einstein condensation.

The four gauge bosons work as mediator particles. They are responsible for the interaction between other SM particles. Besides, a scalar boson, known as a Higgs boson, discovered in 2012 at the Large Hadron Collider (LHC), Conseil Européen pour la Recherche Nucléaire (CERN) [2], is responsible for providing mass to all the fundamental particles in the SM via the spontaneous symmetry breaking. Particles acquire masses through their interaction with the Higgs field. However, SM still cannot explain some questions about dark matter, the mechanism of neutrino mass generation, and so on. There is a possibility that neutrinos acquire mass through either the Higgs mechanism or the Seesaw mechanism. Still, it has not yet been experimentally confirmed which mechanism is responsible for the generation of the three active, weakly interacting neutrinos.[3] However, recent experimental observation has shown the upper bound limit on the electron neutrino mass ≤ 0.45 eV (90% C.L.) as per the recently published results.[4]

1.1 Quantum Chromodynamics (QCD)

Quantum Electrodynamics (QED) corresponds to a U(1) local gauge symmetry in which a massless photon mediates the interaction. In QED, the electromagnetic interaction is described, and the gauge symmetry ensures the conservation of electric charge. On the other hand, Quantum Chromodynamics (QCD) is the quantum field theory of the strong interaction, which is mediated by eight massless gluons corresponding to the eight generators of the SU(3) local gauge symmetry. QCD is described by non-Abelian SU(3) group theory and is invariant under local phase transformations of the colour fields.

$$\psi(x) \rightarrow \psi'(x) = exp[ig_s\alpha(x) \cdot \hat{T}]\psi(x) \tag{1.1}$$

Where $\hat{T}$ =T^a are eight generators of a SU(3) symmetry group related to the Gell-Mann matrices $T^a = \frac{1}{2}\lambda^a$ and $\alpha(x)$ are eight functions of the space-time coordinates. The QCD Lagrangian is given by

$$L_{QCD} = \sum_{f_i} \bar{q}_{f_i}(i\gamma^\mu D_\mu - m_{f_i})q_{f_i} - \frac{1}{4}G^{(a)}_{\mu\nu}G^{\mu\nu}_{(a)} \tag{1.2}$$

$\bar{q}_{f_i}$ is quark field with flavour i.
$D_\mu = \partial_\mu - ig_s\frac{\lambda^a}{2}A^a_\mu$ is a gauge covariant derivative.
$G_{\mu\nu} = \partial_\mu A^a_\nu - \partial_\nu A^a_\mu + g_s f^{abc} A^b_\mu A^c_\nu$ (gauge-invariant gluon field strength tensor) where f^{abc} is a structure constant of SU(3).

In QCD, there are three conserved colour charges (Red, Green, and Blue) for quarks and the corresponding anti-colors for anti-quarks. A strong interaction occurs between particles that carry these colour charges. Leptons, on the other hand, do not carry colour charge and are thus colour-neutral, which is why they do not interact via the strong force. Also, there are eight charge-coloured gluons, while the colourless ninth gluon's existence is unknown or doesn't exist due to its colour singlet nature.[5] Since the gluons are color-charged, self-interaction between them is also possible. which is a unique feature of QCD compared to QED, where photons do not interact with each other.

This self-interaction of gluons leads to the property of confinement. A colour confinement hypothesis states that coloured objects can not be observed as free particles, which means the quarks can not propagate in their free states. They can only be observed as colour singlet states in the form of hadrons. Hadrons, the bound states of quarks, are further classified into baryons (three-quark states) and mesons (quark + anti-quark). At low energy scales, the coupling constant (or the strength) of QCD is large, and the perturbation expansion does not converge. At a higher energy scale, the coupling constant becomes small that quarks behave as quasi-free particles (asymptotic freedom) and can apply perturbative theory to explain the quarks states.

In the following section, we describe the nuclear QCD phase diagram and the theoretical and experimental efforts to study its different regions.

1.2 Nuclear Matter Phase Diagram and Experimental Efforts

Quark-gluon plasma (QGP) is a deconfined state of quarks and gluons in which they move freely. The diagram, as shown in Figure 1.2, illustrates the transition of strongly interacting nuclear matter under varying conditions of the baryon chemical potential (μ_B) and temperature (T). The first attempt to define the hypothetical boundary of confined and deconfined states of nuclear matter was made in 1975[6].

At low temperatures and chemical potentials, quarks and gluons are confined in the form of hadrons, in which the strong nuclear force tightly binds quarks within hadrons, a state known as *hadronic*

matter.

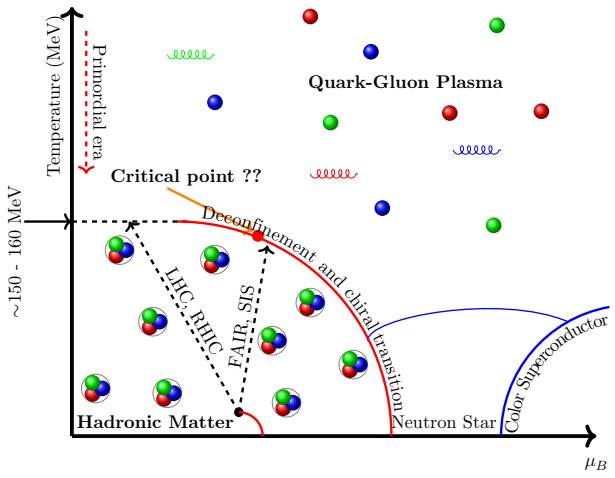

Figure 1.2: QCD phase diagram representing different possible phases of quarks and gluons at different temperatures and baryon chemical potential.

However, at a low chemical potential and high temperature, a condition that is thought to have been present at the time of the Big Bang, the hadronic matter is no longer confined, and quarks and gluons move freely, forming QGP. As the temperature decreased a few microseconds after the Big Bang, quarks recombined again in the form of hadrons. Based on the theoretical 2+1 flavor lattice QCD calculation, such a transition from a QGP to a hadronic phase is a smooth crossover, and it occurs around the temperature 150 - 160 MeV when moving from the high-temperature to the low-temperature regime.

Experimentally, the study of hot and dense strongly interacting matter at vanishing baryochemical potential ($\mu_B \approx 0$) and high temperature is pursued through high-energy heavy-ion collisions. Such conditions are created in the lab by colliding heavy nuclei at different accelerator facilities operating over a broad range of centre-of-mass energies per nucleon pair ($\sqrt{s_{NN}}$), listed as follows.

- **Super Proton Synchrotron (SPS)** at CERN — operating in the low-to-intermediate energy range, $\sqrt{s_{NN}} \sim$ 5–20 GeV;[7]
- **Relativistic Heavy Ion Collider (RHIC)** at Brookhaven National Laboratory (BNL) — covering the intermediate-to-high energy range, up to $\sqrt{s_{NN}} \sim 200$ GeV;[8]
- **Large Hadron Collider (LHC)** at CERN — reaching the highest currently accessible energies, up to $\sqrt{s_{NN}} \sim 5.02$ TeV for Pb+Pb and about 13–14 TeV for p+p collisions.[9]

These experimental programs together span a wide range of high collision energies, thereby probing the transition from the baryon-rich region to the nearly baryon-free regime of the QCD phase diagram. Experimentally measured freeze-out data, along with various theoretical models' predictions of the cross-over, and freeze-out data for a 2+1 flavour QCD phase diagram, is shown in Figure 1.3

Figure 1.3 compares the temperature (T) and baryochemical potential (μ_B) dependence of the QCD phase boundary, as obtained from various theoretical approaches and lattice QCD calculations. At

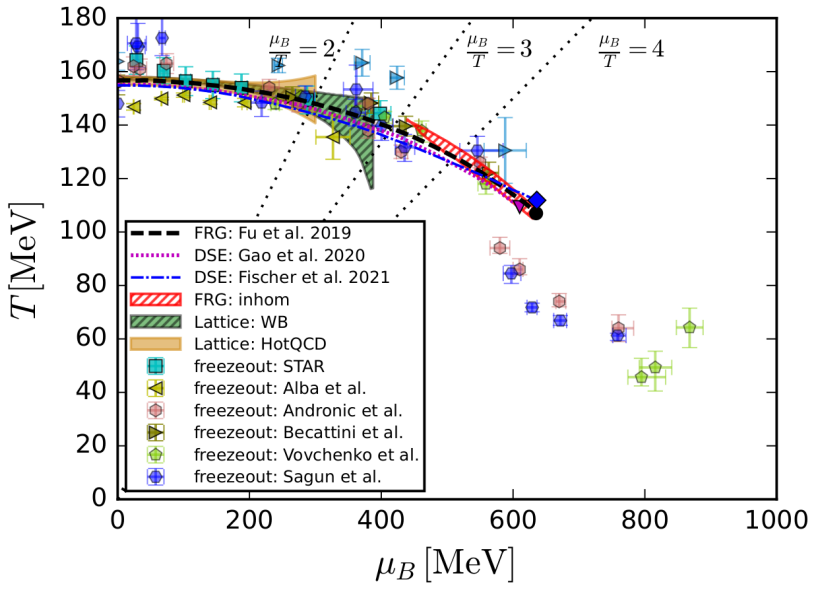

Figure 1.3: QCD phase diagram for the 2+1 flavour in comparison with various theoretical predictions and measured experimental freeze-out data.[10]

small values of $\mu_B/T \lesssim 2$, the predictions from the functional renormalization group (fRG) and Dyson–Schwinger equation (DSE) frameworks show good quantitative agreement with the lattice QCD results (WB and HotQCD). This consistency confirms that the different non-perturbative methods yield a reliable description of the QCD crossover transition in the region where lattice calculations are feasible. For larger baryochemical potentials ($\mu_B/T \gtrsim 2$), direct lattice simulations become unreliable due to the so-called sign problem.[11] Recent calculations by various theoretical approaches have predicted a Critical End Point (CEP) at approximately $(T_{\mathrm{CEP}}, \mu_B^{\mathrm{CEP}}) = (100 - 160,\ 600 - 700)$ MeV, excluding the region $\frac{\mu_B}{T} = 3$. This means the CEP's location is well within the high-baryon-density and moderate-temperature zones.[12, 13, 14, 15]

Additionally, the region of the phase diagram at high net-baryon density and moderate temperature, where theoretical models predict a Critical Point (CP) and a first-order phase transition, remains largely unexplored. To investigate this regime of the phase diagram, several experimental efforts have been undertaken, as discussed earlier, and some of them have been upgraded to explore the region of high density and lower temperature, such as the STAR fixed-target experiment, BES-II Program, ($\sqrt{S_{NN}}$ = 3 - 7 GeV).[16] Also, several new experimental facilities have been proposed and are under construction. These facilities are:

- Baryonic Matter at Nuclotron (BM@N) at Nuclotron-based Ion Collider fAcility (NICA), JINR, is designed to perform nucleon-nucleon Center-Of-Mass (COM) energy between 4 GeV and 11 GeV.[17]

- NA61/SHINE at CERN SPS, focusing on deconfinement and the search for the critical point in the QCD phase diagram in the energy range of beam momenta from 13 AGeV/c to 150 AGeV/c.[18]

- The High-Intensity heavy-ion program at J-PARC (J-PARC-HI), Japan, is intended to explore the QCD phase diagram in high baryon density within a nucleon-nucleon Center-of-Mass energy ($\sqrt{S_{NN}}$) range of approximately 2 to 6.2 GeV.[19]

- Compressed Baryonic Matter(CBM) at a Facility for Anti-proton and Ion Research (FAIR), focusing on exploring the phase diagram at high baryon density in an energy range from 2 AGeV/c to 12 AGeV/c. Further insights on the CBM experiment at FAIR are discussed in the **Section 1.4**.

1.3 Physics Case of the CBM Experiment

As discussed in **Section 1.2**, several recent theoretical calculations suggest that the CEP may be located in the region of high baryon density and moderate temperature. The CBM experiment therefore has a unique opportunity to explore this part of the QCD phase diagram, since its energy range, $\sqrt{S_{NN}}$ = 2.7–4.9 GeV, corresponds to net baryon densities of $\rho_B \sim 2$–$5, \rho_0$, baryochemical potentials[1] of $\mathcal{O}$(800–500) MeV, and temperatures of $\mathcal{O}$(60–120) MeV - all well within the theoretically favored region for a possible Critical Point.

Experimentally, the properties of nuclear matter can be studied through various particle observables. These observables include dilepton studies, event-by-event fluctuations, flow studies, strangeness, and charm measurements. Additionally, the study of abundantly produced particles, such as hypernuclei and multi-strange hyperons, provides valuable insights about the hyperon-nucleon and hyperon-hyperon interaction. However, certain limitations arise in studying these observables experimentally due to constraints on detector acceptance and beam luminosity, as well as their low production multiplicity at low energies, as shown in Figure 1.4.

[1] The baryochemical potential and chemical freeze-out temperature as a function of the Center-of-Mass (COM) energy can be parametrized as [20, 21]:

$$\mu_B(\sqrt{s_{NN}}) = \frac{d}{1 + e\sqrt{s_{NN}}} = \frac{1.308 \pm 0.028 \text{ GeV}}{1 + 0.273 \pm 0.008 \text{ GeV}^{-1}\sqrt{s_{NN}}}$$

$$T(\mu_B) = a - b\mu_B^2 - c\mu_B^4$$
$$= 0.166 \pm 0.02 \text{ GeV} - (0.139 \pm 0.016) \text{ GeV}^{-1}\,\mu_B^2 - (0.053 \pm 0.021) \text{ GeV}^{-3}\,\mu_B^4$$

with μ_B and T expressed in GeV.

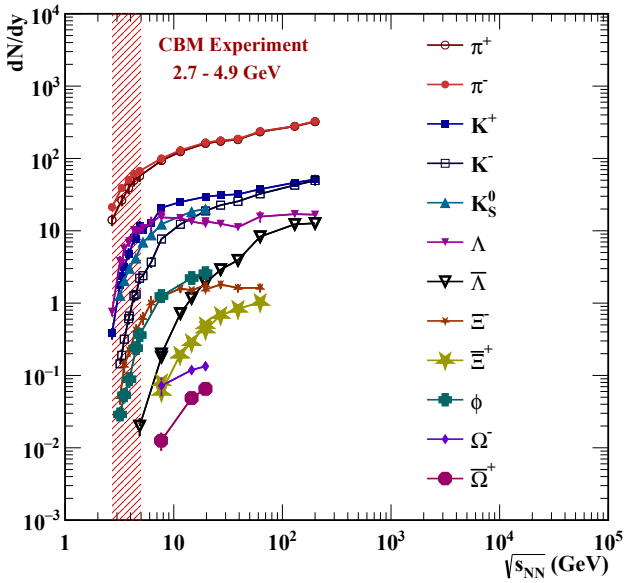

Figure 1.4: Compilation of measured particle yield as a function of the Center of Mass(COM) energy.[22]

Figure 1.5 illustrates the comparison of interaction rates versus collision energy ($\sqrt{S_{NN}}$) GeV for various existing and upcoming heavy-ion physics facilities, covering both fixed target and collider experiments.

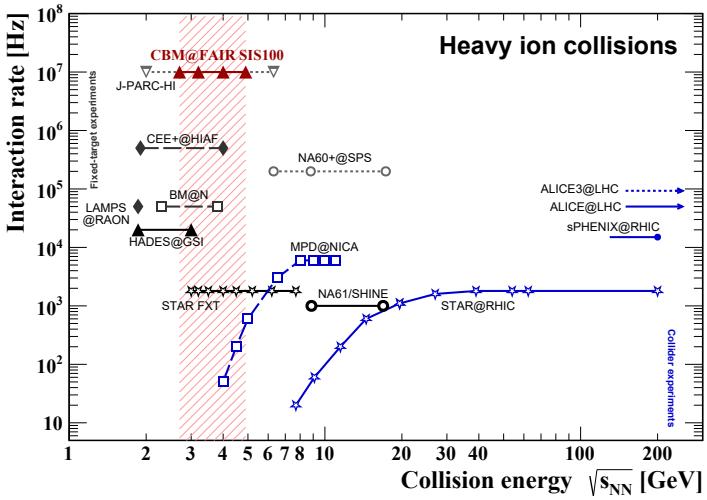

Figure 1.5: Interaction rate of the different heavy-ion physics experiments as a function of collision energy($\sqrt{S_{NN}}$). Various fixed-target and collider-based heavy-ion physics facilities, existing, planned, and under construction, are marked in black and blue colors, respectively, adapted and modified from[23].

Compared to other experiments' interaction rates, as shown in Figure 1.5, the CBM will be operating at a $\sim$ 10 MHz interaction rate, enabling CBM to perform the multi-differential analysis of low multiplicity rare probes such as dileptons, multi-strange hyperons, hypernuclei, etc, with high statistical precision and will contribute to the search for a critical point and many other physics

aspects that are still not probed at high baryon density and moderate temperature. Some of the physics cases that CBM will probe experimentally are discussed in the following sections.

1.3.1 Flow Studies

In relativistic nucleus–nucleus collisions, a hot and dense medium is created and consists of deconfined quarks and gluons at sufficiently high energy densities. The collective motion of the particles produced in response to pressure gradients that build up during the initial stage of a newly created, hot, dense medium is known as flow.[24] The flow directly sheds light on the Equation of State (EOS) by studying differential analysis of the various observables through pressure gradient, viscosity, and entropy density, etc, as the EOS determines how "*Stiff*" or "*Soft*" the medium is and provides information about the transition from a hadronic phase to QGP phase as a stiff EoS directly related to the immense pressure for a given energy density meaning produces strong flow.

At the same time, a soft EoS corresponds to a lower pressure; for example, near a phase transition, it leads to weaker flow. The flow in heavy-ion physics is defined using the Fourier expansion[25] as follows:

$$E\frac{d^3N}{dp^3} = \frac{d^2N}{\pi\, dy\, d(p_t^2)}\left[1 + 2\sum_{n=1}^{\infty} v_n(p_t, y)\, \cos(n(\phi - \Psi_{\mathrm{RP}}))\right] \tag{1.3}$$

where ϕ is the azimuthal angle of the emitted particle, Ψ_{RP} is the reaction-plane angle, and v_n are the Fourier coefficients quantifying the strength of the n^{th} harmonic flow. In particular, v_1 denotes *"directed flow"*, and v_2 *"elliptic flow"*, and higher orders (v_3, v_4, ...) describe finer structures arising from initial-state fluctuations.

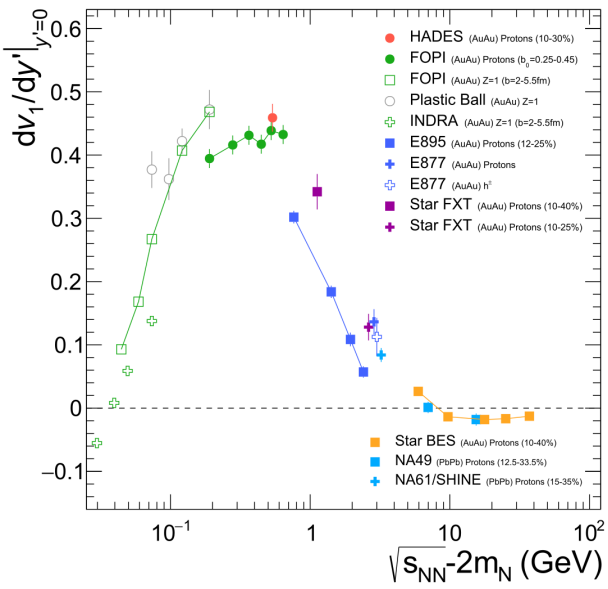

Figure 1.6: Excitation function of the directed flow slope $(dv_1/dy)_{y=0}$ for protons as a function of the subtracted centre-of-mass energy $\sqrt{s_{NN}} - 2m_N$, compiled from various heavy-ion experiments.[26]

The directed flow (v_1) characterizes the sideward collective motion in the reaction plane and the early-stage pressure gradient, therefore sensitive to softening or stiffening of the QCD matter. On the other hand, the elliptic flow (v_2) describes the anisotropy of particle emission between the in-plane and out-of-plane.

Figure 1.6 shows the directed flow measurements in which the slope exhibits a characteristic energy dependence, rising rapidly with in-

creasing beam energy, reaching a maximum around $E_{\text{beam}}/A \approx 1$ GeV, and subsequently decreasing towards zero at higher energies. Such an effect can be understood by considering two scenarios: at low energy, the compression of nuclear matter is higher, increasing pressure and moving the spectator nucleons sideways, resulting in increased directed flow. In contrast, at higher energies, the spectator nucleons pass through the overlap zone very quickly, resulting in reduced pressure transfer to the light nuclei. One can see that the directed flow reaches its highest magnitude in the 1-2 AGeV range, where the compression of the dense baryonic matter and the expansion dynamics are the most significant.

Figure 1.7 shows the results of *"elliptic flow"* from various heavy-ion physics experiments at different energy ranges. We observe the sign of v_2 from negative to positive as we go from a lower energy to a higher energy. The observed signature can be explained by the passage of time for the spectator and the expansion of the fireball. At a lower energy regime, the spectator has a long passage time[2] ($t_{pass} \approx 30$ fm/c); therefore, it affects the medium's expansion.

In addition, the collision dynamics involved at low energy are dominated by attractive nuclear mean-field interactions and long shadowing times of the spectator. These effects lead to a rotational-like *"squeeze-out"* motion, where matter expansion occurs preferentially, in the direction where the spectator's shadowing effect is less (*"out-of-plane"*), resulting in a negative v_2.

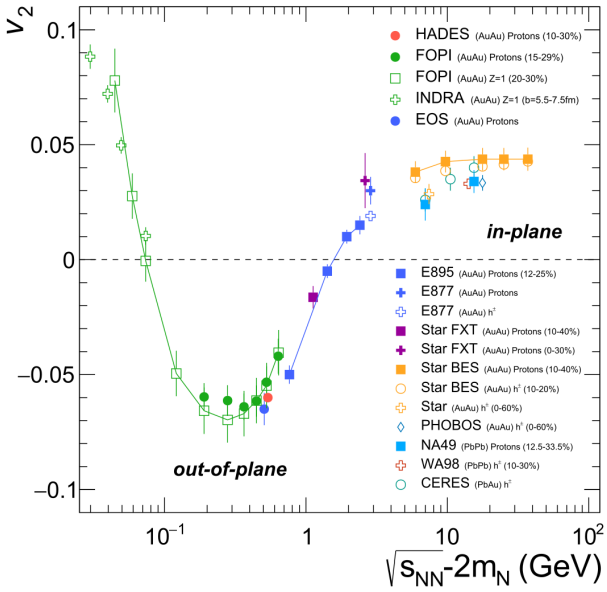

Figure 1.7: Excitation function of the elliptic flow coefficient v_2 for protons and light charged particles from different experiments.[26]

However, as the beam energy increases, spectators pass through the medium more quickly, and multiple nucleon–nucleon scatterings generate a strong repulsive pressure during the early, hot, and dense stage of the collision. This pressure drives an in-plane expansion, the transition from an attractive mean–field–dominated rotational-like flow to a pressure-driven collective expansion of the medium.[27]

[2]The passage time of the spectators is estimated as $t_{\text{pass}} = \frac{2R}{\gamma v_s}$, where R denotes the nuclear radius, v_s the spectator velocity in the center-of-mass frame, and γ the corresponding Lorentz factor. At low beam energies ($t_{\text{pass}} \sim 30$ fm/c), the spectators remain in the vicinity of the participant zone for a long time, hindering the in-plane expansion and leading to negative elliptic flow ($v_2 < 0$). At higher beam energies ($t_{\text{pass}} \sim 10$–15 fm/c), the spectators move away rapidly, allowing the compressed matter to expand freely in the reaction plane, resulting in positive v_2.

1.3.2 Event-by-Event Fluctuation

Event-by-event fluctuations of conserved quantities, such as the net baryon number and net charge, are powerful tools for exploring the properties of strongly interacting matter created in heavy-ion collisions. The fluctuation in the conserved quantity is directly related to the thermodynamic susceptibilities of the QCD matter, which reflects how these quantities respond to the change in temperature and the baryochemical potential. In addition, near the critical point in the QCD phase space, the correlation length of the system is expected to increase, thereby leading to fluctuations in the conserved quantities.[28, 29] This deviation can be studied using higher-order cumulants, such as skewness and kurtosis, of observables like the net-proton number.

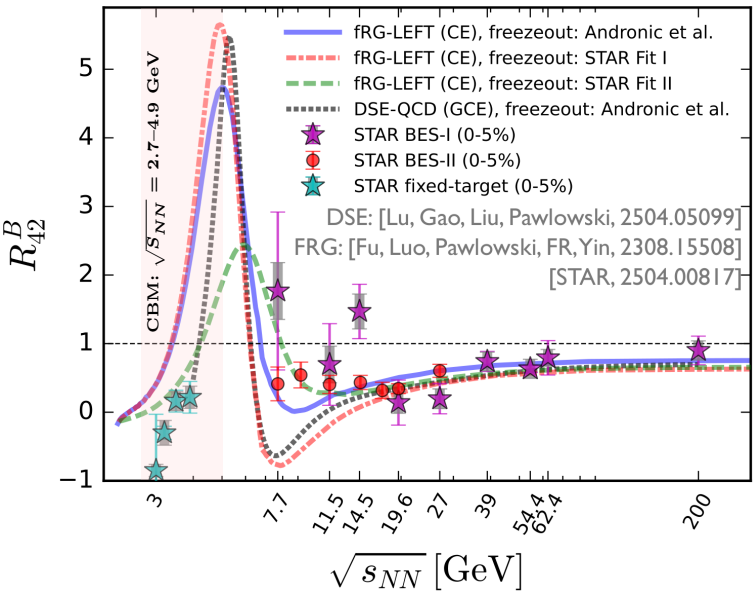

Figure 1.8: Energy dependence of the baryon number fluctuation from various theoretical model-based predictions and net-proton fluctuation data points for kurtosis $\kappa\sigma^2$ in most-central Au+Au collisions measured at the STAR experiment (RHIC) [30, 31]. The shaded band indicates the CBM@FAIR energy window.[33]

Significant measurements of proton and net-proton fluctuations have been performed by the STAR experiment at RHIC, using data from the Beam Energy Scan (BES-I and BES-II, including fixed-target)[31, 32], and by the HADES experiment at GSI[34]. Figure 1.8, represents the ratio of the fourth- to second-order cumulants ($\kappa\sigma^2$) of the net-proton and is directly related to the baryon-number susceptibilities of QCD matter. A non-monotonic dependence of this quantity on the collision energy would indicate the presence of large correlation lengths associated with critical fluctuations near the QCD critical point. At higher energies, where the system is dominated by a partonic phase, $\kappa\sigma^2$ approaches unity, consistent with predictions from hadron resonance gas (HRG) and transport models such as UrQMD, and very recently with the results from a fRG and DSE.

The CBM experiment at FAIR, operating in the beam-energy range corresponding to $\sqrt{S_{NN}}$ = 2.7-4.9 GeV, indicated by the shaded region, will be precisely explored with high statistics in the region of maximum net-baryon density, where such critical phenomena are predicted to become more prominent, as shown by calculations of the fRG and DSE theoretical models.

1.3.3 Dilepton Studies

Dileptons (e^+e^- or $\mu^+\mu^-$ pairs, virtual photons, etc) are clean electromagnetic probes that provide a unique insight into the evolution of the hot-dense medium created during the nucleus-nucleus collision, as they do not participate in hadronic interaction but rather interact electromagnetically. Thus, they can escape the hot, dense, coloured medium undistorted. Consequently, the di-lepton-invariant mass spectrum (M_{ll}) provides a complete picture of the entire collision evolution, as different mass regions are sensitive to the various stages of the fireball evolution and the associated processes, therefore reflecting the conditions at the time of their production.

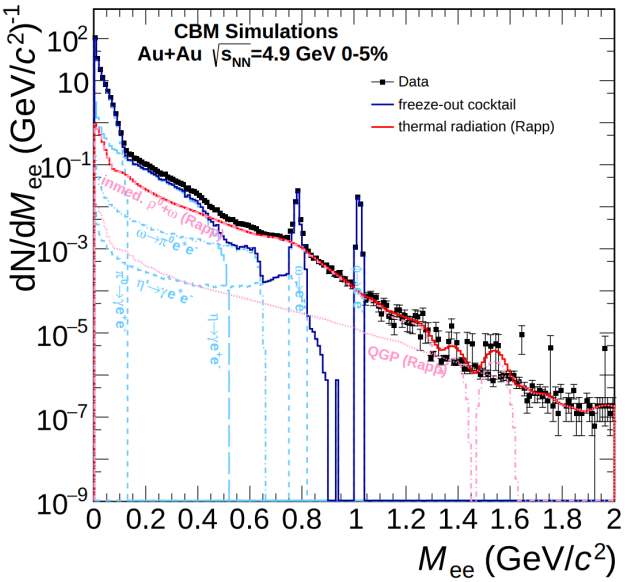

Figure 1.9: Invariavnt mass spectrum of e^+e^- pairs radiated from a central Au+Au collision at 4.9 GeV.[35]

The invariant-mass spectrum of di-leptons comprises distinct characteristic regions as follows:

- **Low-Mass Region (LMR, $M_{ll} < 1.5$ GeV/c^2)**: This region is dominated by decays of light vector mesons (ρ, ω, ϕ) and by Dalitz decays of pseudoscalar mesons (π^0, $\eta \to \gamma e^+e^-$). Among all these probes, the ρ meson is a more interesting probe to investigate because it has a short lifetime ($\tau_\rho \approx 1.3$ fm/c), which is comparable to the lifetime of the fireball created in the collision; therefore, it decays within the medium. Additionally, they undergo

strong interactions with surrounding baryons and mesons, as well as re-scattering.[3,4] These in-medium effects modify the spectra of the ρ meson, typically broadening or melting, which is interpreted as a sign of chiral symmetry restoration. Hence, the LMR serves as a window into the hadronic phase of QCD matter.

- **Intermediate-Mass Region (IMR, 1.5 GeV/c^2 < M_{ll} < 2.5 GeV/c^2)**: In this mass range, contributions from hadronic decays supressed, and the radiation is increasingly dominated by *thermal emission* from the deconfined partonic phase (quark-gluon plasma).[5] The slope of the di-lepton yield as a function of invariant mass in this region directly allows the extraction of an effective temperature T_{slope}. This temperature represents the average space–time temperature of the emitting source and serves as a thermometer of the fireball.

- **High-Mass Region (HMR, M_{ll} > 2.5 GeV/c^2)**: This region is governed by hard QCD processes involving large momentum transfers that produce electromagnetic probes at the earliest stage of the collision. The dominant sources are Drell–Yan pair production and *quarkonium decays* (J/ψ, $\psi' \to l^+l^-$). Since these processes occur before the formation of the thermal medium, they are only weakly influenced by final-state hadronic interactions. Consequently, the high-mass dilepton yield provides a clean probe of the initial partonic dynamics, quarkonium states serves as direct evidence for color screening and the onset of deconfinement in the created medium.

The shape and yield of the di-lepton invariant-mass spectrum therefore provide key information about the temperature, density, and lifetime of the fireball. Figure 1.9 illustrates the invariant

[3] The most relevant processes contributing to the in-medium modification of the ρ meson include:

– **Meson–meson interactions**, such as

$$\rho + \pi \leftrightarrow \pi + \pi \quad \text{and} \quad \rho + \pi \leftrightarrow a_1(1260),$$

which alter the ρ self-energy via coupling to the pion cloud and resonance excitations.

– **Baryon–resonance interactions**, primarily

$$\rho + N \leftrightarrow N^*(1520),\ N^*(1700), \quad \text{and} \quad \rho + \Delta \leftrightarrow N + \pi,$$

which dominate the broadening at high baryon density. The coupling of the ρ meson to these baryonic resonances leads to significant collisional broadening of its spectral function [36, 37, 38].

– **Re-scattering and absorption processes**, such as

$$\pi + \pi \leftrightarrow \rho \leftrightarrow e^+e^-,$$

[4] The first direct measurement of ρ^0 p has been observed through two particle correlation in high-multiplicity ultra-relativistic proton-proton collisions at $\sqrt{S_{NN}}$=13 TeV by the ALICE Collaboration at the LHC[39]

[5] An example of the dominant microscopic process responsible for thermal dilepton production in this region is:

$$q + \bar{q} \to \gamma^* \to \ell^+ + \ell^-,$$

where a quark–antiquark pair annihilates into a virtual photon (γ^*), which subsequently decays into a lepton pair ($\ell^+\ell^-$).

mass spectra of the di-electron pairs from a simulation performed for a central Au+Au collision in the CBM energy at $\sqrt{s_{NN}} = 4.9$ GeV. It displays cocktails from various contributions, such as the decay of various mesons (blue curve) at a chemical freeze-out, also commonly referred to as the *chemical freeze-out cocktail*. In addition, the di-electron pair from a Drell-Yan process and charmonium at this energy is low; therefore, the additional source is from thermal radiation (red curve). Hence, subtracting the chemical freeze-out component from the IMR can provide information about conditions before freeze-out.

By fitting the invariant-mass distribution in the intermediate-mass region with an exponential function of the form[6]

$$\frac{dN_{ll}}{dM} \propto (MT)^{3/2}\, e^{-M/T_{\mathrm{slope}}},$$

The effective *slope temperature* T_{slope} can be extracted and serves as a thermometer of the medium.

As shown in Figure 1.10, the T_{slope} value of the experimental data measured from the High Acceptance Dielectron Spectrometer (HADES) and the North Area (NA)60 experiment, respectively, together with the data point of CBM projections obtained through simulation at different COM energies, delineate the evolution of the medium temperature as a function of collision energy, revealing the "*caloric curve*" of strongly interacting matter. The red curve shows the model-based results at different energy ranges. However, it does not include the first-order phase transition, so it shows a monotonic increase in temperature with increasing energy.[41, 42]

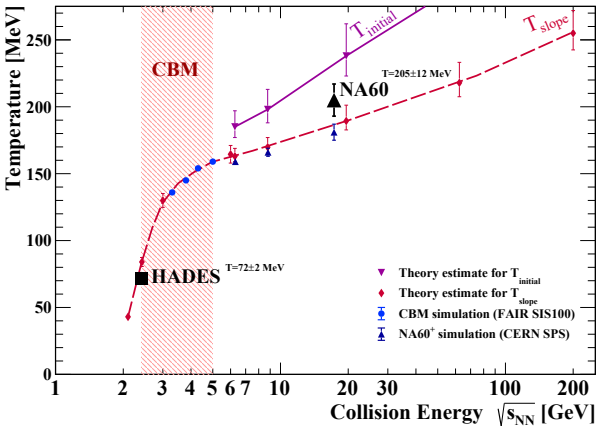

Figure 1.10: Compilation of measured and estimated effective fireball temperatures as a function of the Center-of-Mass (COM) energy per nucleon pair, $\sqrt{s_{NN}}$. The black markers represent experimental results from HADES and NA60, respectively, corresponding to the extracted slope and initial temperatures of the medium. The red dashed curve indicates a theoretical interpolation of the thermal evolution, while the blue circles mark the projected sensitivity and energy coverage of future measurements with the CBM experiment at FAIR.[40]

At the CBM experiment, di-lepton measurements in the beam-energy range 2-12 $A\,\mathrm{GeV}/c$ will bridge the gap between the SIS and SPS domains, exploring the high net-baryon density region where a first-order phase transition is ex-

[6] In the intermediate-mass region ($1.5\ \mathrm{GeV}/c^2 \lesssim M \lesssim 2.5\ \mathrm{GeV}/c^2$), the medium modifications of the electromagnetic spectral function ($\mathrm{Im}\,\Pi_{\mathrm{EM}} \propto M^2$) are relatively small, and under this assumption, a non-relativistic approximation for the thermal dilepton emission rate can be applied in a given form. The expression tells that the invariant-mass spectrum in this range approximately follows an exponential Boltzmann distribution, allowing the extraction of an effective slope temperature T_{slope}.

pected to occur.[43]

1.3.4 Open and Hidden Charm Measurement

The charm quark is heavier, the renormalized charm quark mass $\overline{m}_c = 1.27 \pm 0.02$ GeV [44], than the typical QCD scale that characterizes the onset of non-perturbative dynamics, where the corresponding strong-interaction scale parameter is $\Lambda_{\rm QCD} \simeq 0.2 - 0.3$ GeV.[7] The large mass ($m_c \gg \Lambda_{\rm QCD}$) implies that the creation of charm-anticharm pairs requires significant momentum transfers $Q^2 \gtrsim 4m_c^2$, which predominantly occur in very early stages of a heavy-ion collision, when the relative momenta between interacting partons are still significant. At later times, when the system has thermalized, and the typical energy scales drop to $\mathcal{O}(\Lambda_{\rm QCD})$, the production of additional charm pairs becomes strongly suppressed.[8]

Once they are produced in the early hard interaction, they traverse the hot and dense medium formed in the nucleus-nucleus collision. During this period, they undergo elastic scattering due to interactions with light quarks and gluons, producing a drag force and also changing the direction of their movement (similar to Brownian motion), which steadily reduces their momentum (momentum diffusion). This behaviour can be described by a Langevin equation that incorporates a friction (drag) term and a stochastic diffusion term.[49]

In addition to the elastic scattering, charm quarks also lose energy through inelastic collision when they travel through the colored medium created in the nucleus-nucleus collisions, in which they radiate gluons (*"gluon Bremsstrahlung"*). According to the Baier-Dokshitzer-Mueller-Peigné-Schiff (BDMPS) formalism, the average radiative energy loss increases quadratically with the path length L of the parton,

$$\Delta E = \frac{\alpha_s}{2}\,\hat{q}\,L^2, \tag{1.4}$$

[7] The strong coupling constant of Quantum Chromodynamics (QCD), $\alpha_s(Q^2) = g^2(Q^2)/(4\pi)$, runs with the momentum transfer Q according to the renormalization group equation $\mu\,\mathrm{d}\alpha_s/\mathrm{d}\mu = \beta(\alpha_s)$. At leading order, the QCD β-function is $\beta(\alpha_s) \simeq -\beta_0\alpha_s^2$, with $\beta_0 = (33 - 2N_f)/(12\pi)$ for N_f active quark flavors. Integrating this relation yields the familiar one-loop expression for the running coupling,

$$\alpha_s(Q^2) = \frac{1}{\beta_0\,\ln(Q^2/\Lambda^2_{\rm QCD})},$$

where $\Lambda_{\rm QCD}$ is a constant that defines the non-perturbative energy scale of QCD.[45, 48]

[8] At the beam energies relevant for the CBM experiment at FAIR (2-12 AGeV/c, corresponding to $\sqrt{s_{NN}} \approx 2.7$-4.9 GeV), the production of open and hidden charm occurs near the kinematic threshold. [47] Creating a charm–anticharm pair requires partonic momentum transfers of $Q^2 \gtrsim 4m_c^2 \approx 7$ GeV^2 (for $m_c \simeq 1.3$ GeV), corresponding to hard interactions on a time scale $\tau \sim \hbar c/Q \approx 0.08$ fm/c. Thus, charm quarks are produced within the first $\lesssim 0.1$ fm/c after impact, well before the system reaches local equilibrium. For comparison, the nucleus–nucleus overlap lasts $\sim$ 1–2 fm/c, the fireball thermalizes after $\sim$ 0.5–1 fm/c, and the hadronic expansion proceeds over several tens of fm/c. Consequently, charm quarks traverse the entire evolution of the medium and serve as early-time probes of the high-density QCD matter created in such collisions. [46, 47, 48]

where $\hat{q}$ denotes the diffusion coefficient of the medium, the average transverse momentum squared transferred to the parton per unit length. However, due to the finite mass of the heavy quarks, gluon radiation is suppressed, so-called dead cone effect, at small angles $\Theta < m_c/E$, where E is the charm-quark energy, limiting bremsstrahlung and thus lowering the overall energy loss compared to light quarks.[46, 50]

These interactions may result in partial thermalization and modify the hadronization pattern of charm quarks into open- and hidden-charm hadrons. As a consequence, in-medium effects such as mass shifts, spectral broadening, and suppression of charmonium states are expected. Due to their early formation and subsequent interaction history, charm hadrons serve as sensitive probes of the initial conditions and transport properties of strongly interacting matter at high baryon densities through a nuclear modification factor (R_{AA}) and v_2 flow measurement.

1.3.5 Strangeness and Hypernuclei

"Strangeness" refers to the production of hadrons containing one or more strange (s) quarks, such as hyperons (Λ, Σ, Ξ), and their antiparticles. Strangeness is not present in the initial nuclei, which consist only of u and d quarks; therefore, all strange particles have to be produced during newly created hot and dense matter in the collision. The production of the strange particle is abundant. However, they are interesting probes to study, as their production in strongly interacting matter requires multi-step processes (e.g., such as $N + N \rightarrow N\Lambda K$ or $\pi N \rightarrow \Lambda K$) and is directly linked to the baryon density and lifetime of the fireball.[51]

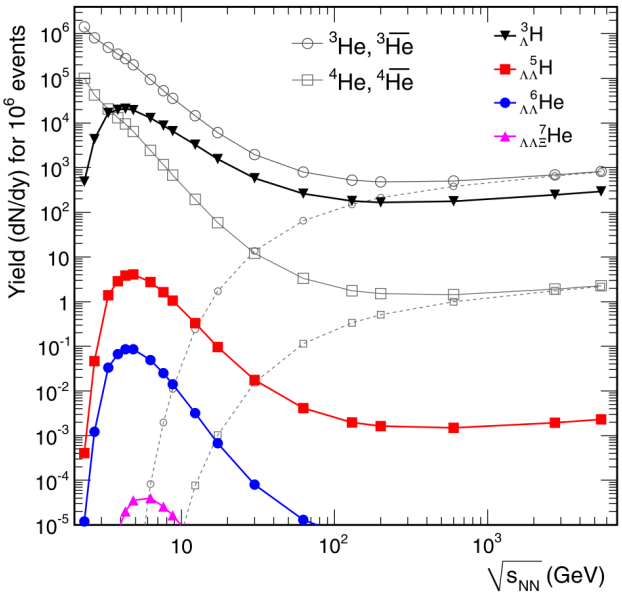

Figure 1.11: Predicted yield of hypernuclei at mid-rapidity vs. energy.[52]

At beam energies accessible at FAIR ($2 - 12$ AGeV/c), the system created in nucleus–nucleus collisions reaches high net-baryon densities ($\rho_B \sim 2{-}5\,\rho_0$) at moderate temperatures. In this regime, hyperons (Λ, Σ, Ξ) are abundantly produced. When a nucleus captures a hyperon, the newly formed nucleus is known as a *hypernucleus*:

$$N + N \to N + \Lambda + K^+, \qquad \Lambda + (A-1)Z \to {}^{A}_{\Lambda}Z.$$

These hypernuclei serve as a unique probe for studying the hyperon–nucleon (Y-N) and hyperon–hyperon (Y-Y) interactions. Precise measurement of the hypernuclear binding energies and lifetimes will help constrain the nuclear equation of state at high baryon densities and address the so-called "*hyperon puzzle*".[53]

We have described in detail the potential physics study at the CBM experiment. In the following section, we provide a brief overview of the FAIR facility at GSI, Darmstadt, and one of its scientific pillars, the CBM experiment.

1.4 The Compressed Baryonic Matter Experiment at FAIR

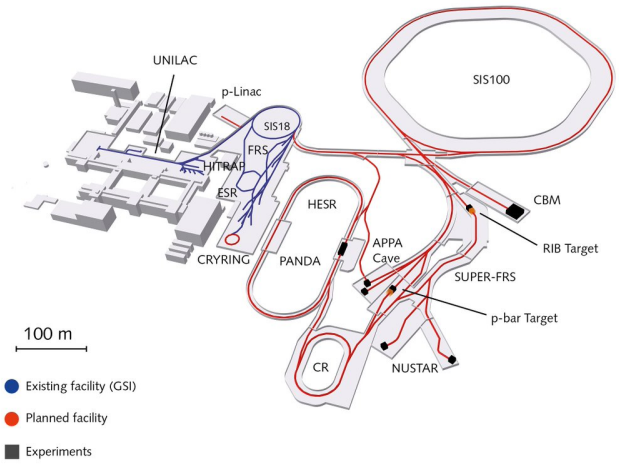

Figure 1.12: Layout of existing and planned GSI-FAIR facility along with the various experimental sites marked in black dots.

The Facility for Antiproton and Ion Research (FAIR)[54] is an under-construction accelerator complex adjacent to the Helmholtzzentrum für Schwerionenforschung (GSI) in Darmstadt, Germany, as shown in Figure 1.12.[9] FAIR will host experiments aimed at studying matter under extreme

[9] FAIR-GSI

conditions found in astrophysical objects, thus providing fundamental insights into its properties.

The scientific program of nuclear and hadron physics at the FAIR will be addressed by its four main scientific pillars:

- Atomic, Plasma Physics, and Applications (APPA)
- Compressed Baryonic Matter (CBM)
- Nuclear Structure, Astrophysics, and Reactions (NUSTAR)
- AntiProton Annihilation at Darmstadt (PANDA)

Currently under construction, the FAIR facility uses the synchrotron accelerator ring, known as Schwerionensynchrotron-100 (SIS-100), to deliver a high-intensity proton beam and various heavy-ion beams. SIS-100 denotes the bending power of the dipole magnets about to be employed in the accelerator ring. The kinetic energy of the beam depends on the actual source based on the Equation 1.5.

$$\frac{T}{A} = \sqrt{\left[0.3 \cdot B \cdot R \cdot \left(\frac{Z}{A}\right)\right]^2 + m^2} \; - \; m, \tag{1.5}$$

Where Z and A are the charge and atomic number, B = Dipole magnet power, R = Synchrotron radius, m = nucleon mass

Source	$P_{lab,max}$	$\sqrt{S_{NN,max}}$
Heavy ions (Au)	12 AGeV/c	4.9 GeV
Light ions (Z/A = 0.5)	14 AGev/c	5.3 GeV
Proton	29 GeV/c	7.5 GeV

Table 1.1: A summary of the beam energy accessible for various species of ions using SIS-100.

Table 1.1 summarizes the accessible energy of the various light, heavy-ion, and proton beams using the SIS-100 accelerator.[54]

1.4.1 Detector Subsystem of the CBM

The fixed target geometry of the CBM, as shown in Figure 1.13, covers the angular polar angle between $2.5^{\circ} < \theta < 25^{\circ}$, enabling the acceptance of particles in the forward and mid-rapidity

regions. The CBM is designed to operate at high event rates $\sim 10^9$ Au+Au particles/sec and beam intensity with an interaction target of 1% (10^7 collisions/sec (10 MHz)) in free-streaming mode. The experiment is currently under construction and is expected to have its first beam data at the end of 2028.[55]

Figure 1.13 illustrates the conceptual arrangement of various detectors along the beam axis in the CBM experiment. Each detector subsystem has been explicitly optimized for a distinct task, including the precise reconstruction and vertexing of all charged hadronic and electromagnetic probes generated in a nucleus-nucleus collision, as well as time-of-flight capabilities and other functions. A brief overview of each detector subsystem and its functionality is provided below.

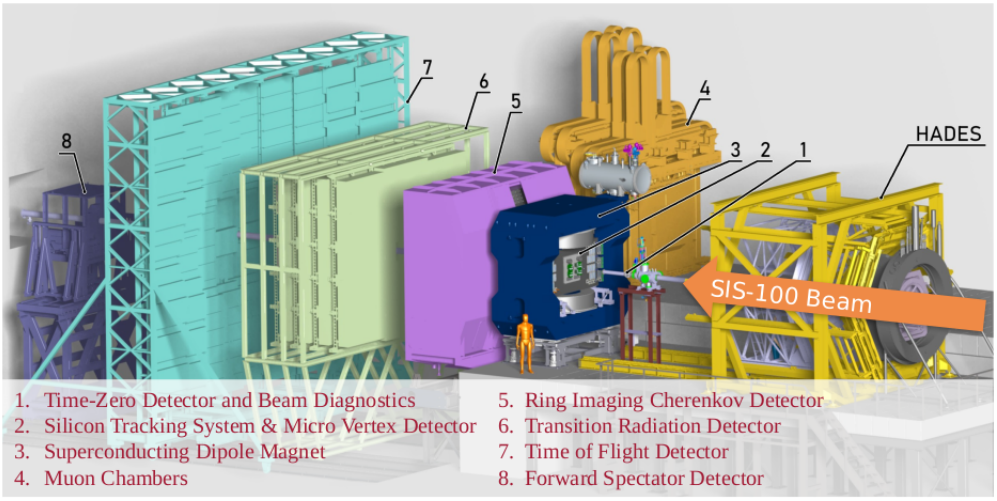

Figure 1.13: CBM experiment detector setup.

- **BMON:** Beam Monitoring detector is a fast and radiation-hard system designed to provide the T0 information for a Time-of-Flight(TOF) requirement for the beam of protons or heavy ions. It is made of either **P**oly-**c**ystiline or **S**ingle-**c**rystal CVD (**pc**-CVD or **sc**-CVD) diamond because of its excellent timing and radiation-hard characteristics.

- **MVD:** The Micro-Vertex Detector consists of four detector stations positioned between 5 cm and 20 cm downstream of the target. It utilizes Monolithic Active Pixel Sensors (MAPS) due to their high spatial resolution, which enables the resolution of the primary and secondary vertices of rare, short-lived particles, such as open-charm and D-meson decays.[10]

- **STS:** Silicon Tracking System uses $\sim$ 876 micro-strip silicon sensors of thickness 320 $\pm$ 15

[10] Typical decay lengths ($c\tau$) of rare probes of interest are: $\Xi^0 \approx 8.7$ cm, $\Xi^- \approx 4.9$ cm, $K_S^0 \approx 2.68$ cm, $\Lambda \approx 7.9$ cm, $\Sigma^- \approx 4.4$ cm, $\Sigma^+ \approx 2.4$ cm, $D^0 \approx 123$ μm, $D^\pm \approx 312$ μm, $D_s^\pm \approx 151$ μm, $\Omega \approx 0.25$ μm, $\Omega^\pm \approx 24.6$ μm. These lifetimes underscore the need for a high-resolution vertex detector to identify short-lived charm hadrons, hyperons, and other particles in the CBM.

μm. These sensors are approximately in four distinct sizes, ((6×2 cm^2), (6×4 cm^2), (6×6 cm^2) & (6×12 cm^2)) assembled in 8 tracking stations. The first STS station is positioned 30 cm downstream of the target, with subsequent stations placed at uniform intervals in both the STS upstream (STSu) and the STS downstream (STSd), maintaining a 10.5 cm gap between them. The STS is designed to reconstruct the trajectories of primary and secondary particles, determine their momenta, and accurately identify both primary and secondary vertices.

- **Superconducting dipole magnet:** The dipole magnet houses the MVD and STS detectors, and generates a vertical magnetic field with an integrated field strength of 1 T·m.

- **RICH:** The Ring-Imaging Cherenkov detector operates on the principle of Cherenkov radiation. It is designed to identify the dielectrons using UV photodetector equipped with multi-anode photomultipliers.

- **MUCH:** The Muon Chambers (MUCH) detector consists of four stations, where stations 1 and 2 utilize Gaseous Electron Multipliers (GEMs), and stations 3 and 4 employ Resistive Plate Chambers (RPCs). The detector system is equipped with absorber layers made of graphite and iron, placed between the active detection layers, to filter out hadrons. The MUCH detector identifies di-muon pairs produced from the decays of low-mass vector mesons (ρ, ω) and J/ψ.

- **TRD:** When a charged particle traverses from one medium to another with a different dielectric constant, there is an emission of electromagnetic radiation known as transition radiation. TRD utilizes the Multi-Wire Proportional Counter, filled with Xe/CO_2 gases, along with an adequate radiator. The TRD detector plays a critical role in the CBM experiment by performing the following tasks, such as identifying the electron and positron pairs with momentum $\geq$ 1.5 GeV/c and extending the electron identification capabilities of the RICH detector above $\geq$ 5 GeV/c. Additionally, it suppresses the pion effectively, resulting in a better signal-to-background ratio for the electron pairs. Furthermore, it provides valuable information for measuring nuclear fragments via their energy loss in TRD, which cannot be achieved alone with the Time-of-Flight detector.

- **TOF:** Time-of-Flight serves the purpose of identifying the hadrons, such as pions, kaons, protons, and the light nuclei, by measuring their velocity to calculate the mass of the particles in combination with the momentum information provided by the STS detector. It uses the Multi-gap Resistive Plate Chamber as an active detector. TOF detector is located $\sim$ 7m downstream from the target position.

$$\beta = \frac{L}{t_{flight}} = \frac{p}{E} \tag{1.6}$$

where L and t_{flight} are denoted as the track length and time-of-flight.

Equation 1.6 can be rewritten as:

$$\beta = \frac{p}{\sqrt{p^2 + m^2}} \tag{1.7}$$

$$m^2 = p^2\left(1 - \frac{1}{\beta^2}\right) \tag{1.8}$$

- **FSD:** Forward Spectator Detector uses a scintillator detector placed at the very end of the setup. It is used to measure the spectators, i.e, nucleons that do not participate during the collision. This measurement helps determine the orientation of the reaction plane and the centrality of the collision beam.

The CBM physics program will be conducted using two distinct setup configurations, optimized for specific types of particle identification:

- Hadron and Electron identification
- Muon identification

The core difference in the setup configuration lies in the placement of the RICH and MUCH detectors. When running the experiment for the hadrons and the electron physics program, the RICH detector will be used. However, by swapping the RICH detector placement, the MUCH detector will be used for muon identification. The need for two distinct setup configurations in the CBM experiment arises because the MUCH detector consists of graphite absorber plates interspersed between its active detector layers. These absorber layers effectively filter the hadrons, preventing them from reaching further downstream detectors, such as the TOF and FSD.

The combination of precise tracking, particle identification, and secondary-vertex reconstruction in CBM will enable the measurement of multi-strange hyperons and light hypernuclei, providing new insights into the properties of dense baryonic matter and the role of strangeness in the QCD phase diagram. Therefore, in the CBM experiment, two tracking sub-detector systems are used. One of them is known as the Micro-Vertex Detector (MVD), which is placed very close to the target. MVD consists of four detector stations, placed consecutively in a range of 4 cm to 12 cm. The

primary purpose of this detector is to provide the precise reconstruction of the short-lived particles. Another detector system is called the Silicon Tracking System (STS), and further details about this system are discussed in **Section 1.5** and its physics performance in **Chapter 5**.

1.5 Silicon Tracking System

The Silicon Tracking System[56], known as STS, is one of the tracking detector subsystems of the CBM experiment, located inside the dipole magnet (see Figure 1.14), playing a crucial role in tracking charged particles produced in nucleus-nucleus collisions and determining their momentum.

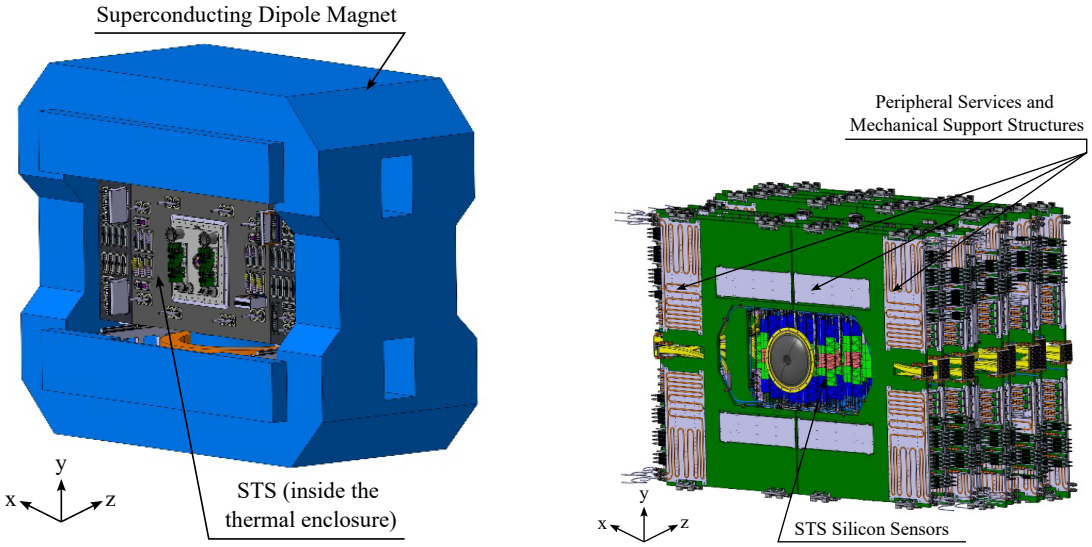

(a) (b)

Figure 1.14: Figure 1.14a shows a CAD model of the STS detector system placed inside the magnet, and Figure 1.14b represents the active area and peripheral mechanical support structure.

There are specific requirements that STS must meet, listed below.

- Acceptance polar angle $2.5^\circ < \theta < 25^\circ$
- Momentum resolution $\frac{\Delta p}{p} \sim 1.5\%$.
- Track reconstruction efficiency $\geq 95\%$ for particles with momentum >1 GeV/c.
- Radiation hard $\sim 10^{14}$ MeV n_{eq} cm^{-2}
- Low material budget to reduce multiple scattering.

STS uses the double-sided micro-strip, n-type, silicon sensors of the four distinct sizes, approximately, 6.2×2.2 cm^2, 6.2×4.2 cm^2, 6.2×6.2 cm^2, and 6.2×12.4 cm^2 manufactured at Hamamatsu

Photonics K.K.[57] as can be seen from Figure 1.15.

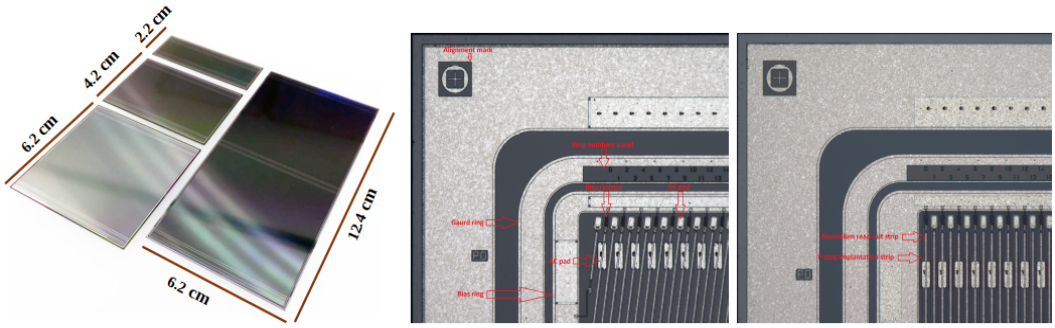

Figure 1.15: Double-sided double metal microstrip silicon sensor of four different variants used in the eight tracking stations of the STS detector

These sensors consist of 1024 implanted strips of p^+ and n^+ on each side, with a pitch width of 58 μm. The pitch width of a sensor provides a spatial resolution $\frac{58\ \mu m}{\sqrt{12}} \sim 16.7\ \mu$m. The strips on the $p-$side of the sensors are inclined at an angle of 7.5° w.r.t the $n-$side. The strip stereo angle of 7.5° was chosen to reduce ghost hits. Each variant of the sensors has a thickness of $320 \pm 15\ \mu$m, which contributes to the material budget $\sim 0.34\% X_0$ per sensor.

Parameter	Specification
Sensor size	6.2×2.2 cm^2, 6.2×4.2 cm^2, 6.2×6.2 cm^2, 6.2×12.4 cm^2
Silicon type	$n-$Type
Crystal orientation	$< 100 >$
Sensor thickness	$320 \pm 15\ \mu$m
Number of strips ($p-$ & $n-$side)	1024
Strip pitch ($p-$ & $n-$Side)	58 μm
Strip implant width (p & $n-$side)	10 μm
Strip angle ($p-$side)	7.5°
Strip metal width	20 μm
Bias resistor	Poly-silicon (1 MΩ)
Readout	AC - readout
Guard ring ($p-$ & $n-$side)	Single
Double metal	$p-$side
$p-$side metal/ Thickness	Al / double layer (1.5 μm)
$n-$side metal/ Thickness	Al / (1.5 μm)

Table 1.2: Specification of the microstrips silicon sensors.

The choice of using different sensor sizes aims to cover the maximum area while minimizing the number of readout channels. Specifically, the smallest sensor size 6.2×2.2 cm^2 has been planned to be used near the beam-pipe area due to the high granularity being essential, enhances the spatial resolution in areas with high particle density, allowing for more precise tracking and measurement of particle interactions of about 700 particles in Au+Au collision at the highest beam momentum

12 AGeV/c, based on UrQMD model simulations of minimum-bias events (see **Appendix E**, Figure E.2). Further details on the sensor specification, such as crystal orientation, the material used in the bias resistor, and the strip metal width and thickness, are described in Table 1.2.

As shown in Figure 1.16, each sensor strip is connected to 32 ultra-thin micro-cables. These micro-cables are composed of aluminium and polyimide, with thicknesses of 14 μm and 10 μm, respectively.

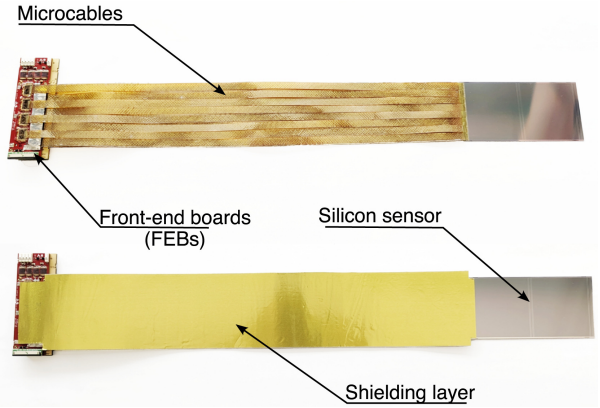

Figure 1.16: Sensors with micro-cables and Front-end-Electronics Boards known as Module.

The other end of the micro-cables is connected to the Front-End Electronics Boards (FEBs), which are responsible for signal amplification and processing. Each sensor is interfaced with two FEBs: one dedicated to the $p-$side and the other to the $n-$side. When a particle passes through the sensor, it generates an electrical signal proportional to the energy it deposits. This signal is transferred via micro-cables to the FEBs, where Application Specific Integrated Circuit processes the signal, called ASICs. Each side of the FEBs is equipped with 8 custom-designed self-triggering SMX2 ASICs, with each providing 128 channels. These ASICs measure the signal amplitude in a dynamic range of ($<$ 15 fC; 5-bit) and time resolution $\sim$ 5 ns, allows the STS for precise measurement of the 3D coordinates(x, y *and* z) along with time and energy loss (dE/dx) measurements in particle tracking.

The readout electronics are positioned in the peripheral area of the active region, minimizing the material budget within the physics acceptance. The micro-cables maximum length from the detector's core to the peripheral area is $\sim$ 500 μm, of about thickness 784 μm, contributing approximately $\sim 0.124\% X_0$ per module. Silicon sensors connected to the micro-cable and FEBs are called *Module*.

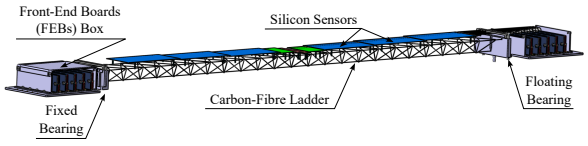

Figure 1.17: CAD model of the CF-ladder along with a sensor mounted on it and other electronics components.

Each sensor module is overlaid on the support structure known as the *ladder*, with additional support provided by L-legs, achieving an alignment accuracy of ± 100 μm[58] (see Figure 1.17). The ladder is made of carbon fibre, ensuring light weight and mechanically stable structure. Nearly 106 ladders of different lengths are used, with a maximum ladder length span-

ning up to 970 mm, and can host $\sim$ 10 modules. The corresponding FEBs connected to the modules are housed in the so-called FEB box, placed outside the physics acceptance as shown in Figure 1.18.

In total, the detector comprises $\sim$ 876 silicon sensor modules, resulting in approximately 1.8 million channels. These modules are arranged on varying ladders and mounted onto a C-shaped aluminium support structure, called the C-Frame (see Figure 1.18). A total of 20 such C-frames, each with a thickness of 1.5 cm, are used, with each C-frame capable of accommodating up to four ladders on either side of it. Also, C-frames accommodate the GBT-based readout boards, FEASTMP-based power boards (POBs) and various cooling components essential for the operation of readout electronics and sensors, providing a compact integration of the various detector hardware elements.

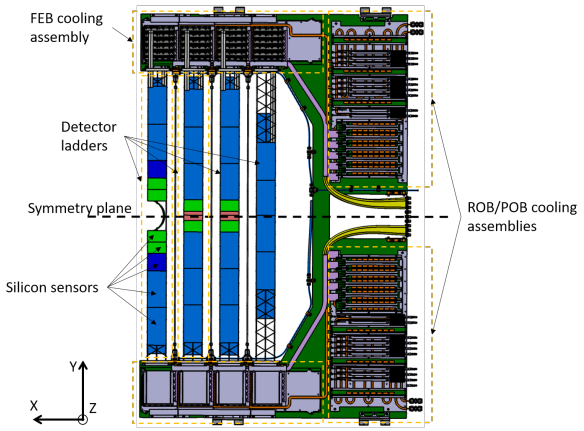

Figure 1.18: CAD model of the C-frame support structure for the ladders and other electronics components.

The C-frames are arranged at equal 105 mm intervals along the z-axis, maintaining left-right symmetry. Together, they form a total of eight tracking stations. These tracking stations are enclosed in a thermal enclosure, consisting of a sandwich structure made of carbon fiber and Airex foam. With a section of the beam-pipe, made of carbon fiber, at the center of the tracking stations. Overall, integrating all hardware components except the ladders, sensors, micro-cables, and beam pipe ensures a low material density in the active area of the STS, thereby optimizing particle tracking and momentum resolution.

In addition, efficient thermal management is crucial for the long-term operation of the STS detector, at least considering 10 years of operational scenario (referred to as End of Lifetime (EOL)), to nullify the effect of the radiation damage in the silicon bulk due to the high radiation environment and the STS designed must withstand a non-ionising fluence (Φ_{eq}) of up to 10^{14} n_{eq} (1 MeV)/cm^2. The study has been varied using sensor prototypes from 2014 to 2015. The study focused on the full-depletion voltage and charge collection efficiency of the irradiated sensors. Moreover, the FLUKA calculation shows that accumulated Φ_{eq} over the expected operational scenario of the CBM will sum up to 0.24×10^{14} n_{eq} (1 MeV)/cm^2(see Figure 1.19), which means the EOL Φ_{eq} will only be accumulated after 40 years of operation.

The fully integrated STS is placed inside a thermally insulated box. During operation, the electron-

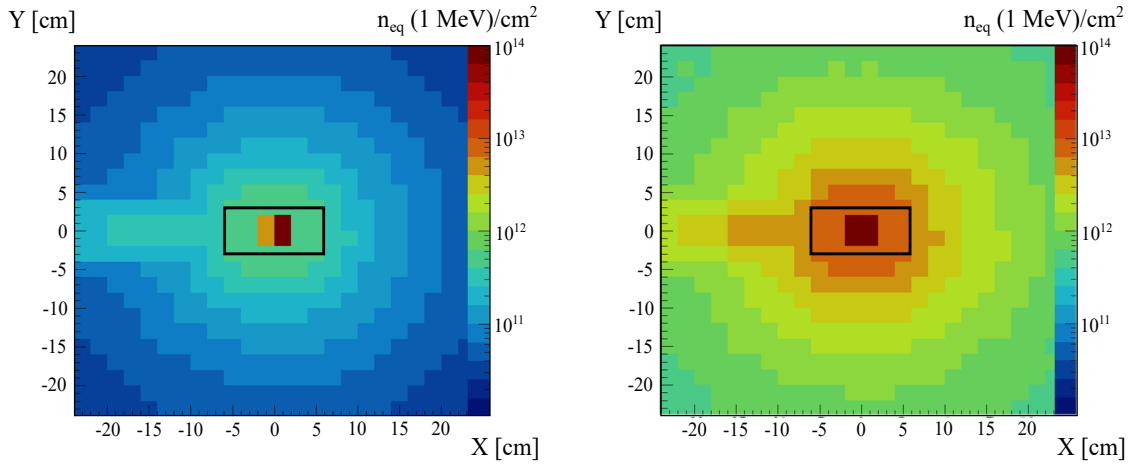

Figure 1.19: Fluence distribution of the first STS station located 30 cm away from the target. The simulation was performed using FLUKA, considering the 3-year running scenario with the highest beam intensity.[59, 60]

ics generate approximately 40 kW of heat, which will be removed by the mono-phase 3M NOVEC 649 cooling system, capable of removing up to 50 kW. However, to mitigate the radiation effect on the sensors, additional cooling measures are required. It has been seen from a FLUKA calculation (see Figure 1.19) that the inner-most sensor, near the beam-pipe area, i.e., Δ x = Δy $\leq$ 10 cm, receives the highest radiation dose, producing 40 kW/cm^2 at +10°C at EOL Φ_{eq}. Therefore, to prevent reverse annealing, maintain a high Signal-to-Noise (S/N) ratio, and reduce leakage currents, the sensors closest to the beam pipe will be actively cooled using air through perforated tubes. In contrast, sensors located in the peripheral areas will be cooled through natural convection. Further detailed information on the cooling concept can be found in[60].

1.6 Scope of the Thesis

As discussed earlier, the Compressed Baryonic Matter (CBM) experiment is a fixed-target experiment currently under construction at the Facility for Antiproton and Ion Research (FAIR) in Darmstadt, Germany. The first beam operation is expected toward the end of 2028. The CBM will operate at very high interaction rates of up to $\sim$ 10 MHz using a continuous beam of heavy ions in the energy range of 2$-$12 AGeV/c, ($\sqrt{S_{NN}} = 2.7 - 4.9$ GeV), corresponding to $\mu_B \approx 750 -$ 550 MeV. The experiment is designed for *"free-streaming"* data acquisition, where detector signals are continuously read out without a hardware trigger, and event reconstruction and selection will be performed online. This unique approach enables the measurement of rare probes and short-lived particles over a wide range, providing unprecedented precision into the properties of strongly interacting matter at high net-baryon densities. Therefore, the detector and its readout system must be capable of handling extremely high hit occupancies and complex event topologies arising from interaction rates of up to 10 MHz.

The Silicon Tracking System (STS), which acts as the central tracking detector of the CBM, is positioned close to the target region, at a distance of approximately 30$-$100 cm along the Z-axis. It is designed to provide a precise reconstruction of charged-particle trajectories and primary and secondary vertices.

With this requirement, the main objective of the thesis was as follows:

- **Chapter 2** provides a detailed description of the simulation geometry of the Silicon Tracking System (STS). It explains how the active and passive detector components were implemented using ROOT primitive solids, along with their materials and the corresponding overall material budget for the entire detector system. Additionally, the chapter presents an alternative geometry-construction workflow that directly converts CAD models into ROOT geometry files and compares its performance with the primitive-solid approach. Finally, the momentum-resolution performance of the STS detector is presented, highlighting the impact of geometry precision on tracking quality.

- **Chapter 3** focuses on the study of data-rate performance of the mini-Silicon Tracking System (mSTS), a prototype of the full STS detector. The analysis is based on experimental data from Ni+Ni collisions at 1.93 AGeV at SIS-18, with an approximately 717 kHz rate, collected during the 2024 beam time, and corresponding simulation data generated under identical conditions. This includes contributions from hadronic interactions (UrQMD) as

well as beam-target interactions, transported through the detector using GEANT4 and digitized in a free-streaming-like mode (Time-based), according to the interaction rate measured in the real experiment. The simulated data include realistic modeling of the front-end electronics and readout parameters, such as ENC, Thresholds, and dead channels, to reproduce the conditions during the experiment. A detailed comparison between measured and simulated results enables the evaluation of the free-streaming readout system's performance in the STS detector. It validates its capability to operate under high-rate conditions.

- **Chapter 4** presents an analysis of expected data rates in the STS detector using a time-based mode approach, with detailed Monte Carlo simulations. The analysis is performed by applying a common configuration of electronic noise (ENC) and threshold values to all 876 silicon sensors. In addition, a more realistic scenario is investigated by assigning individual ENC values to each sensor, calculated as a function of the sensor length and the corresponding micro-cable length. For each sensor, an adaptive threshold is applied that corresponds to four times the noise level (4σ). The results provide a comprehensive understanding of the expected data rates in the STS under various noise and threshold conditions, which are necessary to determine the detector readout bandwidth requirements.

- **Chapter 5** concentrates on the physics performance of the STS, including its geometrical acceptance, hit-reconstruction efficiency, and the tracking efficiency. The influence of key detector parameters, such as threshold settings and front-end dead time, on the hit-reconstruction efficiency is studied in detail. Furthermore, the characteristics of charge clusters in silicon sensors are analyzed to understand charge distribution on the $n-$ and $p-$sides of the sensor, the magnetic-field effect, and the detector's spatial resolution. The chapter also discusses particle identification techniques: the identification of charged particles using the Time-of-Flight (TOF) detector, and particle identification of various reconstructed singly and doubly charged particles, as well as light hypernuclei within the STS itself via specific energy-loss (dE/dx) measurements.

- **Chapter 6** summarizes the key findings obtained from the comparative analysis of the simulation and experimental data related to the mSTS data-rate performance. The comparison provides valuable insight into the expected signal and data output under realistic operating conditions, serving as a basis for estimating the requirements of the front-end electronics and the free-streaming readout system. Furthermore, the physics-performance studies presented in this work establish a baseline for future improvements in the STS geometry layout and

its material budget, which will eventually enhance momentum resolution, hit rates, track reconstruction efficiency, and particle identification within the STS.

The outcome of this thesis provides a quantitative baseline for the key performance parameters of the STS detector, including detector geometric acceptance, hit and track reconstruction efficiencies, momentum resolution, and the maximum expected data rate. These studies were conducted using a realistic detector geometry and simulations that incorporate the full beam–target interaction and noise. The findings also demonstrate the expected tracking efficiency and vertexing precision for both primary and secondary particles in the high-rate environment of the CBM experiment, thereby providing essential input for the detector's final optimization and physics performance assessment.

Chapter 2

The Silicon Tracker System Simulation Geometry

Accurate detector-physics simulation requires two elements: (i) a realistic description of all active and passive components, including their material composition, and (ii) a fast, reliable particle transport with robust navigation through the detector geometry.

The standard, widely used approach is to build the geometry from "*primitive solids*" provided by toolkits such as CERN–ROOT[61] and GEANT4[62]. These toolkits let users define each volume's dimensions, orientation, placement, and material. More complex shapes can be formed by Boolean operations (union, intersection, subtraction) on the basic primitives. This method is simple, transparent, and well-validated, and is being used for large-scale simulations across many particle physics experiments. Its main limitation is that fine engineering details are time-consuming to model and often require controlled approximations that, if not carefully checked, can bias the material budget, leading to a flawed physics interpretation.

To cope with these limitations, recent developments in CERN–ROOT[1] and GEANT4[62] support the import of CAD-based geometry (for example, via Geometry Description Markup Language (GDML))[63] directly into the simulation as tessellated solids. This enables high-fidelity representations of complex components while preserving compatibility with standard transport and navigation of particle events.

In this chapter, in **Section 2.2**, we present a detailed description, as state-of-the-art, of the simulation geometry of the Silicon Tracking System (STS), which is a core tracking detector of the

[1] https://root.cern/doc/v634/classTGeoTessellated.html

CBM experiment. The current STS geometry is built from simple primitive solids (boxes, tubes, cones, trapezoids, extrusions). At the same time, more complex features are formed by Boolean operations (union, intersection, subtraction) between primitives and resulting volumes are placed hierarchically to reproduce the detector layout using CERN-ROOT[61], where it mimic all active (silicon sensors) and passive (ladders, micro-cables, C-frames, Cooling perforated tubes, pipes and plates, Low- & H- Voltage cables and optical services, Front-end Electronics Boards (FEBs)/ Read-out Boards (ROB) / Power Boards(POB), enclosure walls) components as implemented in the CAD model.

In addition, in **Section 2.3** and **Section 2.4**, we discuss the approach and workflow that import engineering CAD models as *"Tessellated solids"* via GDML, a file format compatible with CERN-ROOT[61] and GEANT4[62]. Using the mini-STS (mSTS) as a case study, we demonstrate the CAD-based import and compare it with the primitive-solid implementation. This comparison, presented later in the chapter, evaluates physics consistency, navigation reliability, and computational cost. The primary objective was to evaluate the performance of the alternative approach and determine how it would help in preparing the high-fidelity STS geometry for large-scale simulation and its targeted design, where detailed mechanical features and material budgets must be modeled accurately.

Finally, in the **Section 2.5**, we discuss the contribution of different geometry components to the material budget, the consequences for the physics performance, and momentum resolution for the STS detector.

2.1 Material budget and its Influence on Multiple Scattering, Tracking Performance and Momentum Resolution

In modern particle physics experiments, the momentum of charged particles is determined from the curvature of their trajectories in a magnetic field, mainly reconstructed from space points (hits) produced by ionization in the tracking layers. The detector that provides those measurements also induces multiple Coulomb scattering, which broadens the track and biases the curvature fit as illustrated in Figure 2.1. For a detector layer of thickness x, the r.m.s. projected scattering angle is well described by the Highland approximation (see Equation 2.1) [64, 65]

$$\theta_{plane} \simeq \frac{13.6 \text{ MeV}}{\beta c \cdot p} \cdot |z| \cdot \sqrt{\frac{x}{X_0}} \left[1 + 0.038 \cdot \ln\left(\frac{x}{X_0}\right)\right] \propto \frac{1}{p}\sqrt{\frac{x}{X_0}} \; (\beta \approx 1) \tag{2.1}$$

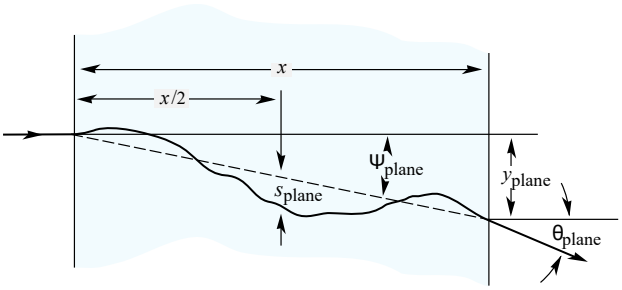

Figure 2.1: Illustration of dispersion of incident particle by θ_{plane} due to multiple Coulomb scattering while passing through the detector layer of the thickness x.[48]

Where p, βc, and z are the momentum, speed, and charge of the incident particle in units of e, respectively, and X_0 is the property of the detector material. The values of the X_0 for elements and the compound can be computed from the Equation 2.3 and Equation 2.4.

In a uniform magnetic field, the transverse momentum resolution (Gluckstern formalism)[66, 67] can be written as a quadratic sum of a measurement term and a scattering term as per the Equation 2.2a

$$\frac{\sigma(p_T)}{p_T} = \sqrt{\left(\frac{\sigma(p_T)}{p_T}\right)^2_{\text{meas}} + \left(\frac{\sigma(p_T)}{p_T}\right)^2_{\text{ms}}} \tag{2.2a}$$

$$\left(\frac{\sigma(p_T)}{p_T}\right)_{\text{meas}} \simeq \frac{p_T \cdot \sigma_{\text{hit}}}{0.3\,|z|\,B\,L^2}\,\sqrt{\frac{720}{N+4}} \tag{2.2b}$$

$$\left(\frac{\sigma(p_T)}{p_T}\right)_{\text{ms}} \simeq \frac{0.0136\ \text{GeV}/c}{0.3\,\beta\,B\,L}\,\sqrt{(N-1)\,\frac{x/\sin\theta}{X_0}} \tag{2.2c}$$

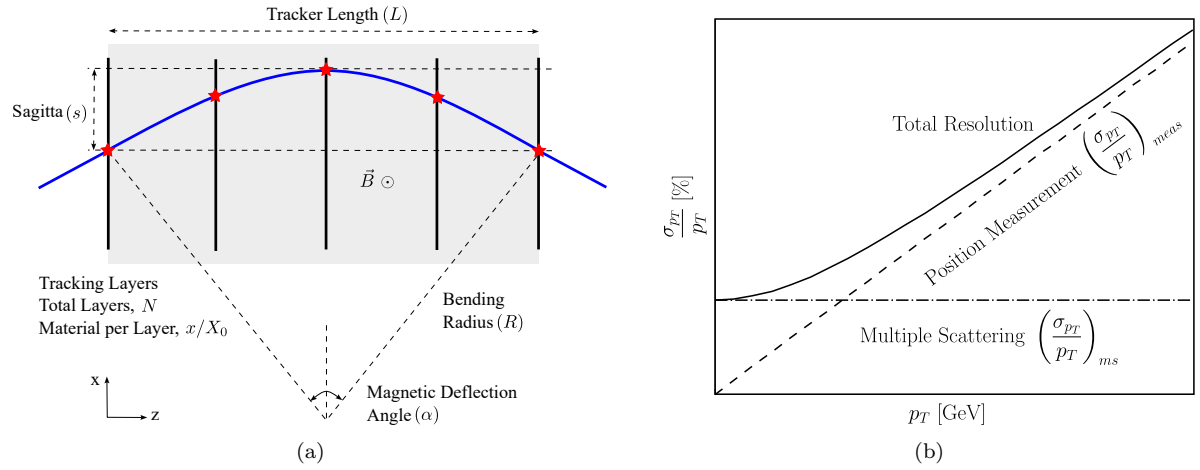

Figure 2.2: Figure 2.2a Particle trajectory in a forward detector shown perpendicular to the magnetic field (x-z plane; beam along z-axis) and Figure 2.2b The variation of transverse momentum resolution with transverse momentum.[68]

where B is the magnetic field, L the lever arm of the measured track segment, N the number of detector layers where hit by particle, and σ_{hit} the single–point precision. Equation 2.2b shows the measurement term increases linearly with p_T, whereas Equation 2.2c is essentially independent of p_T for relativistic particles ($\beta \simeq 1$) and scales with the square root of the material budget. Consequently, at low momenta, the resolution is limited by multiple scattering, and from the

Equation 2.1 it is clear that $\theta_{\text{plane}} \propto \sqrt{x/X_0}$, therefore minimizing the material budget x/X_0 in the active tracking volume is essential to control the multiple scattering and to achieve the targeted momentum resolution. While at high momenta, the measurement term dominates, and improvements require better hit precision and/or a larger lever arm.

The material budget can be determined using the Equation 2.3[69]

$$X_{0,i} = \frac{716.4\, A_i}{Z_i\,(Z_i+1)\,\ln\!\left(\frac{287}{\sqrt{Z_i}}\right)} \quad [\text{g/cm}^2], = \frac{716.4\, A_i}{Z_i\,(Z_i+1)\,\ln\!\left(\frac{287}{\sqrt{Z_i}}\right)\cdot\rho} \quad [\text{cm}] \tag{2.3}$$

$$\frac{1}{X_0^{\text{mix}}} = \sum_i \frac{w_i}{X_{0,i}} \tag{2.4}$$

The material budget of any detector component can be expressed in terms of its *"radiation length"* (X_0), which is a characteristic quantity that describes how high-energy charged particles interact with materials. Overall, it provides a convenient measure of the material thickness relevant for *"multiple Coulomb scattering"*, *"energy loss"*, etc, inside a detector.

For an elemental material, the radiation length $X_{0,i}$ can be empirically estimated using Equation 2.3, where Z_i and A_i are the atomic number and atomic mass of the element, respectively. ρ is the density of the given material. The logarithmic term in the denominator accounts for the screening effect of atomic electrons.[70, 71]

In the case of compounds or mixtures, the effective radiation length X_0^{mix} can be obtained using the mass-weighted mean of the constituent elements, as expressed in Equation 2.4. Here, w_i represents the fractional mass contribution of each component i, and $X_{0,i}$ is its radiation length calculated from Equation 2.3. This mixture rule assumes that energy loss processes are additive and that the fraction of energy loss per radiation length scales linearly with mass fraction.

Once $X_0^{\text{material/mix}}$ is known, the fraction of radiation length (material budget) traversed by a particle through a given layer of density ρ and thickness t can be calculated as

$$\frac{x}{X_0} = \frac{t}{X_0^{(\text{material})}}$$

This is commonly expressed as a percentage to quantify each detector element's contribution to the total material along the particle's trajectory and is one of the most critical parameters for detector design, as it directly affects multiple scattering and, therefore, the precision of momentum

reconstruction. The details on the momentum resolution for the STS detector obtained through simulation for all particles and separately for primary and secondary charged particles, are discussed in **Section 2.5** and Subsection 2.5.1.

2.2 Silicon Tracking System Simulation Geometry

As described in **Chapter 1** and **Section 1.5**, the Silicon Tracking System (STS) detector plays a crucial role in accessing the physics in the CBM experiment. To accurately assess simulation performance, a detailed, realistic representation of both active and passive hardware components is essential.

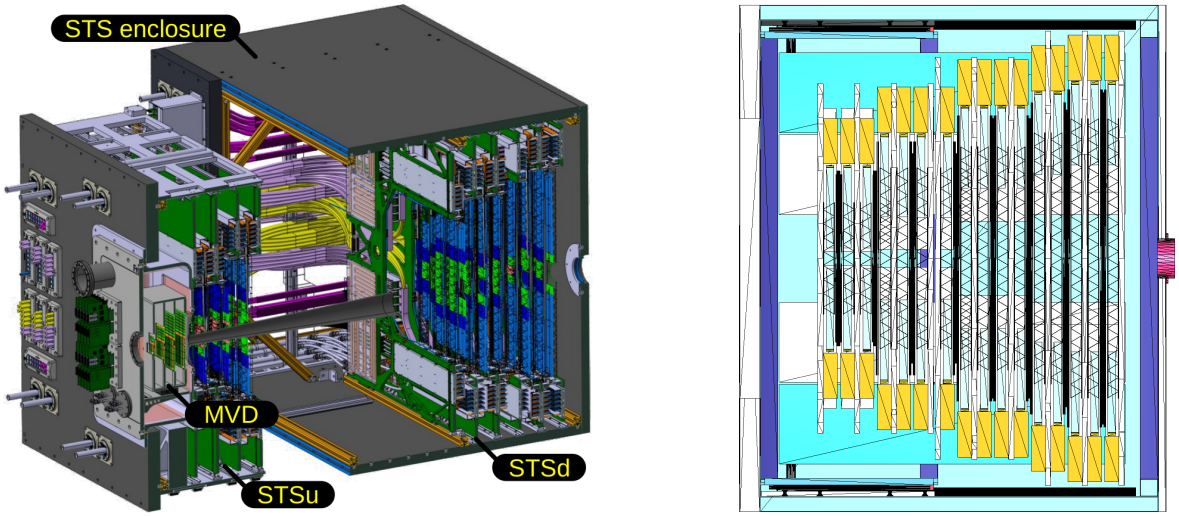

(a) CAD model of the Silicon Tracker[72]

(b) STS simulation geometry prepared using ROOT primitive solids (side-view with half-cut).

Figure 2.3: CBM–STS views: Figure 2.3a CAD geometry, represents STSu (Three station) and STSd (Four station) and Figure 2.3b Simulation geometry.

To achieve this, Computer-Aided Design (CAD) models (Figure 2.3a), prepared by engineers, serve as a reference for constructing the simulation geometry. The CERN-ROOT framework has been utilized to prepare active elements, such as sensors, the support structure known as ladders, read-out micro-cables, etc., and other passive components (C-frames, power cables, cooling pipes, FEB boxes, and beam-pipe holders). These components were prepared utilizing primitive solids defined within the ROOT framework. The complete ROOT-based STS geometry used in the CBM-ROOT simulation framework is shown in Figure 2.3b. In this geometry, components such as ladders, micro-cables, cooling perforated tubes, and various sizes of silicon sensors are located in the active physics acceptance area. At the same time, the FEBs, FEB box, C-frames, various electronics and their connecting wires, cooling pipes, and STS enclosure box walls and other support structures

are considered part of the passive components and are located outside the physics acceptance. The reason for this layout was to reduce the material budget in the active area of the STS, thereby minimizing multiple scattering, which plays a crucial role in determining the quality of track reconstruction and the overall detector performance. A low material budget in the physics acceptance of the STS detector, $2.5^{\circ} < \eta < 25^{\circ}$ from a target position (a region where particles passes through active detector volume), is highly desirable because it minimizes the particle interaction and multiple Coulomb scattering; therefore, the probability of the secondary particle production is low, resulting overall in more precise measurements of particle trajectory of primaries, secondaries and various decay products and their better momentum and vertex resolution as described the concept already in **Section 2.1**.

2.2.1 Ladder

Figure 2.4 shows the geometry of a single ladder from a CAD and the one implemented in the simulation geometry. A single sensor with a ladder is called *"sector"* . A sensor, along with micro-cables called *"module"*, is stacked to build the full ladder with the desired number of sensors. A silicon sensor of varying sizes, along with micro-cables as shown in Figure 2.5, on a ladder. Each variant of the sensors has a thickness of 320 ± 15 μm, contributes to the material budget $\sim 0.34\% X_0$ per sensor.

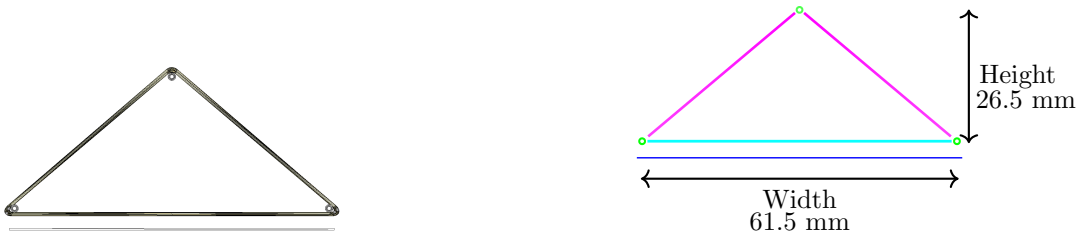

(a) Ladder structure in CAD model

(b) Ladder structure in simulation geometry

Figure 2.4: Comparison between the ladder structure in the CAD Model and its simulation geometry

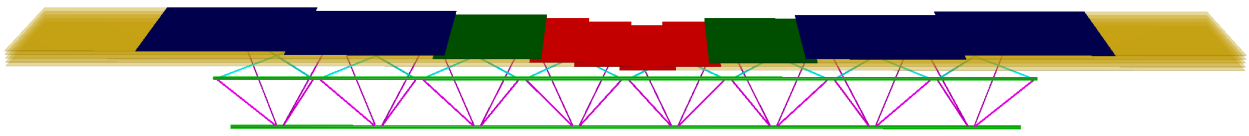

Figure 2.5: Complete ladder with different sensors for Unit 0 Ladder type 09.

The carbon-fibre ladder consists of three supporting tubes with outer diameters of 1.5 mm and inner diameters of 0.7 mm. Additionally, a winding structure is incorporated to provide mechanical

support for sensor placement. This winding has an approximate thickness of 0.1 cm, while the knots securing the whole structure contribute an additional thickness of $\sim$ 0.17 cm. Ladder's material budget comprises multiple contributions as listed below:

- Knots account for approximately $\sim 0.35\%X_0$
- Supporting tubes, considering their effective thickness, contribute $\sim 0.62\%X_0$
- Knots on the tubes further add $\sim 0.597\%X_0$

For the maximum ladder length of 120 cm and total mass of 14.8 g, the average material budget is $\sim 0.047\%X_0$. The study of the ladder development, its specification and Quality Assurance (QA) performance has been performed and is described in detail in [58, 73].

2.2.2 Central Ladder

The CBM experiment is designed as a fixed–target forward spectrometer, with the Silicon Tracking System (STS) installed inside the dipole magnet aperture, at a distance of roughly between 30–100 cm downstream of the target. As shown in Figure 2.3, the conical beam pipe passes through the active area of the STS detector. Consequently, cut–outs must be introduced in the central ladders at the position corresponding to a polar angle of about 2.5° relative to the target.

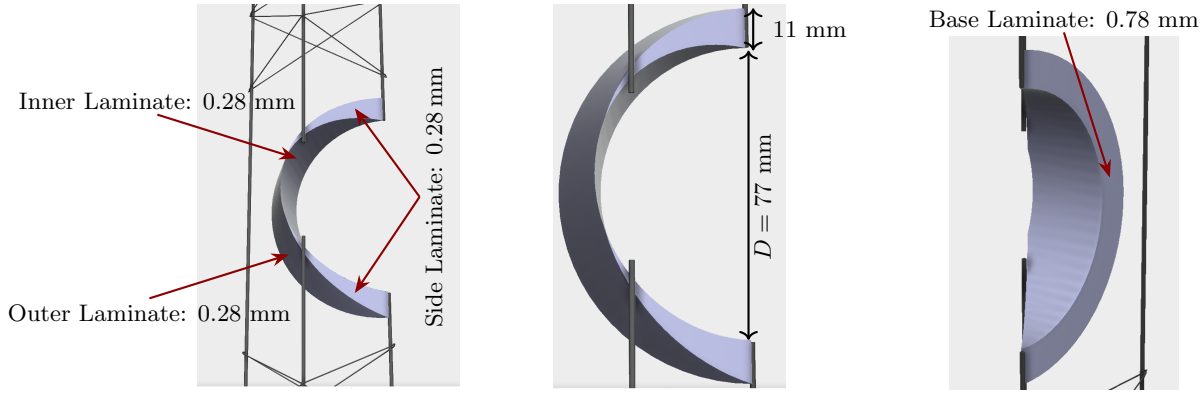

Figure 2.6: An example of a CAD-model prototype of the central ladder with hollow curved rib.

A prototype central ladder has been developed that incorporates a hollow, curved carbon fibre rib. The primary geometry parameters - including the inner, outer, side, and base laminate thicknesses - are indicated in the CAD model-based geometry as shown in Figure 2.6. While the overall structural design and material properties remain the same across different central ladder types, the diameter of the hollow curved rib varies to accommodate the conical shape of the beam pipe.

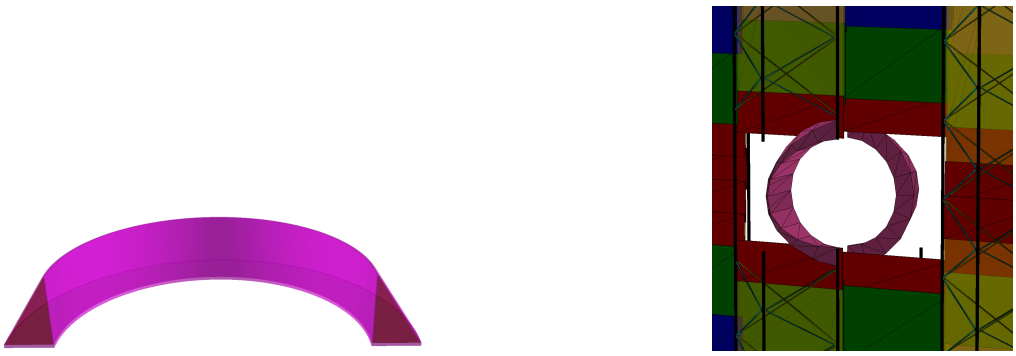

(a) (b)

Figure 2.7: CBM–STS views: Figure 2.7a Hollow curved rib for the central ladders prepared using TGeoPcon[2] primitive solid using ROOT and Figure 2.7b Central ladder along with curved rib in STS simulation geometry.

Figure 2.7 shows an example of a hollow curved rib for one of the central ladders, prepared using the `TGeoPcon` primitive solid in ROOT, along with its integration into the STS detector geometry. The laminate layers of the rib contribute minimally to the material budget of the tracking system. The inner, outer, and side laminates - each with a thickness of 0.28 mm - correspond to a radiation length of approximately $x/X_0 = 0.0984\%$ per layer. The thicker base laminate, with a thickness of 0.78 mm, adds roughly 0.274% to the radiation length. In total, the combined material budget of the curved rib structure is approximately $0.569\%\, X_0$ for a normal particle incident, which remains within the acceptable range for maintaining high tracking performance in the CBM–STS detector.

2.2.3 Micro-Cable

In the Silicon Tracking System (STS), double-sided silicon sensors are utilized, requiring both sides of the microstrips to be connected to micro-cables for signal transmission. These micro-cables play a crucial role in transferring the signals generated within the sensor to the dedicated readout electronics for further processing.

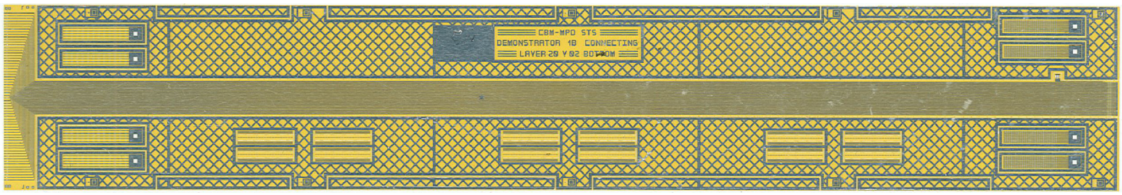

Figure 2.8: Top view of the micro-cable of length 60 cm.

To achieve this, ultra-thin micro-cables made of polyimide and aluminium, with thicknesses of 14 μm and 10 μm, respectively, are used, along with the various layers of the foams and mesh made of different materials. The total thickness of the micro-cable is calculated to be 774 μm, including

[2] https://root.cern/doc/v636/classTGeoPcon.html

both ($p-$ & $n-$) sides of the sensors. These cables are directly connected to the sensors to ensure efficient signal transfer with minimal material contribution.

Figure 2.9 illustrates the cross-sectional structure of the micro-cable used to connect the p-side and n-side micro-strips of the silicon sensor. Additionally, Figure 2.8 presents the top view of the 60 cm long micro-cable. In the simulation geometry, the micro-cable thickness is approximated to 320 μm, similar to the sensor thickness. The material budget was found to be 0.124%X_0 per cable. To determine the equivalent material composition, the empirical Equation 2.3 and Equation 2.4 were used.

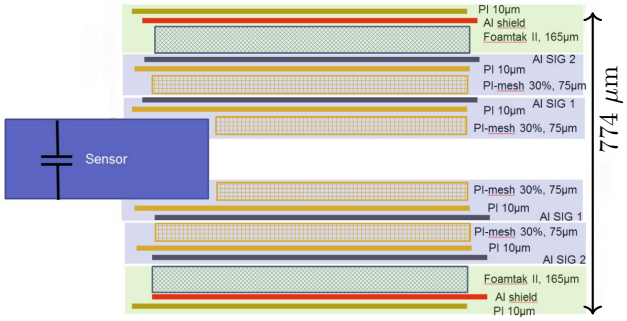

Figure 2.9: Cross-sectional view of the Micro-cable.

From here, it was concluded that manganese (Mn) can be used as an approximate equivalent material for the micro-cable, with a density of 0.5656 $\frac{g}{cm^3}$.

2.2.4 C-Frame

The C-shaped holding structure, referred to as the *"C-frame"*, is fabricated from 1.5 cm-thick aluminum. Its primary role is to provide rigid mechanical support, holding the ladders and simultaneously enabling the integration of services and readout electronics for the Silicon Tracking System (STS). Figure 2.10 illustrates a CAD cross-sectional view of the half C-frame, annotated with the main active and passive components mounted on or routed through the structure. In the full STS system, a total of 20 C-frames will be used.

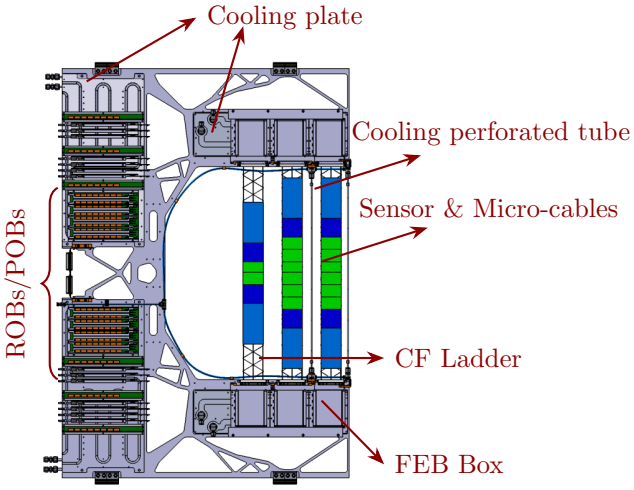

Figure 2.10: CAD geometry of aluminium-made C-shaped support frame along with different active and passive components.

The central region of the frame accommodates the ladders, each carrying the double-sided silicon strip sensors. The sensors are connected to the readout chain via thin micro-cables. To ensure proper thermal management, cooling perforated tubes are closely integrated with the sensors, providing efficient heat extraction from the sensors

and cooling plates for the front-end electronics located on the C-frame, thereby maintaining stable operating conditions during high-rate operation. The Front-End Board (FEB) boxes and cooling plates are mounted at the periphery of the frame.

In addition, the peripheral parts of the frame host the Read-Out Boards (ROBs) and Power Boards (POBs), which distribute power and collect data from the sensors via the FEBs. Their location outside the tracking acceptance reduces material in the active region and therefore minimizes the contribution of passive material to the overall detector material budget.

2.2.5 Low-Voltage SUMIDA & SMT 50 High-Voltage HABIA Cables

In the STS, two additional cable types are used: Low-Voltage (LV) SUMIDA flat cables and High-Voltage (HV) coaxial HABIA cables. Both serve as connections between the power boards, placed on the side part of the C-frame, and the Front-end Boards (FEBs), placed on the top and bottom of the C-frame, and both are out of the physics acceptance.

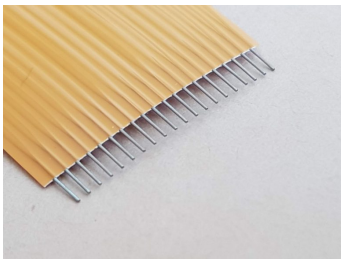

(a) SUMIDA cable

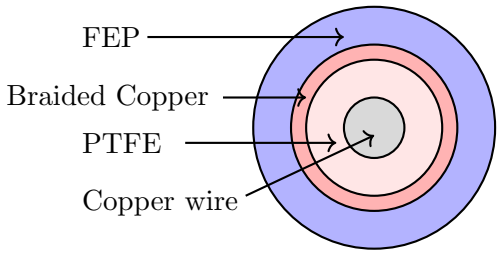

(b) Schematic cross-section of the HABIA HV cable

Figure 2.11: Figure 2.11a SUMIDA Low-Voltage (LV) cable and Figure 2.11b Cross-sectional view of the HABIA High-Voltage (HV) cable.

SUMIDA LV Cable

The SUMIDA LV cables are placed horizontally to the C-frames and consist of copper conductors laminated in polyimide (Kapton). The total thickness of a cable is 0.030 cm, of which 0.016 cm is copper and 0.014 cm polyimide, with an overall width of 2.2 cm. The elemental composition of the SUMIDA cables is listed in Table 2.1.

The mass contribution per cm of length is dominated by copper (86%), with polyimide contributing only 13%. In total, the SUMIDA cables contribute about 23.2 kg to the STS material budget, corresponding to an average effective density of $4.96\,\mathrm{g/cm^3}$.

Element	Atomic Mass (u)	Weight Fraction (%)
H	1.008	0.35
C	12.011	9.23
N	14.007	0.98
O	15.999	2.79
Cu	63.550	86.65

Table 2.1: Effective material composition of the SUMIDA LV cables used in the STS.

HABIA HV Cable

The HV distribution employs coaxial HABIA cables, which consist of a central copper conductor surrounded by PTFE insulation, a braided copper shield (fill factor 70%), and an FEP jacket (see Figure 2.11b). The material composition is given in Table 2.2.

Element	Atomic Mass (u)	Weight Fraction (%)
C	12.011	8.17
Cu	63.550	65.99
F	18.998	25.84

Table 2.2: Effective material composition of the HABIA HV cables used in the STS.

Each HABIA cable has a mass of 0.03 g/cm. With ∼1752 cables required in the whole system, their combined mass contribution amounts to 4.14 kg, corresponding to an effective density of 3.77 g/cm^3. For the simulation geometry, the coaxial HABIA cables are approximated as flat volumes with equivalent material composition, similar to the treatment of the SUMIDA cables, to make the geometry computationally reliable.

2.2.6 Low-Voltage and High-Voltage Power Cables

The reliable operation of the Silicon Tracking System (STS) requires both Low-Voltage (LV) and High-Voltage (HV) power supplies, which provide a stable power distribution to the detector modules. Therefore, both cable types are crucial components of the whole detector infrastructure. They are positioned along the z-axis, moving from upstream to downstream outside of the physics acceptance of the STS detector.

The LV cables are made of copper conductors embedded in a halogen-free, flame-retardant polypropylene-based insulation. The specific type used is `SABIX D 320 FRNC C1 16×0.75 mm`^{2}, which contains 16 individual conductors. Each LV cable is capable of providing power to up to 4 detector modules. In contrast, the HV cables, procured from the CERN and have a specification `CABLE HT 37×0.14 mm`^{2} `SnCu, 3 kV DC`, consist of 37 tinned copper wires insulated by flame-

(a) Low-voltage (LV) cable

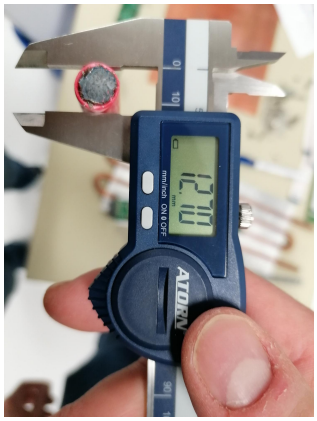

(b) High-voltage (HV) cable

Figure 2.12: Measured outer diameters of the Low- and High-Voltage (LV and HV) power cables used in the STS.

retardant polypropylene-based insulation and are used to deliver bias voltage to up to eight detector modules, with four wires assigned per module.

The measured external diameters of the LV and HV cables are 11.5 mm and 12.7 mm, respectively (see Figure 2.12). Based on the number of modules per STS station unit and the required cable lengths along the detector's z-direction, the total mass of the complete power distribution system is estimated as follows:

- LV cables: approximately 43.6 kg,
- HV cables: approximately 16.8 kg,

resulting in a combined mass of about 60.3 kg.

Element	**Atomic Mass (u)**	**Weight Fraction (%)**
H	1.008	0.07
C	12.011	41.58
Cu	63.550	51.44

Table 2.3: Effective elemental composition of the combined LV and HV power cables implemented in the STS simulation geometry. The fractions are determined from the measured mass ratios of copper and polymer components.

In the simulation geometry, modelling each individual conductor within the multi-core cables would be computationally prohibitive. Therefore, the LV and HV cables are represented by homogeneous rectangular volumes, with an effective material composition that reproduces the total measured mass and average density. This approach ensures that the simulated material budget accurately reflects the real system while maintaining computational efficiency. The equivalent material has an effective density of $0.104\,\mathrm{g/cm}^3$, derived from the measured cable masses and their geometrical dimensions. The fractional contributions of the primary elemental components, obtained by

weighting the copper and polymer constituents of both cable types, are summarised in Table 2.3.

2.2.7 Optical Cable

In the STS, single-core optical cables are used for high-speed data transmission from the Readout Boards (ROB) and the Power Boards (POB). They are placed in the detector's peripheral area, near the ROB and POB boxes. Each optical fibre consists of a central core with a diameter of 62.5 μm, a cladding with a diameter of 125 μm, and an outer protective jacket with a thickness of 3 mm.

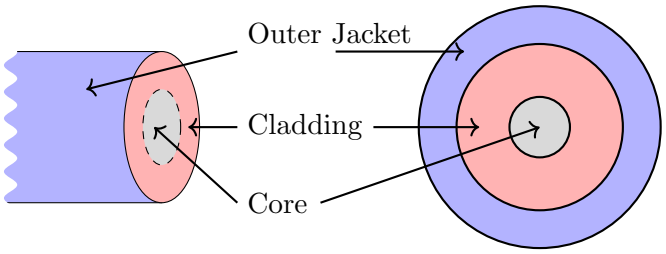

Figure 2.13: Single core optical cable.

The core and cladding are composed of silica glass, which provides the necessary optical transmission properties. Surrounding the cladding, a layer of aramid fibres offers mechanical reinforcement and tensile strength. The outer jacket is manufactured from a mixture of polyethylene and LSZH (Low Smoke Zero Halogen) compounds, ensuring both durability and fire safety.

Element	Atomic Mass (u)	Weight Fraction (%)
H	1.008	6.35
C	12.011	30.30
O	15.999	43.91
N	14.007	0.02
Si	28.085	0.20
Mg	24.305	4.76
Al	26.982	14.44

Table 2.4: Effective material composition of the optical fibre cable used in the STS simulation geometry.

In total, approximately 3456 optical fibres are deployed throughout the STS, contributing about 46 kg to the detector mass. The elemental composition used to model the cable materials is listed in Table 2.4.

For the simulation geometry, modelling each fibre strand would be computationally impractical. Therefore, the optical cables are approximated as rectangular volumes with equivalent material composition and density. The calculated effective density of the optical cable material is 0.148 g/cm^3.

2.2.8 STS Enclosure Wall

The STS enclosure wall is an essential structural element of the detector assembly, designed to provide both mechanical rigidity and thermal insulation for the sensitive detector components. Its primary function is to maintain a stable thermal environment while supporting the structural integrity of the overall detector system.

The enclosure consists of four main panels - the front, back, top, and bottom walls - along with two vertical side walls, forming a closed housing around the active detector volume. Each wall is realized as a "*sandwich composite structure*" comprising two outer carbon-fiber sheets and an Airex® T92.60 structural foam core sandwiched between them. The total thickness of each wall depends on the foam layer, which varies according to the mechanical and thermal requirements of the detector design.

All carbon-fibre sheets have a thickness of 0.2 cm and a density of 1.5 g/cm^3, while the Airex T92.60 foam has an average density of 0.065 g/cm^3. Such a configuration ensures an optimal balance between mechanical stiffness, low mass, minimal thermal conductivity, and minimal material budget contribution.

Wall Section	**Carbon Fibre Sheet [cm]**	**Airex Foam Core [cm]**	**Material Budget (x/X_0) [%]**	
			Carbon Fibre Sheet	**Airex Foam Core**
Top / Bottom wall	0.2	4.0	0.70	0.65
Vertical wall	0.2	3.6	0.70	0.582
Back wall	0.2	3.6	0.70	0.582
Front wall	0.2	5.6	0.70	0.91

Table 2.5: Structural composition and individual material budget contributions of the STS enclosure walls.

Thermally, the Airex T92.60 foam exhibits a low thermal conductivity of 0.037 W/m·K at 10°C, effectively minimizing heat transfer through the enclosure wall. This suppresses temperature gradients across the detector housing, protecting the front-end electronics and silicon sensors from thermal instabilities during operation.

The Table 2.5 summarizes the thickness parameters and material budget contributions of individual carbon fibre and foam sheets. In terms of material budget, each carbon-fibre sheet contributes approximately 0.7% X_0, while the Airex T92.60 foam adds about 0.582% X_0, for a 3.6 cm thick layer. For thicker panels, the foam contribution scales proportionally with its thickness, as reflected in Table 2.5.

In general, the enclosure design provides a compromise between mechanical robustness, thermal stability, and a minimal material budget, ensuring optimal performance of the Silicon Tracking

System under varying experimental operating conditions.

Until now, we have discussed in detail how the various STS hardware components were constructed using primitive solids within the ROOT[61] framework, along with the selection of their effective material compositions for accurate detector representation and the momentum resolution performance of the STS detector. In the following **Section 2.3**, we discuss an alternative approach for implementing the geometry directly from CAD models as tessellated solids. Using the mini-STS (mSTS) as a test example, this section describes the workflow for the CAD-to-ROOT conversion, its integration into the simulation framework, and a comparison of its performance with that of the primitive-solid-based geometry.

2.3 Tessellated solid-based Simulation Geometry

In traditional approaches to simulation using ROOT[3][61] and GEANT4[4][62], the detector geometry is often defined using primitive solids provided by these software frameworks, as already discussed earlier. However, this approach presents several challenges. One of the main difficulties is the time required by the user to prepare and define the geometry. Additionally, when approximating complex structures, there is the risk of losing accuracy in representing intricate details. Careful consideration is also necessary when approximating the materials used in the geometry, as incorrect material properties or simplifications can affect the simulation's precision.

Accurately representing the intricate details of detector geometry, as defined in Computer-Aided Design (CAD) models used for engineering purposes, is a key challenge in simulation geometry. However, in recent years, significant efforts have been made to enhance the accuracy of detector geometry descriptions to improve physics performance within the ROOT[74] and GEANT4[75] frameworks. One promising approach is the direct integration of CAD-based geometry models into simulations. To achieve this, CAD geometry models need to be converted into a format that can be read by tools like the ROOT `GDMLParser`[5] or the GEANT4 `G4GDMLParser`[6]. This is typically done by converting the models into the GDML, an XML-based format supported by various software toolkits. The geometry extracted from CAD models and represented in GDML format often consists of tessellated solids[7], typically composed of triangular or quadrilateral facets, a closed surface

[3] https://root.cern.ch

[4] https://geant4.web.cern.ch/

[5] https://root.cern.ch/doc/v614/group__Geometry__gdml.html

[6] https://gitlab.cern.ch/geant4/geant4/tree/75c7fd177dc4853b8a93aaedc78d6037aa36dba6/examples/extended/gdml

[7] https://root.cern/doc/master/TGeoTessellated_8cxx_source.html

made from many small flat facets which are defined by its vertices and outward normal.

2.3.1 Workflow for CAD geometry to ROOT

Figure 2.14 shows the procedure to convert the CAD geometry to ROOT/GEANT4 readable format. Several commercial and open-source CAD tools such as `FreeCAD`[76], `CATIA`[77], and `MRADSIM`[8][78] can export CAD geometry assemblies in STEP format directly to GDML[5], an XML schema that describes geometry, placements, and materials, etc, as these tool-kits provide built-in functionality to export or convert STEP file format to GDML format.

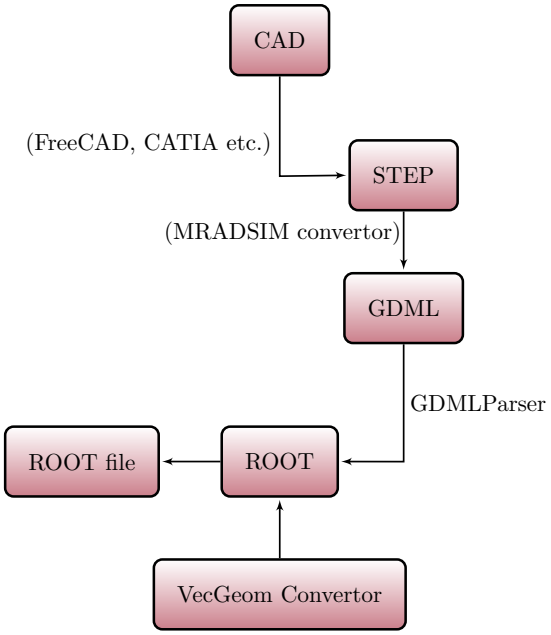

Figure 2.14: Flow chart for conversion of the CAD-based geometry model to ROOT geometry.

Also, one can explicitly control the number of tessellated facets to be used. Additionally, material definitions can be assigned to each volume in the CAD model before export, or they can be set (or overridden) after import within ROOT/GEANT4, where densities and compositions are explicitly controlled. In our case, we have used the free version of the commercial toolkit Matter-RADiation Interactions SIMulations (MRADSIM)[79] for the conversion of the Standard for the Exchange of Product Model Data (STEP) file to GDML, as mentioned in the flow chart.

Figure 2.15 shows two distinct approaches for defining C-frame geometry into ROOT. Figure 2.15a shows the geometry prepared to be used in the simulation based on primitive-solids in ROOT, while Figure 2.15b represents the Tessellated solids-based geometry prepared using ROOT after conversion of the CAD model into GDML format.

[8] `https://www.mradsim.com`

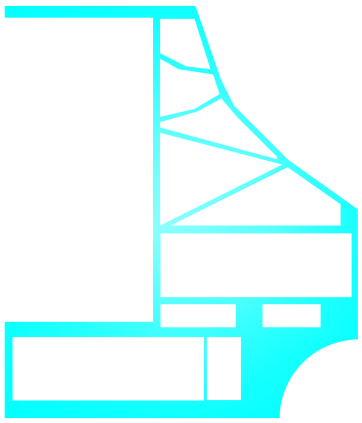

(a) C-frame prepared using a primitive solid in ROOT

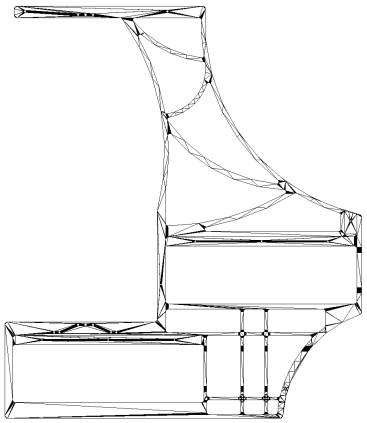

(b) C-frame prepared directly from CAD to ROOT

Figure 2.15: Figure 2.15a C-Frame along with FEB box based on Primitive ROOT Solids and Figure 2.15b Tessellated Solids based geometry.

The approach demonstrates an accurate representation of complex geometrical shapes within the simulation framework (Figure 2.15b) which would be hard-to-impossible to achieve using the primitive TGeoVolume[9] (Figure 2.15a) This difference in geometric fidelity is evident from the visual comparison of the two representations.

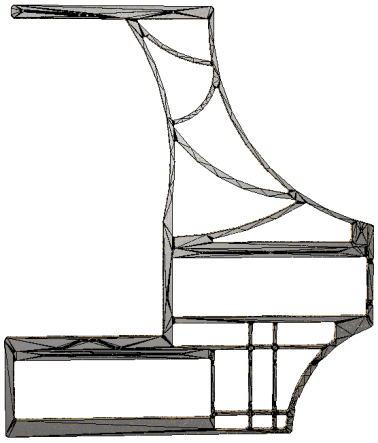

Figure 2.16: Test of the C-frame throwing random points on it using ROOT after the successful conversion into VGshapes.

The Tessellated-based geometry can not be used in ROOT directly for the physics simulation because the TGeoNavigator of CERN-ROOT failed to accurately trace the true shape, and boundaries of `TGeoTessellated` volumes (e.g. when doing for random-ray entry/exit tests). This limitation arises from the current implementation of the `TGeoTessellated` class[7], which lacks navigation functionality, particularly for the tessellated solids as of now. Consequently, as a result, such volumes behave like a simple box, inheriting the characteristics of their parent class, `TGeoBox`[10].

However, it is noteworthy that ROOT does support navigation functionality for tessellated solids when compiled with the Vectorised Geometry (VecGeom)[80] package[11] and utilising the VecGeom converter during the geometry modelling and writing the shapes into the root file before closing

[9] https://root.cern.ch/doc/master/classTGeoVolume.html
[10] https://root.cern/doc/master/TGeoBBox_8cxx.html
[11] https://gitlab.cern.ch/VecGeom/VecGeom

the geometry. The `VecGeom` package provides a converter that essentially transforms all the shapes in each `TGeoVolume` (including Tessellated) into VGShapes as defined within the CERN-ROOT, `TGeoVGShape` class[12].

This integration enhances navigation capabilities for tessellated shapes within the ROOT framework, as illustrated in Figure 2.16. Furthermore, previous versions of ROOT contained bugs that also affected this functionality; these have been fixed and added to at that time recent version of ROOT (version: $\geq$ 6-32-00 patch). A detailed study of the issue and its solution has already been discussed in [81]. In our case, the ROOT version 6.33.01 tag branch, which complied with VecGeom, was used for further simulation analysis, as discussed in **Section 2.4**.

2.3.2 Vectorized Geometry (VecGeom)

Detector physics simulation in High Energy Physics (HEP) simulation is one of the resource-intensive processes. There are three main components as described below.

- Simulation detector geometry modelling
- Physics processes involved within the detector, involving the physical processes such as radiation, multiple scattering, energy deposition, particle track navigation, and many more.
- Code defined by the users for the detector response and analyzing it, and re-optimisation of the geometry.

Traditionally, HEP experiments use CPUs for particle transport and simulation. However, an upgrade of the accelerator for high luminosity particle beam and an upgrade of the detector subsystems for handling the rate required to process the data requires considerable computing resources and High-Performance Computing(HPC); therefore, the GPU is becoming more popular to be used for the upcoming High-Luminosity(HL)-HEP experiments.[82, 83] Of course, detector modelling and simulation are also not exceptional from what was described prior because detector physics simulation is essential in all kinds of HEP experiments for designing the detector system based on the response provided by the particle transport models libraries such as GEANT4[84], FLUKA[85], etc. Since a large number of the complex tasks involved in different particle transport models are computationally intensive, they require fast simulation techniques. The current HEP experiment resources are not directly compatible with newer resources, such as GPUs, because they are not

[12] https://root.cern/doc/master/dir_f659b5a9ca37b079a242c72a02a19916.html

optimized to efficiently utilize Single Instruction Multiple Data (SIMD) and Single Instruction Multiple Threads (SIMT), which are typically found in GPUs.

For example, the detector simulation library GEANT4 currently performs consecutive steps on a single track until the track completes its transport. The whole process of the track/s involves different steps, such as track propagation in electric or magnetic fields, physics processes, and subsequent tasks that move it from one point to another. Using SIMD and SIMT requires significant changes in code locality, grouping tracks that go into the same stepping tasks, and regrouping tracks according to the functions to be executed, rather than the classical approach used in GEANT4. This requires a complete re-engineering of the classical workflow used in GEANT4, which is one of the main goals of the GEANTV R&D project.[86, 87, 88]

In the case of the detector, physics simulation relies heavily on the methods to describe and construct the detector model by making use of geometric primitives solids. GEANT4 and ROOT TGeo library packages are examples of geometry modeller libraries that allow users to define the geometries in hierarchical descriptions of solids and their containment within each other. To mitigate the requirement needed and to make use of GPU, R&D projects such as AdePT[89] at CERN and CELERITAS[90] in the U.S.A. are ongoing and are currently integrated into the VecGeom for the development of the GPU-friendly geometry library as a part of the GEANTV R&D[13].

Vectorized Geometry (VecGeom) [80] is a geometry modeling library under development that focuses on the efficient use of SIMD and SIMT in heavily multi-threaded frameworks. VecGeom aims to run and compile on both CPUs and GPUs, and to provide an environment that supports the traditional scalar-level approach, e.g., single particles, to ensure backward compatibility with GEANT4 and the ROOT TGeo library package. Another geometry project called USolid, funded by the EU-AIDA project, aims to modernize and unify the GEANT and TGeo geometry code base for better maintainability. VecGeom also joins this project to utilize available resources better.

In practice, VecGeom delivers notable speedups primarily through algorithmic redesign and data layouts tailored for SIMD/SIMT execution. For simple geometry primitives, the basketized execution model (grouping tracks that undergo the same operation) enables parallelism; in the tube–segment example, measured speedups of $\sim 2\times$ were obtained with AVX using the VecCore/Vc backends. For more complex solids, VecGeom still improves the scalar interface via better navigation and distance algorithms, but additional SIMD gains are often constrained by divergence among tracks within a basket. Even in these cases, vector units can be effectively utilized by selectively

[13] https://geant.web.cern.ch/geant/geant.html

vectorizing inner loops or local computations-a strategy applied extensively to tessellated solids, polyhedra, and multi-union shapes-thereby recovering a significant fraction of the nominal SIMD throughput despite divergence.[87]

One of the issues that VecGeom has observed is a bottleneck problem with the current GPU implementation, where it has been observed that two different geometries, one with a simple calorimeter with box layers and a complete CMS setup show similar compute and memory usage per streaming multiprocessor, but many stalled instructions in the completed cases due to the divergence of the threads in a wrap. However, in the more complex geometry, a large number of instructions become stalled due to thread divergence within GPU warps. Measurements indicate that increasing the geometric complexity leads to a rapid rise in computation time because, during parallel execution, simple geometrical primitives are forced to wait for more complex shapes to complete their processing [91]. To address this divergence problem, the Surface Model was introduced. Further detailed information about the concept and approach can be found in[92, 93, 94].

2.4 mSTS Geometry: Primitive vs Tessellated Comparison

To compare the geometries created using two distinct methods for simulation purposes, we explore two approaches: one utilising primitive solids within ROOT's TGeo library and another utilizing tessellated shapes derived from CAD files, after converting the STEP file to a format readable by ROOT's `TGDMLParser` through GDML.

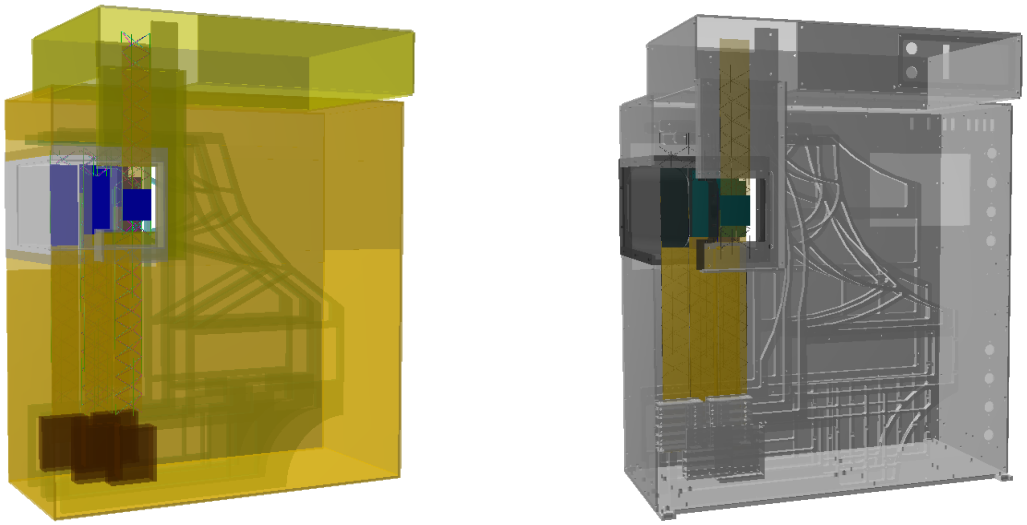

(a) Primitive solid-based mSTS geometry

(b) Tessellated Solid-based mSTS geometry

Figure 2.17: Figure 2.17a Simulation geometry of mSTS using primitive solids using ROOT and Figure 2.17b mSTS simulation geometry based on tessellated solid.

The first method utilizes ROOT's built-in primitive shapes, including boxes, tubes, spheres, trapezoids, and extruded solids, to construct the geometry, as shown in Figure 2.17a. This approach is efficient for assembling geometries composed of different volumes. However, defining and approximating material properties across various volumes requires significant human effort, especially when modelling complex components. While suitable for simple geometries, this method proves challenging for creating highly detailed models with intricate cut-outs and sophisticated structures.

In contrast, the second method converts CAD models, typically stored in STEP format, to a format that ROOT can interpret using the `TGDMLParser`. This process generates geometries composed of tessellated solids, which are triangular facets that approximate the surfaces of the various volume structures defined in the STEP files. An example of a geometry is depicted in Figure 2.17b. This approach significantly reduces manual effort and offers greater flexibility for representing fine details and complex shapes. However, it introduces trade-offs, such as increased computational time and much higher complexity in handling the geometry. Nevertheless, studies, such as those found in [91], suggest that simulation times can be considerably reduced by utilizing advanced navigation methods, such as the VecGeom navigator.

2.4.1 Comparison of CPU run-time

In High-Energy Physics (HEP) experiments, advancements in technology and upgrades require faster computational performance for simulations. Run-time refers to the total time required to

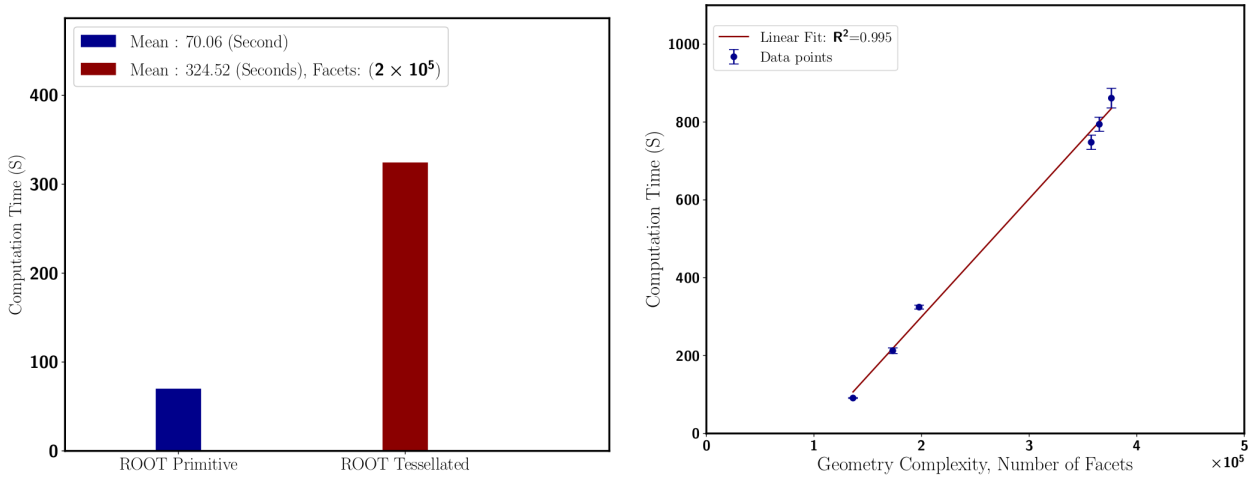

(a) CPU time comparison between Primitive solid-based and Tessellated solid-based mSTS geometry

(b) Computation time of the mSTS geometry containing a varying number of facets (increasing geometry complexity).

Figure 2.18: Figure 2.18a Computation time required to process 100 events per job for UrQMD model event transport using GEANT4 on the central cluster system at GSI for a geometry composed of primitive ROOT solids and tessellated solids, and Figure 2.18b Computation time of the mSTS geometry with increasing geometry complexity.

complete all transport events[14] in a simulation. Figure 2.18a compares the mean run-time for 10 jobs, each containing 100 events, using GEANT4 and the TGeoNavigator for both primitive solid based and tessellated solid based geometry, performed on the GSI Virgo cluster[15] where a system equipped with an Intel Xeon Gold 6248R CPU (3.0 GHz). It is observed that tessellated solid-based geometry takes nearly 4.63 times larger processing time to complete the transported events. The runtime is also influenced by various GEANT4 settings, including the number of steps after which the event transport stops, as well as different physics process cuts. These parameters also play a crucial role in physics performance and in determining computational efficiency. However, the current run-time comparison was done with the default settings[16] of those parameters that we had in the CBM-ROOT.

Figure 2.18b presents the average processing time for tessellated geometries, which contain varying numbers of facets, using the same settings applied to the ROOT-based geometry. From these results, it is clear that increasing the number of triangular facets in tessellated geometries significantly enhances event processing time. This increase appears roughly linear with the number of facets, leading to considerably higher computation times than for geometries based on ROOT primitive solids.

2.4.2 Comparison of Particle Production

This section discusses fundamental physics comparisons between geometries prepared using primitive ROOT solids and those prepared using tessellated solids.

Figure 2.19 presents a comparison of simulated data of the primary particle distribution based on their PDG ID, for two distinct representations of the mSTS geometry. Since the primary particles originate directly from the input source of the UrQMD events, there is no difference in the ratio.

Additionally, Figure 2.20 illustrates the various electromagnetic and hadronic processes that occur during event transport through the detector. We observe that a few Geant processes, such as Compton scattering, Hadronic interaction, and Coulomb scattering, exhibit a variation in the ratio of 2-5%. Apart from these, the ratio for the remaining process shows no differences. Moreover, Figure 2.21 shows the various secondary particles generated, categorized by PDG ID. The ratio

[14] In this case, we have used the UrQMD model-generated minimum-bias events of Ni+Ni collision at beam momentum 1.93 AGeV/c

[15] https://virgo-docs.hpc.gsi.de/user-guide/overview/software.html

[16] In the version of CBM-ROOT used for this analysis, the default GEANT4 runtime configuration was `geant4Settings->SetG4RunConfig("geomRoot", "QGSP_BERT_EMV+optical", "stepLimiter");`, i.e. without enabling the `specialCuts` option.

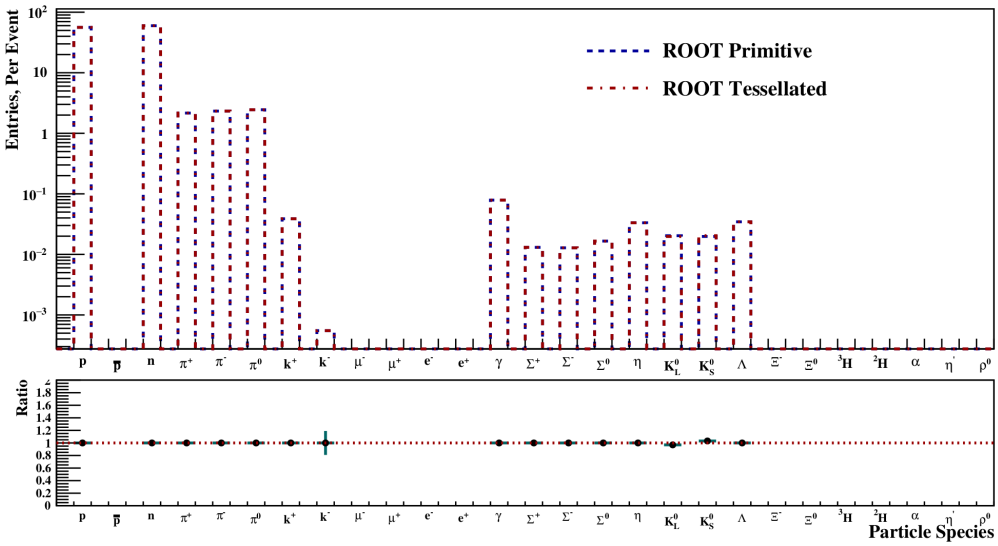

Figure 2.19: Comparison of primary particles based on their PDG Id.

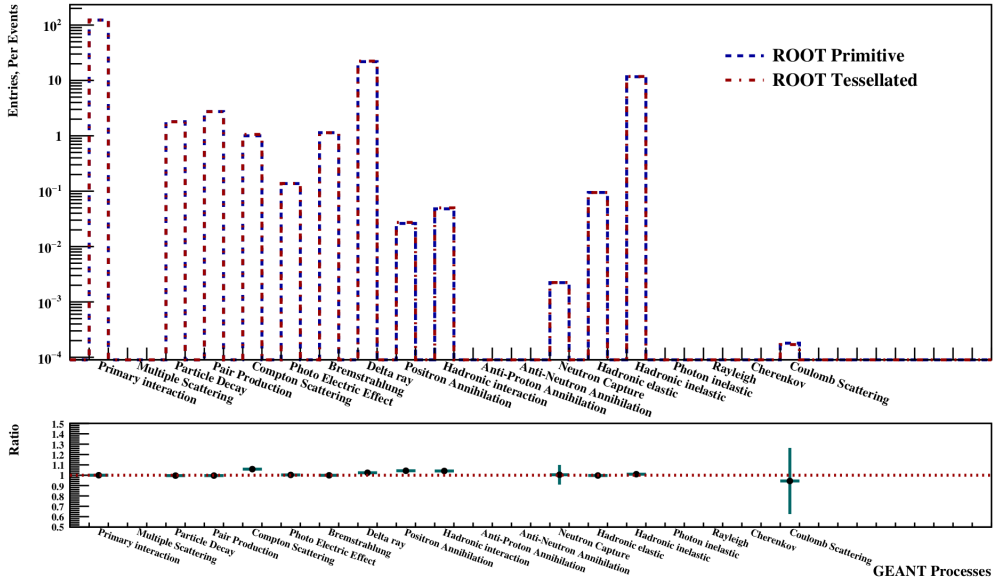

Figure 2.20: Comparison of different GEANT4 processes between different geometries.

distribution shows that most of the secondary particle distribution doesn't show any changes between the two different geometry representations. However, in some cases of the particle species, the ratio shows variations, either higher or lower, within the statistical error bars.

Figure 2.22 presents the distribution of the secondary particles' start Z vertex positions, which indicates the location along the z-axis (the beam direction), where secondary particles originate within the detector setup. Also, in this case, we observe that the ratio remains almost constant across the mSTS detector area, spanning the 16−58 cm range. There are instances before the mSTS detector, where the ratio differs, which needs further investigation.

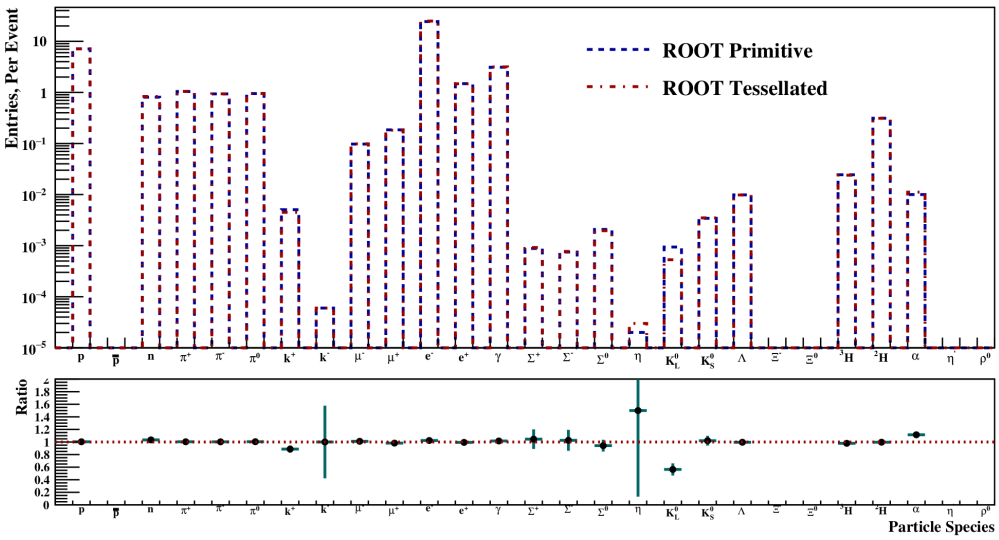

Figure 2.21: Comparison of secondary particles based on their PDG Id between two geometries.

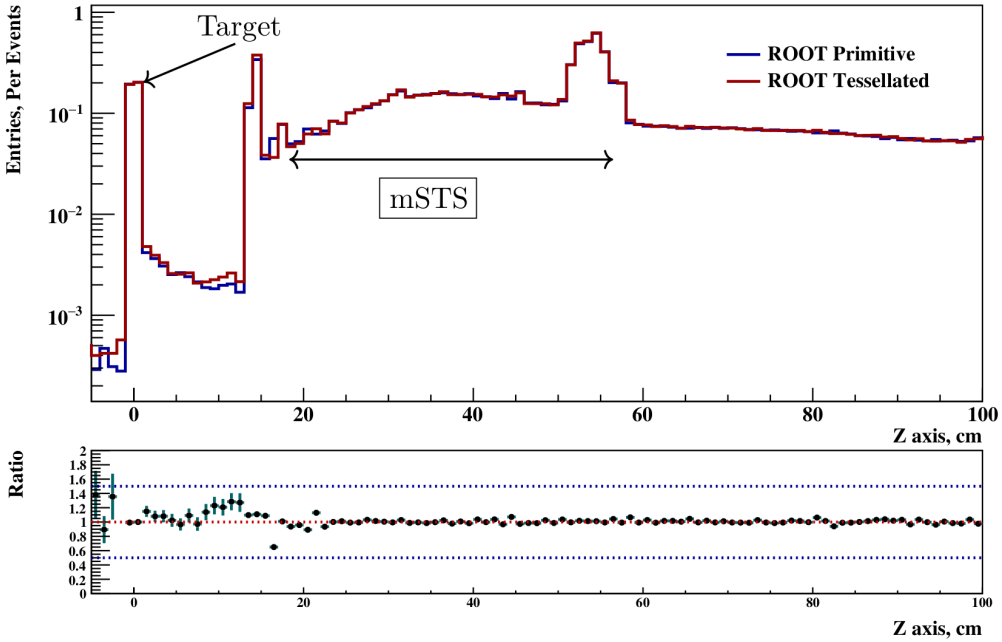

Figure 2.22: Start *"z-vertex"* of the secondary particles.

Overall, it is evident that when the geometry is accurately defined using ROOT primitive-solids, and the corresponding material properties are adequately approximated, the particle ratios remain consistent between the two geometries. Furthermore, the direct conversion of CAD models to ROOT simplifies the integration of complex structures into simulations, enhancing workflow efficiency. Moreover, the CAD-to-ROOT offers a significant advantage by enabling quick assessments of the material budget of any volume. It also enables faster integration of any hardware changes that need to be reflected in the simulation, facilitating a quick evaluation of their impact on detector performance. As a result, we can analyze the effects of design adjustments on time and, based

on simulation outcomes, make necessary optimizations more effectively. Our performance analysis, as discussed in the **Section 2.4.1**, shows that tessellated solid-based geometry demands a significantly higher computational run-time compared to those built from primitive solids. The increased run-time for the geometry based on tessellated solids is attributed to the algorithm iterating over all the surfaces through which the particle traversed. However, there is ongoing development to make the simulation faster for tessellated solids by optimizing algorithms such as the Bounding Volume Hierarchy (BVH) at CERN[95], which can only make the simulation faster to some extent. Furthermore, it was found that careful preparation of geometry using primitive solids available in ROOT and with meticulous optimization of the volume representations and rigorous approximation of the material properties can lead to results consistent with those obtained from the detailed tessellated geometry. This observation suggests that there is a significant advantage from the CAD-to-ROOT tessellated solid geometry in terms of physics accuracy compared to the traditional approach, but, on the other hand, it imposes a substantial computational expense. Thus, it is advantageous to employ a tessellated-solid-based geometry during the early stages of detector development, when frequent design iterations and rapid optimisation are required. Once the geometry layout becomes stable, an optimized primitive–solid–based geometry can be adopted for large-scale simulation data production, ensuring higher computational performance and consistency in physics performance.

2.5 Material budget in the STS Acceptance

Within the acceptance of STS, $2.5^{\circ} < \eta < 25^{\circ}$ (from a target position), the material budget is primarily contributed by components such as the silicon sensor, micro–cable, ladder support structure that holds the sensors and micro-cables, etc. For a normal incidence particle track that hits one sensor per station, a 320 ± 15 μm silicon wafer contributes:

$$\left(\frac{x}{X_0}\right)_{\mathrm{Si}} \simeq \frac{t}{X_0^{\mathrm{Si}}} = \frac{0.032 \text{ cm}}{9.36 \text{ cm}} \approx 0.00342 \;\Rightarrow\; 0.342\%,$$

and a typical micro–cable contributes about $\sim 0.124\%$ X_0. In addition, carbon–fibre tube wall of thickness $t = 0.04\,\mathrm{cm}$ where the inner and outer diameter are 0.07 cm and 0.15 cm, respectively, corresponds to:

$$\left(\frac{x}{X_0}\right)_{\mathrm{CF,\,1\,wall}} \simeq \frac{t}{X_0^{\mathrm{C}}} = \frac{0.04 \text{ cm}}{18.89\ cm} \;\Rightarrow\; 0.212\% \quad (\text{two walls: } \sim 0.42\%).$$

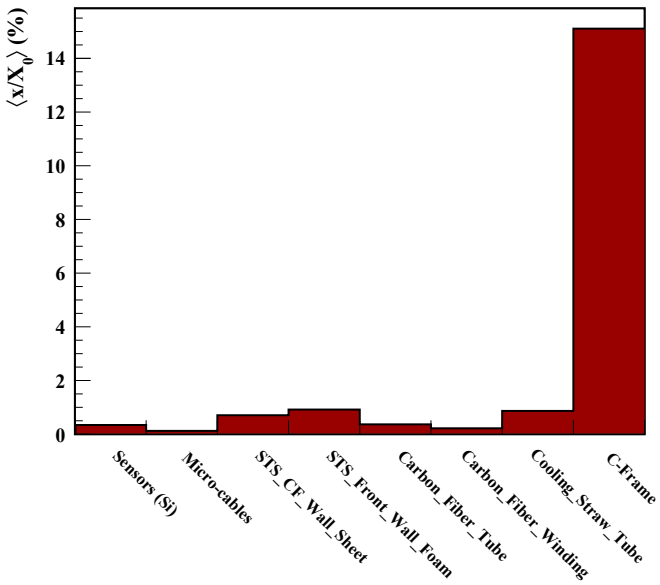

Figure 2.23: Material budget ($\frac{x}{X_0}\%$) per volume of various components in the STS detector through simulation.

On the other hand, the larger material budget contributing components, e.g, Al C-frames (see Figure 2.23) are outside of the acceptance area; therefore, the core performance of the STS is governed by the sum of $x/X_0\%$ of the components within the active region. Figure 2.23 shows the per volume material budget of the various components in the STS detector, where the components that could affect the momentum resolution have a per volume material budget $< 0.5\%$.

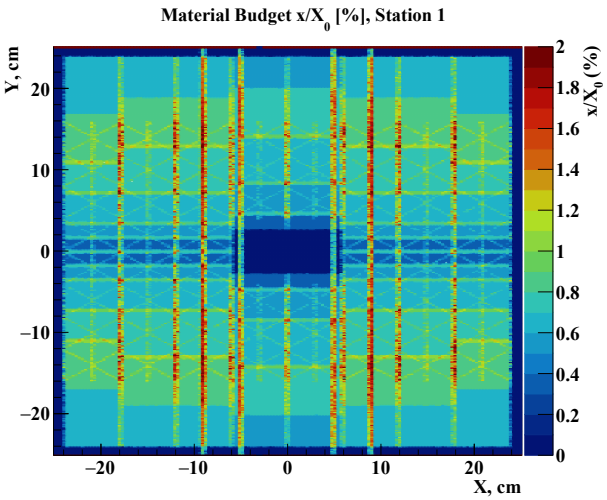

Figure 2.24: Illustration of the material budget for station 1 of the STS detector.

Figure 2.24 shows the two-dimensional profile of the material budget distribution for Station 1 of the STS detector. The histogram illustrates the variation of $x/X_0\%$ across the detector acceptance area in the transverse plane (X–Y), highlighting the spatial distribution of the material within the first tracking station. The overall material budget ranges from approximately 0.3% to 1.5%X_0, with the lowest values corresponding to regions dominated by the active detector components, such as the silicon sensors and readout micro-cables, and the higher values associated with passive structures, including mechanical supports, cooling lines, and electronics enclosures. The material budget for all the station is shown and discussed in **Appendix A**.

2.5.1 Impact of Material on Momentum Resolution

In **Section 2.1**, we outlined the theoretical considerations regarding how detector material influences track and vertex reconstruction. In this section, we examine, through simulation, the momentum resolution achievable with the STS detector.

Figure 2.25 shows the relative momentum resolution, $(\frac{\Delta p}{p})\%$, as a function of particle momentum for all charged particles, as well as for primary and secondary particles, reconstructed in the STS tracking system. The results correspond to events generated at a beam momentum of 12 AGeV/c and transported through the detector setup using the CBM-ROOT simulation framework. It is clear from the obtained results that over a broad momentum range of approximately 1.0 GeV/c < p < 5.0 GeV/c, the STS achieves a momentum resolution better than 1.5%, demonstrating the excellent precision of the tracking system within its design range. At low momenta (p < 1 GeV/c), the resolution is slightly degraded due to the increased impact of multiple Coulomb scattering in the detector material. As described by the Highland formula (Equation 2.1), the

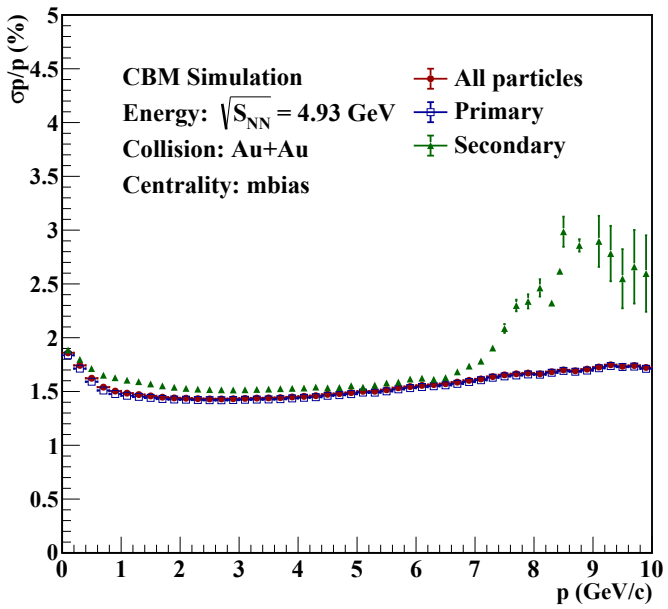

Figure 2.25: Momentum resolution $\frac{\Delta p}{p}\%$ as a function of momentum for all charged, primary and secondary particles reconstructed in the STS, for an event generated for Au+Au collision at a beam momentum of 12 AGeV/c and transported through the detector setup using CBM-ROOT.

scattering angle scales inversely with particle momentum and proportionally with $\sqrt{x/X_0}$. Consequently, angular deviations for low-momentum particles also broaden the track curvature and increase the momentum uncertainty.

Secondary particles, which are produced by hadronic interactions or decays within the detector

material, experience slightly worse momentum resolution compared to primaries over most of the measured momentum range. This degradation arises from their more complex topologies, such as displaced vertices and increased path lengths through detector material, which amplify the effects of multiple scattering and reconstruction uncertainties. Despite this, the secondary-particle resolution remains within about 2% even at momenta up to 7 GeV/c.

It is noticeable that beyond the particle momenta 6 GeV/c, the resolution begins to increase slowly. This behaviour can be understood well from the Gluckstern formula for the transverse momentum resolution as described in the Equation 2.2a where the second term, dominated by multiple scattering, decreases with increasing momentum and becomes negligible at high particle momenta. The first term, governed by spatial resolution and tracking geometry, scales linearly with momentum; therefore, it becomes dominant at high momentum. As a result, once multiple scattering no longer contributes significantly, the intrinsic detector resolution and finite lever arm precision impose a stringent limit, causing the relative momentum resolution $\frac{\Delta p}{p}\%$ to rise with increasing particle momenta p as can be seen from a Figure 2.2a and Figure 2.2b.

Chapter Summary

- In the beginning of the chapter, we discussed the implementation method used for representing the various active and passive detector volumes and its material budget in the simulation geometry, and their realization was done using the traditional approach based on ROOT primitive solids.

- We also explored an alternative approach in which we used a workflow to prepare the simulation geometry by directly importing the CAD model into the simulation after converting the CAD's STEP file to a ROOT- or GEANT4-readable GDML format.

- We used the mSTS, a small prototype of the CBM-STS detector, as a test case and compared runtime performance between the primitive-solid-based and tessellated-solid-based geometries. We have also shown some basic comparisons of particle production between the two. We found that the tessellated-solid-based geometry requires a significantly longer computational time during event transport using GEANT4 and is therefore not very reliable for producing large datasets. Additionally, the comparison of secondary particle production shows consistent performance. However, the CAD-to-ROOT approach facilitates quick assessment of the material budget for any detector volume, enables rapid evaluation of its impact on physics performance, and allows rapid design adjustments based on simulation outcomes, thereby enabling prompt optimization during the early phase of detector R&D. In addition, this method helps in preparing effective volume approximations when constructing more complex geometric volumes using ROOT primitive solids.

- At the end, we discussed the STS detector momentum resolution performance for primary and secondary particles through simulation of minimum-bias events at beam momentum 12 AGeV/c. The results obtained through simulation reveal that the STS has a momentum resolution of $\leq$1.5% for the particle momentum range between 1.0 GeV/c $< p <$ 5.0 GeV/c for primaries. For secondaries, the momentum resolution remains within 2% up to a momentum range of 7 GeV/c.

Chapter 3

Data Rate Study for the mini-Silicon Tracking System at mCBM Experiment

The mini-CBM (mCBM) experiment has been operational since 2018 at GSI Helmholtzzentrum für Schwerionenforschung, and it is using the SIS-18 synchrotron accelerator facility. SIS-18 accelerator facility can deliver the beam of various heavy ions, i.e., Au, Ag, Ni, and U, ranging from 1-2 AGeV/c. The mCBM experiment serves as a full-system demonstrator, combining prototype or pre-series components of all major CBM detectors integrated with the complete readout and online analysis chain. The main goals of mCBM are to[96]:

- commission and validate detector technologies and their front-end electronics under real beam conditions,
- verify the synchronization and data transport concept for high-rate operation, and
- develop and test the time-based reconstruction and online selection algorithms and offline data analysis, required for the CBM physics program.

Within the mCBM detector setup, the mini-Silicon Tracking System, known as mSTS, plays a vital role in tracking charged particles. The mSTS consists of 12 silicon strip sensors mounted on lightweight ladders and arranged in three tracking stations along with an aluminium-made C-shaped frame called the *"C-frame"* support structure. The signals from sensors are read out by Front-End Boards (FEBs) equipped with ASICs of different uplink configurations, and are further

connected to Common Readout Boards (C-ROBs). This configuration enables detailed studies of detector occupancy, channel-by-channel response, and data rates at moderate to high interaction rates.

This chapter focuses on data rate studies of the mSTS detector, conducted using both real experimental data and detailed simulations. The main objectives are to characterize the spill structure, estimate the collision rate, compare digi-channel distributions, evaluate per-channel signal rates, and to study off-spill noise behavior.

The results will provide essential validation of the free-streaming readout concept and noise modeling strategy for the STS detector, and they will help refine the simulations in preparation for full-system operation of the STS detector at the upcoming FAIR facility.

3.1 mCBM Experimental Setup

The experimental test setup of the mCBM[1] includes detector modules from all CBM detector subsystems, e.g., BMON, mSTS, mTRD, mTOF, mRICH, mMUCH/mPASTA, and mFSD, etc, using pre-series production components, and are positioned downstream of a nuclear target at an angle of 25° with respect to the beam axis. The detector setup is illustrated in Figure 3.1. There is no magnetic field.

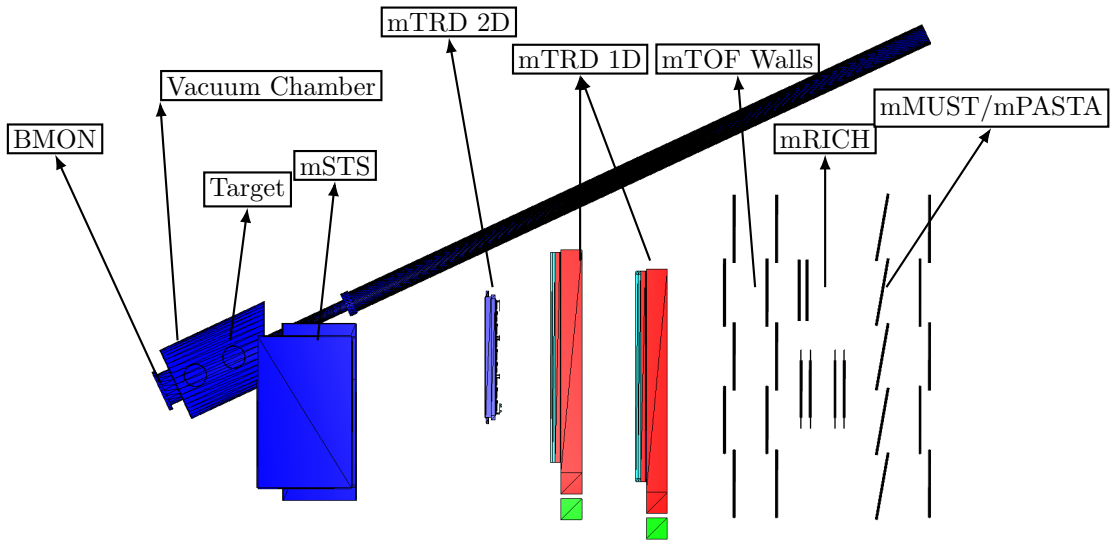

Figure 3.1: mCBM experimental setup (top view) with various detectors prototypes.

[1]The mCBM setup serves as the prototype of the CBM detector. For consistency and simplicity in notation, all sub-detector systems within this prototype are denoted as `mXXX`, where `XXX` refers to the corresponding CBM sub-detector (e.g., mSTS, mTOF, mTRD).

- **Target:** In the mCBM experimental setup, the target is positioned at the coordinate origin $(0, 0, 0)$ with a polar angle orientation of 25°. The target ladder is designed to accommodate various target materials and thicknesses, allowing rapid exchange of target samples between beam runs without the need for manual intervention during the beam-time campaign.

  Typical thin and thick targets used in mCBM include gold (Au) foils with thicknesses of 0.025 cm and 0.25 cm, and nickel (Ni) targets with thicknesses of 0.04 cm and 0.4 cm. These correspond to interaction probabilities of approximately $\sim$1% and 10%, respectively, for the incident beam. The flexibility in target configuration enables systematic studies under different interaction conditions.

- **The Beam Monitoring (BMON):** BMON detector is based on diamond sensors fabricated from either **p**oly-**c**rystalline or **s**ingle-**c**rystal chemical vapour deposition (**pc**-CVD or **sc**-CVD) material, which is employed to provide a precise time reference (T_0). It has an outstanding timing performance and exceptional radiation hardness, making it ideally suited for operation in intense radiation environments.

  It is positioned upstream of the target and delivers accurate time measurements for incoming beam particles, serving as the global start-time reference for subsequent event reconstruction. Currently, two BMON detectors are installed, oriented in the X–Y plane, which allows simultaneous monitoring of the beam profile and position in both transverse directions with high spatial precision.

- **mSTS:** The mini-STS (mSTS) comprises 12 silicon micro-strip sensors with a thickness of 320 ± 15 μm, available in different sizes and integrated onto lightweight carbon-fiber support structures known as *"ladders"*. These ladders are arranged into three tracking stations (see Figure 3.2), forming a compact detector system designed for precise reconstruction of charged-particle trajectories.

- **mTRD:** The Transition Radiation Detector (TRD) exploits the emission of transition radiation, which occurs when a charged particle crosses the boundary between two media with different dielectric constants. This radiation is produced in a dedicated radiator and subsequently detected by a Multi-Wire Proportional Chamber (MWPC) filled with a Xe/CO_2 gas mixture.

- **mTOF:** The Time-of-Flight (TOF) detector enables identification of hadrons such as pions, kaons, protons, and light nuclei by precisely measuring their flight time over a known distance.

Combined with STS momentum information, this allows for the accurate determination of the particle mass. The TOF system is based on Multi-Gap Resistive Plate Chambers (MRPCs), providing excellent time resolution and high detection efficiency for charged particles.

- **mRICH:** The Ring-Imaging Cherenkov (RICH) detector is based on the emission of Cherenkov radiation. When charged particles traverse through a radiator medium with a velocity exceeding the speed of light in that medium, it is known as Cherenkov radiation. It is specifically designed for the identification of dielectrons by detecting the Cherenkov photons produced along their paths. These photons are collected onto a UV-sensitive photo detector plane equipped with multi-anode photomultiplier tubes, allowing for the precise reconstruction of Cherenkov rings and reliable particle identification.

- **mMUST/mPASTA:** The MUon STraw (MUST), also referred to as the PAnda STraws (PASTA) detector, is a straw-tube tracking system designed for efficient muon detection. It was recently installed in 2024/25 within the mCBM experiment and is currently undergoing testing. The detector employs straw tubes with a Kapton XC cathode and a gold–tungsten anode, filled with an $Ar/CO_2/O_2$ gas mixture (70/28.5/1.5). Its lightweight design and high spatial resolution make it well-suited for precise muon tracking.

- **mFSD:** Forward Spectrometer Detector is also installed in the mCBM experiment. The primary purpose of the detector is to determine the orientation of the reaction plane and the centrality of the collision beam.

3.2 mSTS Detector Setup

As illustrated in Figure 3.2, the mSTS detector configuration, installed during the 2024 beam-time campaign, consists of a systematic arrangement of 12 silicon sensor modules distributed across three detection planes, referred to as *"stations"*, to achieve optimal spatial resolution and tracking efficiency. The sensor modules in Stations 1 and 2 originate from earlier development phases (since 2021). In contrast, the sensor in Station 0 was integrated more recently during the 2024 upgrade phase to enhance detector coverage and improve overall tracking performance.

All silicon sensors are mounted on lightweight carbon-fiber support structures known as *"ladders"*, which are further mounted laterally onto a mechanically stable, custom-designed aluminium frame referred to as the *"C-frame"*. The current position of Station 0 is 16 cm downstream of the target, while Stations 1 and 2 are located at positions 28 cm and 42 cm, respectively, in the global

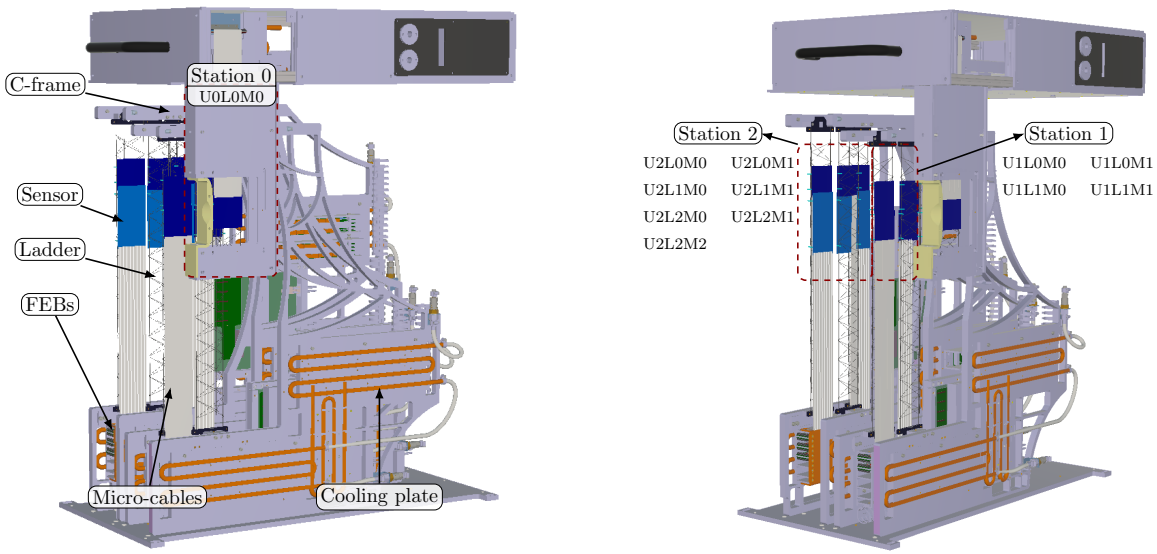

Figure 3.2: mSTS experimental setup with various active and passive components.

coordinate system relative to the target position.

Station 0 hosts a single sensor with dimensions of 6.2 cm × 6.2 cm, and it is mounted with a separate service box, placed on top of the existing mSTS box. Station 1 consists of two ladders carrying a total of four sensors, with two modules on each ladder, all of size 6.2 cm × 6.2 cm. Station 2 comprises three ladders: the middle ladder and the one closest to the beam pipe hold sensors of sizes 6.2 cm × 6.2 cm and 6.2 cm × 12.4 cm, respectively, while the ladder farthest from the beam pipe accommodates three modules, each of the size 6.2 cm × 6.2 cm.

For data readout, the front-end ASICs in the two downstream stations (Stations 1 and 2) utilize a single uplink, while the one in the upstream Station 0 employs FEB8-5 with all five uplinks to cope with higher data throughput. The system is equipped with seven Common Read-Out Boards (C-ROBs) for signal readout and five Power Boards (POBs) that supply the required voltages to the front-end boards (FEBs).

3.2.1 Module Naming Convention

Each of the 12 sensor modules in the mCBM setup is assigned a unique identification code, referred to as the *"module address"*. This address consists of a three-character alphanumeric code that specifies the exact location of a sensor within the detector geometry. It is composed of three essential constituents: the Unit index (U), the Ladder index (L), and the Module index (M).

This naming convention provides a clear, unambiguous way to identify and reference any sensor module. For example, a module labeled as (`U1L0M1`) refers to the sensor located on Unit 1, Ladder 0,

Module 1. Using this addressing scheme, one can directly infer hierarchical information, such as the position of each sensor within the mSTS layout, including its associated unit, ladder, and station, which facilitates easy identification during analysis.

3.3 Data-Rate Characterization from Simulation and Real Experimental Data

The STS detector employs Front-end Boards (FEBs) with three uplink configurations: one, two, or five uplinks, depending on the expected data rate. Therefore, it is essential to validate the data-handling capabilities of these configurations under realistic experimental conditions and their performance under similar operational conditions using simulation results.

For this purpose, in the mCBM experiments, ASICs with different uplink configurations are used for various sensor modules based on their position relative to the target and the beam pipe, as described earlier in **Section 3.2**. This approach enables a realistic assessment of readout performance across different occupancy regions of the detector, ensuring system meets the data throughput requirements of the full STS.

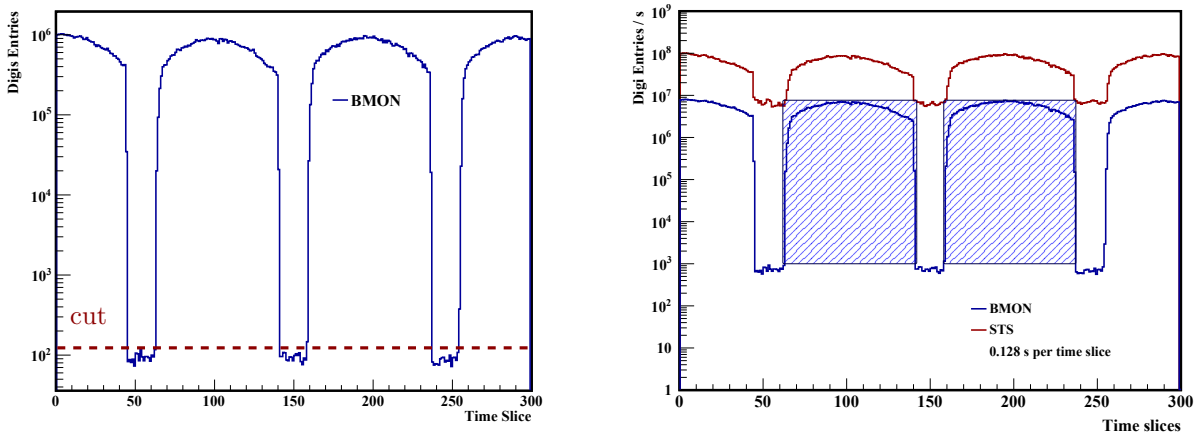

(a) Spill structure for a BMON detector

(b) Spill structure for a BMON and mSTS detector

Figure 3.3: Figure 3.3a Distribution of the spill structure for a BMON detector; red dashed line shows the applied cut for selecting the On-spill and Off-spill for an analysis. Figure 3.3b Spill structure for both BMON and mSTS detectors, normalized by a time-slice time. Blue hatched boxes represent the two full spill distributions.

Figure 3.3 shows the spill structure of consecutive time slices, for the Beam Monitoring (BMON) and mSTS detectors for run Id 2984. The distribution is normalized to the duration of a single time slice, which is 0.128 s. The two highlighted regions correspond to complete two-beam spills, which were selected for further analysis of the beam interaction rate.

3.3.1 Identification of On-Spill and Off-Spill Periods

To distinguish between beam-on and beam-off periods, a simple selection criteria was applied based on the number of digis recorded by the BMON detector in each time slice (see Figure 3.3a):

- **Off-spill:** Number of BMON digis ≤ 120
- **On-spill:** Number of BMON digis $\geq$ of the maximum digi count observed during the Off-spill

The criteria mentioned here were found to be reliable for run Id 2984 and are sufficient for identifying beam-on and beam-off intervals in the current dataset. Although the exact numerical thresholds may vary from run to run, depending on beam conditions. However, the approach provides a practical base for selecting the relevant time slices and performing subsequent rate calculation.

3.3.2 Estimation of Detector Dark Rate

To estimate the dark current contribution of the BMON detector, we used the off-spill condition by applying a threshold cut as mentioned in Subsection 3.3.1. Time slices below this value are considered to be dominated by dark counts. The corresponding dark current rate is then calculated as:

$$\text{Dark Rate} = \frac{120}{0.128\ \text{s}} \cdot \frac{1}{1000} \approx 0.0935\ \text{kHz}. \tag{3.1}$$

3.3.3 Estimation of Beam-Rate

To estimate the average beam rate, we focused on the two complete stable on-spill regions identified earlier, after removing the off-spill contribution as described in the previous section. These selected regions, highlighted in Figure 3.3, correspond to the stable beam-on intervals and were used for the beam-rate calculation. The corresponding spill-averaged rate, expressed in kHz as a function of time slice, is shown in Figure 3.4.

The mean number of digis recorded by the BMON detector within the two on-spill regions was determined to be

$$(8.92 \times 10^5) \pm 172.86 \quad \text{and} \quad (9.45 \times 10^5) \pm 176.61,$$

respectively. These values represent the average signal collected over the stable plateau of each spill, after subtracting the dark current contribution.

Taking into account the time-slice duration of 0.128 s and assuming a 10% target interaction probability, the average collision rate R can be calculated as:

$$R = \frac{N_{\text{digis}}}{0.128 \text{ s}} \times 0.10 \times \frac{1}{1000} = 717.28 \pm 0.10 \text{ kHz},$$

Where N_{digis} denotes the mean digi count per time slice, the factor 0.10 accounts for the interaction probability of the target, and the factor 1/1000 converts the result into kHz.

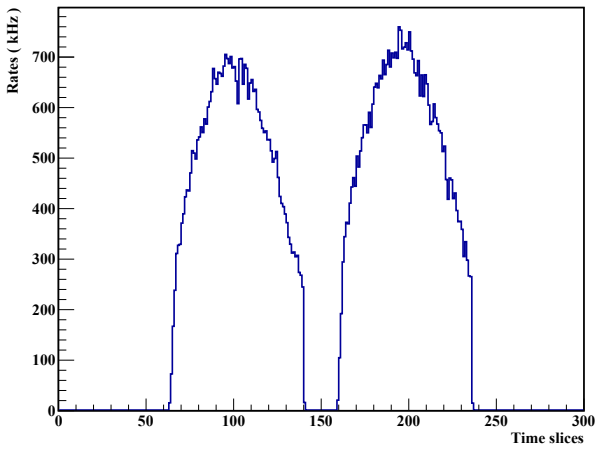

Figure 3.4: BMON detector spill rates

This result reflects the rate observed during the beam spills in run Id 2984. It is consistent with the plateau regions visible in Figure 3.4, which depict the spill-averaged beam intensity over the whole time structure of the extraction cycle.

3.4 Simulation Configuration for mCBM

The simulation was performed in *"Time-based"* mode within the CBM-ROOT framework, utilizing UrQMD to model minimum-bias nuclear interaction events transported through the detector using GEANT4. For the beam events, we employed the same transport engine to prepare the beam-background ($\delta-$electrons). To generate the simulation data with a beam-target interaction probability of 10%, the target thickness for Ni+Ni collisions at a beam momentum of 1.93 AGeV/c was set to 0.4 cm (4 mm). The required interaction probability for the given target thickness can be obtained from the equation:

$$P = 1 - e^{-(n \cdot \sigma_{\text{int}} \cdot x)} \tag{3.2}$$

Where P is the probability that a projectile nucleus interacts within the target, n is the number

density of target nuclei, σ_{int} is the inelastic interaction cross section, and x is the target thickness. The number density n is given by

$$n = \frac{\rho N_A}{A}, \tag{3.3}$$

with ρ the mass density of the target material, N_A Avogadro's number, and A the molar mass of the target nucleus.

Equation 3.2 shows that the probability for a projectile to traverse the target without interacting decreases exponentially with increasing thickness. Consequently, the interaction probability rises with target thickness and asymptotically approaches unity for sufficiently thick targets. For the present study, a target thickness of $x = 0.4$ cm results in an interaction probability of approximately 10%, meaning that about one in ten incident Ni beam particles undergoes an inelastic collision within the target.

Based on this configuration, the event generation for the simulation was performed using the GEANT4 transport engine[62], with the Ni target correctly configured in the simulation setup. A total of 10^6 minimum-bias events generated with the UrQMD event generator and 10^7 beam-only events were produced independently.

For the beam-event sample, the GEANT4 physics list was configured to include only the `emStandard` physics list[2], which accounts exclusively for electromagnetic interaction processes. This setup allows the study of the detector response to the electromagnetic component of the beam background, mainly delta electrons, which is separate from the hadronic and electromagnetic interactions described by the UrQMD events.

After event generation, the next step in the simulation is to digitize the detector response. This stage was performed in time-based mode, where events from both sources were combined within a given time interval and sampled at a fixed rate determined from the real data (see **Section 3.3**), according to a Poisson distribution to reproduce the stochastic time structure of the beam. In addition, electronic noise was sampled (see further discussion in Subsection 3.5.3) using the Rice formula based on a Gaussian probability distribution, with its amplitude determined by the specified ENC (Equivalent Noise Charge) threshold values. This approach ensures that the digitized simulation data accurately reflects the detector operating conditions in the real experimental scenario, including both signal and noise contributions.

[2] GEANT4 Electromagnetic physics (EMStandard, Opt0)

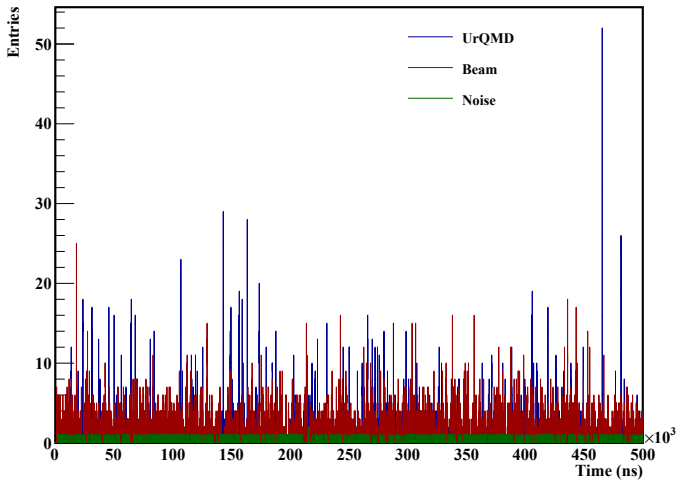

Figure 3.5: Signal and noise time distribution for the different sources (UrQMD, Beam and Noise) in time-based simulation.

The Figure 3.5 demonstrates the distribution of digitized signal times obtained in the time-based simulation of the mCBM setup. As shown in the distribution, the UrQMD contribution yields a significant signal concentrated in specific time intervals corresponding to real physical activity. In contrast, the Beam contribution is smaller, but at a rate 10× larger. At the same time, the Noise component remains roughly flat, indicating uncorrelated and random signal occurrences in a specific time window.

Events from both sources were merged at event rates of 7.17×10^5 events/s and 7.17×10^6 events/s, respectively, corresponding to an overall interaction rate of about 717 kHz and to a total simulated time interval of approximately 1.4 s.

3.4.1 Broken Channel Identification

Before performing comparison between simulation and experimental data, it is essential to incorporate real detector imperfections into the simulation. These imperfections primarily involve broken, unresponsive, or noisy readout channels, which can significantly affect both detector performance, such as spatial resolution and efficiency, as well as the measured observables.

Such problematic channels arise due to various hardware-related issues. Some originate from defects on the sensor surface that emerged during the production process, as illustrated in Figure 3.6. Other defects could have occurred during sensor testing in the laboratory, such as mishandling or accidental damage. Additional causes include defective front-end electronics, faulty bonding connections, or radiation damage during operation. As a result of these issues, specific channels

may fail to register signals even when particles pass through the active detector area, leading to biased measurements of spatial resolution, efficiency, and sometimes other observables, if not correctly accounted for.

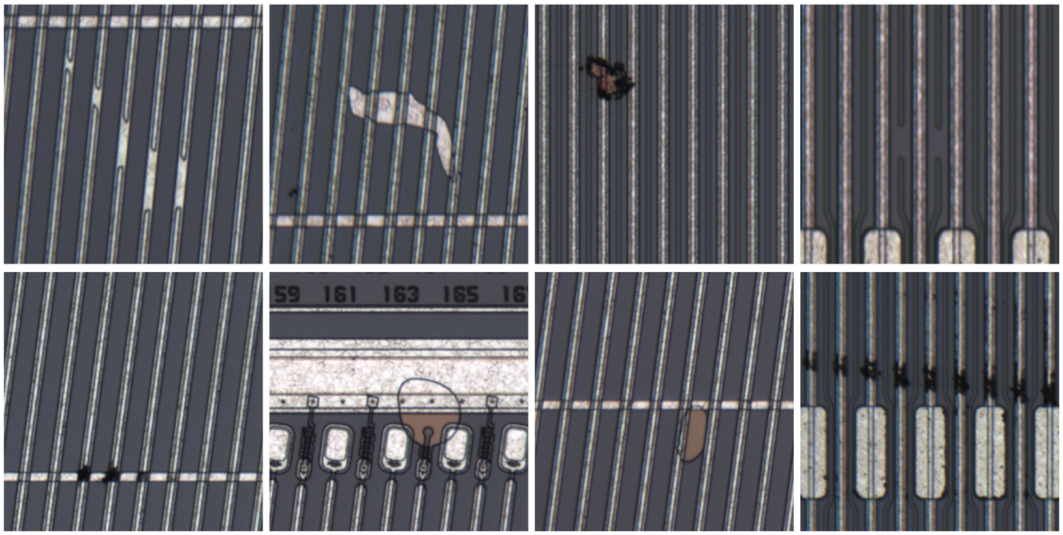

Figure 3.6: Examples of surface defects on the sensor. Top panel (left to right): implant break, aluminium short, aluminium open, P-stop break. Bottom panel (left to right): double metal line break, resistor fault, passivation open, and scratch.[97]

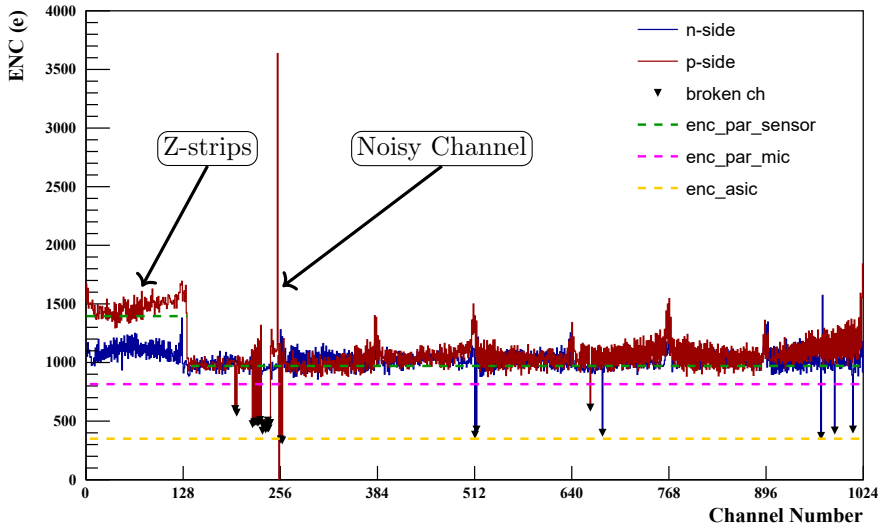

Figure 3.7: Example of a laboratory calibration measurement for one of the tested modules, showing the distribution of the equivalent noise charge (ENC) across all readout channels. The plot highlights defective channels, such as those exhibiting abnormally high noise or no response, and illustrates the relative ENC contributions from different electronic components.

To ensure a realistic comparison between simulation and experimental data, these channels must first be identified through optical inspection of the sensor surface and calibration in the lab, or sometimes by analyzing data taken with the source or from real experimental data. As illustrated in Figure 3.7, the channel distribution map obtained from a lab calibration clearly reveals defective

channels, either excessively noisy or completely unresponsive, along with their corresponding ENC values. Notably, the z-strips, which are shorter in length compared to other strips but have a longer signal path due to the double-metal connection, and therefore exhibit systematically higher ENC values due to their larger capacitive load.

Once identified, these channels are then incorporated into the Monte Carlo (MC) simulation by masking them so that no signal is recorded during digitization or reconstruction. This procedure replicates the actual detector conditions in the simulation, ensuring that the performance study is conducted under realistic conditions. Therefore, to mask a broken or noisy channel in the simulation, we have already implemented this scheme in the CBM-ROOT during MC event signal digitization and have accounted for it when preparing the simulation data.

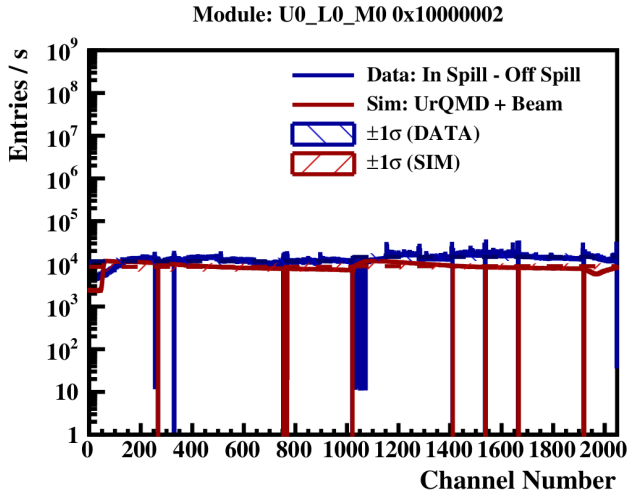

Figure 3.8: An example of the registered signal on an active channel for both n- and p-side of the sensor, along with a discarded inactive channel obtained from lab measurement.

Figure 3.8 clearly shows the distribution of the signal obtained for module `U0L0M0` located around 16 cm downstream from the target location from experimental data and from a simulation, along with the discarded dead channels in the simulation, to reproduce the situation as it is in the experiment.

3.5 Comparison of mSTS Detector Data with Simulation

As already outlined in **Section 3.3**, for the comparison between experimental data and simulation, a complete full-spill structure spanning a time-slice range of 50-250 was used for the analysis. This time-slice interval encompasses both the on-spill and off-spill regions, ensuring it includes the full detector response during the beam-target interaction and the off-spill period when there is no beam-target interaction. The off-spill analysis is particularly important for assessing detector noise in the

absence of particle interaction, as it reveals the detector's baseline performance in the experimental environment.

To reliably separate on-spill digis from off-spill digis in the mSTS data, a dedicated selection criterion was applied, as described in Subsection 3.3.1 and also illustrated in Figure 3.3b, where the on-spill structure is highlighted, and from Figure 3.4 two complete on-spill obtained after applying an appropriate cut. In the following sections, we compare the data with the simulated samples, focusing on the per-channel signal and noise data rates for each sensor module of the mSTS.

3.5.1 Signal-Rate Comparison between Data and Simulation

For the experimental data, only digis recorded during the on-spill period were considered; the contribution from the off-spill region was subtracted to suppress background noise. On the other hand, in the simulation, signal counts mainly originate from sources described as:

- **UrQMD & Beam :** The events from both sources represent the physics signal and the $\delta-$electron background, respectively.
- **Electronics noise:** generated during the digitization stage of the detector response, implemented in simulation based on the Rice formula, to reproduce the situation in the simulation as it is in the case of off-spill digis from experimental data. The noise level depends on the ENC[3] and threshold (see detailed discussion in **Section 3.5.3**). Although an accurate description of the noise is not reached because of the charge calibration and pick-up noise, its contribution, both in data and simulation, is mostly observed $\leq$1%. Therefore, any imperfection becomes negligible.

Figure 3.9 shows the signal recorded in each readout channel for all modules of the mSTS detector, separately, for different source contributions (UrQMD, Beam, and Noise). A clear trend is observed as one moves from upstream to downstream stations: the signal contribution from the beam background gradually decreases. This reduction arises because the majority of δ-electrons produced in the target region are absorbed or lose energy as they traverse successive detector layers, leading to a lower signal from beam background in the downstream modules.

Figure 3.10 shows the digi channel distributions for different silicon modules of the mSTS, separately for the experimental data and for the simulation. Each sensor module contains 2048 channels,

[3]ENC: Equivalent Noise Charge. In simulation, a single effective ENC and threshold value were assigned to each module side.

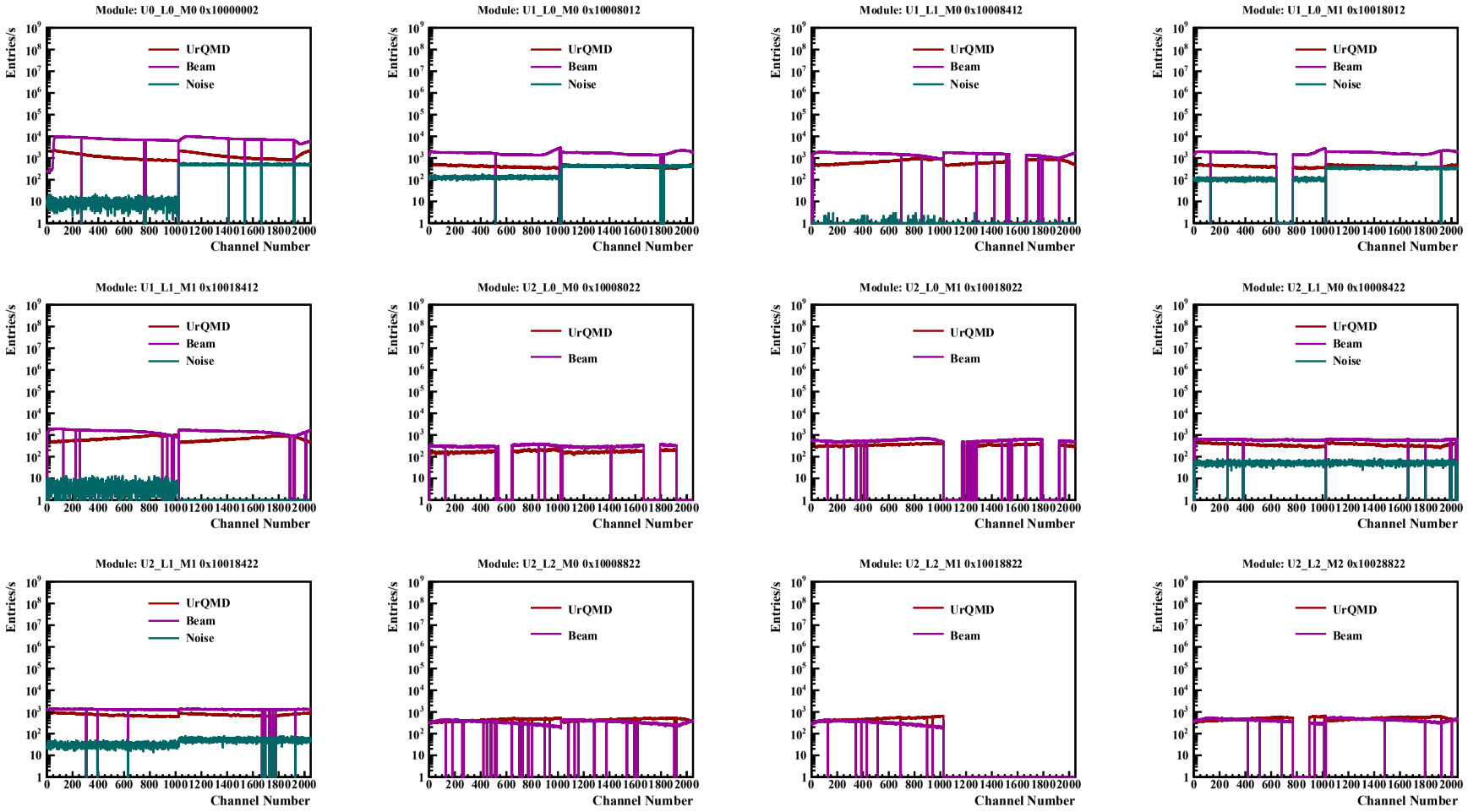

Figure 3.9: Digi channel distributions for different silicon sensor modules of the STS, from individual sources. Each module contains 2048 channels, with channels 0-1023 belonging to module side 0 ($n-$side) and channels 1024-2047 belonging to module side 1 ($p-$side).

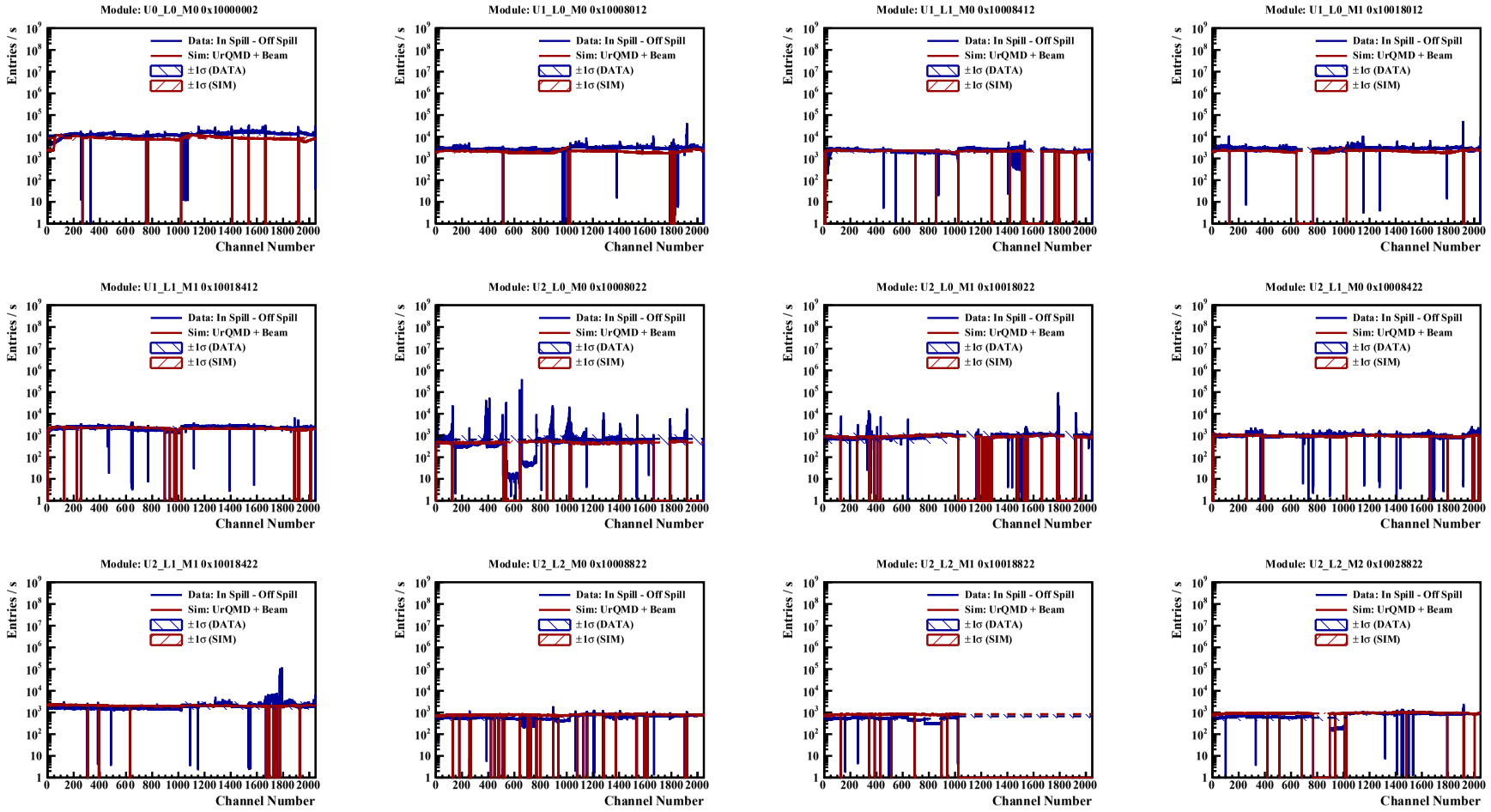

Figure 3.10: Digi channel distributions for different silicon sensor modules of the STS. Experimental data (on-spill digis after subtraction of off-spill background) are compared with simulations including UrQMD + Beam events. Each module contains 2048 channels, with channels 0-1023 belonging to module side 0 ($n-$side) and channels 1024-2047 belonging to module side 1 ($p-$side).

where channels 0−1023 correspond to module side 0 (n-side), and channels 1024−2047 correspond to module side 1 (p-side). Further details on (In-spill - Off-spill) and only for the Off-spill digi distribution and the comparison of Off-spill digis from data vs. noise obtained in simulation when using the given ENC and threshold value, which have been set in the real experiment, can be found in **Appendix B**.

Overall, the Figure 3.10 illustrates that the simulated digi channel distributions reproduce the shape and occupancy patterns observed in the data across different silicon sensors located at different positions of the tracking stations. The comparison shows that, for several modules, the simulation and experimental data are in good agreement, while for others, the agreement is only partial.

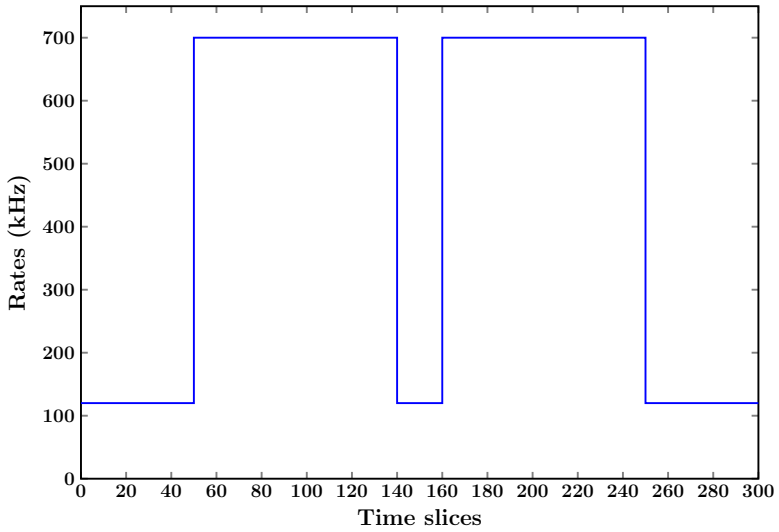

Figure 3.11: Illustration of an idealized step-function behaviour of the BMON rate as a function of time slice.

One likely reason for the observed discrepancies is that, in the simulation, events are transported through the detector assuming a constant (flat) interaction rate over time, as shown in the idealized situation in the Figure 3.11. However, in reality, the interaction rate during the experiment varies when ramping up and ramping down the system, also, it is not stable even when it is fully ramped-up but, somewhat fluctuating within a spill which is observed from a Figure 3.4, where one can see that the beam interaction rate is having a kind of Gaussian shape. Another reason is that in the simulation, the single noisy channels are not masked, as illustrated in Figure 3.10, for example, for the module Id `U2L0M0`, which belongs to station 2.

3.5.2 Signal-Rate Analysis for mSTS Detector Modules

As discussed in **Section 3.5.1**, and based on the selection criteria applied to both experimental data and simulation, the signal rates per channel were evaluated separately for the n- and p-sides of each

silicon sensor module. These rates were derived from the corresponding digi channel distributions (see Figure 3.10) and are presented in Figure 3.12.

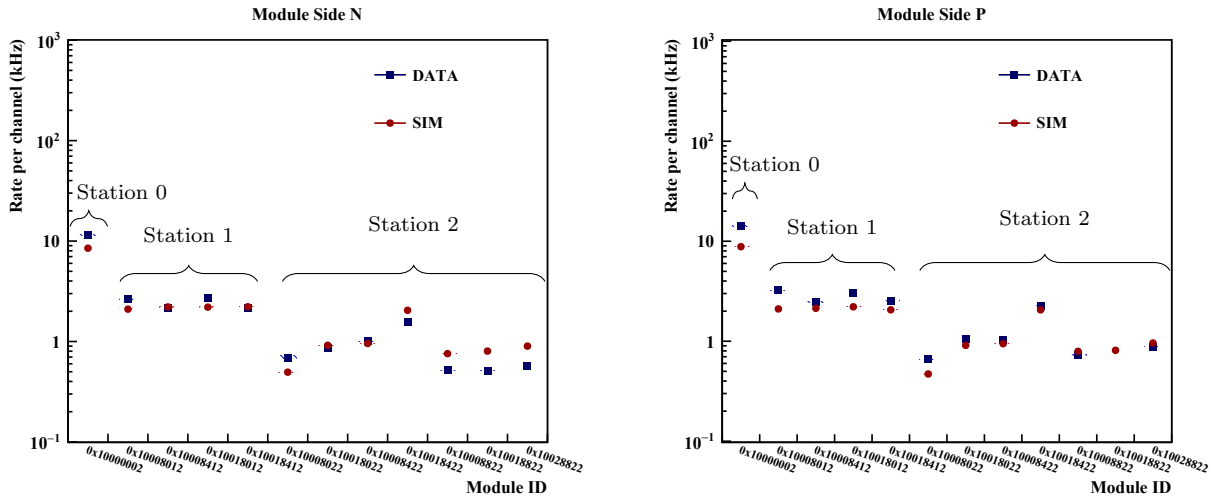

Figure 3.12: Signal rates per channel for different silicon sensor modules of the mSTS detector. Modules belonging to Station 0, Station 1, and Station 2 are indicated, separately for $n-$ and $p-$side.

For calculating the average signal rate per channel for a given sensor module, only channels with non-zero counts (i.e., active channels) were included. In contrast, channels without a signal (dead channels) were excluded from the averaging procedure. The comparison shows that, for most detector modules, the simulated and measured signal rates are in good agreement.

Furthermore, the average per-channel signal rate across all 12 modules on the $n-$side was measured to be 2.23 kHz, compared to 2.01 kHz in the simulation, corresponding to a relative difference of approximately 9.9%. On the $p-$side, the measured average rate was 2.92 kHz, while the simulation yielded 2.03 kHz, resulting in a relative difference of about 30%.

Overall, the comparison indicates that the simulation reproduces the correct order of magnitude of the signal rates at the given effective ENC and threshold settings, following the general trend of the measured data with reasonable accuracy. Nevertheless, differences at the level of individual modules remain, as seen in Figure 3.12.

These discrepancies likely arise from experimental conditions, such as variations in spill structure and module-specific effects, including threshold dispersion, channel-to-channel response variations, and the presence of noisy channels, all of which can influence the observed occupancy and rate in the data but are not fully represented in the simulation.

3.5.3 Noise Rate Measurement and Comparison with the Rice Model

During the off-spill period of the BMON detector, there is no beam present, which means that no beam–target interactions occur. Consequently, any signals recorded in the mSTS detector during this time are not associated with particle interactions but instead originate from intrinsic detector activity, such as dark current or electronic noise. As described earlier, the off-spill period is identified by applying a threshold cut on the BMON detector signal, ensuring that only time slices without beam-induced activity are considered.

The noise rate of the mSTS detector during the off-spill period can then be determined using Equation 3.4. It provides direct information on each sensor's noise contribution in the absence of beam interaction, serving as a reference for validating the simulation's noise model. The noise rate is defined as

$$R_i^{\text{data}} = \frac{N_i^{\text{off}}}{N_{\text{slices}}^{\text{off}}\,\Delta t}\,, \tag{3.4}$$

Where N_i^{off} is the total number of digis recorded in channel i^{th} during the off-spill period, $N_{\text{slices}}^{\text{off}}$ is the number of time slices identified as off-spill, and Δt is the duration of a single time slice. By comparing the measured noise rate with the corresponding simulated value, one can assess how accurately the digitization model reproduces the detector's noise behavior.

In the simulation, noise digis are generated during the digitization stage using the Rice formula [98, 99]. The expression is given by

$$f = \frac{f_0}{2} \cdot e^{\left(-\frac{v_{\text{th}}^2}{2\sigma^2}\right)}, \tag{3.5}$$

Where v_{th} is the discriminator threshold voltage, σ is the root-mean-square (RMS) noise voltage, and f_0 is the zero-crossing frequency, determined by the front-end bandwidth of the shaping amplifier. Equation 3.5 effectively describes the rate of spurious discriminator triggers caused by random Gaussian fluctuations of the preamplifier–shaper baseline crossing a fixed discriminator threshold. Thus, it effectively models the stationary, Gaussian part of the noise, providing a good first-order description of the noise in the detector system.

However, the real detector environment is typically complex, and the noise rate observed in the off-spill data contains many additional effects beyond the Gaussian assumption. One such effect arises from the random emission of the charge carriers and thermal noise, also known as *"Johnson*

noise" In contrast, impurities and imperfections in the silicon bulk can also contribute to noise, as charge carriers can trap and de-trap within the sensor bulk over a characteristic time. This leads to a frequency-dependent power spectrum noise. The charge trapping and de-trapping with different time constants introduce Lorentzian spectral components; superpositions of many time constants can mimic $1/f$ behavior. These effects broaden the noise distribution and produce non-Gaussian tails in the occupancy spectrum. This frequency-dependent noise is called *"flicker noise"*. Moreover, coherent disturbances from external sources, such as power supply ripple, digital cross-talk, clock or ground coupling, and mechanical vibrations (microphonics), can also induce low-frequency baseline motion across multiple channels. Variations in discriminator offsets and gain (threshold dispersion) also broaden the effective noise distribution. Accounting for these additional contributions is therefore essential to achieve a realistic description of the detector noise environment and to ensure meaningful comparisons between simulation and experiment.[100]

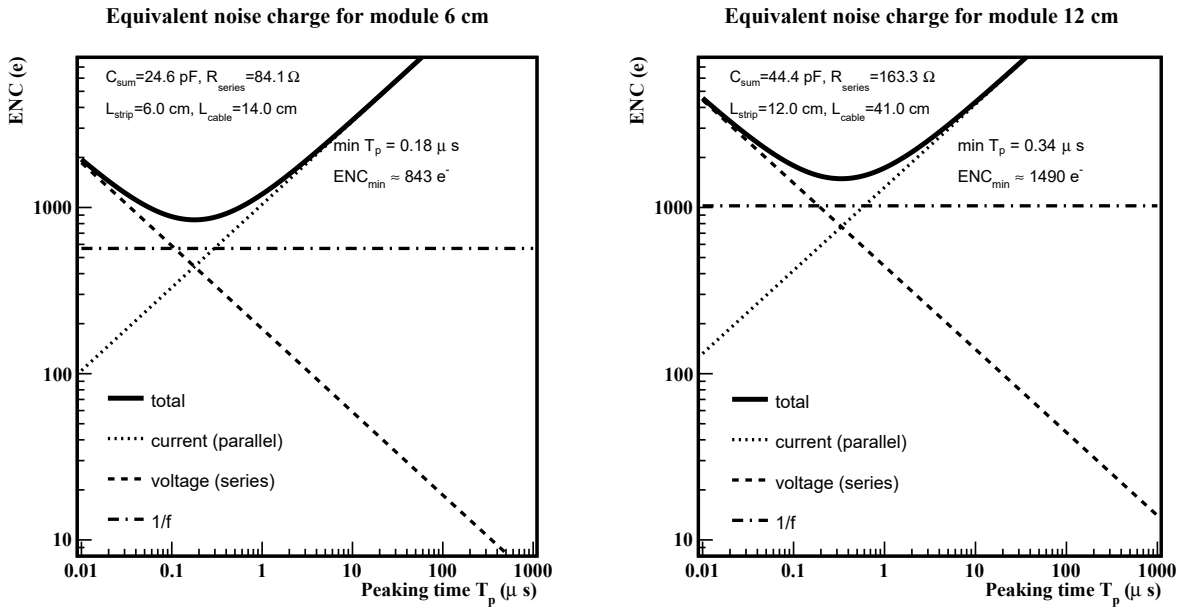

Figure 3.13: Equivalent noise charge (ENC) versus shaper peaking time (T_{p}) obtained analytically for silicon micro-strip sensors with 6 cm and 12 cm strip lengths. The total ENC and its individual noise contributions (series, parallel, and $1/f$) are shown for different micro-cable lengths.

Figure 3.13 shows an analytical description of the ENC vs. shaper peaking time (T_p) for the two different modules, which have a strip length of 6 cm and 12 cm, respectively. The total curve (thick solid) is decomposed into the three standard contributions of a shaper.

An STS readout channel can be represented by four main elements preceding the charge-sensitive amplifier (CSA):

- The sensor strip with capacitance C_{det} and leakage current I_{leak},

- The bias network represented by a resistor R_{bias},
- The series resistance of the strip and cable, $R_{\text{series}} = R_{\text{strip}} + R_{\text{cable}}$,
- The CSA input stage with its feedback network ($R_{\text{fb}}, C_{\text{fb}}$).

Each of these components contributes to the overall electronic noise. The total parallel (current) noise density is

$$i_n^2 = \underbrace{2qI_{\text{leak}}}_{\text{shot noise}} + \underbrace{\frac{4kT}{R_{\text{bias}}}}_{\text{bias resistor noise}} + \underbrace{\frac{4kT}{R_{\text{fb}}}}_{\text{feedback resistor noise}}, \qquad i_{na}^2 = \frac{4kT}{R_{\text{fb}}} \tag{3.6}$$

while the series (voltage) noise density is

$$e_n^2 = 4kT(R_{\text{strip}} + R_{\text{cable}}) + e_{na}^2, \qquad e_{na}^2 = 4kTR_{fb} \tag{3.7}$$

where q is the elementary charge, k is Boltzmann's constant, and T is the absolute temperature. The total capacitance seen by the CSA input is

$$C_{\text{sum}} = C_{\text{det}} + C_{\text{cab}}, \tag{3.8}$$

with C_{cab} the capacitance contribution of the cable.

After shaping, the noise can be expressed as an equivalent noise charge (ENC) referred to the detector input. For a CR–$(\text{RC})^2$ shaper, the mean-square ENC is given by

$$\text{ENC}^2 = \underbrace{i_n^2 F_i T_s}_{\text{current (parallel) noise}} + \underbrace{e_n^2 F_v \frac{C_{\text{sum}}^2}{T_s}}_{\text{voltage (series) noise}} + \underbrace{A_f F_{vf} C_{\text{sum}}^2}_{1/f \text{ noise}} \tag{3.9}$$

where T_s is the charateristic peaking time, A_f is the flicker $(1/f)$ noise coefficient of the input transistor, and F_i, F_v, and F_f are shaping coefficients (for a CR–$(\text{RC})^2$ shaper, $F_i \approx 0.85$, $F_v \approx 0.64$, $F_{vf} \approx 3.41$).[104]

From Figure 3.13, the following key features of the ENC dependence on shaping time T_p can be identified:

- The **series noise** term decreases approximately as $1/T_s$. It grows with the total input capacitance C_{sum} and with any series resistance present in front of the CSA input. Increasing

the transconductance g_m of the input transistor reduces the contribution $e_{n,\text{asic}}$.

- The **parallel noise** term increases linearly with T_s. It is dominated by the detector leakage current I_{leak} and by the thermal noise contributions of R_{bias} and R_{fb}. Detector operation at lower temperature and the use of higher-value bias and feedback resistors help reduce the contribution.

- The **1/f noise** term is independent of the shaping time. It appears to be a flat contribution with respect to T_s and sets a fundamental noise floor determined by the total input capacitance C_{sum}.

Since the series noise decreases with shaping time while the parallel noise increases, their quadratic sum exhibits a clear minimum. By differentiating Equation 3.9 with respect to T_p (noting that the $1/f$ term does not affect the position of the minimum), one obtains the condition for the optimum value of the ENC and shaping time T_{opt}. The noise contributions appearing from individual electronic components can be minimized through the following design and operational strategies:

Reduction of series noise: Series noise can be mitigated by minimizing the total input capacitance, including both the detector capacitance (C_{det}) and the cable capacitance (C_{cab}). This can be achieved by employing shorter detector strips and interconnects, as well as by optimizing the layout to reduce parasitic capacitances. Furthermore, increasing the transconductance of the input transistor (g_m) enhances noise performance, while minimizing the series resistances of the detector strips (R_{strip}) and signal cables (R_{cable}) further suppresses this contribution.

Reduction of parallel noise: Parallel noise can be reduced by lowering the detector leakage current (I_{leak}), typically achieved by operating the detector at lower temperatures. In addition, using larger values for the bias resistor (R_{bias}) and feedback resistor (R_{fb}), within the limits imposed by stability and response-time requirements, helps to minimize the associated current noise contribution.

Reduction of $1/f$ noise: This contribution determines the baseline noise level but does not affect the optimal shaping time (T_{opt}). The low-frequency $1/f$ noise component can be minimized by carefully optimizing device geometry.

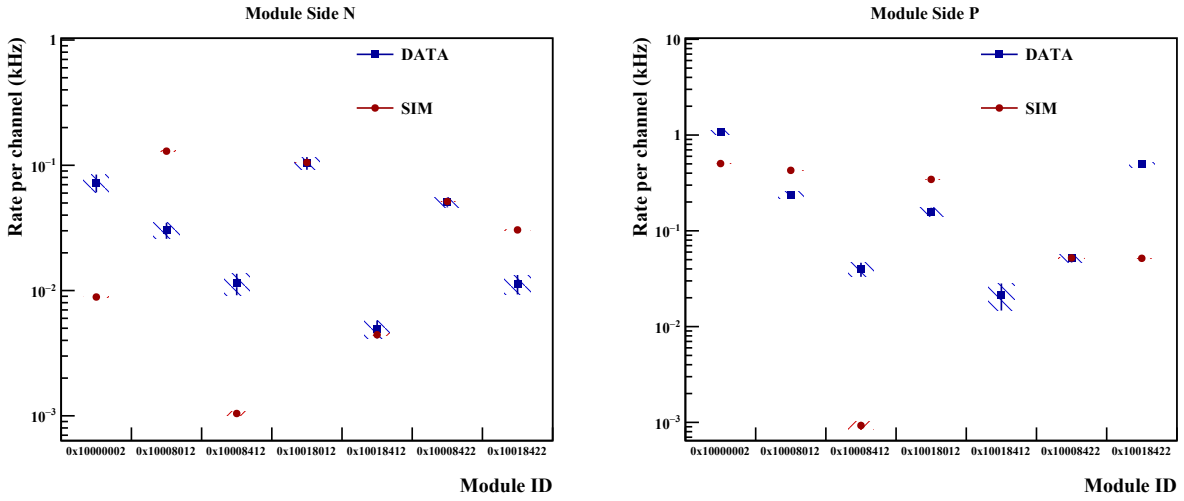

Figure 3.14: Average noise rates per channel for different silicon sensor modules: data measured during off–spill periods (left: $n-$side; right: $p-$ side) compared with simulation, where noise generation follows the Rice threshold level–crossing formula. Error bands indicate the statistical uncertainty on the mean noise rate per module channel.

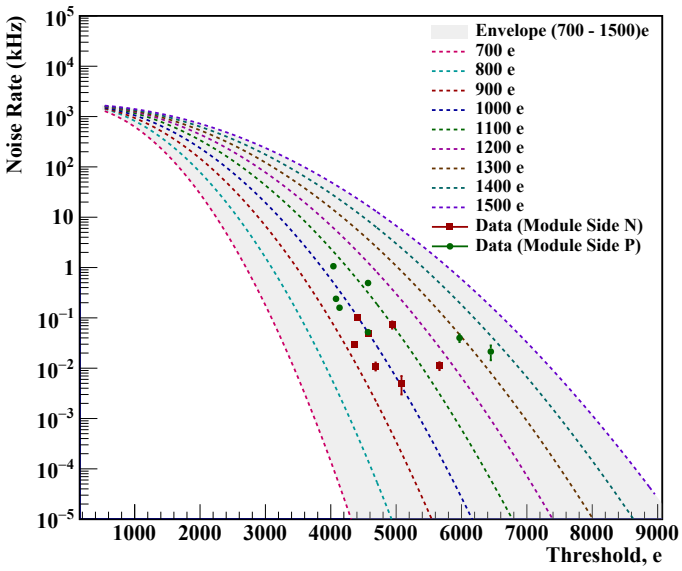

Figure 3.15: Noise rate as a function of discriminator threshold compared with Rice level–crossing predictions for different equivalent noise charge (ENC) values. The data points correspond to measured noise rates from run 2984.

Figure 3.14 presents the average noise rate per channel for the $n-$ and $p-$sides of all modules, measured during off–spill periods (left and right panels, respectively). For many sensor modules, the simulation accurately reproduces the correct order of magnitude and the overall trend of the data, indicating that the dominant Gaussian, bandwidth-limited noise component, primarily governed by input capacitance and shaping time, is well described by the Rice formula. However, noticeable deviations remain for specific modules, where the simulated noise rate either overestimates or underestimates the data. These discrepancies may arise from additional effects not yet implemented in the simulation, such as threshold dispersion, leakage current variations, or module–specific pedestal shifts.

Figure 3.15 shows the measured off–spill noise rate as a function of the discriminator threshold, overlaid with analytical Rice level–crossing predictions calculated for different equivalent noise charge (ENC) values, ranging from 700–1500 e, with the zero–frequency intercept set by the front–end

bandwidth (i.e., the shaping time). The gray band highlights the expected range $\sigma \in [700, 1500]$ e expected from laboratory measurements.

The square and circular markers correspond to measured off–spill noise rates on the $n-$ and $p-$sides of various modules for the ENC configuration used in run Id 2984. As predicted by the Rice formalism (Equation 3.5), the noise rate decreases steeply with increasing threshold. Most data points fall between the $\sigma \sim 800$–1200 e curves, indicating that the Rice model with a single effective ENC per module provides a good description of the dominant bandwidth–limited noise component.

Overall, this comparison demonstrates that the Rice model enables direct estimation of the effective ENC on each module side at a given threshold, with relatively small uncertainties. Such information is essential for validating the noise performance of the front–end electronics and for refining future simulation models. Based on the off-spill digi analysis of individual mSTS detector modules for run Id 2984, an average, typical dark noise rate was found to range from about 0.4 kHz per channel (minimum) up to approximately 1.4 kHz per channel (maximum) ,which is $\leq 1\%$ of the saturation bandwidth of the electronics used.

Chapter Summary

- In this chapter, a comprehensive analysis of the experimental data rate measurements for run Id 2984, recorded in the year 2024 using the SIS-18 accelerator facility at GSI, and their comparison with detailed simulations has been presented for the mini-Silicon Tracking System (mSTS) - a prototype of the full CBM-STS detector. The study aims to validate the free-streaming readout concept and to evaluate the detector response and front-end electronics performance under realistic experimental conditions.

- In the beginning, we discussed the detailed description of the mCBM experimental setup and conditions, including the beam–target interaction rate (10% interaction of the Ni beam with the Ni target), beam spill structure, beam rate, and identification of broken channels, etc.

- The simulation data sample was generated using the UrQMD event generator for Ni+Ni collisions and a beam background simulated with GEANT4 using the `emStandard` physics list, which includes only electromagnetic processes (no hadron–ion interactions), and therefore only δ-electrons. After that, a time-based simulation was performed, where the events from both sources were merged at the digitization stage, using the beam interaction rate obtained from the experimental data, which is approximately $\sim$ 717 kHz. At the same time, detector imperfections, such as broken channels, as well as module-dependent ENC and threshold parameters, were incorporated to mimic the actual conditions accurately. Additionally, the noise was generated at the digitization level using the Rice approximation formula, which produces a noise signal in the simulation by assuming Gaussian fluctuations based on the zero-frequency rate, the module's effective ENC, and the discriminator threshold value.

- The signal rate-per-channel comparison was performed for each module. The average per-channel signal rate shows a discrepancy of 10%–30% between simulation and experimental data on the $n-$ and $p-$sides of the module, respectively.

- The average noise rate per channel obtained from the data during the off-spill period for the $n-$ and $p-$sides of the module, when compared with the simulated data, shows that it reproduces the order of magnitude and trend of the data. This indicates that the noise is primarily dominated by the Gaussian bandwidth-limited noise component, which includes the detector capacitance, input capacitance, shaping time, and other factors, and is well described by the Rice formula for good working modules.

- Finally, we have shown the theoretically expected noise performance using the Rice formula

by varying the discriminator threshold at different ENC values and compared it with the per-channel noise rate obtained for the $n-$ and $p-$sides of the module from the experimental data, showing that most of the good module data points fall within the $\sigma \in [800, 1200]$ e band. Overall, the average dark rate was found to be 0.4 kHz (minimum) to 1.4 kHz (maximum) per channel, which is $\leq 1\%$ of the electronics' saturation bandwidth.

Chapter 4

Data Rate Study for the Silicon Tracking System

The CBM is a fixed-target, free-streaming experiment designed to sustain interaction rates of $\mathcal{O}(10\ \text{MHz})$. In this regime, the Silicon Tracking System (STS) should continuously deliver time-stamped data from particle interactions without a trigger, while maintaining tracking performance and timing fidelity. Data rate studies have been a crucial step in designing the optimal readout system. As the experiment will run in free-streaming mode to collect collision data, it is necessary to verify the readout electronics and components' ability to handle the rate and transfer the data to the storage system. This verification should be conducted in the lab and also through simulation before commissioning the final STS detector.

We present, in this chapter, a time-based simulation assessment of the entire STS detector data rates, which comprises 876 silicon sensors of four variants differing in length and, as per its current configuration, planned for initial CBM-STS operation. Evaluating data rates for the STS through simulations provides a deeper understanding of the system's capabilities in a complex and high-interaction-rate environment. The structure of the chapter is organized as follows:

In **Section 4.1**, a general description is provided of the front-end electronics used in the STS silicon sensors for the data readout system.

In the **Section 4.2**, we describe the procedure applied to the preparation of Monte Carlo (MC) event samples, which combine both physics events and beam-related background events (mainly δ-electrons). Then, the transport of these events through the entire detector geometry is performed using the GEANT4 transport engine[62], implemented within the CBM-ROOT framework. The

detailed digitization procedure carried out in the time-based mode is discussed in the following step, enabling a realistic evaluation of the STS detector response under foreseen experimental conditions. The following Subsection 4.4 describes the noise modeling approach applied in CBMROOT. The background noise is simulated at the same digitization stage using the Rice formula, which incorporates the effective Equivalent Noise Charge (ENC), the discriminator threshold, and zero-frequency noise parameters. It enables the generation of a realistic noise signal based on a Gaussian bandwidth-related noise signal, thereby reproducing the conditions expected in the actual experimental environment.

Later in **Section 4.5**, the influence of the discriminator threshold setting for both signal and noise is investigated, highlighting how changes in threshold level affect the actual physics event signal and noise occupancy. This provides valuable input for optimizing detector operation parameters.

Finally, in **Section 4.6**, we discuss the results of data rates obtained through simulation for the entire STS system, as well as individual contributions from UrQMD events, beam-induced background, and electronic noise, for a common configuration of ENC = 1000 e and threshold = 4000 e. Comparisons have also been made with the case where ENC and threshold are set individually for each sensor, accounting for physical parameter variations across sensors, such as sensor length and micro-cable length. This would give insight into how sensor-specific variations in ENC and threshold settings influence overall readout performance.

4.1 STS Front-End Readout Electronics and ASIC Architecture

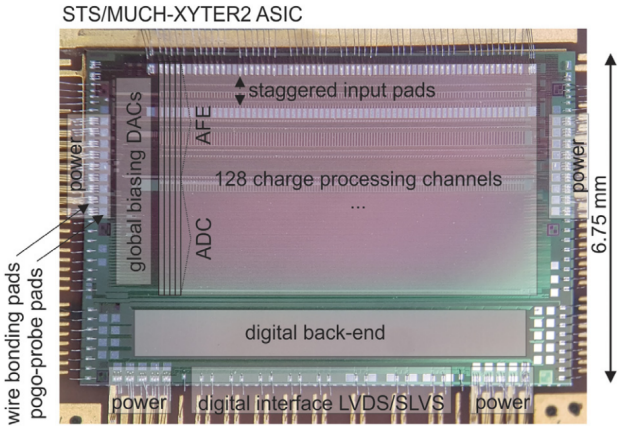

Figure 4.1: Layout of so-called STS-MUCH XYTER ASICs.[101]

As already mentioned in the Section, across the entire STS system, we used microstrip sensors of different sizes, identified by their strip length. These silicon sensors, on one side, are connected to an ultra-thin polyamide-Al-made micro-cable, and, on the other hand, to the readout electronics. They are called STS-XYTER SMX ASICs, as illustrated in the Figure 4.1. Each silicon sensor is interfaced with 16 ASICs[1], with 8 ASICs connected to the $n-$side and 8 to the $p-$side of the sensor.

[1] Application-Specific Integrated Circuit

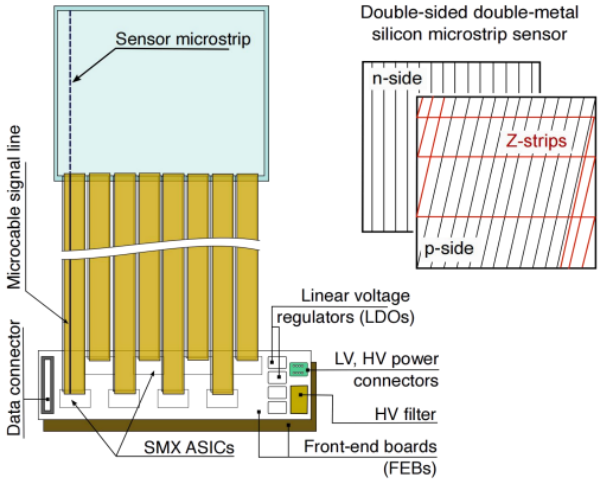

Figure 4.2: Schematic of the silicon sensors and their connection with the micro-cables and the ASICs.[102]

The self-triggering function, charge measurement, and timing measurement functionalities are integrated into this chip, an ASIC designed to meet specific custom needs. It features a 5-bit ADC for the measurement of charge amplitude and a 14-bit TDC for accurate timing. This design enables the precise measurement of the pulse amplitude and its time information, generated by the incident particle as it deposits charge in the silicon sensor, followed by digitization and data processing at the front-end.

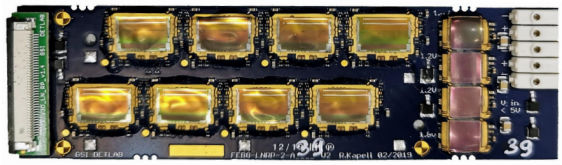

(a) Front-End Board Type A

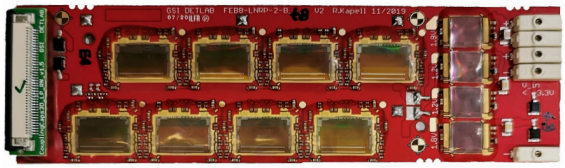

(b) Front-End Board Type B

Figure 4.3: Illustrations of the two types of Front-End Boards (FEBs).[103]

Each ASIC contains 128 readout channels and can be configured to operate with 1, 2, or 5 data uplinks, depending on the data rate expected at a given detector location. ASICs are mounted on dedicated Front-End Boards (FEBs) for both FEB Type A and Type B configurations as shown in Figure 4.3. Additional information regarding laboratory measurements, characterization, and optimization of the ASICs' performance is presented in [103, 104].

4.2 Simulation Configuration for STS Data-Rate Evaluation

Simulation studies were performed in the *"Time-based"* mode using the CBM-ROOT software framework to validate the data-rate capability of the whole STS detector under the highest expected

interaction-rate conditions. The simulation scenario corresponds to gold–gold collisions (Au+Au) at a beam momentum of 12 AGeV/c ($\sqrt{S_{NN}}$ = 4.9 GeV), which is the maximum energy, for the nucleus-nucleus collision, foreseen for the CBM using the SIS-100[2] accelerator at FAIR[3].[105] This represents the upper limit of the CBM experiment's operational energy range and therefore provides the highest possible rate conditions for testing the STS readout system.

To realistically simulate the free-streaming operation of the experiment, two main event sources were considered: First, minimum-bias events generated using the UrQMD model of nuclear interactions, and Second, beam-related background events, dominated by $\delta-$electrons produced through electromagnetic interactions of the primary beam with the target. A total of 10^5 UrQMD events and 10^7 beam events were simulated separately. Both datasets were then transported through the entire STS detector using the GEANT4 transport engine.

Following the successful event transport, the next step is to digitize the MC point information. In this step, both sources were combined at rates of 10^7 events/s and 10^9 events/s, respectively, corresponding to an operational scenario with a 1% target interaction probability[4] and an overall interaction rate of $\mathcal{O}$(10 MHz). Additionally, at the same stage, the noise for the STS detector was modeled using the Rice formula, accounting for the effective ENC and discriminator threshold values relevant to the STS front-end electronics. Such a combination represents free-streaming data-acquisition conditions, during which physics and background events overlap within the detectors' time window.

Overall, the configuration closely reproduces the realistic running conditions foreseen for the CBM experiment at FAIR. Consequently, the total data-rate estimation for the STS detector accounts for the combined contribution of three major sources listed as follows:

- **Nuclear collisions:** Au+Au interactions generated using the UrQMD model, representing the main physics events of interest.
- **Beam-induced background:** δ-electrons that originate from beam–target interactions and are transported through the detector.
- **Detector noise:** Random electronic noise generated at the digitization level to simulate realistic detector operating conditions.

[2] SchwerIonen Synchrotron

[3] Facility for Antiproton and Ion Research

[4] In the simulation setup, an Au target with a thickness of 0.025 cm corresponds to an interaction probability of about 1% for the incident beam, whereas increasing the target thickness to 0.25 cm would yield an interaction probability of approximately 10%, based on the equation: $P = 1 - e^{-(n \cdot \sigma_{\text{int}} \cdot x)}$

4.2.1 Delta Electron

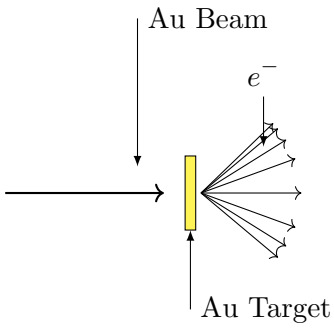

Figure 4.4: Au beam interaction with Au target.

Delta electrons are secondary electrons knocked out of the atoms by charged particle interaction or ions. Most of the non-hadronic interactions between the incoming beam and the target result in the production of the delta electrons, as shown in Figure 4.4 as an example, where the continuous incoming Au beam interacts with the Au target located at a fixed position, in simulation using GEANT4 within the CBM-ROOT framework. The possible source of the delta electrons is:

- Beam-target interaction
- Beam-pipe interaction
- Particle interaction with passive volumes within the detector system.

The production of δ-electrons can be quantitatively described in terms of the energy transfer from a fast charged projectile to the bound atomic electrons of the target material. When an ion of charge Ze and mass M passes through matter, it interacts electromagnetically with orbital electrons, transferring a small fraction of its kinetic energy through Coulomb scattering. The corresponding differential cross section for the production of secondary electrons with kinetic energy T, including the Mott correction, which takes into account the possible spin flip of the target electron[5], is given by

$$\frac{d\sigma}{dT} = \frac{2\pi z^2 \alpha^2 \hbar^2}{m_e \beta^2} \frac{1}{T^2} \left(1 - \beta^2 \frac{T}{T_{\max}}\right), \tag{4.1}$$

where z is the charge of the projectile, $\beta = v/c$ its velocity, and $T_{\max}$ denotes the maximum kinetic energy that can be transferred to an electron in a single collision. For a relativistic heavy ion ($M \gg m_e$), the maximum energy transfer is given by

[5]The contribution from the spin flip of the projectile can be neglected since the magnetic coupling, responsible for spin flips, scales as $\mu \sim Q/M$, therefore, the spin–flip cross-section probability goes roughly as $(Q/M)^2$. For heavy projectiles, this term is strongly suppressed due to their large mass, making the effect negligible compared to the target electron spin flip.

$$T_{\max} = \frac{2m_e c^2 \beta^2 \gamma^2}{1 + 2\gamma\frac{m_e}{M} + \left(\frac{m_e}{M}\right)^2} \approx \begin{cases} 2m_e c^2 (\beta\gamma)^2, & \text{for } \gamma m_e \ll M, \\ \gamma M c^2 = E, & \text{for } \gamma \to \infty, \\ m_e c^2 (\gamma - 1) = E - m_e c^2, & \text{for } M = m_e \ . \end{cases} \tag{4.2}$$

$$T_{\max} \approx 2m_e c^2 \beta^2 \gamma^2 \tag{4.3}$$

The differential cross-section Equation 4.1 varies with $1/T^2$, indicating that low-energy δ-electrons are produced much more abundantly than high-energy ones, whereas $T_{\max}$ increases with $\beta^2\gamma^2$.[68, 106], indicating that higher projectile energy producing more energetic δ-electrons. Therefore, at high beam energies, these electrons may escape the target material. In contrast, at lower beam energies, where the projectile velocity becomes comparable to the orbital velocities of the atomic electrons, the energy transfer per collision is considerably smaller. As a result, most interactions do not impart sufficient energy to overcome the electron binding energy and instead lead to excitation of the atom. This means that only a small fraction of collisions produce ejected electrons with low kinetic energy. This lower-energy delta electron could be quickly absorbed or rescattered by surrounding passive materials or deflected under the high magnetic field. Consequently, δ-electron production and its contribution to the detector occupancy become negligible at the lowest beam energies.

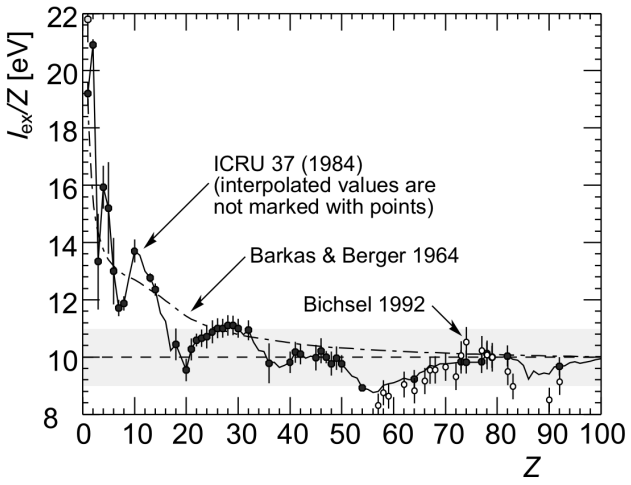

Figure 4.5: Average excitation energies divided by the atomic number as a function of Z.[106]

Figure 4.5 shows the variation of the average excitation energy I divided by the atomic number Z as a function of Z for different elements. It represents the mean energy required to ionize or excite an electron in an atom. It is a fundamental material-dependent parameter that enters the Bethe–Bloch equation for ionization energy loss. It is clear from here that the ratio I/Z, above $Z \gtrsim 20$, remains approximately constant between $\sim$ 9-11 eV) across a wide range of elements. Moreover, this trend suggests that the ionization potential per electron does not change strongly with atomic number on average. The inner-shell electrons in heavier elements

are bound much strongly due to the stronger nuclear Coulomb field. Still, the outer electrons, which dominate the mean excitation energy, are efficiently screened, leading to only a weak overall dependence of I/Z on Z.

In the context of $\delta-$electron production, this behaviour implies that materials with higher atomic numbers require marginally greater energy transfer to liberate bound electrons. Consequently, for a given projectile velocity, the probability of $\delta-$electron emission decreases slightly for high-Z materials compared to light elements. However, because the overall dependence is weak, δ-electron production primarily depends on the projectile energy and charge rather than the target atomic number.

The dependence of $\delta-$electron production on the beam energy and the material properties can be further understood in the framework of the Bethe–Bloch equation for the mean energy loss $\langle dE/dx \rangle$ of a charged particle traversing matter.[6] Figure 4.6 illustrates the Bethe–Bloch curve for pions in silicon as a function of $\beta\gamma = p/(mc)$, showing the characteristic $1/\beta^2$ rise at low velocities, the minimum-ionizing region near $\beta\gamma \approx 3$ - 4, and the slow logarithmic increase due to relativistic effects and density corrections at high energies. The mean excitation potential I, whose variation with atomic number Z was shown in Figure 4.5, enters directly in the Bethe - Bloch formula[68] as a material-dependent parameter:

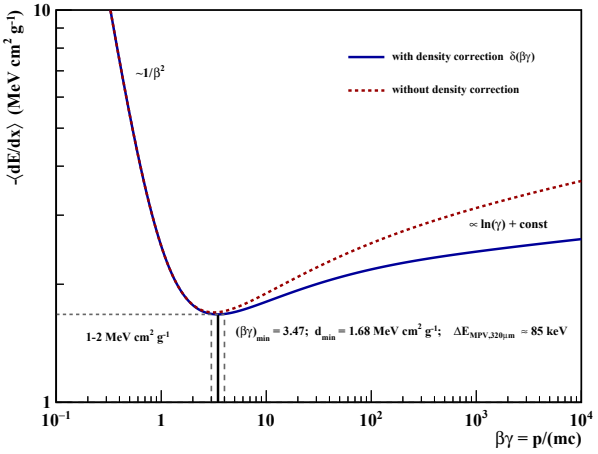

Figure 4.6: Mean energy loss ($\langle dE/dx \rangle$) of charged pions in silicon sensor of thickness 320 μm as a function of $\beta\gamma$.

$$-\left\langle \frac{dE}{dx} \right\rangle = K \frac{Z}{A} \rho \frac{z^2}{\beta^2} \left[\frac{1}{2} \ln \left(\frac{2m_e c^2 \beta^2 \gamma^2 T_{\max}}{I^2} \right) - \beta^2 - \frac{\delta(\beta\gamma)}{2} - \frac{C(\beta\gamma, I)}{Z} \right] \tag{4.4}$$

where $K = 4\pi N_A r_e^2 m_e c^2 = 0.307$ MeV cm^2/g is a constant, Z and A are the atomic number and mass number of the target material, ρ is its density, and z is the charge number of the incident

[6] In silicon at room temperature, the mean energy required to create one electron–hole pair is $w \simeq 3.62$ eV. Due to Landau–Vavilov fluctuations, the most probable energy loss (MPV) for a 320 μm Si detector traversed by a minimum-ionizing particle, $\Delta E_{\rm MPV} \approx 75$–$85$ keV, corresponding to

$$N_{eh}^{\rm MPV} = \frac{\Delta E_{\rm MPV}}{w} \simeq (2.1\text{–}2.4) \times 10^4 \text{ e–h pairs.}$$

This ∼22–24k range corresponds to the typical MIP signal observed as a Landau peak in silicon detectors.

particle. The term $\beta = v/c$ denotes the particle velocity, $\gamma = (1 - \beta^2)^{-1/2}$ is the Lorentz factor, I represents the mean excitation potential of the medium, and $T_{\max}$ is the maximum transferable kinetic energy to an atomic electron in a single collision, as given by Equation 4.2. The last two terms, $\delta(\beta\gamma)$ and $C(\beta\gamma, I)$, are the density-effect and shell corrections, respectively, which becomes significant at high and low particle energy.

Materials of higher mean excitation potential I require more energetic projectiles to produce a given amount of ionization. This behavior, together with the fact that the ratio I/Z is almost constant for most elements, explains the very weak dependence of the ionization energy loss on the atomic number displayed in Figure 4.5. Simultaneously, the stopping power is dependent on the electron density of the material, which scales approximately with $(Z/A)\rho$, but this variation remains relatively small.

As the energy of the projectile increases, both $\beta\gamma$ and $T_{\max}$ increase, enabling the transfer of a greater fraction of the kinetic energy of the projectile to atomic electrons. This results in a higher probability of producing energetic δ-electrons that can escape the target region and reach the surrounding detector planes. At lower beam energies, the $1/\beta^2$ term in the Bethe–Bloch equation is dominant while the smaller value of $T_{\max}$ limits the number and energy of electrons that can be ejected. In this regime, most collisions result in excitation rather than ionization, and the few electrons that are liberated have very low kinetic energy and can travel only short distances. Figure 4.5 and Figure 4.6 together show how the $\delta-$electrons production happens and its yield relevant to the STS detector.

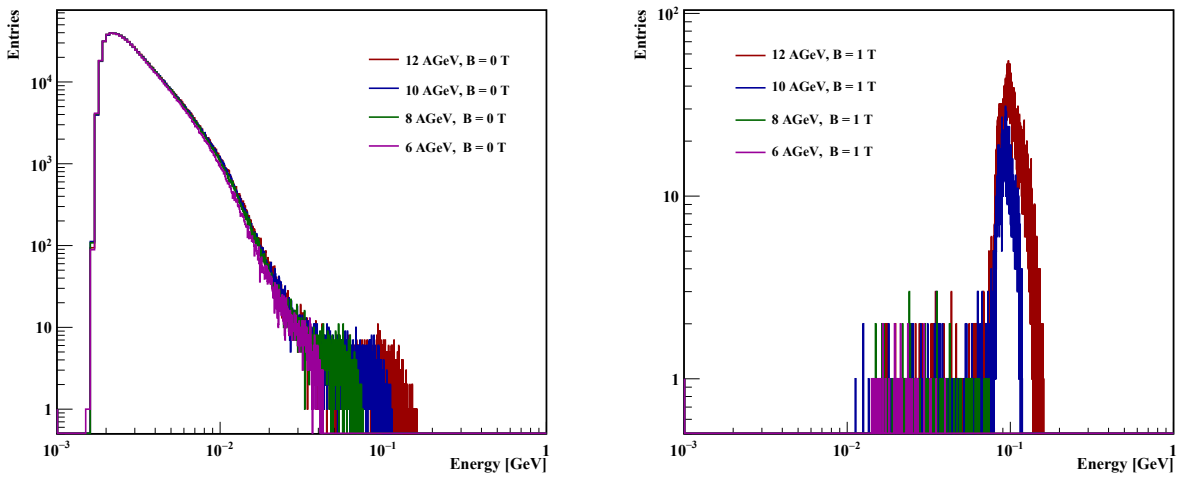

(a) (b)

Figure 4.7: Energy distribution of delta electrons produced in beam-target interaction for a different beam energy. Panel (a) shows the distribution without magnetic field, and (b) shows the distribution under magnetic field 1 T·m.

Figure 4.7 shows the $\delta-$electron energy distribution for a beam energy in terms of beam momentum between 12−6 AGeV/c. During the simulation analysis, we considered the delta production cut in GEANT4 at 1 MeV. The energy distribution is produced by considering delta-electron tracks that have been created at least 1 MC point. In the left panel Figure 4.7a, the energy distribution is shown without a magnetic field, where we can clearly see that lowering the beam energy produces fewer energetic delta electrons in the beam-target interaction. Although Figure 4.7b shows the same distribution but with a magnetic field, other conditions were taken similar to those used to prepare the energy distribution without a magnetic field case. We observe that delta electrons with energies above 10 MeV can reach the STS detector layers. In contrast, delta electrons with energies below 10 MeV are deflected out by the magnetic field and cannot reach the detector.

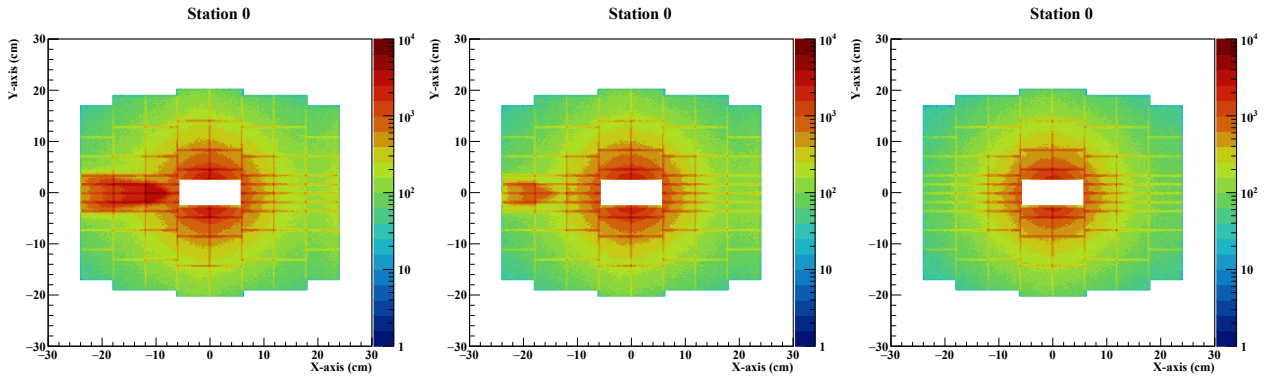

(a) 12 AGeV/c (b) 10 AGeV/c (c) 8 AGeV/c

Figure 4.8: MC distribution of the UrQMD and beam-target interaction induced $\delta-$ electron at beam momentum Panel (a) for 12 AGeV/c, (b) 10 AGeV/c, and (c) 8AGeV/c at 1T magnetic field.

Figure 4.8 shows the distribution of the MC points created on the detector plane of the STS detector, located 30 cm downstream of the target, for a different beam momentum energy under the magnetic field 1T. We can observe that the yield of the $\delta-$electron MC point at beam momentum 12 AGeV/c is more concentrated in the left part of the detector plane in a concentrated area, which is because the delta-electron produced through a beam-target interaction spirals under the magnetic field as it travels further toward the downstream detectors. Additionally, it is evident that as the beam energy decreases, the effect of the delta electrons on the detector plane decreases, as discussed earlier. The theta distribution with and without a magnetic field and the MC point distribution, at different beam energies, for each STS station, is shown in the **Appendix C**, **Section C.4.1**, and **Section C.4.2**, respectively.

Moreover, the produced delta electrons can be distinguished further by

- Event-uncorrelated

- Event-correlated

In event-uncorrelated delta electrons are produced even if no collision occurs. By contrast, event-correlated δ-electrons arise from real collisions between the beam and the target. Delta electrons produced during these interactions exhibit a range of energies. Low-energy delta electrons spiral under the influence of the magnetic field, as the STS detector operates under the magnetic field, as illustrated in Figure 4.9.

In the CBM simulation framework (CBM-ROOT), event transport using GEANT4 is typically performed by setting the faster set of physics list (`QGSP_BERT_EMV`[7]) available. It includes both electromagnetic and hadronic interaction models. This configuration results in the production of δ-electrons as well as various hadrons such as protons (p), antiprotons ($\bar{p}$), neutrons (n), pions (π^0, $\pi^{\pm}$), and kaons ($K^{\pm}$, K^0), etc together with their respective decay products when producing the beam-background data. However, to simulate the pure δ-electron background without contributions from hadronic interactions and processes, the GEANT4 physics list `emStandard`[8] is employed. This physics list option restricts event transport to electromagnetic interactions, ensuring that the simulated background arises exclusively from δ-electron production.

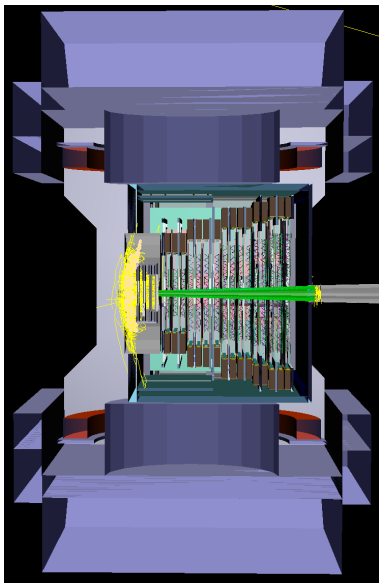

Figure 4.9: Beam of Au-ions interaction with Au target of thickness 0.025 cm and diameter of 2.5 cm using GEANT4 shows the production of delta electrons (yellow in coloured) for a single event.

4.3 Digitization and Front-End Readout Modeling of the STS

Once the event transport step is completed, the subsequent stage involves digitizing the Monte Carlo (MC) points recorded within the active regions of the silicon sensors. In this stage, the energy deposited by a particle in the sensor at a given time is converted into electronic signals. A detailed description of the digitizer being used for the STS detector can be found in [107].

[7] QGSP_BERT_EMV stands for Quark–Gluon String model with Precompound de-excitation (QGSP), combined with the Bertini cascade model (BERT) for intermediate-energy hadronic interactions. EMV is a fast, optimized simulation of electromagnetic processes, with less precise modelling.

[8] EMStandard: It is also known as a **EM Opt0** in GEANT4, Further details can be found from: `https://geant4.web.cern.ch/documentation/dev/plg_html/PhysicsListGuide/electromagnetic/Opt0.html`

During the time-based digitization stage, events from various input sources can be merged to simulate realistic detector conditions. Two types of input data have been considered: events generated using the UrQMD model, which represent physics collisions; and beam-background events (δ-electrons).

At this point, the distribution of event times can be set to be either uniform or Poisson in its time structure. In the uniform case, events of both sources are sampled at fixed intervals, assuming a Gaussian-like distribution in time; in contrast, a Poisson time structure introduces randomness in the event arrival times at which events from both sources are selected at discrete, randomly distributed intervals. This stochastic time structure reflects the characteristics of fundamental beam–target interactions. Additionally, noise signals are generated using the Rice formula based on the given ENC, threshold, and zero-frequency noise rate, ensuring that electronic noise is accurately simulated. It is being produced throughout the entire time window.

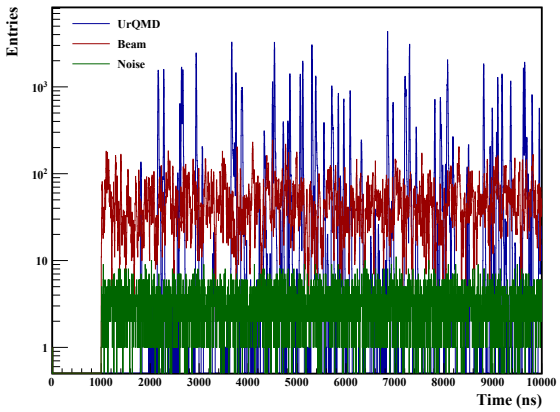

Figure 4.10: Signal time distribution of the events from the two sources (UrQMD and Beam background) along with the noise sampled

The simulation presented here employs the Poisson-distributed time structure for event sampling, as illustrated in Figure 4.10. It demonstrates how the digitizer alternates between events from both sources at random time intervals, representing the stochastic time structure, while the noise contribution remains approximately constant throughout the acquisition period.

The ASICs that process the signal generated in the silicon sensors provide two signal paths.

- **Fast shaper:** Generates a precise time stamp when the signal exceeds a pre-defined threshold.
- **Slow shaper:** measures the signal charge amplitude via a time-over-threshold (ToT). When a signal in the fast shaper crosses a pre-defined threshold and the amplitude in the slow shaper falls below a second threshold, the signal in the slow shaper is evaluated, and a message is reported to the DAQ system to consider it as a hit. the DAQ system

The slow shaper in the XYTER defines how closely spaced two input signals can be resolved as separate hits. To simulate this, each analogue signal pulse is simplified to a δ-like (ideal pulse) object, which carries three key attributes as follows:

- **Start time (t_{start}):** time stamp the moment the signal pulse exceeds the configured threshold.
- **Duration time (t_{dead}):** duration time being the dead time of the ASICs. A period during which the channel is unable to process a new signal because it is still processing the previous one.
- **Amplitude:** the total charge (Q).

In a case, if the two signal pulse are too close in a time, for example: If another pulse arrives within the dead time of a previous one, both signal are merged considering the t_{start} from the first signal, t_{stop} from the second one and the total charge (Q) will be the sum of both $Q_1 + Q_2$. After that, each individual or merged signal is temporarily stored in the front-end readout buffer, digitized, and considered a hit once the system time exceeds the signal's stop time. Once processed, the signal amplitude (Charge) is discretized into 31 bins for the 5-bit ADC, and the timestamp of the digital signal is smeared by a Gaussian distribution representing the time resolution of the ASICs.

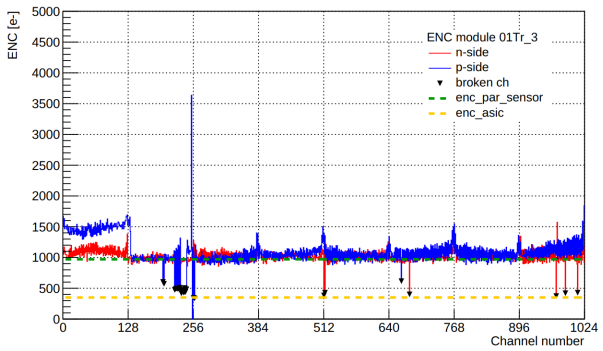

(a) ENC noise measurement performed in the lab[102]

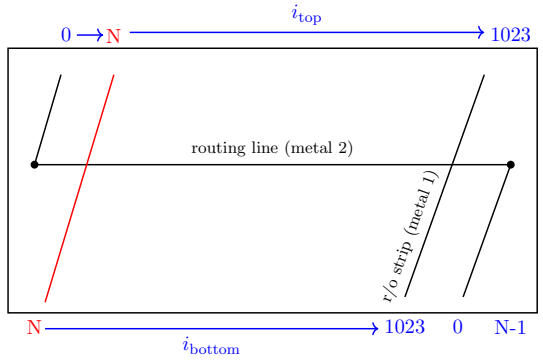

(b) Schematic of silicon sensors' micro-strips layout

Figure 4.11: Figure 4.11a shows the lab measurement of the ENC noise for an $n-$ and $p-$side of the sensor, and Figure 4.11b represents the schematic of the channel routing of the normal and double metal strip of the sensor.

The STS-XYTER will operate in a self-trigger mode, meaning that noise is considered only for channels with a signal. The noise amplitude is assumed to follow a Gaussian distribution with a standard deviation σ that corresponds to the Equivalent Noise Charge (ENC). The value of the ENC depends on the sensor size and the length of the micro cable. In addition, the ASICs themselves contribute to the total noise through their internal analogue components.

The primary sources contributing to the electronic noise in the system include:

- **Shot Noise:** Shot noise is associated with the statistical fluctuations in the leakage current of the detector sensor. It increases with the reverse-bias current and is a dominant contributor

in silicon sensors with large leakage currents.

- **Thermal Noise:** Caused by the random thermal motion of charge carriers in the sensor, thermal noise is proportional to temperature and resistance.

- **Amplifier (Electronic) Noise:** This includes intrinsic noise from the front-end amplifier and the ASIC's shaping circuitry. It comprises both voltage and current noise sources and is influenced by the amplifier design, shaping time, and bandwidth.

Figure 4.11a displays the ENC measurements of all channels of the module `01Tr_3`, a symmetrically biased module at 150 V, ensuring complete depletion of the sensor. The measurements include both the $p-$ and $n-$sides of the module, highlighting dead channels, as well as the theoretically calculated ENC for the sensor and the intrinsic ASIC noise. The observed noise level of 1000 e is in good agreement with the estimation derived from Equation 4.5. However, the ENC for the first block of the ASIC is notably higher than that of the other module channels. This discrepancy can be attributed to the z-strips on the p-side of the sensor, where the varying length of the z-strips, as shown in the Figure 4.11b, affects the series resistance and capacitance, resulting in a higher load at the amplifier's input. Additionally, differences in ENC are observed between the $p-$ and $n-$sides of the channel. This is primarily due to the routing of the micro-cables connected to each channel of the ASIC, which increases the effective capacitance, resulting to varying noise levels on both sides.

$$ENC = \left[\underbrace{L_{\text{Sensor}} \times 1.02 \frac{pF}{cm}}_{\text{Sensor}} + \underbrace{L_{\text{microcable}} \times 0.38 \frac{pF}{cm}}_{\text{Microcable}} \right] \times 25 \frac{e^-}{pF} + \underbrace{350 e^-}_{\text{ASIC}} \tag{4.5}$$

For the given module size of 6.2 cm and micro cable length of 49 cm, Equation 4.5 provides an ENC value of 974 e. The term 25 $\frac{e}{pF}$ is derived from a noise measurement for the electrons and holes polarity for a given input load capacitance.[102]

The digitization step requires several parameters to be defined, which determine the front-end electronics' response to the analog signals generated by the silicon sensors. These parameters are summarized in Table 4.1.

The dynamic range indicates the maximum charge the readout electronics can process before saturation, which was set to 75,000 e in simulation, corresponding to the upper limit of measurable signal amplitude. The discrete output of the analog-to-digital converter (ADC) is digitized, and 31 discrete steps represent the digitized charge information.

Parameter	Value
Dynamic range	75000 e
Number of ADC levels	31
ENC	1000 e
Threshold	4000 e
Dead time	200 ns
Time resolution	5 ns
Noise	Yes
Lorentz shift	Yes
Charge diffusion	Yes
Cross-talk	Yes
Dead channel fraction	0%

Table 4.1: Digitization parameters setting for the simulation.

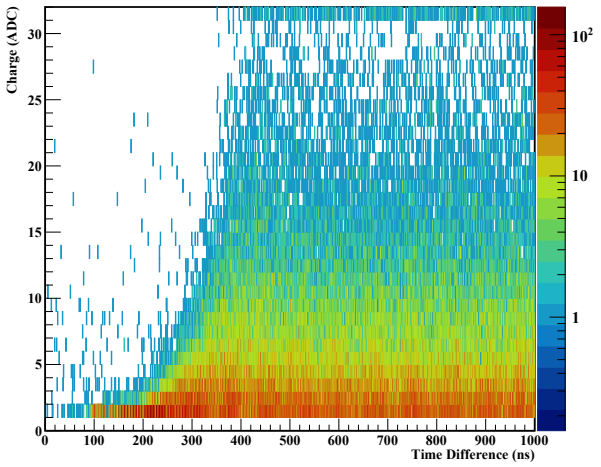

Figure 4.12: ADC charge of the first signal on the channel vs. time difference between two consecutive signals on the same channel.

The ENC represents the RMS noise, an intrinsic noise of the front-end amplifier, detector module, etc, as described in Equation 4.5. A threshold of 4000 e is applied to ensure that signals above this level are registered as valid hits and that triggers induced by the noise are suppressed.

The dead time of 200 ns corresponds to the minimal recovery time of the readout channel after a signal, a time during which it is insensitive to new signals, which can be seen from the Figure 4.12. It shows that the signal, measured as an ADC value, of the first arrival on the silicon sensor microstrip channels vs. the time difference between consecutive signals on the same channel is available in the mCBM data run ID 2984. From this, we conclude that for the STS, the good approximation of the dead-time ranges between 200 and 300 ns. Further detailed discussion is done in the **Chapter 5**. Moreover, the Time resolution of 5 ns reflects the precision with which the signal arrival time is measured.

Several additional physical effects are also included to model the detector behaviour realistically. Noise is turned on to simulate the stochastic electronic fluctuations observed in real measurements. The Lorentz force acting on charge carriers in a magnetic field causes a lateral displacement of the collected charge on the sensor surface. Charge diffusion describes the spreading of charge carriers during drift through the silicon bulk, thereby affecting the cluster size and shape. Cross-talk models

the capacitive coupling between neighbouring readout channels, which may cause small correlated signals. A detailed description is already discussed in the **Chapter 5**. The dead channel fraction is set to 0%, indicating that all readout channels are assumed to be operational in this simulation scenario. Furthermore, we have already implemented the functionality in the CBM-ROOT to consider dead channels and noisy channels in the simulation, and is discussed in **Chapter 3**.

4.4 Modeling the Noise Rate in Self-Trigger Detector System

In high-rate experiments with Poisson-distributed events and self-triggered readout electronics, accurately estimating the noise rate is crucial due to the nature of signal acquisition. Unlike conventional triggered experiments, where noise hits are generated when a noise fluctuation coincides with a global trigger, this approach allows for more precise measurements. However, in self-triggered systems, a noise hit is recorded every time the instantaneous noise amplitude exceeds a predefined threshold. Therefore, self-triggered systems are inherently more sensitive to noise, leading to a higher rate of false hits. This drawback may introduce an excessive background if the noise rate is underestimated. On the other hand, overestimating the noise rate may lead to overly conservative thresholds and reduced detector efficiency. To overcome the problem of a self-triggered system, it is necessary to estimate the system's noise rate.

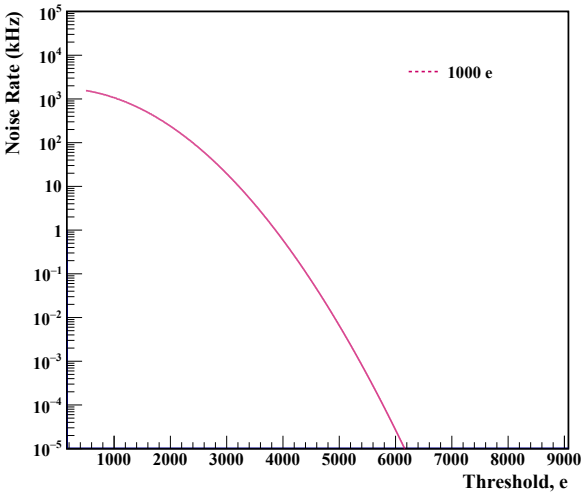

Figure 4.13: Analytical representation of noise rate estimation prepared by random number generation using the Rice formula (see Equation 4.6).

To address this, the noise rate in the STS-XYTER is estimated using the Rice formula (Equation 4.6), which relates the threshold crossing rate to the statistical properties of the noise and the system bandwidth.

$$f = \frac{f_0}{2} \cdot e^{\left(-\frac{v_{th}^2}{2\sigma^2}\right)} \tag{4.6}$$

where v_{th} is the threshold voltage, σ is the RMS amplitude of the noise, and f_0 is the zero-crossing rate, e.g., the rate at which the noise waveform crosses the zero level, determined by the shaper

bandwidth. For example, for the SMX chip tested with a fast shaper with a 90 ns rise time, the estimated zero-crossing noise rate is 3.5 MHz, calculated using the following formula.

$$f_0 = \frac{1}{\pi \cdot \tau} \tag{4.7}$$

Where τ is the rise time, for the n-XYTER, the rise time value can be found in [108].

Figure 4.13, analytically modeled noise rate, demonstrates how increasing the threshold value decreases the noise rate. The rice formula has been implemented in the CBM-ROOT to simulate the noise rate for the STS detector, as already explained in **Chapter 3** and **Section 4.5**.

4.5 Impact of Threshold Settings on Signal and Noise Digitization

In time-based simulation within the CBM-ROOT framework, digitization was performed using two input sources: UrQMD and Beam, along with noise, to assess the impact of the threshold on a given ENC and threshold values for all 876 silicon sensors. To test the effects of various cases, we considered two scenarios with ENC 1000 e and 1500 e, varying the threshold values while keeping the remaining parameters constant, as shown in Table 4.1.

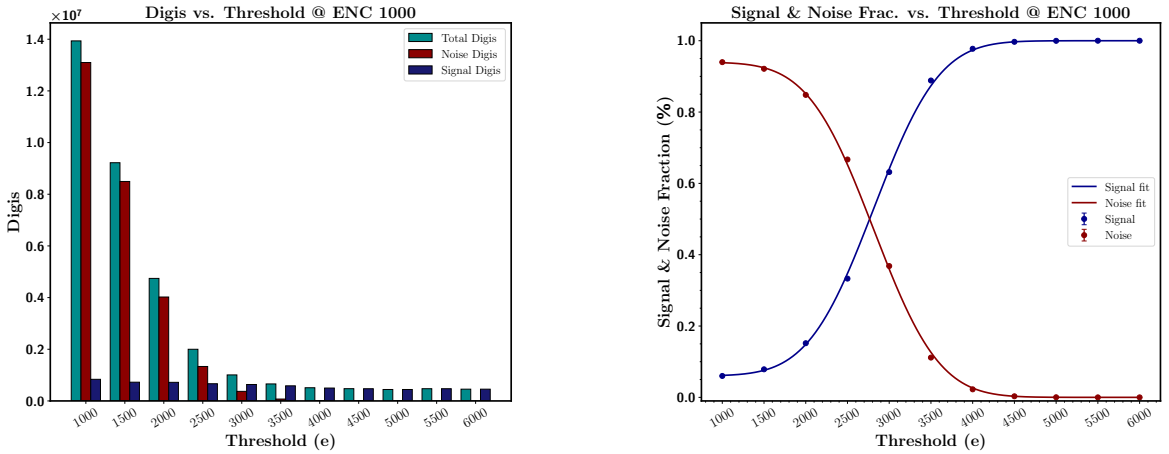

(a) (b)

Figure 4.14: Figure 4.14a shows total, noise, and signal digis distribution at ENC 1000 e while Figure 4.14b represents Signal to Noise fraction at varying threshold values.

Figure 4.14b and Figure 4.15a show the variation of the total, signal, and noise digis[9] as a function

[9] In the simulation, a *digi* represents a registered electronic signal whenever the amplified pulse height exceeds the discriminator threshold. Noise digis correspond to signals generated purely from electronic noise fluctuations crossing the threshold, while signal digis originate from genuine charge deposits produced by particles traversing the silicon sensor.

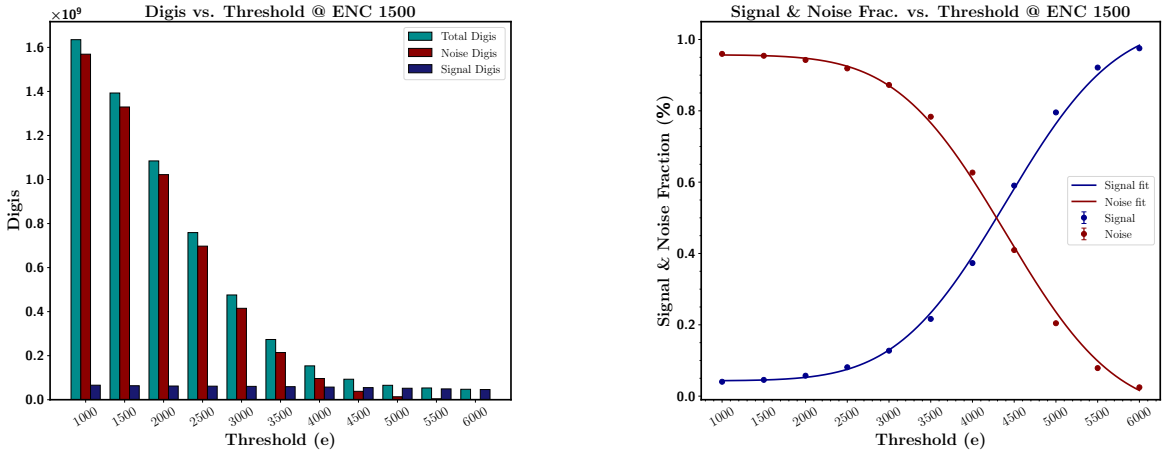

(a) (b)

Figure 4.15: Figure 4.15a shows total, noise, and signal digis distribution at ENC 1500 e while Figure 4.15b represents Signal to Noise fraction at varying threshold values.

of the discriminator threshold, which was incremented in steps of 500 e. Moreover, Figure 4.14b and Figure 4.15b show the corresponding fractions of signal and noise digis in the case of various noise conditions. The simulation results demonstrate a clear trend: as the threshold value increases, the number of noise digis decreases, while the fraction of actual signal digis increases. This behaviour indicates effective suppression of low-amplitude noise hits at higher threshold settings.

In the case of an ENC of 1000 e, a threshold of about 4000 e provides an optimal balance between noise rejection and signal preservation. Similarly, for an ENC of 1500 e, a threshold around 6000 e offers the best compromise. These correspond to a threshold level of about 4σ above the noise RMS and confirm that a setting like this ensures an optimal signal-to-noise ratio and minimizes the contribution from spurious electronic noise in the digitized data.

Furthermore, Equation 4.5 was used to calculate the ENC for the specified sensor dimensions and corresponding micro-cable lengths. The calculation was done for all 876 silicon sensors, and a 4σ threshold value was applied to each module based on the calculated ENC.

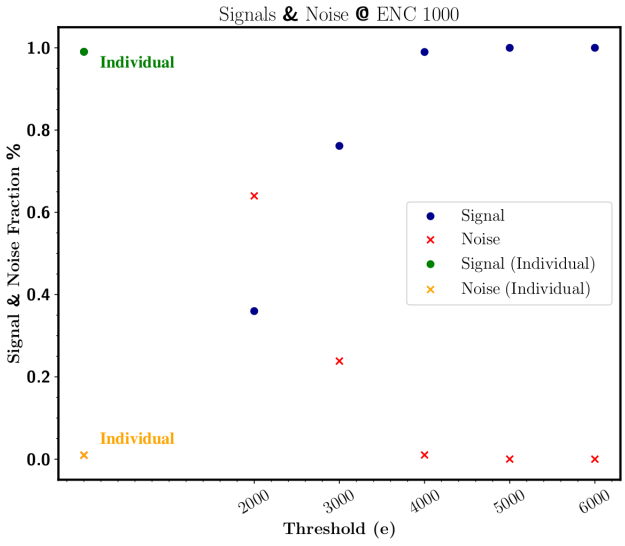

Figure 4.16: Signal-to-Noise fraction for an ENC 1000 e and varying threshold, along with the points extracted based on individual parameter settings of ENC and threshold for all 876 silicon sensors.

Figure 4.16 shows the signal-to-noise fraction for an ENC value of 1000 e with varying threshold value, along with the data points representing signal and noise fractions obtained for an individually calculated ENC and 4σ threshold value for each silicon sensor.

Further analysis was conducted to evaluate the data rate for the STS, using fixed thresholds of 1000 e and 4000 e for all sensors. Additionally, the rate analysis was performed by setting the ENC and threshold values, which were adjusted based on sensors' strip length and micro-cable lengths, as determined using Equation 4.5. The results are further discussed in the **Section 4.6** and the comparison between the two cases.

4.6 Data-Rate Performance of the STS Under High-Rate Conditions

In this section, the data rate performance of the STS detector is analyzed under time-based simulation conditions, incorporating contributions from UrQMD-generated physics events, beam-related background, and electronic noise. All relevant digitization parameters, as previously discussed and shown in Table 4.1, were applied to ensure a realistic modeling of the detector response. The simulation was carried out for the worst-case operational scenario, corresponding to the highest expected interaction rates, using minimum-bias Au+Au events at a beam momentum of 12 AGeV/c and a magnetic field of 1 T. Based on these conditions, the number of registered digis per second was evaluated for each sensor and readout channel, providing a detailed estimation of the data load across the detector system.

Figure 4.17 illustrates the total number of digis recorded across all ASICs (16 ASICs, including both the $p-$ & $n-$sides of the sensor) for various sources, with ENC and threshold settings of 1000 e & 4000 e, respectively, for all sensors. The figure presents the digis from different sources for all STS stations, as detailed in the Appendix. From the total digis (see Figure 4.17a), it is evident that delta electrons, generated through beam-target interaction, which bend under the influence of the magnetic field towards the negative side of the traverse detector plane, contribute significantly to the registered digis. Their effect is particularly pronounced in a small region on the left side of the station, where the highest number of digis is observed. As we move further downstream, the impact of the delta electrons decreases, as can be seen from the MC distribution shown in **Appendix C**, **Section C.4.2**. Therefore, the effect on the data rates is also lowered, as shown in the **Appendix D**, **Section D.1**, **Section D.2**, and **Section D.3**. The maximum peak rate was

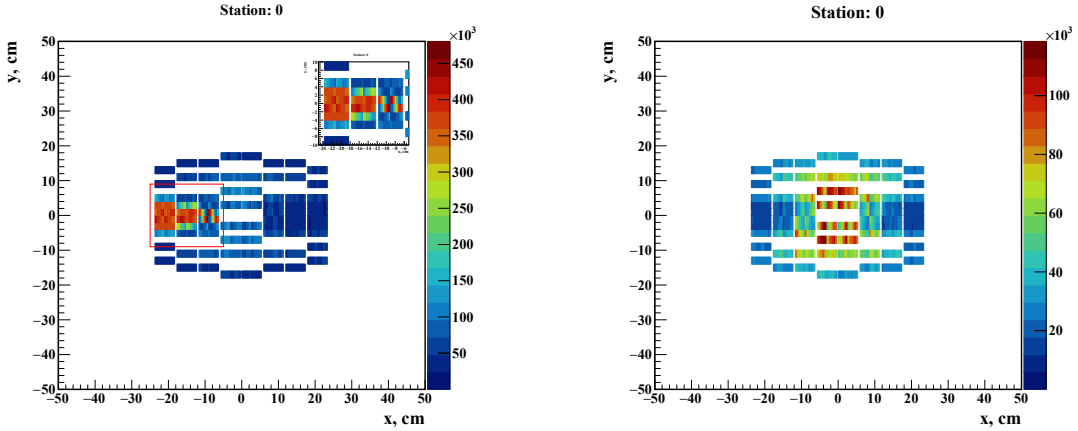

(a) Total digis

(b) UrQMD digis

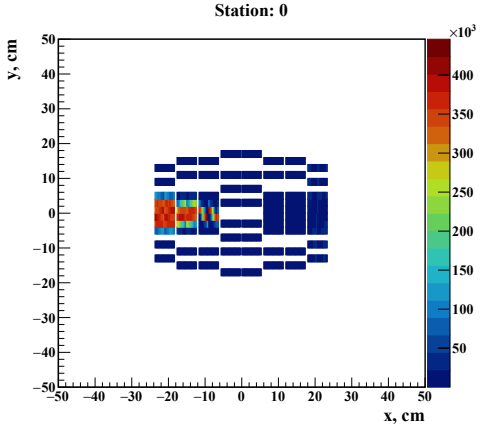

(c) Beam digis

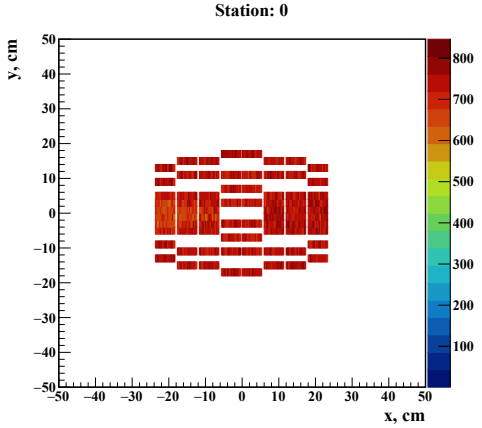

(d) Noise digis

Figure 4.17: Illustration of digis for the first station of the STS: total digis, UrQMD digis, Beam digis, and Noise digis using ENC 1000 e and Threshold 4000 e

calculated for the given station by taking the maximum number of digis multiplied by the transport message bytes (4 Bytes) as shown in the Table 4.2. While Table 4.3 shows the data rates for a full STS in GB/s by summing the N of digis across all stations.

Data Rates (MB/s)				
Station	**Total**	**UrQMD**	**Beam**	**Noise**
0	114.778	28.306	106.566	0.2022

Table 4.2: Maximum data rate for Station 0 of the STS detector located 30 cm away from the target position.

Data Rates (GB/s)				
Station	**Total**	**UrQMD**	**Beam**	**Noise**
All	136.86	94.27	40.16	2.42

Table 4.3: Total data rate for the entire STS detector, which includes all 8 stations and 876 sensors of varying size distributed among each station plane.

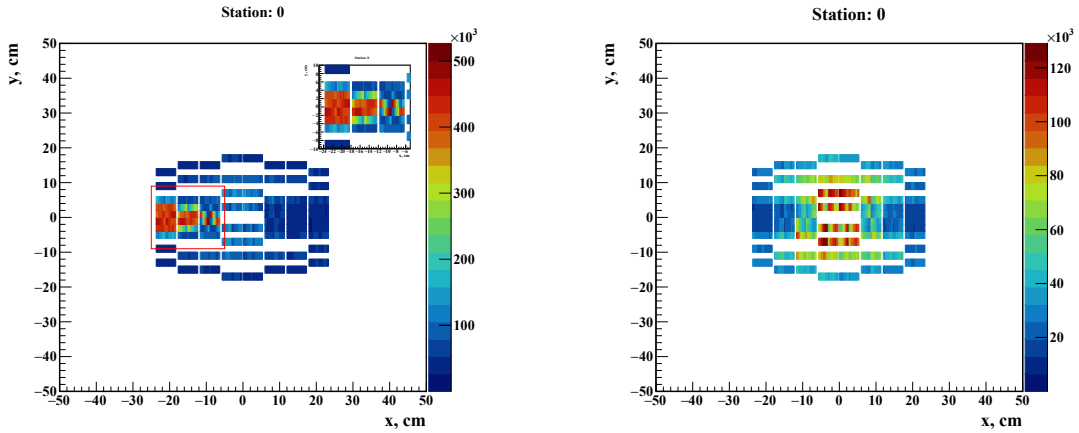

(a) Total digis

(b) UrQMD digis

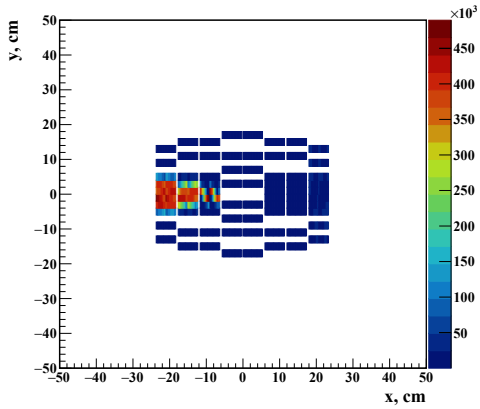

(c) Beam digis

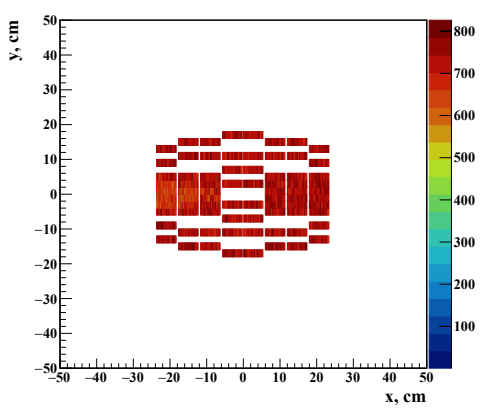

(d) Noise digis

Figure 4.18: Illustration of digis for the first station of the STS: total digis, UrQMD digis, Beam digis, and Noise digis obtained using individual calculations of ENC and Threshold.

Figure 4.18 illustrates the total number of digis recorded across all ASICs (16 ASICs, including both the $p-$ and $n-$sides of the sensor) for various sources. The ENC and threshold settings used for these calculations are determined individually for each sensor based on Equation 4.5, which accounts for electronic noise and threshold levels while keeping the remaining parameters as shown in Table 4.1.

Data Rates (MB/s)				
Station	**Total**	**UrQMD**	**Beam**	**Noise**
0	126.11	30.91	117.27	0.198

Table 4.4: Maximum data rate for Station 0 of the STS detector located 30 cm away from the target position, using individual sensor ENC and threshold values.

Table 4.4 presents the peak data rates in MB/s for a given station, showcasing contributions from different sources, including UrQMD events, beam interactions, and noise Table 4.5 extends the rate

Data Rates (GB/s)				
Station	**Total**	**UrQMD**	**Beam**	**Noise**
All	144.37	98.52	43.41	2.43

Table 4.5: Total data rate for the entire STS detector, which includes all 8 stations and 876 sensors of varying size distributed among each station plane, using individual settings of the ENC and threshold of the sensors.

in GB/s for the entire STS, illustrating the impact of the ENC and threshold on the data rates from various sources. These results emphasize the importance of optimizing the digitization process to efficiently manage the high data rates generated in the STS and fine-tuning the detector settings to ensure reliable operation at high interaction rates, thereby improving the signal-to-noise ratio. The maximum peak data rates for each STS station for both scenarios, individually for each source, are shown in the **Appendix D**.

A comparison of total data rates for the entire STS system shows an increase of 5.49% when using individually calculated ENC and threshold values, compared to the previously set values of ENC 1000 e and threshold 4000 e. Furthermore, the rates for UrQMD source increased by 4.51%, and those for beam sources rose by 8.1%. Interestingly, the noise rate decreased by 0.41% when an individually set value was used. This increase in total data rate arises because the individually assigned ENC and threshold values account for sensor-specific features, such as variations in sensor length, capacitance, and micro-cable length, which are relevant to electronic noise and, consequently, the threshold for signal amplitude. Consequently, some sensors operate with slightly lower effective thresholds, resulting in a larger number of registered digis and, therefore, a low-to-modest increase in the overall data rates.

Figure 4.19 shows the distribution of ASIC counts for different rate bands, representing the number of required uplinks per ASIC for data readout.[10] In the whole STS detector, three varieties of Front-End Board exist, denoted FEB8, each differentiated by its uplink configuration. The FEB8-1 version with a single uplink supports a maximum data rate of about 73 kHits/s per channel. With two uplinks, the FEB8-2 board can sustain rates of up to about 146 kHits/s per channel. A five-uplink version of this board, the FEB8-5, can achieve data rates of up to 367 kHits/s per channel. These configurations ensure that each ASIC operates within its optimal bandwidth range, enabling efficient data transmission under varying local hit rates across the STS detector.

In addition, we can see that when moving from a uniform (default) ENC/threshold to individually tuned values, a small fraction of ASICs migrates from the lowest band to higher bands, as expected.

[10] The rate bands here are $[0, 73)$, $[73, 146)$, and $[146, 367)$ kHits/s per channel, corresponding to ASICs equipped with 1, 2, and 5 uplinks, respectively, based on the nominal link bandwidth.

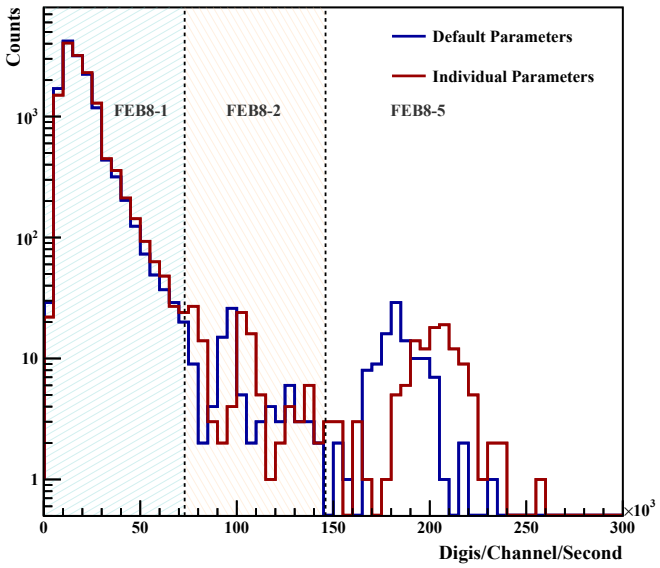

Figure 4.19: Comparison of ASIC counts per channel digi-rate for two configurations: (i) a *default* setting with uniform ENC and threshold for all sensors, and (ii) an *individual* setting where each sensor uses its own ENC and corresponding 4σ threshold.

ASIC Counts Signal/channel/s		
Asic Rate	**Default**	**Individual**
1 Uplink $(0-73)$	13816	13774
2 Uplink $(73-146)$	90	126
5 Uplink $(146-367)$	110	116
Total	**14016**	**14016**

Table 4.6: ASIC counts for all the 876 silicon sensors with default and individual parameter settings of ENC and threshold

Table 4.6 shows counts of ASICs, distinguished by the different uplinks required in the STS detector for the readouts, and their allocation in different STS stations will be done based on the rate observed through simulation. From this, we can conclude that sensors with better noise performance (lower ENC) require lower threshold values, thereby increasing hit efficiency. However, it will increase the hit rate, which remains affordable given our FEB assignment for the detector layout.

Chapter Summary

In this chapter, a comprehensive study of the data rate performance of the complete STS detector was presented. The detector comprises 876 double-sided silicon micro-strip sensors of four variants, distinguished by their strip lengths, which are mounted on ladders and arranged across eight tracking stations. The simulations were carried out in Time-based mode using UrQMD events for physics signals and beam-background ($\delta-$electron) events to account for secondary background contributions. The study corresponds to Au+Au collisions at 12 AGeV/c, which represents the highest beam energy foreseen for nucleus-nucleus collisions at the CBM experiment using the SIS$-$100 accelerator at FAIR. The simulations assumed a 1% beam-target interaction probability[11] and an overall interaction rate of $\mathcal{O}$(10MHz), representing the expected operational conditions of the experiment.

A detailed discussion of the digitization procedure implemented for the time-based simulation, including the noise modeling adopted for the STS detector, was also provided. The electronic noise was introduced following the Rice formula, which parametrizes the Gaussian bandwidth-related noise as a function of the Equivalent Noise Charge (ENC) and the discriminator threshold. Although this approach does not explicitly account for noise components arising from calibration inaccuracies, electronic instabilities, or environmental pickup, it provides an effective first-order estimate of the intrinsic detector noise. A comparison of simulated noise behavior with real detector measurements has been presented and discussed in detail in **Chapter 3**.

Furthermore, the dependency of signal and noise occupancies on the discriminator threshold was analyzed for ENC values of 1000 e and 1500 e. From this study, it was concluded that, for any given ENC value, a discriminator threshold of approximately 4σ effectively suppresses the electronic noise while preserving high detection efficiency. This threshold criterion was therefore adopted for subsequent data-rate calculations for the STS detector.

In addition, a new functionality was implemented in the CBM-ROOT framework to automatically assign the ENC value (as computed from Equation 4.5) based on each sensor's geometry, specifically its strip length and connected micro-cable, and to apply the corresponding 4σ discriminator threshold for the digitization process. The rate simulation was then repeated using these individualized sensor parameters, allowing for a more realistic representation of detector performance.

The results obtained with this sensor-specific configuration were compared with those from the

[11] Probability of interaction can be derived based on the equation: $P = 1 - e^{-(n \cdot \sigma_{\text{int}} \cdot x)}$

default setup, assuming a uniform ENC of 1000 e and a threshold of 4000 e. The comparison, summarized in Table 4.6 and Figure 4.19, shows that only a small fraction of ASICs shifted from the lowest rate band (single uplink) to higher rate bands (two or five uplinks). This confirms that the STS detector configuration, even when operated with realistic sensor-dependent noise and threshold settings, remains entirely within the designed readout bandwidth and data-rate capacity.

Chapter 5

Physics Performance of the Silicon Tracking System Detector

This chapter presents a comprehensive characterization of the Silicon Tracking System (STS) detector performance. The studies are based on detailed Monte-Carlo (MC) simulations using events generated with the UrQMD[1] model[109] and beam events at a beam momentum of 12 AGeV/c, followed by event transport through the whole detector geometry using the GEANT4 transport engine. The simulated signals are then processed through the complete time-based digitization and reconstruction chain. The simulated setup corresponds to Au+Au collisions on a 0.025 cm thick gold target, yielding an interaction probability[2] of about 1%, and represents realistic operational conditions of the CBM experiment under high-rate (∼10 MHz) time-based simulation conditions.[3]

The simulation performance described in the chapter covers several key aspects of the STS detector, listed as follows:

Section 5.1 discusses the geometrical acceptance of the detector and its coverage in pseudorapidity and transverse momentum.

Section 5.2 focuses on the hits reconstruction efficiency performance, by comparing the reconstructed hits to the corresponding MC points under different threshold and dead-time settings, as well as the STS detector track reconstruction efficiency.

[1] Ultrarelativistic Quantum Molecular Dynamics

[2] In the simulation setup, an Au target with a thickness of 0.025 cm corresponds to an interaction probability of about 1% for the incident beam, whereas increasing the target thickness to 0.25 cm would yield an interaction probability of approximately 10%, based on the equation: $P = 1 - e^{-(n \cdot \sigma_{\text{int}} \cdot x)}$, further discussion see **Chapter 3**

[3] In Time-based simulation where events from sources, e.g., UrQMD: 10^7 events/s and Beam: 10^9 events/s, are transported through the detector at a given rate, Overall 10 MHz rates.

Section 5.3 addresses the cluster characteristics in double-sided silicon strip sensors, which include the cluster size versus the inclination angle of the particle, the correlation of clusters from both sides of the sensor, and the study of single-hit residuals and intrinsic spatial resolution.

In **Section 5.5**, the framework for particle identification (PID) within the CBM experiment is introduced, highlighting the potential of the PID of the different charged particles using the Time-of-Flight detector. Finally, **Section 5.5.5** demonstrates the particle identification capabilities of the STS detector itself, using specific energy-loss (dE/dx) measurements derived from the reconstructed hits and cluster charges.

5.1 Detector Acceptance

In experimental high-energy physics, the pseudo-rapidity (η) is often used as an alternative to rapidity, since it depends only on the polar angle θ of the particle with respect to the beam axis:

$$\eta = -\ln\left(\tan\frac{\theta}{2}\right). \tag{5.1}$$

Unlike rapidity, which requires the knowledge of the particle mass and energy, pseudo-rapidity can be calculated directly from the measured track angle. This makes η particularly useful in detector analyses where particle identification is limited or when only the trajectory is reconstructed.

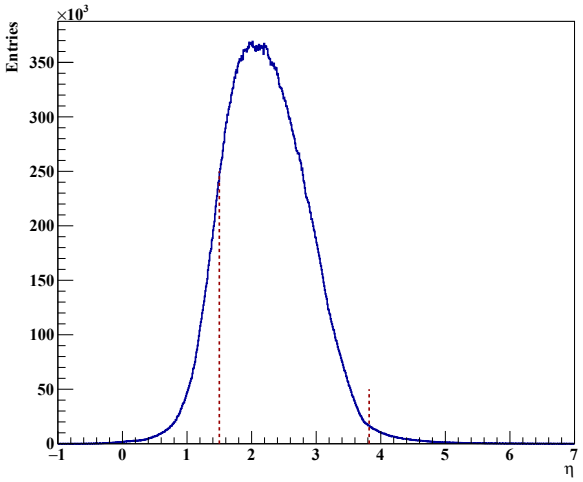

Figure 5.1: Pseudo-rapidity distribution of primary particles through simulation using Au+Au collisions events generated by UrQMD at beam momentum 12 AGeV/c.

At high momenta ($p \gg m$), the pseudo-rapidity approximates the true rapidity, $\eta \simeq y$, and therefore provides a good measure of the longitudinal phase-space distribution of produced particles. The η

distribution of primary particles also reflects the geometry of the collision: it is symmetric around mid-rapidity in the Centre-Of-Mass (COM) frame for symmetric systems, and its shape broadens with increasing collision energy as particle production extends to larger forward and backward rapidities.

Figure 5.1 shows the pseudo-rapidity distribution of primary particles at beam momentum 12 AGeV/c, where the marked lines show the detector acceptance in $1.5 \leq \eta \leq 3.82$.

5.1.1 Rapidity and Transverse Momentum

Rapidity is a convenient variable in relativistic heavy-ion physics as it transforms additively under Lorentz boosts along the beam axis. It is defined as

$$y = \frac{1}{2} \ln \left(\frac{E + p_z}{E - p_z} \right) = \frac{1}{2} \ln \left(\frac{1 + \beta}{1 - \beta} \right) \tag{5.2}$$

where E is the particle energy, p_z is the longitudinal momentum and $\beta = p/E$ is the velocity in units of c.

When transforming from the COM frame to the laboratory frame, rapidity shifts by a constant amount corresponding to the beam rapidity:

$$y_{\text{lab}} = y_{\text{COM}} + y_{\text{boost}} \ , \qquad y_{\text{boost}} = \frac{1}{2} \ln \left(\frac{1 + \beta}{1 - \beta} \right) \tag{5.3}$$

Thus, the rapidity distribution in the laboratory frame depends on the beam rapidity, which increases with beam energy and directly affects the particle population around mid-rapidity.

In addition to rapidity, the transverse momentum (p_T) is a key observable that characterizes the momentum component perpendicular to the beam axis:

$$p_T = \sqrt{p_x^2 + p_y^2} \tag{5.4}$$

Together, rapidity and transverse momentum provide a natural phase-space representation of the particles produced in heavy-ion collisions.

Table 5.1 summarizes the mid-rapidity intervals chosen for different beam energies. For each energy, the analysis window is defined as ± 0.5 units around y_{mid}. It is essential for analysis because of the minimized trivial kinematic effects and the maximum collision happens in this region.

Beam Momentum (AGeV/c)	Rapidity Range ($y_{\text{mid}} \pm 0.5$)
12	$1.12 \leq y \leq 2.12$
10	$1.03 \leq y \leq 2.03$
8	$0.92 \leq y \leq 1.92$
6	$0.77 \leq y \leq 1.77$
4	$0.58 \leq y \leq 1.58$

Table 5.1: Rapidity intervals around mid-rapidity for different beam momenta.

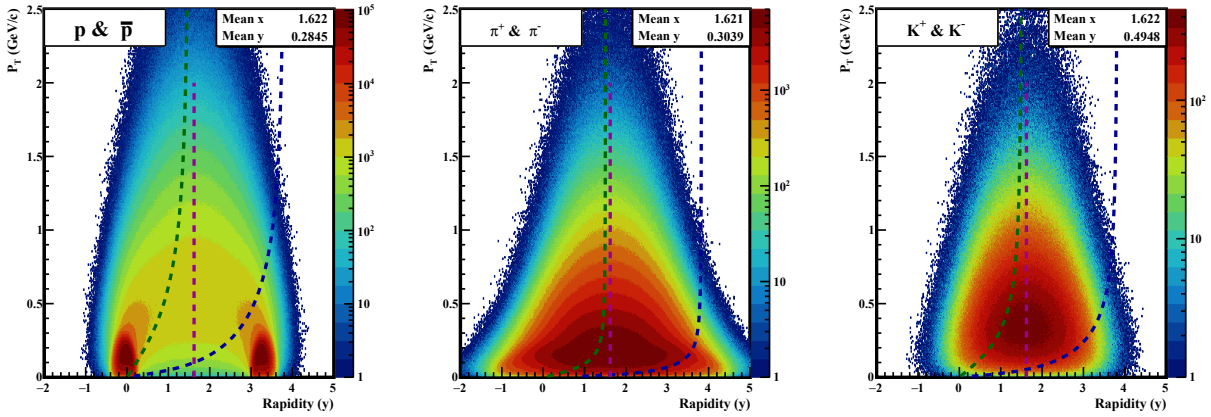

Figure 5.2: 4π distribution of transverse momentum (p_T) vs. rapidity (y) for protons, antiprotons, charged pions, and charged kaons from UrQMD minimum-bias events from Au+Au collisions at beam momentum 12 AGeV/c. The line at mean X in each panel shows the mid-rapidity. The green and blue lines represent the kinematic cuts of detector acceptance, $1.5 \leq \eta \leq 3.82$, representing polar angle $2.5^{\circ} < \theta < 25^{\circ}$. The full 4π distribution is shown here for reference.

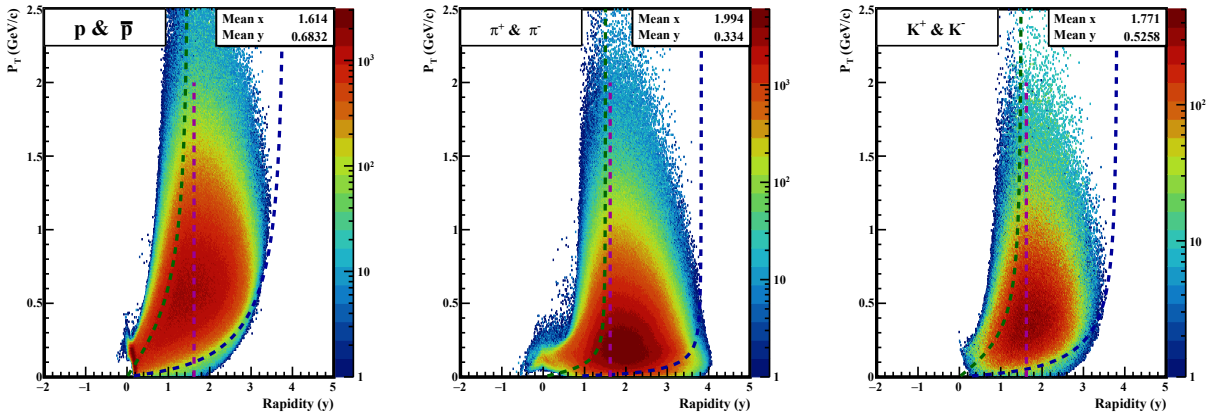

Figure 5.3: Distribution of transverse momentum p_T versus rapidity y for protons, antiprotons, charged pions, and charged kaons within the STS detector acceptance using minimum-bias events generated through UrQMD at beam momentum 12 AGeV/c.

Figure 5.2 delineates the distribution of produced particles as a function of p_T vs. y while Figure 5.3 shows a similar distribution, but of accepted particle species (mainly p, $\bar{p}$, $\pi^{\pm}$, $K^{\pm}$) within the acceptance of the STS detector. Compared to the full 4π distribution (Figure 5.2), The detector acceptance imposes a strong kinematic constraints, especially at forward rapidity and for higher

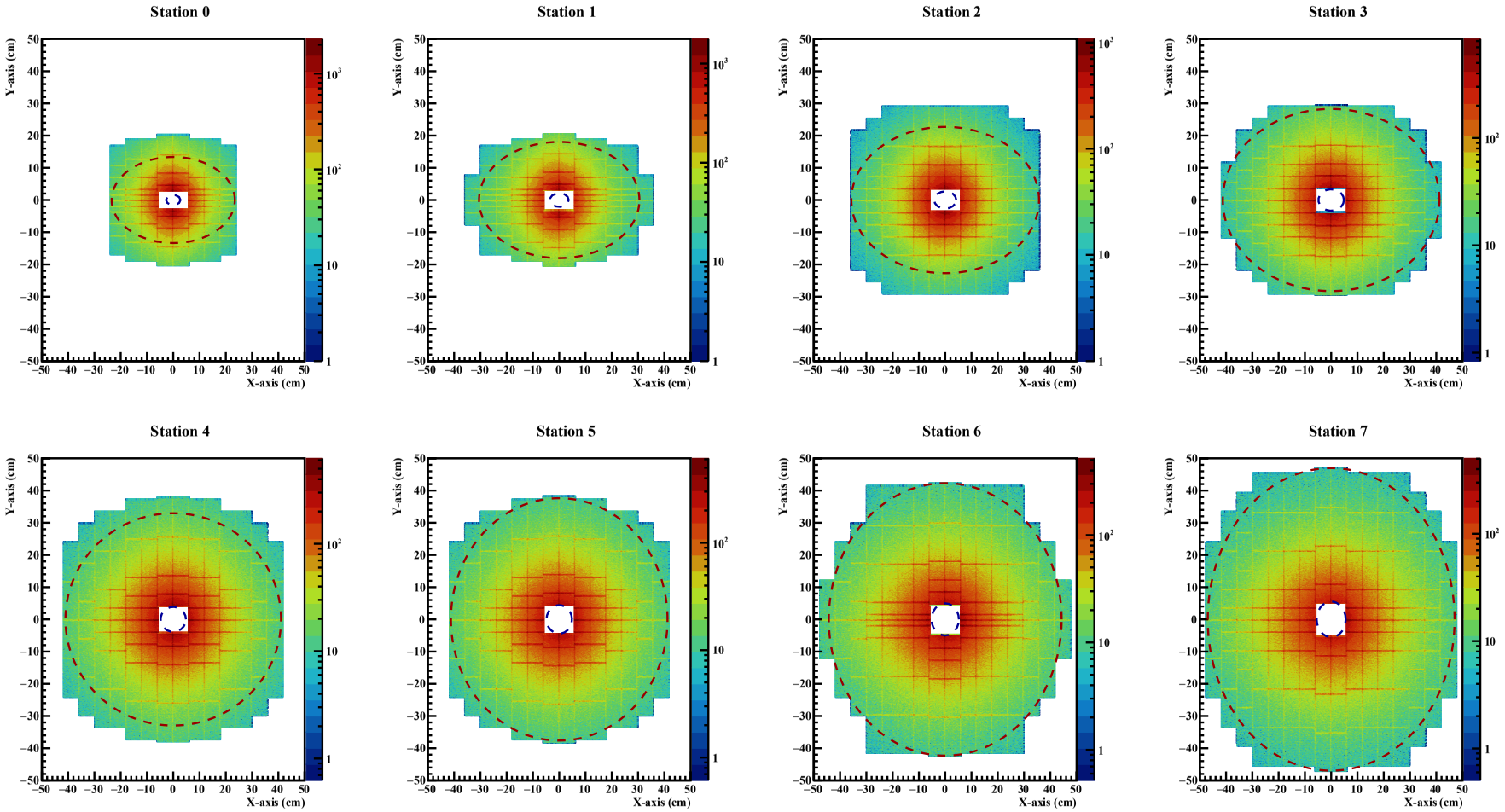

Figure 5.4: STS detector stations acceptance in η range 1.5 - 3.82 corresponds to polar angle θ range (2.5° - 25°) from the target position.

transverse momenta. We observe that for p and $\bar{p}$, the acceptance covers mid-rapidity, while for charged $\pi^{\pm}$ and $K^{\pm}$, it is shifted toward forward rapidity.

Figure 5.4 exhibits the distribution of accepted particles as a function of x, y in the different STS detector stations of various sizes. The first few stations are extended in the horizontal direction to provide efficient reconstruction of low-momentum particles in the magnetic field. The subsequent stations have identical construction and cover the full polar acceptance requirement of 25°. In each station, the inner (Blue) and outer (Red) circles denote the acceptance in the polar angle range from 2.5° to 25°.

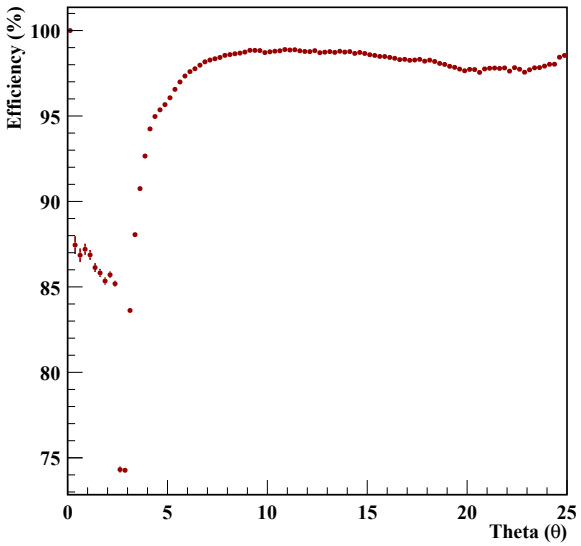

Figure 5.5: STS detector efficiency vs. theta (θ).

Figure 5.5 demonstrates the reconstruction efficiency as a function of theta θ. As can be seen from here, the drop in efficiency at small θ is attributed to geometric effects and acceptance losses in the most forward region, occupied mainly by high p_T particles, where tracks cross fewer detector layers or hit the edges of the first stations. Beyond this region, the detector coverage becomes uniform, and the efficiency gradually rises and remains well above $\geq$ 96 % up to $\theta \approx 25^{\circ}$, fulfilling the design requirement of the STS acceptance. The efficiency performance of individual particle species for different physics quantities is presented in **Appendix F**.

5.2 Hits Reconstruction Efficiency

In this section, we focus on the efficiency performance of the STS detector. The hit reconstruction efficiency is evaluated by comparing reconstructed hits with their corresponding Monte Carlo (MC)

points. Moreover, we studied the hit reconstruction efficiency considering the following dependencies:

- the digitization threshold while keeping the sensor ENC and dead time fixed, and
- the sensor dead time at a constant digitization ENC and threshold.

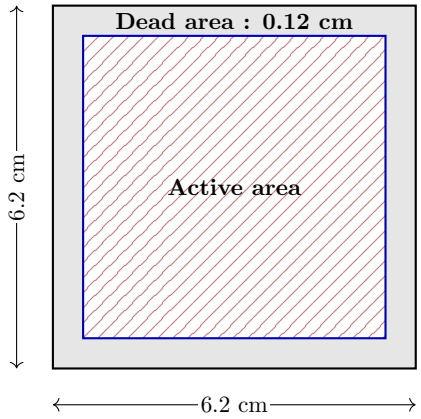

Figure 5.6: Illustration of the sensor (6.2×6.2 cm) with inner *"Active area"* and outer *"Dead area", mentioned with the dead area value of the sensor used in the simulation.*

The geometrical acceptance of the sensors includes both an active and an inactive (dead) area; it is essential to distinguish between the two clearly. Only the active region contributes to the detector response, whereas the dead margins surrounding it are insensitive to traversing particles. Figure 5.6 illustrates this concept, showing a sensor with dimensions $6.2 \times 6.2\,\mathrm{cm}^2$, where the inner hatched region corresponds to the active area and the shaded gray band represents the dead area.

For the efficiency calculations presented in this work, only the active area of each sensor is considered. The dead area is neglected, as it does not contribute to the reconstruction of the hit. Based on this definition, the hits reconstruction efficiency is evaluated both for individual sensors within a given station and as an average over the whole station. This approach ensures that the performance results reflect the detector's true sensitive region. During the analysis, MC points are considered to be found only if it has a matched link to a corresponding reconstructed hit within the same area.

Figure 5.7 shows the ratio between the reconstructed hits and the total MC points recorded within the active area of the sensor for a given STS station. We can observe from here that the innermost area of the station, where the sensors are close to the beam pipe, shows a drop in the efficiency in all the stations, while going from the inner region (from the beam pipe) to the peripheral region of the station exhibit small drop in the efficiency because in the inner central area, the particle

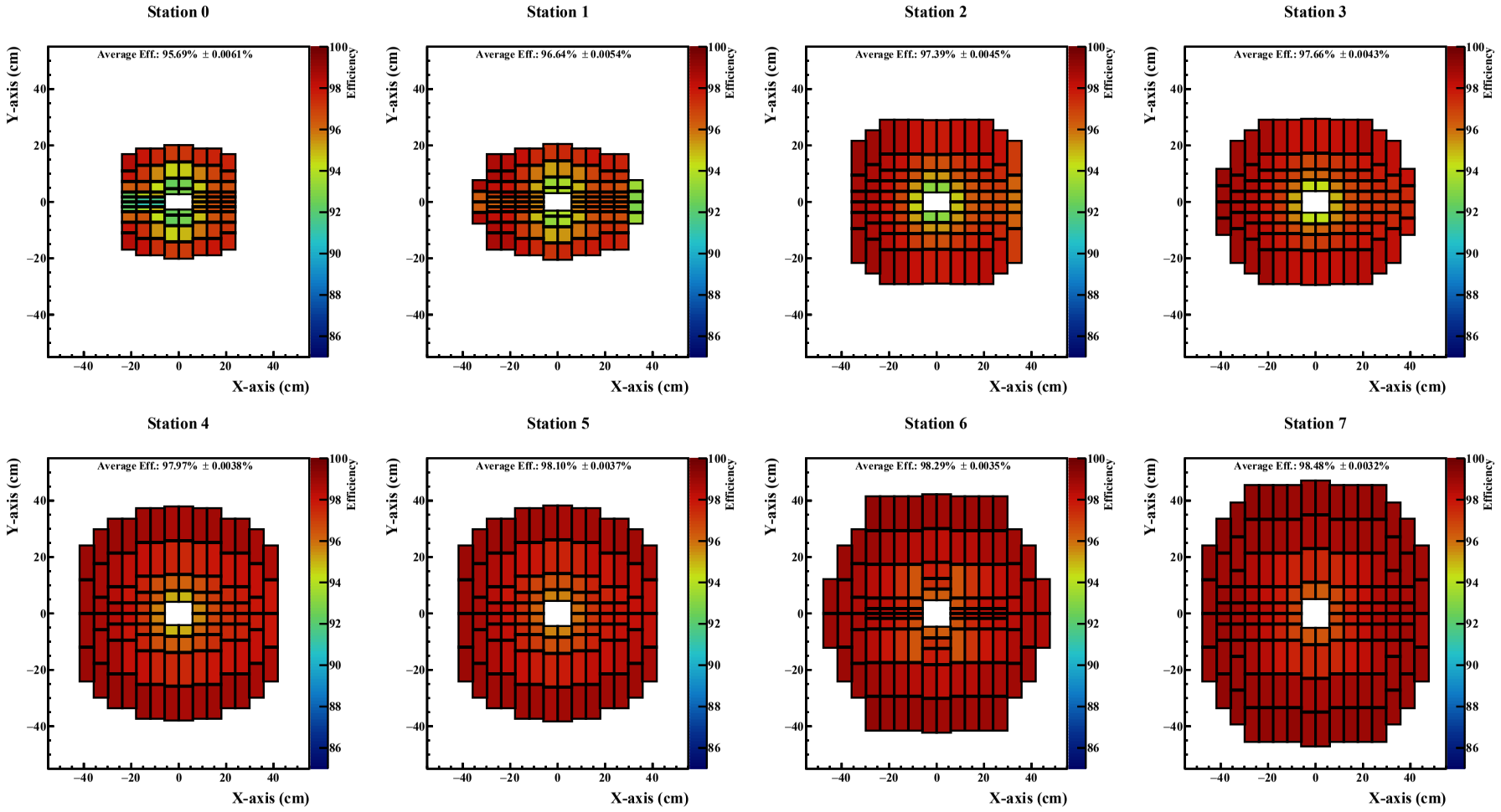

Figure 5.7: Average hits reconstruction efficiency of the different STS stations, together with UrQMD and Beam events sources at an ENC 1000 e, threshold 4000 e, and dead time 200 ns.

density is higher, occupied mainly by the high p_T particles, compared to the peripheral region.

On the other hand, we can also observe that in the first two stations the left part of the station sensor also has a drop in the efficiency which is due to the additional beam source which we have simulated for the delta electron background in the time-based simulation where at the high rate of the experiment could have a events pile-up which also could affect the efficiency. The efficiency of the STS station for the individual source and its dependencies on different thresholds and dead times is described in **Section 5.2.1** and **Section 5.2.2**. The distribution of hits reconstruction efficiency for individual sources, e.g., UrQMD and Beam, can be found in **Appendix G**.

5.2.1 Threshold Dependent Hits Reconstruction Efficiency

As discussed in **Chapter 3** and **Chapter 4**, how the digitization procedure works for the STS within CBM-ROOT. The signal registered as a hit only when the amplitude of the deposited charge exceeded the discriminator threshold. Therefore, the choice of the threshold directly affects the hit reconstruction efficiency.

Figure 5.8 schematically illustrates the interplay between signal amplitude, discriminator threshold, and channel recovery time and shows how it influences the hit reconstruction efficiency in a self-triggering readout system. A hit is registered only when the signal crosses the defined threshold (Red line), while the orange line indicates the baseline level to which the preamplifier output eventually resets.

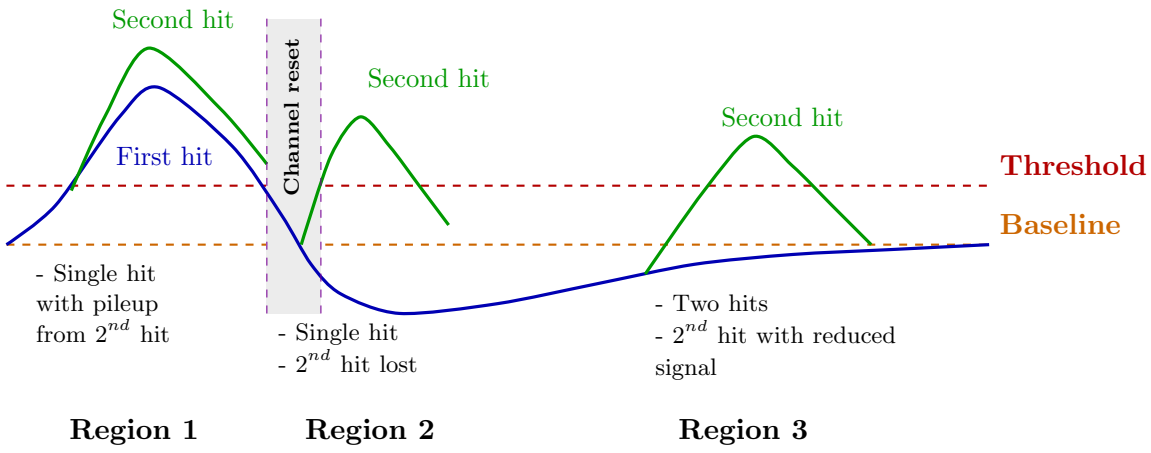

Figure 5.8: Illustration of different pileup or saturation scenarios in a self-triggering readout channel.

As shown in region 1, the second hit arrives shortly after the first and builds on it, resulting in a *"pile-up"* condition. In this scenario, the charges from the first and second hits are combined and reconstructed as a single hit with increased amplitude. Such pile-up scenarios result in a slight

overestimation of the hit amplitude but no apparent loss in efficiency, provided the combined signal remains above the threshold.

However, in region 2, the second hit occurs while the channel is still resetting (gray-shaded area). Because the preamplifier baseline has not yet fully recovered, the second pulse appears on a reduced pedestal and may not reach the threshold level. As a result, the system registers only one hit. In contrast, the subsequent hit is lost, especially at higher discriminator thresholds or when the arrival time of the second hit is shorter.

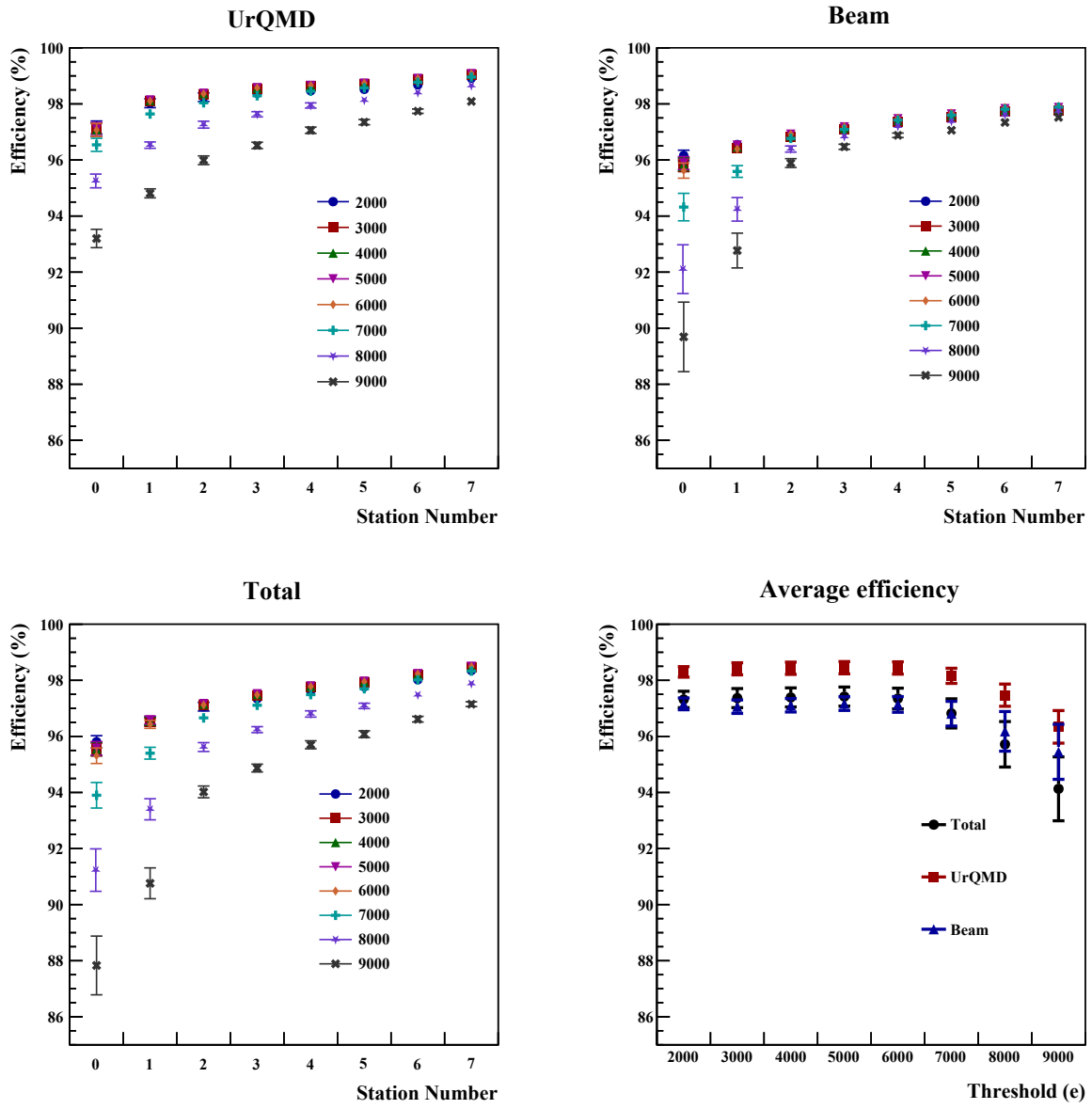

Figure 5.9: Hits reconstruction efficiency as a function of station number and digitization threshold for UrQMD (top-left), beam (top-right), and combined from both event sources (bottom-left). The bottom-right panel shows the average efficiency across all stations as a function of threshold for UrQMD, Beam, and total samples at a fixed dead-time of 200 ns and ENC 1000 e.

In Region 3, the second hit arrives after partial baseline recovery. Both pulses are detected separately, but the second one has a reduced amplitude, which could shift it below threshold if the threshold is set higher. This regime explains how an overly high threshold or insufficient shaping time can suppress valid signals, thereby reducing efficiency. Overall, this explains the origin of the efficiency loss observed in Figure 5.9 at high digitization threshold. While low thresholds ensure nearly complete hit detection, higher thresholds enhance the probability that signals affected by pile-up or incomplete baseline recovery fail to exceed the discriminator level, resulting in a reduced hit reconstruction efficiency.

Figure 5.9 presents the threshold-dependent efficiency for all STS stations, for different simulation event inputs used. The results for UrQMD events are shown in the top-left panel. A high efficiency, ranging from 97% to 99%, is observed for stations 2 to 7 across all threshold values. However, the efficiency of the first station exhibits a stronger dependence on the threshold, decreasing from approximately 97% at 2000 e to roughly 93% at 9000 e. This reduction is attributed to high particle density, event pile-up, lower energy deposition at the initial station, and a higher probability of signals falling below the increased threshold.

The top-right panel shows the corresponding results for the beam source, which contains only $\delta-$electron events. The events from a beam source exhibit a strong dependence on the hit reconstruction efficiency compared to the UrQMD because the amplitude created by the delta electrons is lower than that of the UrQMD events. The strong dependencies are evident for the first two stations. In contrast, other stations show consistent efficiency because most of the δ-electrons are either absorbed or lose their energy as they traverse through the detector or are mostly bent out under the magnetic field.

The bottom-left panel portrays the results from combining both UrQMD and beam event inputs. The combined efficiency follows the same trend as the individual sources, with stable performance above 97% for stations $2-7$ and a clear threshold dependence for station 0. At the highest threshold, the efficiency in stations 0 and 1 drops significantly.

Finally, the bottom-right panel summarizes the average efficiency across all stations as a function of threshold. The results are shown separately for UrQMD, beam, and total samples While the average efficiency remains above 97% at low thresholds, it gradually decreases as the threshold is raised, particularly in the UrQMD case. At 9000 e, the average UrQMD efficiency drops to about 96.5%, whereas for the beam source it is $\sim$ 95.5%. The total efficiency reflects this trend, and it is roughly 94%.

In summary, the analysis demonstrates that the digitization threshold primarily determines the STS detector's hit reconstruction efficiency, which drops notably at very high thresholds. This highlights the importance of optimizing the threshold to achieve uniform efficiency across the detector.

5.2.2 Dead-time Dependent Hits Reconstruction Efficiency

In this section, the hit reconstruction efficiency of the STS detector is studied for fixed ENC and threshold values (1000 e and 4000 e, respectively), while varying the sensor dead time from 200 ns to 800 ns. The dead time represents the time period following a signal that is registered during which the front-end electronics cannot process any new incoming signals. Any particle crossing the detector within this interval will not produce an additional recorded hit; it will be ultimately lost.

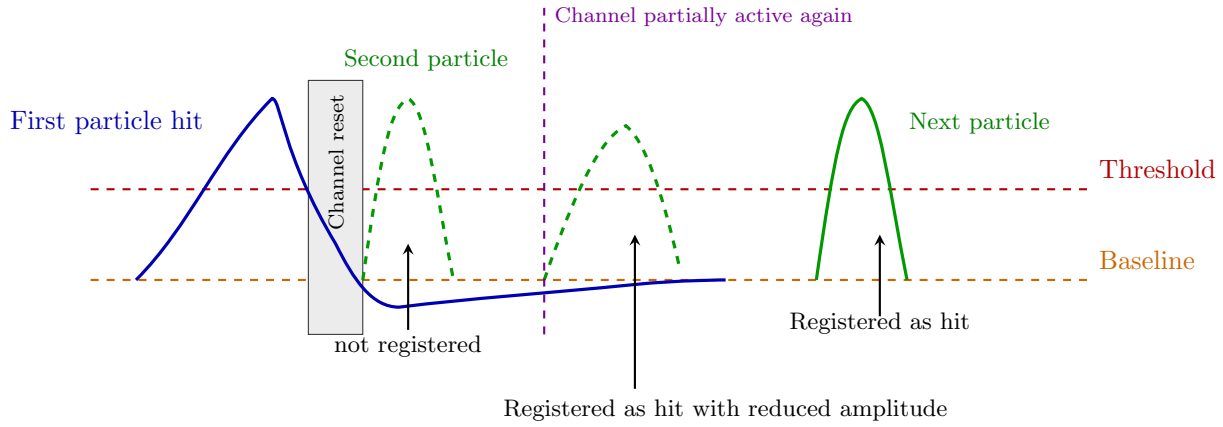

Figure 5.10: Dead time concept in a self-triggering silicon strip readout. After a first hit crosses the threshold, the front-end enters a dead time interval (gray). A second particle arriving during this interval produces an analog pulse (dashed green) but is not recorded as a new hit. Only signals arriving after the channel has recovered are registered again (solid green).

Figure 5.10 illustrates this concept for the STS front-end electronics. When a charged particle passes through the silicon sensor, it deposits a charge that is amplified and shaped by the preamplifier. If the resulting pulse exceeds the discriminator threshold, it is registered as a valid hit. Immediately after this, the readout channel enters a short recovery phase, known as the *"dead time"*, during which the signal baseline has not yet fully recovered.

If the second particle passes through the sensor during the dead-time interval, its pulse (shown as the dashed green curve) is still present at the analogue output but will not be recognized as a new hit by the electronics. The second hit is therefore lost. Once the channel baseline has fully recovered, the electronics become sensitive again, allowing subsequent pulses (solid green curve) to be recorded as a hit.

A longer dead time increases the chance that successive signals overlap, leading to a reduction in

the number of reconstructed hits and, consequently, a lower hit reconstruction efficiency. Further details about the event pile-up and saturation have been discussed in Subsection 5.2.1.

By increasing the dead time, the likelihood of such overlaps grows, particularly in regions or event types with higher particle occupancies. This effect manifests as a decrease in the overall hits reconstruction efficiency. The following analysis, therefore, quantifies the extent to which STS performance depends on the assumed dead time, complementing the threshold-dependence study presented in the previous Subsection 5.2.1.

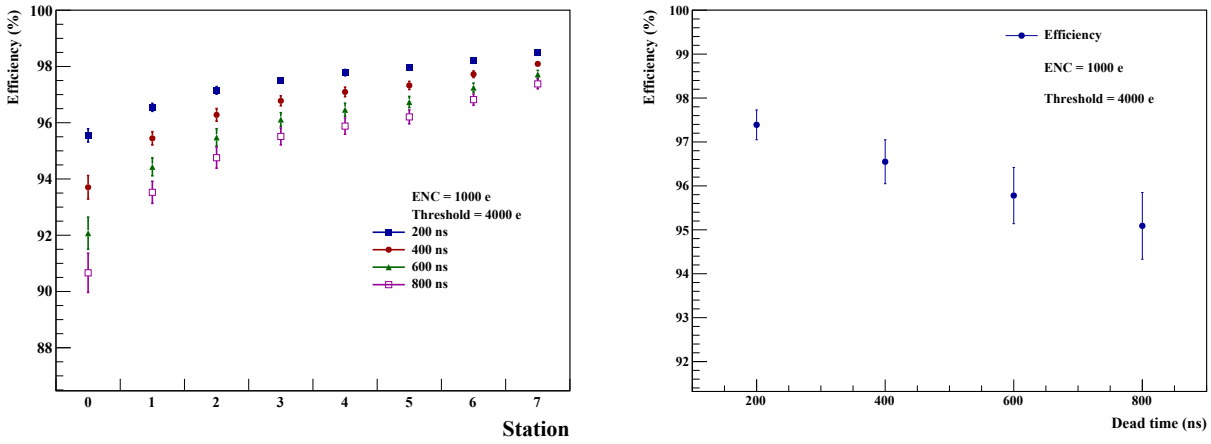

(a) Per-station efficiency vs. dead time.

(b) Average efficiency vs. dead time.

Figure 5.11: Hits reconstruction efficiency at fixed ENC (1000 e) and threshold (4000 e): (a) per-station efficiency by varying dead-time; (b) station-averaged efficiency as a function of dead time.

Figure 5.11 summarizes the dependence of the hits reconstruction efficiency on the detector dead time at fixed ENC (1000 e) and threshold (4000 e). Figure 5.11a shows the per-station efficiency for the dead-time interval between 200 ns and 800 ns. For all settings, stations 2 to 7 exhibit efficiencies above 96%, with only a modest reduction as the dead time increases. The first stations are again the most affected, with their efficiency decreasing from approximately 96% at 200 ns to below 91% at 800 ns. This sensitivity is expected, as the initial station is more exposed to higher particle flux, increasing the probability of signal overlap within the dead-time window.

Figure 5.11b presents the average efficiency across all stations as a function of dead time. The average efficiency decreases steadily from approximately 97.5% at 200 ns to around 95% at 800 ns. The error bars widen with increasing dead time, indicating larger fluctuations in the reconstructed hit statistics under conditions of reduced detector response.

Overall, the analysis demonstrates that the STS maintains high efficiency even during dead times of up to 400 ns, with only moderate degradation at longer dead times. However, the pronounced

effect observed in the first station underscores the importance of minimizing dead time to ensure uniform performance across the entire detector.

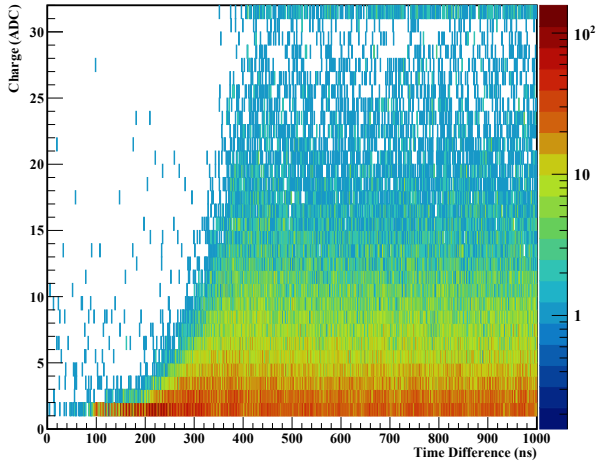

Figure 5.12: Experimental measurement of signal amplitude as a function of time difference between consecutive signals on the same readout channel, illustrating the detector dead-time behaviour. The suppression of low time differences (left side) reflects the period during which the front-end electronics remain insensitive following a previous signal pulse.

Figure 5.12 displays an experimental measurement of the dead-time behaviour obtained from the time-based readout of the STS front-end electronics, where it is presented for the amplitude of a first signal arrived on the channel as a function of the time difference between consecutive signals recorded on the same channel.

For very short time intervals (below approximately 100–200 ns), almost no signals with significant amplitude are observed. This region corresponds to the electronics dead-time window, during which the channel is still processing or recovering from the previous signal and cannot process any new incoming signals. As the time difference exceeds this interval, the recorded amplitude gradually recovers, indicating that the preamplifier baseline and gain have returned to their nominal values.

As the time difference between consecutive signals on the same channel increases, the amplitude distribution becomes uniform, indicating that the channel has fully recovered from the previous signal.

This observation from the experimental data confirms the electronic behaviour illustrated in the Figure 5.10. Also, it supports and explains the reduction in the hit reconstruction efficiency, particularly at high rates and when the particle flux is higher, as in the first few stations of the STS detector.

5.2.3 Tracking Efficiency

The tracking performance of the STS detector has been simulated with the following settings: digitization parameter ENC = 1000 e, threshold = 4000 e, dead-time = 200 ns, and time-resolution = 5 ns for all 876 silicon sensors, arranged across different STS stations. The track reconstruction efficiency for all particle tracks, as well as for primary and secondary particle tracks, is shown in Figure 5.13. From here, it is noticeable that the track reconstruction efficiency, for a particle momentum ($p \geq 1$ GeV/c), for all types of particle tracks, remains around 97%, while for the primary particle track, it is approximately 98%. On the other hand, we can observe that the efficiency for the secondary particle tracks drops to 92-93%.

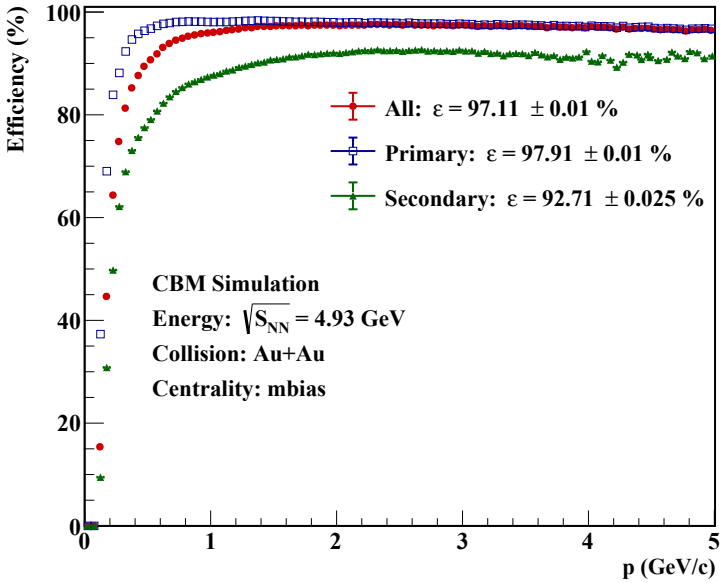

Figure 5.13: Tracking efficiency for the STS detector through simulation for primary, Secondary, and combined to all particles.

The analysis shown for the hits reconstruction done with changing the threshold and dead-time also reveals that it has a direct impact on the reconstruction efficiency and matches the observation previously seen in **Section 5.2** and its Subsection 5.2.1 & Subsection 5.2.2.

5.3 Cluster Characterization

When a charged particle traverses a silicon micro-strip sensor, it releases electron–hole pairs along its path. The carriers drift in the electric field and spread laterally by diffusion before being

collected. The root-mean-square (r.m.s.) diffusion width after a drift time t [68, 110] is

$$\sigma_{\text{diff}} \simeq \sqrt{2D\,t}, \qquad D = \frac{kT}{q}\,\mu, \qquad t = \frac{d}{v_d}, \quad v_d = \mu E, \tag{5.5}$$

where D is the diffusion constant, μ the carrier mobility, E the electric field, d the thickness of the sensor.

A charged particle that crosses a planar thickness sensor d at an incidence angle $\theta_\perp$ (projected perpendicular to the direction of the strip) creates charge along a slanted path.

$$\Delta x_{\text{geom}} \simeq d\,\tan\theta_\perp. \tag{5.6}$$

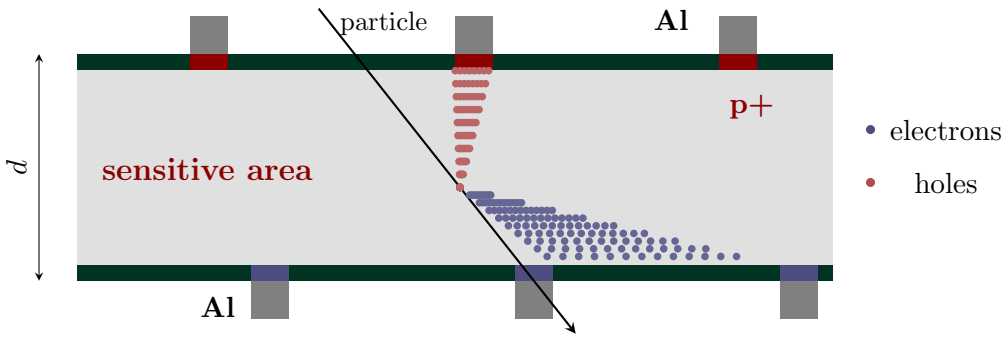

Figure 5.14: An illustration of the electrons and holes drift under a magnetic field

In a magnetic field B (with $\mathbf{E} \perp \mathbf{B}$), charge carriers drift at the *Lorentz angle* α_L, which deflects their trajectories laterally as they traverse the sensor thickness. Since the velocity of the electrons and holes is different, the Lorentz force acting on them also differs. The measured lateral shift is[107, 111]

$$\Delta x_B \;=\; d\,\tan\alpha_L, \qquad \tan\alpha_L \;\simeq\; \mu_H\,B \;=\; r_H\,\mu\,B, \tag{5.7}$$

where μ is the (conduction) mobility, $\mu_H = r_H\mu$ the Hall mobility, and r_H the Hall scattering factor (of order unity and carrier dependent).

In addition, carriers broaden stochastically by diffusion during drift as described earlier in Equation 5.5. The field-dependent drift mobility is[112]

$$\mu(E) \;=\; \frac{\mu_{\text{low}}}{\left[1 + \left(\dfrac{\mu_{\text{low}}\,E}{v_{\text{sat}}}\right)^{\beta}\right]^{1/\beta}} \tag{5.8}$$

where μ_{low} is the low–field mobility, v_{sat} the saturation velocity at high fields, and β an empirical

constant.

With T in Kelvin, the following temperature dependences are:

$$\textbf{Holes: } \beta_h = 1.213 \left(\frac{T}{300}\right)^{0.17}, \mu_{\mathrm{low},h} = 470.5 \ \frac{\mathrm{cm}^2}{\mathrm{V\,s}} \left(\frac{T}{300}\right)^{-2.5}, \ v_{\mathrm{sat},h} = 8.37 \times 10^6 \ \frac{\mathrm{cm}}{\mathrm{s}} \left(\frac{T}{300}\right)^{0.52}, \tag{5.9}$$

$$\textbf{Electrons: } \beta_e = 1.109 \left(\frac{T}{300}\right)^{0.66}, \ \mu_{\mathrm{low},e} = 1417 \ \frac{\mathrm{cm}^2}{\mathrm{V\,s}} \left(\frac{T}{300}\right)^{-2.2}, \ v_{\mathrm{sat},e} = 1.07 \times 10^7 \ \frac{\mathrm{cm}}{\mathrm{s}} \left(\frac{T}{300}\right)^{0.87}. \tag{5.10}$$

Let d be the sensor thickness, U_{bias} the applied bias, and U_{depl} the full depletion voltage. The z–dependent electric field (in one-dimensional depletion) is taken as[113]

$$E(z) \ = \ \frac{U_{\mathrm{bias}} - U_{\mathrm{depl}}}{d} \ + \ \frac{2\,U_{\mathrm{depl}}}{d} \left(1 - \frac{z}{d}\right), \qquad 0 \le z \le d. \tag{5.11}$$

If the sensor is fully depleted or overdepleted, the average electric field (e.g. at $z = d/2$) reduces to $E_{\mathrm{avg}} \simeq U_{\mathrm{bias}}/d$. If the detector cannot be fully depleted, the field drops to zero in the undepleted region; in Equation 5.11, d then denotes the depleted thickness with $U_{\mathrm{bias}} = U_{\mathrm{depl}}$. At typical operating biases, the field is sufficiently high that one may use an *average* mobility $\mu\left(E_{\mathrm{avg}}\right)$ in Equation 5.8 and compute the Lorentz deflection via

$$\Delta x_B \ = \ d_{\mathrm{eff}} \tan\alpha_L, \qquad \tan\alpha_L \ = \ \mu_H(E,T)\,B \ = \ r_H\,\mu(E,T)\,B,$$

with Hall factor r_H (here $r_H = 0.7$ for holes and $r_H = 1.15$ for electrons) and an effective drift distance d_{eff} (for MIPs, $d_{\mathrm{eff}} \approx d/2$ per side).

Figure 5.15 shows the cluster size distribution for each station. A sharp peak is expected at small cluster sizes ($N = 2$–3) if the charge diffusion and the charge sharing with neighbouring strips are small. And it corresponds to nearly perpendicular tracks, where the geometrical broadening (Equation 5.6) and Lorentz shift (Equation 5.7) are both small, and diffusion (Equation 5.5) leads to only limited charge sharing.

Furthermore, Figure 5.16 illustrates the cluster size distributions separated by source and sensor side (n and p). The most probable value (MPV) of the cluster size for the UrQMD event sample remains approximately constant at 2 across all stations, indicating minimal charge sharing and diffusion effects. In contrast, the Beam event sample, containing mostly δ-electrons, exhibits significantly larger MPV values and a broader Landau peak.

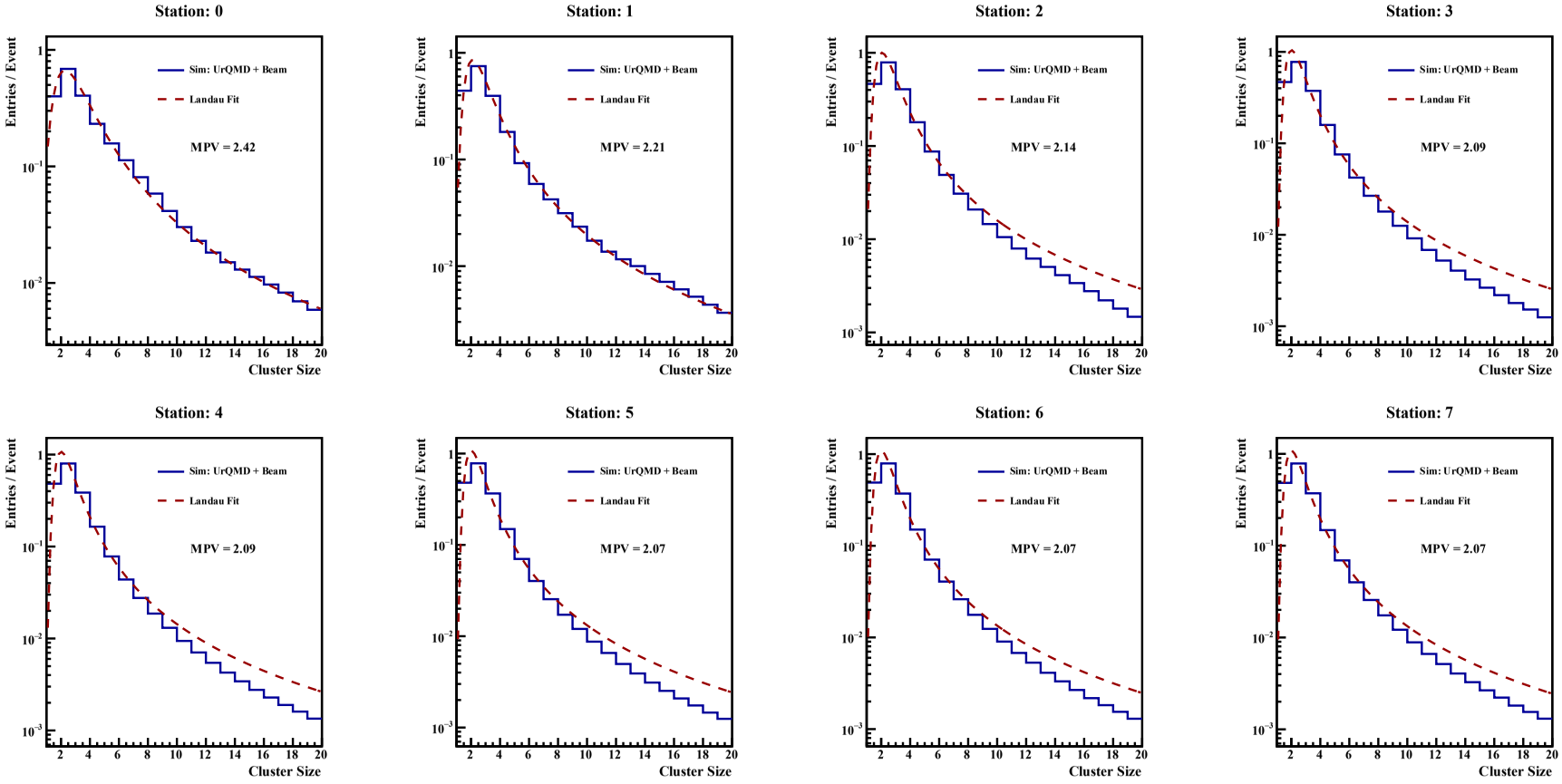

Figure 5.15: Cluster size distributions for simulated events (UrQMD + Beam). Each panel shows the distribution of cluster size N for the STS station (0-7). The most probable value (MPV) extracted from the fit is annotated in each panel.

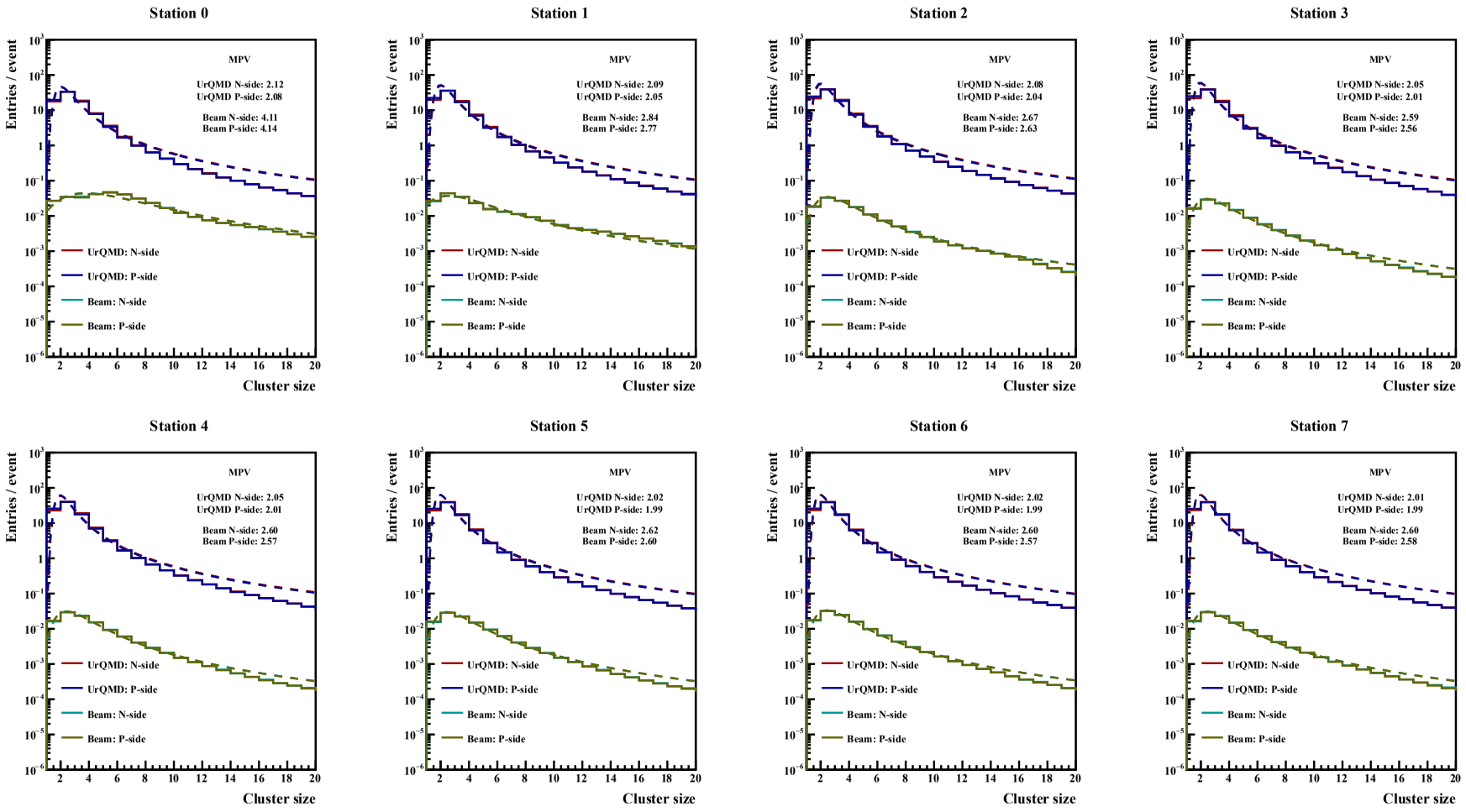

Figure 5.16: Cluster size distributions obtained from simulation separately for $n-$ and $p-$sides of the sensor of UrQMD and the beam source. Each panel shows the distribution of cluster size N for the STS station (0-7). The most probable value (MPV) extracted from the fit is annotated in each panel.

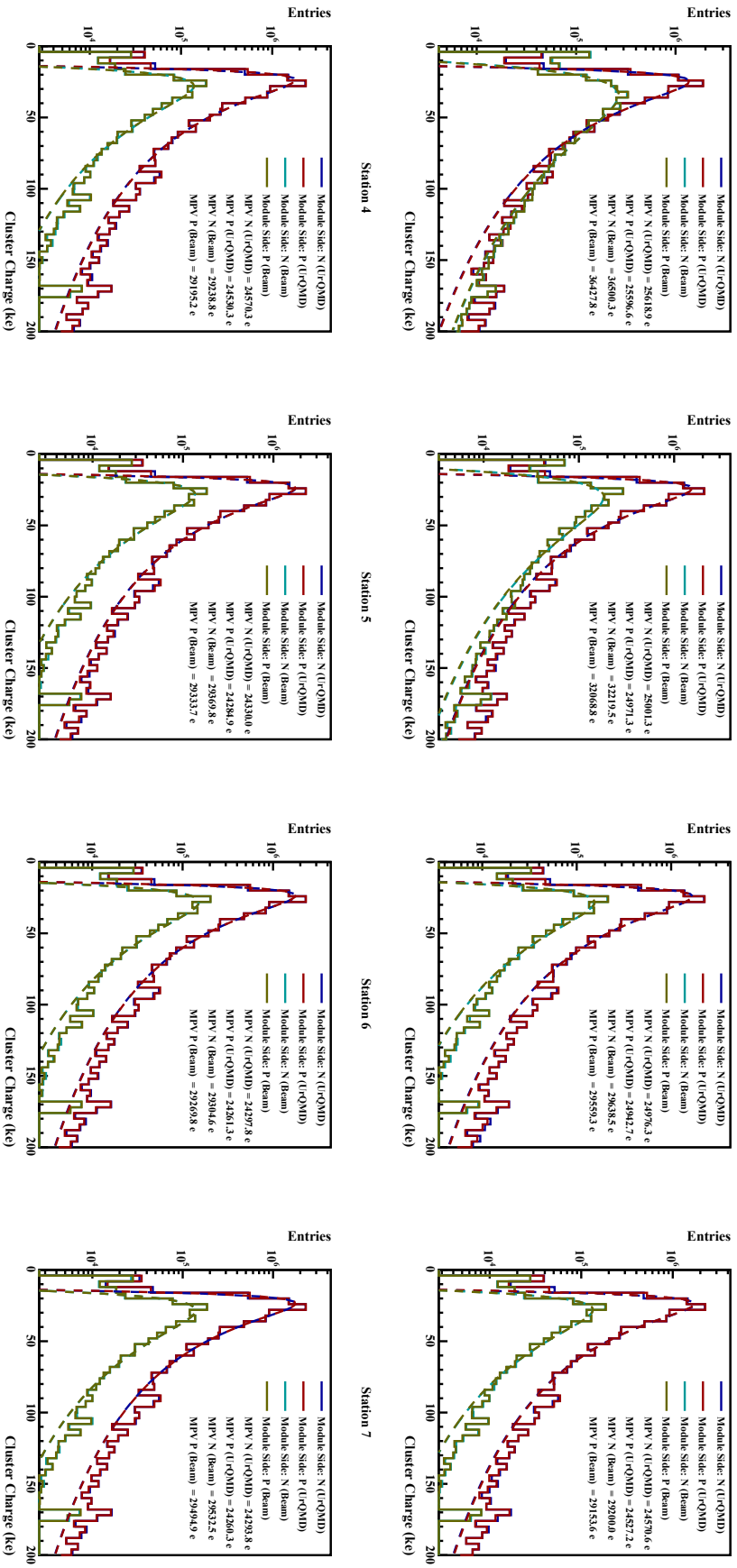

Figure 5.17: Cluster charge for each STS station, separated by the source (UrQMD and Beam) and side of the sensor(n and p).

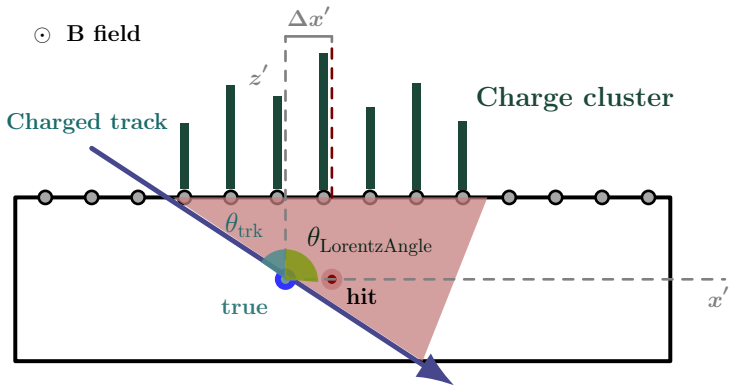

Figure 5.18: Schematic illustration of charge sharing in a silicon strip detector and the relation between true hit position and reconstructed cluster position.

In addition, Figure 5.17 shows the cluster charge distribution separated by the source and the sensor side. We can see that the MPV value in the case of a beam source is larger compared to the UrQMD source, which is due to fact that it has a dependency on the incident angle; therefore, when a charged particle traverses the detector at an incident angle θ relative to the sensor normal, as shown in Figure 5.18, the path length inside the sensitive volume increases according to

$$\ell = \frac{d}{\cos\theta}$$

Consequently, the energy deposited and therefore the number of electron–hole pairs produced increases proportionally to the path length:

$$N_{eh}(\theta) = \frac{(dE/dx)\,\ell}{I_0} = \frac{(dE/dx)\ \cdot d}{I_0 \cdot \cos\theta}$$

Hence, the signal scales as

$$N_{eh}(\theta) \propto \frac{1}{\cos\theta}$$

This explains the pronounced broader Landau peak and the MPV value in the case of the beam source, which contains δ-electrons, mainly in the upstream STS stations near the target. Moreover, these low-energy secondary electrons are deflected by the magnetic field and absorbed as they traverse the detector material, leading to a gradual reduction in their contribution to downstream stations.

Also, δ–electrons often enter the silicon sensor under oblique angles with respect to the normal under the magnetic field, causing both an enhanced energy deposition and a wider lateral spread of the charge cloud due to diffusion and Lorentz drift. Consequently, the induced charge collected

across multiple adjacent readout strips produces larger cluster sizes and charge.

Figure 5.19 shows the corresponding profile histograms of the cluster size across the detector area. In the central regions of the stations, the average cluster size remains small. This behaviour is attributed to high-momentum particles travelling predominantly along the z-axis in the forward direction, which minimizes the transverse spread of the charge and thus limits charge sharing. By contrast, the peripheral regions exhibit larger cluster sizes. In these areas, low-momentum particles, bent under the magnetic field, cross the detector at larger inclination angles, resulting in charge spreading over several adjacent strips. Additionally, in the first three stations, a localized region on the left side of the active area shows an enhanced cluster size. This effect is due to delta electrons, as explained earlier.

Figure 5.22 shows the mean cluster size as a function of the *local* incidence angle in the strip–normal plane. For a micro-strip sensor, the relevant angle is the tilt with respect to the sensor normal, projected onto the measured (u, w) plane (where u is the strip–normal direction and w the sensor thickness). Let $\vec{p}$ be the track direction and (p_u, p_v, p_w) its components in the module's local (u, v, w) frame. The incidence angle that drives charge sharing is

$$\theta_u \equiv \arctan\left(\frac{|p_u|}{|p_w|}\right) \tag{5.12}$$

Equivalently, using the simulated entry/exit points inside the silicon $(u_{\text{in}}, v_{\text{in}}, w_{\text{in}})$ and $(u_{\text{out}}, v_{\text{out}}, w_{\text{out}})$ one may compute it from the straight segment across the sensor,

$$\theta_u \equiv \arctan\left(\frac{|u_{\text{out}} - u_{\text{in}}|}{|w_{\text{out}} - w_{\text{in}}|}\right) \tag{5.13}$$

For perpendicular tracks ($\theta \simeq 0$), the cluster size remains small. In this case, the charge deposition is localized, the effective path length through the silicon is minimal, and only limited charge sharing occurs, resulting in clusters close to a single strip. In contrast, inclined tracks traverse a longer path within the sensor, thereby increasing the lateral spread of charge carriers due to diffusion. This leads to a larger fraction of the deposited charge being shared among neighbouring strips. Additionally, capacitive crosstalk enhances the induced signals on adjacent strips, raising them above the readout threshold and thereby increasing the effective cluster size. As a result, cluster size systematically increases with the track inclination angle, reflecting the combined effects of charge diffusion and cross-talk. The cluster size vs. inclination angle distribution for an individual source is shown in the **Appendix H**, **Section H.1**.

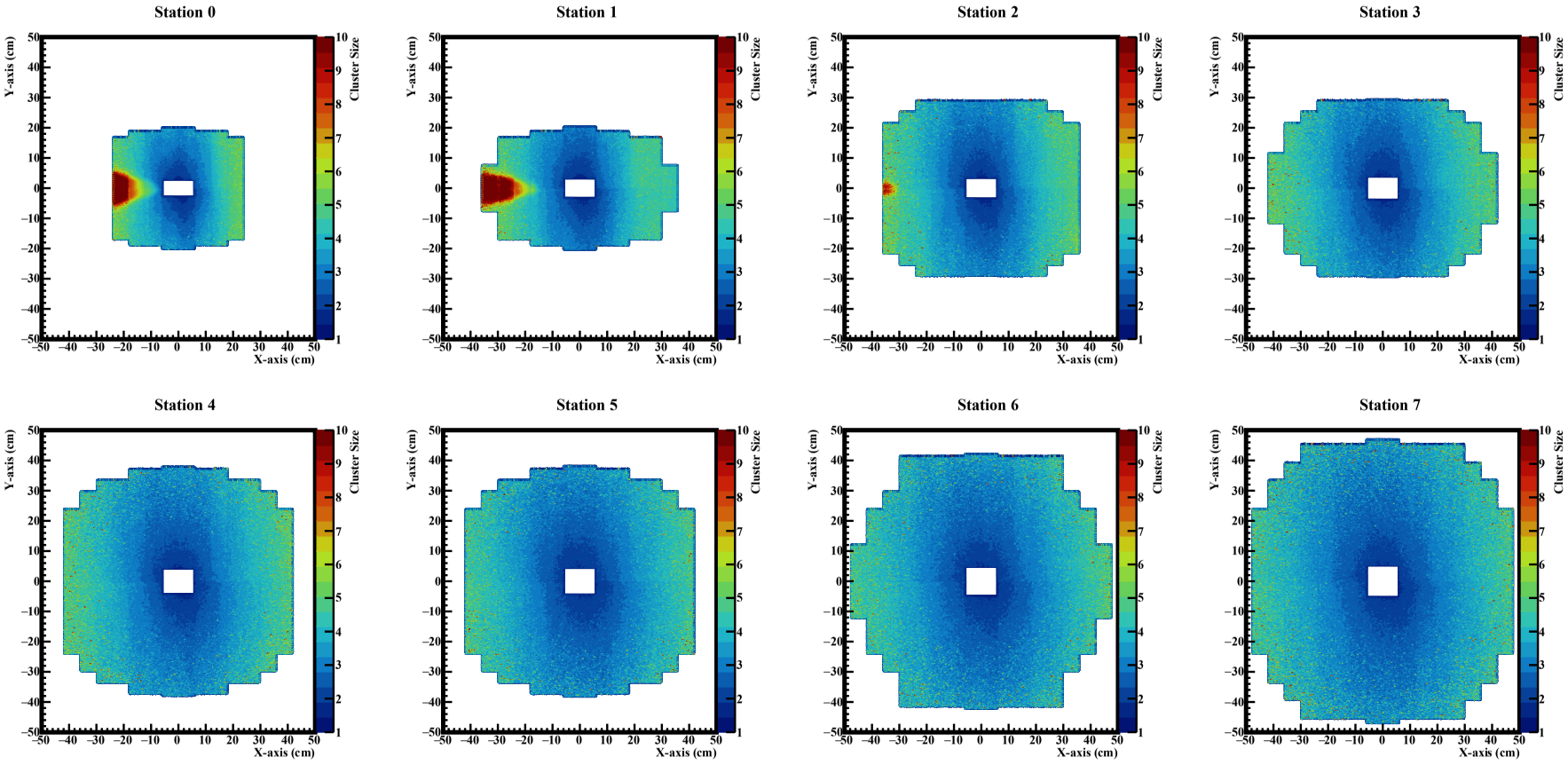

Figure 5.19: Profile distribution of cluster size for each STS station for UrQMD and Beam; the z-axis range was arbitrarily set to 10 for better visualization.

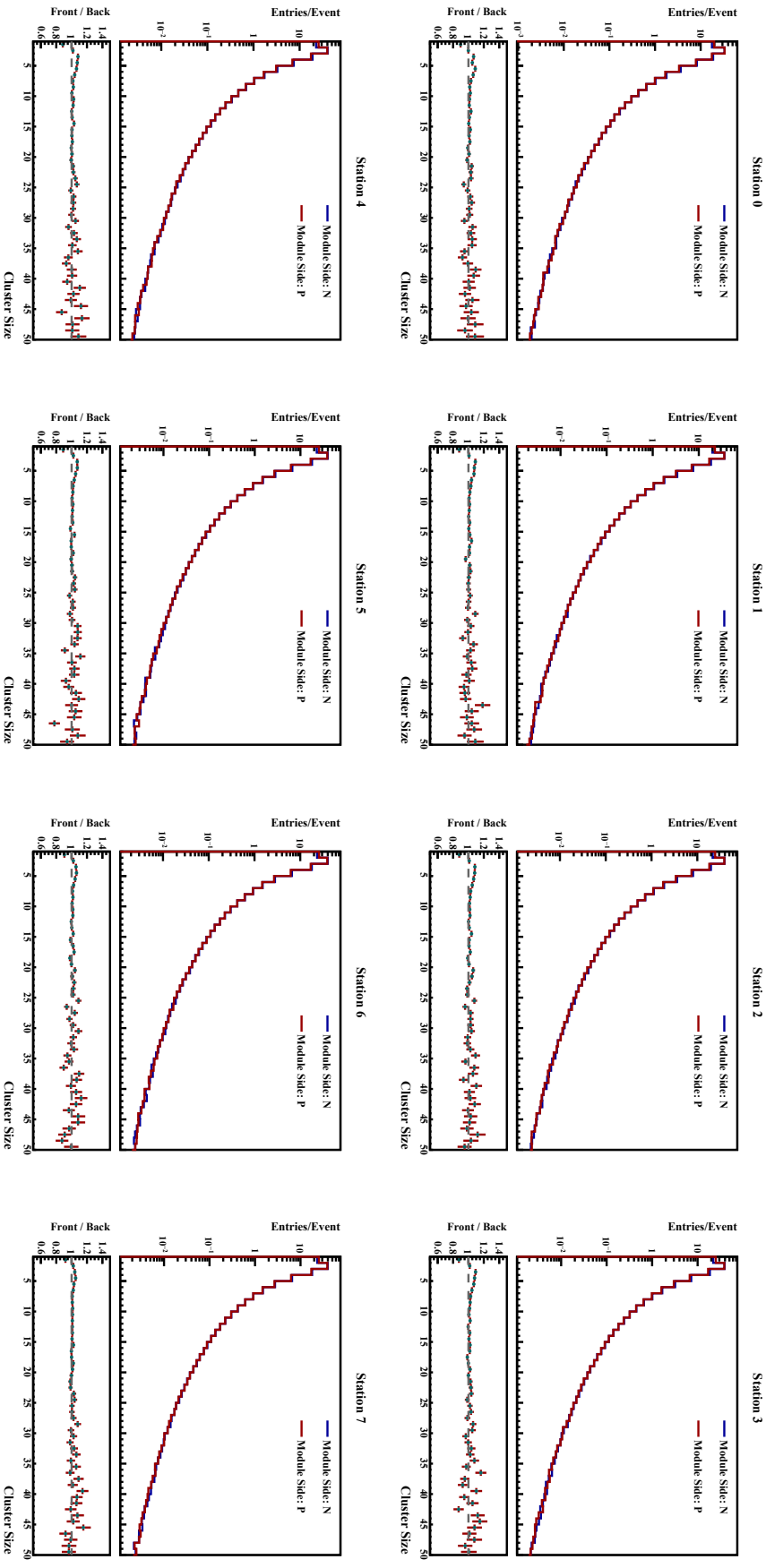

Figure 5.20: Cluster size and ratio ($n-/p-$side) distribution for each STS station for the UrQMD events.

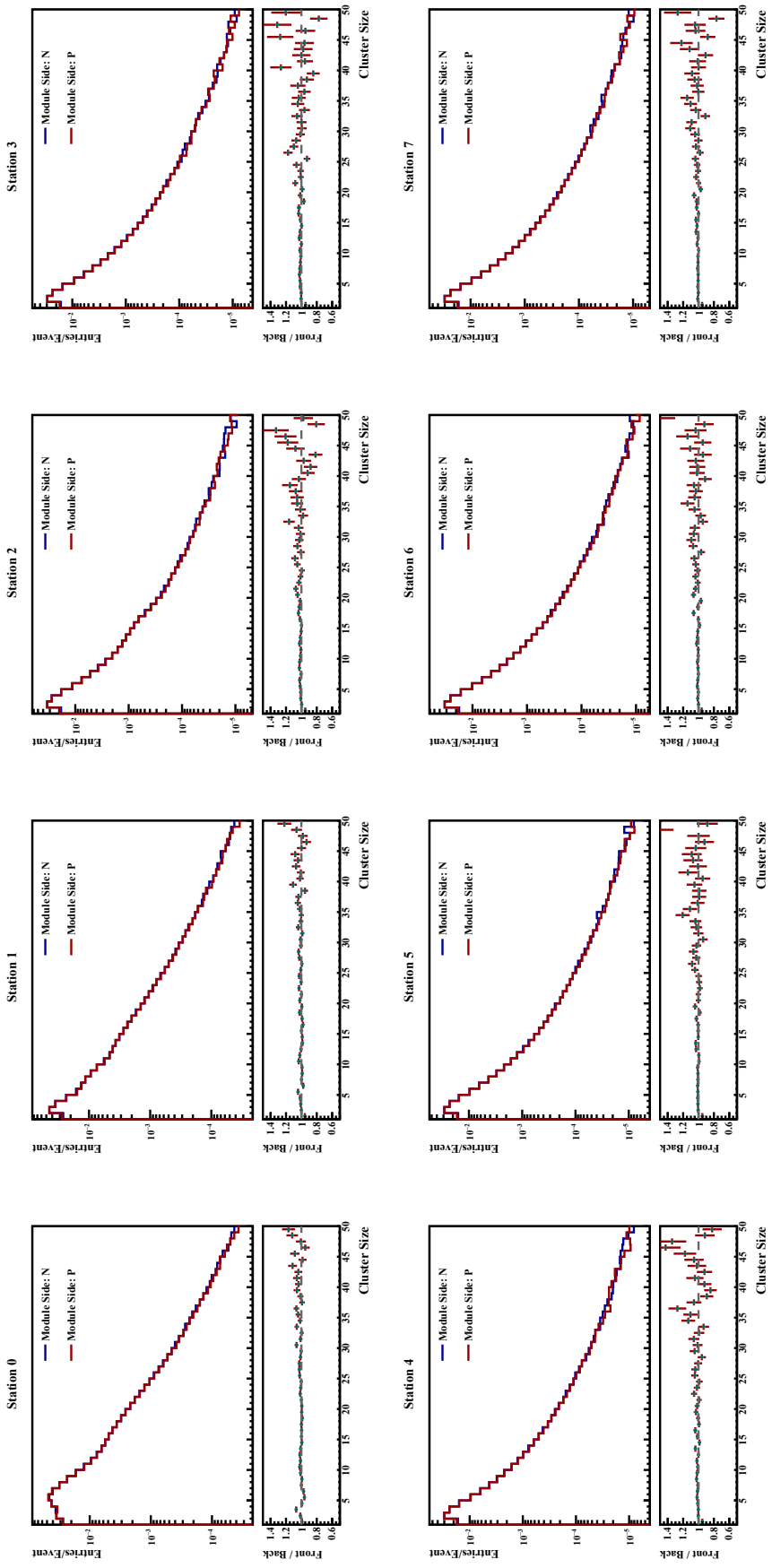

Figure 5.21: Cluster size and ratio ($n-/p-$side) distribution for each STS station for the Beam events.

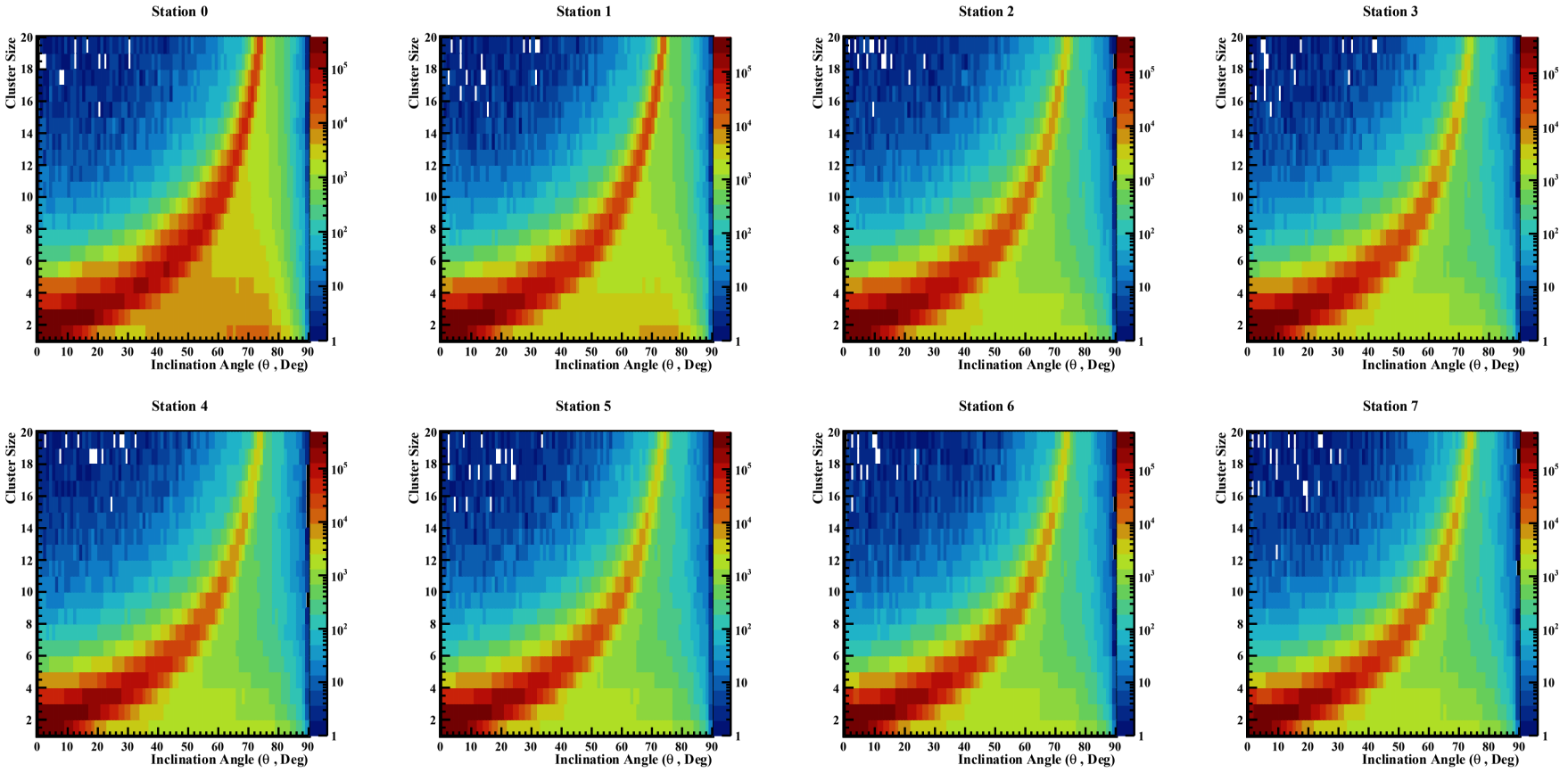

Figure 5.22: Cluster size as a function of the inclination angle for all STS stations, together for UrQMD and Beam events (all particles).

Figure 5.20 and Figure 5.21 show the measured cluster-size distributions for the n and p sides for UrQMD and Beam events, respectively, together with the n/p side ratio.[4] For small cluster sizes, the ratio is consistent with unity, reflecting the mechanisms described in **Section 5.3**. In this regime, both carrier species are collected with only a slight lateral deflection, and the induced charge on neighbouring strips rarely exceeds the threshold. At larger cluster sizes, which mainly arise from tracks incident at large inclination angles, deviations of the n/p ratio from unity appear in the high-cluster-size tail. The core region remains symmetric. The station-by-station ratios indicate that these effects are well controlled. They are consistent with expectations from the inclination-angle dependence (Figure 5.22) and the position profiles (Figure 5.19). The correlation between cluster size on $n-$ and $p-$side is shown in **Appendix H**, **Section H.2**.

5.4 Space Resolution

For each STS hit, we compare the reconstructed impact point on the sensor to the Monte-Carlo (MC) truth at the same sensor plane. All positions are expressed in the module's local coordinate system (u, v, w), where u is the strip–normal (measured) direction, v runs along the strips, and w is orthogonal to the sensor plane. The MC transport provides the entry and exit points of the track in the sensitive volume,

$$\mathbf{r}_{\text{in}} = (u_{\text{in}}, v_{\text{in}}, w_{\text{in}}), \qquad \mathbf{r}_{\text{out}} = (u_{\text{out}}, v_{\text{out}}, w_{\text{out}}).$$

We approximate the trajectory inside the thin sensor by a straight segment $\mathbf{r}(t) = \mathbf{r}_{\text{in}} + t\,(\mathbf{r}_{\text{out}} - \mathbf{r}_{\text{in}})$, $t \in [0, 1]$. Let $(u_{\text{hit}}, v_{\text{hit}}, w_{\text{hit}})$ be the reconstructed hit position. The MC point at the same plane $w = w_{\text{hit}}$ is obtained by intersecting the segment with that plane,

$$t^* = \frac{w_{\text{hit}} - w_{\text{in}}}{w_{\text{out}} - w_{\text{in}}}, \qquad u_{\text{MC}} = u_{\text{in}} + t^*(u_{\text{out}} - u_{\text{in}}), \quad v_{\text{MC}} = v_{\text{in}} + t^*(v_{\text{out}} - v_{\text{in}}). \tag{5.14}$$

The position resolution quantified by

$$r_u \equiv u_{\text{hit}} - u_{\text{MC}}, \qquad r_v \equiv v_{\text{hit}} - v_{\text{MC}}. \tag{5.15}$$

The distributions of r_u for all stations are shown in Fig. 5.23. They are well described in the core by a Gaussian,

[4] In the simulation, the Front side of the sensor is considered $n-$side while the back side is $p-$side of the sensor.

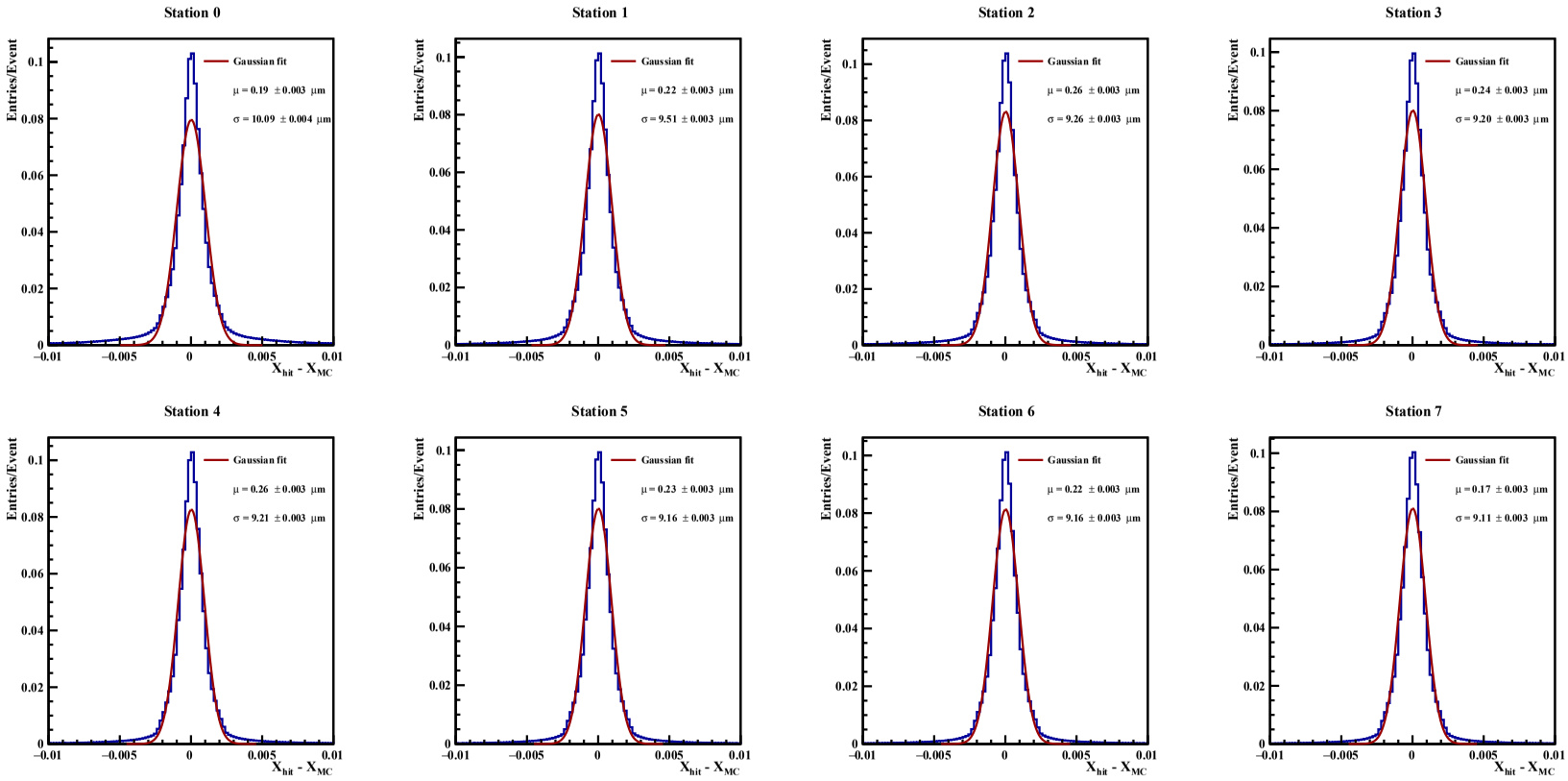

Figure 5.23: Distributions of the local strip–normal residual $r_u = u_{\mathrm{hit}} - u_{\mathrm{MC}}$ for STS stations 0–7.

Across stations, we measure

$$\mu \simeq (0.17\text{–}0.26)\ \mu\text{m} \quad \text{(consistent with 0)}, \qquad \sigma \simeq (9.1\text{–}10.1)\ \mu\text{m}.$$

and is consistent with the expectation for a single strip cluster where

$$\sigma \simeq \frac{58}{\sqrt{12}}\mu\text{m} = 17\mu m$$

Residual tails expected from tracks at large incidence angle (longer projected path and more charge sharing), δ–electrons and, to a lesser extent, multiple scattering, which could affect the spatial resolution.

5.5 Potential for Particle Identification

Particle identification (PID) is a fundamental requirement in the study of nucleus-nucleus collisions at all beam energies. It enables the determination of the species of a particle by measuring its basic properties such as electric charge, momentum, and velocity. Since the mass of an elementary particle produced in heavy-ion collisions cannot be measured directly, it is inferred from the combined measurement of momentum and velocity.

5.5.1 PID in the CBM Experiment

In the CBM experiment, the momentum is reconstructed from the curvature of a charged track in the magnetic field, which depends on both the charge Z and the momentum p of the particle. The relevant observable of a magnetic spectrometer is the *rigidity* $R = p/Z$. The complementary measurement of the velocity $\beta = v/c$ is performed by the Time-of-Flight (ToF) detector, which measures the travel time of a particle between the interaction point and the detector plane.

A particle of mass m and momentum p has velocity

$$\beta = \frac{p}{\sqrt{p^2 + m^2}} \tag{5.16}$$

$$m^2 = p^2 \left(\frac{1}{\beta^2} - 1 \right) \tag{5.17}$$

For a path length L the flight time T is

$$T = \frac{L}{v} = \frac{L}{c\,\beta} \tag{5.18}$$

Thus, particles with identical momentum but different masses arrive at the ToF detector with different flight times. The corresponding time difference is

$$\Delta T = T_1 - T_2 = \frac{L}{c}\left(\sqrt{1+\frac{m_1^2}{p^2}} - \sqrt{1+\frac{m_2^2}{p^2}}\right) \approx \frac{(m_1^2 - m_2^2)\,L}{2c\,p^2} \tag{5.19}$$

where the last expression holds in the high-momentum approximation.

5.5.2 The CBM-ToF Detector

The CBM Time-of-Flight (ToF) detector uses the Multi-gap Resistive Plate Chambers (MRPCs), which are well-established for their excellent timing resolution.[114] The ToF wall will cover an area of $\sim$120 m^2, with dimensions 9 m (height) $\times$ 13.5 m (width), and will be installed 10 m downstream of the target.[115] There are two PID strategies foreseen as listed below;

- the standard $n\sigma$ method and
- the Bayesian method

5.5.3 Standard nσ Method

The $n\sigma$ method is the most widely used approach in high-energy physics for particle identification based on time-of-flight or dE/dx measurements [116]. The reconstructed mass squared of a track is given by Equation 5.17, where the velocity β is calculated from the time-of-flight. For each particle species α (e.g. π, K, p), the expected mean value $m_\alpha^2(p)$ is known from kinematics. The deviation of the measured value from the expectation is expressed in units of the detector resolution σ_{m^2}:

$$n\sigma_\alpha(p) = \frac{m^2_{\text{meas}}(p) - m^2_\alpha(p)}{\sigma_{m^2}(p)}\,. \tag{5.20}$$

The method is straightforward and robust, and provides clean separation at low momenta where the time-of-flight differences between species are large. However, Its performance degrades at higher momenta as the m^2 bands converge (see Figure 5.24), and it does not optimally exploit correlations

between multiple PID detectors.

5.5.4 Bayesian Method

While the $n\sigma$ approach provides a straightforward way to perform PID in a single detector, it does not fully exploit the combined capabilities of multiple detectors. A more powerful approach is the Bayesian method, which expresses the detector responses in terms of probabilities and folds them with the expected particle abundances (priors). This provides a statistically consistent framework for combining different PID signals and optimally identifying particles.[117]

Each detector α provides a raw signal S_α, such as the flight time t_{TOF} from the ToF detector or the specific energy loss dE/dx measured in the detector, e.g., STS. To make use of this signal, one defines a discriminating variable ξ that relates the measurement S_α to the expected detector response $R_\alpha(H_i)$ for a particle species H_i:

$$\xi_\alpha = f(S_\alpha, R_\alpha)\,, \tag{5.21}$$

where the response R_α depends on the momentum of the particles p, charge Z, and the length of the track L.

For a detector with an approximate Gaussian response, the deviation of the measured signal from the expectation for a given species H_i is expressed as the $n\sigma$ variable:

$$n\sigma_\alpha^i = \frac{S_\alpha - \hat{S}_\alpha(H_i)}{\sigma_\alpha^i}\,, \tag{5.22}$$

where $\hat{S}_\alpha(H_i)$ is the expected mean signal and σ_α^i is the resolution.

The conditional probability that a particle of species H_i will produce a signal S_α in detector α is then

$$P_\alpha(S_\alpha|H_i) = \frac{1}{\sqrt{2\pi}\,\sigma_\alpha^i} \exp\left[-\frac{1}{2}\left(n\sigma_\alpha^i\right)^2\right]. \tag{5.23}$$

For detectors with non-Gaussian response, $P_\alpha(S_\alpha|H_i)$ is obtained from an appropriate parameterization of the response function.

When combining information from several independent detectors, the joint probability is simply the product of the single-detector probabilities:

$$P(\vec{S}\,|H_i) = \prod_\alpha P_\alpha(S_\alpha|H_i)\,, \tag{5.24}$$

where $\vec{S} = (S_{\mathrm{TOF}}, S_{\mathrm{STS}}, S_{\mathrm{TRD}}, \ldots)$ is the vector of signals from the available detectors.

The quantity of real interest is the probability that a track belongs to a species H_i given the measured set of signals $\vec{S}$. This is the *posterior* probability, obtained by Bayes' theorem:

$$P(H_i|\vec{S}) = \frac{P(\vec{S}\,|H_i)\,C(H_i)}{\sum_k P(\vec{S}\,|H_k)\,C(H_k)}\,. \tag{5.25}$$

Here, $C(H_i)$ denotes the *prior probability* (i.e. the expected abundance of species H_i in the physics sample), while $P(H_i|\vec{S})$ is the *posterior probability* that the track corresponds to particle type H_i.

In practice, priors can be obtained either from external measurements or from the data sample itself using iterative methods. When all priors are taken equal, the Bayesian PID reduces to a likelihood-based identification.

The Bayesian approach offers several advantages for CBM:

- It allows different PID detectors with Gaussian and non-Gaussian responses to be combined in a unified way.
- It maximizes the separation power in momentum regions where the responses of different species overlap in a single detector.
- It incorporates prior knowledge of particle yields, thereby improving identification in physics analyses where abundances are known or can be constrained.

This makes the Bayesian method the most powerful PID strategy for CBM, ensuring robust $\pi/K/p$ separation across the full acceptance when combining the ToF, STS (dE/dx), TRD, and RICH responses.

The mass-squared representation shown in Figure 5.24 provides an alternative view of the same information. Here, particles group along horizontal bands at their respective m^2 values, allowing direct identification of $\pi^{\pm}$, $K^{\pm}$, and $p/\bar{p}$. The $\pm 2\sigma$ fit drawn around the theoretical positions demonstrates the selection windows typically applied for PID. The plots clearly show that the CBM-ToF detector achieves excellent separation of pions, kaons, and protons up to a few GeV/c, beyond which the m^2 bands overlap and the identification capability gradually diminishes. With the $\pm 2\sigma$ fit, we can segment the kaons to pions up to 3.0 GeV/c and the Proton to Kaons up to 5.5 GeV/c momentum range.

The distribution of $1/\beta$ versus momentum, shown in Figure 5.25, illustrates the principle of velocity-

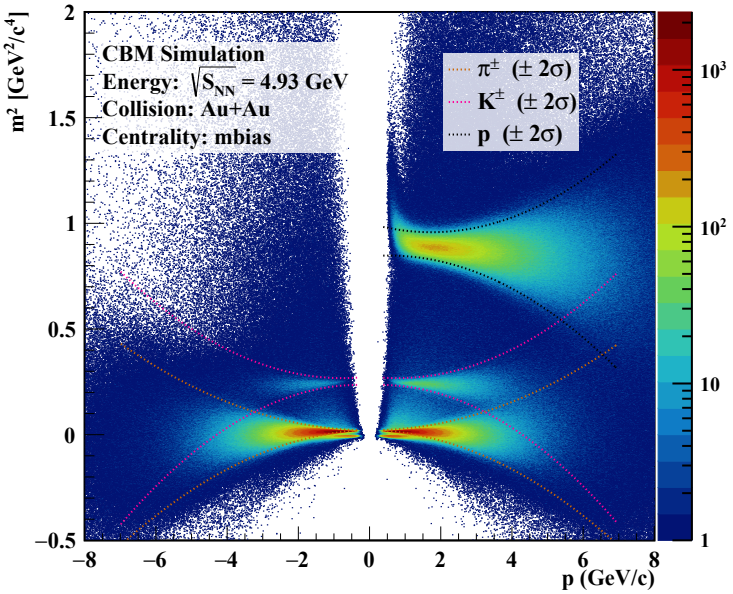

Figure 5.24: Mass-squared (m^2) distribution as a function of momentum, calculated from the time-of-flight and track length. Bands corresponding to pions, kaons, and protons are visible and match the expected positions. The dotted curves represent $\pm 2\sigma$ fit selection windows for each particle species.

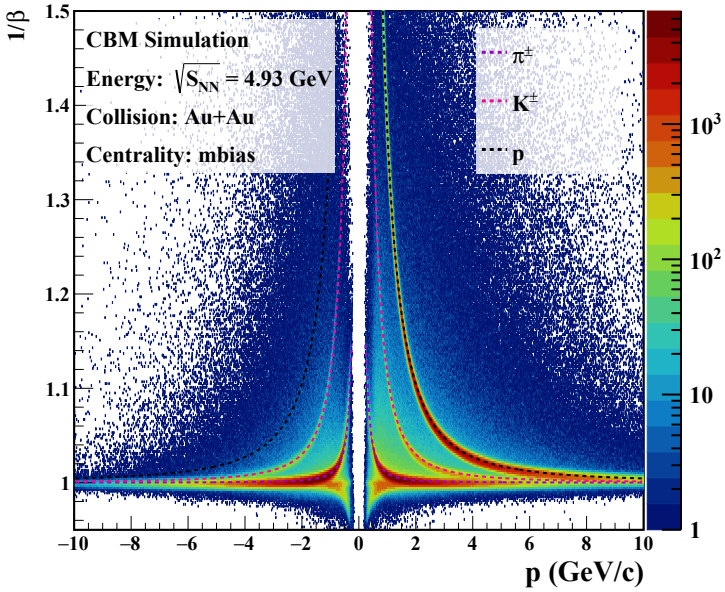

Figure 5.25: Inverse velocity ($1/\beta$) as a function of momentum reconstructed from ToF measurements. The dashed curves indicate the expected positions of $\pi^{\pm}$, $K^{\pm}$, and $p/\bar{p}$. Distinct bands are observed, which converge at higher momenta where $\beta \to 1$, reducing the separation power.

based particle separation. At low and intermediate momenta, the characteristic curvature of the bands allows a clear distinction between pions, kaons, and protons. The separation originates from the mass dependence of $\beta = p/\sqrt{p^2 + m^2}$, which produces well-separated $1/\beta$ values at the same momentum for different particle species. As the momentum increases, all species approach the speed of light, $\beta \simeq 1$, and their $1/\beta$ values converge toward unity. Consequently, the discrimination

power of ToF measurements diminishes in the high-momentum region.

Quantitatively, the ToF detector provides π/K separation up to about 3.0 GeV/c and K/p separation up to roughly 5.5 GeV/c, in agreement with the performance seen in the m^2 representation. Together, the $1/\beta$ and m^2 plots confirm the high-quality PID capabilities of the CBM-ToF system across the low- and mid-momentum ranges.

5.5.5 Particle Identification with STS using Energy Loss

While the CBM experiment relies primarily on dedicated PID detectors such as the Time-of-Flight (ToF) detector, the Silicon Tracking System (STS) itself can also provide complementary identification capability by exploiting the specific energy loss (dE/dx) of charged particles in the silicon sensors.[118, 119] This information is particularly valuable in several cases:

- low-momentum particles that do not reach the downstream detectors,
- particles decaying inside the STS volume, and
- nuclei with the same m/Z ratio (e.g. deuterons and ^{4}He), which cannot be distinguished by ToF measurements alone.

For the present study, the dE/dx response of the STS was simulated for Au+Au collisions at beam momentum 12 AGeV/c using 10^6 events generated with the PHQMD[5] model.[120] A realistic detector response was assumed, including an equivalent noise charge (ENC) of 1000 e and a discriminator threshold of 4000 e. Each reconstructed track in the STS consists of at least three hits, with each hit composed of two clusters, thus providing multiple independent measurements of the deposited charge along the track trajectory. The energy loss per unit length is obtained by normalizing the cluster charge to the effective path length in the silicon sensors, $\Delta x = \frac{320\ \mu\text{m}}{\cos\theta}$, where θ is the angle between the particle momentum and the normal to the sensor plane.

To mitigate the effect of electronic saturation, clusters where the deposited charges exceeding the dynamic range of the STS-XYTER ASIC (15 fC) are excluded, since if the charge in a given channel exceeds 15 fC (overflow), the energy loss measurement for the entire cluster cannot be relied on. Finally, the mean energy loss, $\langle dE/dx \rangle$, is then calculated as the median of the per-hit values, which improves robustness against fluctuations from Landau tails.

[5] Parton-Hadron-Quantum-Molecular Dynamics

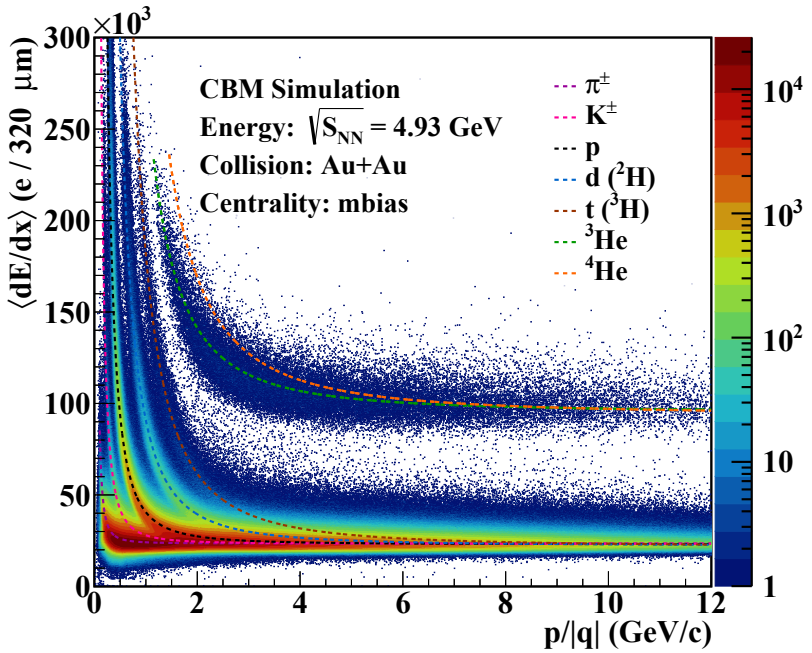

Figure 5.26: Specific energy loss $\langle dE/dx \rangle$ (normalized to 320 µm) as a function of momentum-to-charge ratio $p/|q|$, reconstructed with the STS from PHQMD-simulated Au+Au collisions at beam momentum 12 AGeV/c. The dashed curves indicate the expected Bethe-Bloch dependence for different particle species.

Figure 5.26 shows the $\langle dE/dx \rangle$ vs momentum-to-charge ratio $p/|q|$. Distinct Bethe-Bloch fit bands are visible for $\pi^{\pm}$, $K^{\pm}$, p, d, t, ^{3}He, and ^{4}He over a momentum range extending up to 12 GeV/c. At low momenta, a clear separation between singly and doubly charged particles is achieved, and isotopic separation of the hydrogen family (d, t) is possible up to $\sim$ 2.5 GeV/c. For helium isotopes, the separation remains effective over the entire measured range. The only limitation arises at low momenta for heavy ions, where the deposited charge saturates the dynamic range of the read-out ASICs, and overflows are frequent.

In summary, this proof-of-concept study demonstrates that the STS can provide valuable complementary particle identification via dE/dx. The method ensures robust separation of light hadrons and nuclei in the low- to mid-momentum region. It is particularly promising for reconstructing rare signals, such as light hyper-nuclei. It is therefore expected to play an essential role in the CBM software framework as a PID tool alongside ToF and other dedicated detectors.

Chapter Summary

- In this chapter, at the beginning, we discussed the STS detector acceptance and efficiency for all particles within the STS detector performance through simulation, which shows that the STS detector efficiency remains at approximately 97%.

- The hit reconstruction efficiency performance was carried out through time-based simulation, where events from both the UrQMD and beam sources were sampled. It reveals the impact of beam events containing only $\delta-$electrons on the upstream stations, due to the low-energy delta electrons bending under the magnetic field and taking an oblique path, which causes them to concentrate in a localized area of the detector plane. We observed a drop in hit reconstruction efficiency for the detector modules located in that region of the detector plane. Additionally, there is a drop in efficiency for modules near the beam pipe across all STS stations, attributed to high-p_T particles, event pile-up, and dead time.

- Next, we carried out the threshold-dependent and dead-time-dependent hit reconstruction efficiency studies for the STS detector individually for each STS station, as well as the average efficiency, by varying the threshold and dead time. It shows that the overall efficiency stays $\geq 97\%$ at ENC 1000 e and threshold 4000 e with a dead time of 200 ns, while a slight drop in efficiency ($\sim 1-2\%$) is observed at ENC 1000 e, threshold 9000 e, and dead time of 200 ns. The dead-time-dependent hit reconstruction efficiency at ENC 1000 e and threshold 4000 e demonstrates that at a detector dead time of 200 ns, the efficiency remains $\geq 97\%$, while at a dead time of 800 ns, it drops slightly to about 95%.

- The cluster characterization of the STS detector indicates that the cluster size across all stations remains around 2, and the cluster charge, as expected theoretically for the 320 μm sensor, is roughly 25,600 e in the case of the UrQMD source. However, the cluster size for the beam source is slightly larger ($\sim 3-4$) at the upstream stations near the target. It gradually decreases at downstream stations, because most of the delta electrons are deflected by the magnetic field. In addition, as they move toward the downstream detectors, they are absorbed. In addition, the cluster charge for beam events is higher compared to UrQMD events, which is due to their longer travel path in the detector plane, since the number of electron–hole pairs is directly proportional to $1/\cos\theta$.

- Moreover, we discussed the particle identification of various species using the STS and TOF. It shows that we can achieve π/K separation up to about 3.0 GeV/c and K/p separation up

to roughly 5.5 GeV/c within a 2σ fit.

- At the end, we discuss the particle identification using the STS itself, based on energy loss. It shows that the STS can reconstruct light hypernuclei above 2 GeV/c. STS is capable of separating singly and doubly charged particles in the low-momentum range.

Chapter 6

Summary

The Compressed Baryonic Matter (CBM) experiment at the Facility for Antiproton and Ion Research (FAIR) aims to explore the QCD phase diagram at high net-baryon density. Operating with beam momentum energies from 2 to 12 AGeV/c, CBM accesses regimes of dense nuclear matter characterized by baryochemical potentials of $\mathcal{O}$(800–500)MeV, and temperatures of $\mathcal{O}$(60–120)MeV. The physics program includes the high-statistics measurement of rare probes, the search for the critical point, studies of first- and second-order phase transitions, the restoration of chiral symmetry in the given phase space range through differential analysis and measurement of dilepton spectra, collective flow, and event-by-event fluctuations of net-proton and net-charge, etc as in detail outlined in **Chapter 1**.

To achieve these goals, CBM will operate with a continuous nucleus beam in a free-streaming, triggerless data-taking mode at interaction rates up to $\mathcal{O}$(10)MHz. In this mode, detector signals are continuously read out, and online event selection and reconstruction are performed in real-time. This innovative approach allows the detection of rare probes and short-lived particles with a high statistical precision, providing unprecedented insight into the properties of strongly interacting matter at high baryon densities.

Two complementary tracking subsystems provide precise vertexing and tracking in the CBM experiment. The Micro-Vertex Detector (MVD), based on Monolithic Active Pixel Sensor (MAPS) technology featuring the *"MIMOSIS"* chip, is optimized for high-precision tracking and vertex reconstruction of short-lived particles. Downstream of the MVD is the Silicon Tracking System (STS). It is the main tracking system for primary and secondary charged particles and provides momentum measurements under the magnetic field.

The STS, once conceptualized and prototyped, is now transitioning from its embryonic state to its physical realization, with full detector assembly expected by the end of 2027. It comprises eight tracking stations located inside the dipole magnet, housing a total of 876 double-sided silicon micro-strip sensors of four variants, arranged on lightweight support structures (see Figure 2.3 and Figure 2.5). It is designed to handle thousands of charged-particle tracks per event in nucleus-nucleus collisions. It plays a key role as a tracking system, ensuring precise momentum and charged-particle track reconstruction, while coping with the highest interaction rates foreseen for CBM at FAIR. To meet all these stringent requirements, the STS detector has a low material budget, in the active physics acceptance area ($2.5^{\circ} < \eta < 25^{\circ}$, from a target position), ranging roughly between 0.3% - 1.5% per Station layer. It has a momentum resolution ($\Delta p/p$) $\approx \leq 1.5\%$ for the primary particle up to particle momentum 8 GeV/c and for the secondary charged particle $\leq 2\%$ till momentum range 7 GeV/c as already mentioned in the **Chapter 2**.

Detector Geometry

A central component of this work is the detailed implementation of the detector geometry, including both the active sensor material and the complex arrangement of passive structures such as support frames, cooling components, cabling, and readout infrastructure. The geometry model has been developed to ensure that the material budget, acceptance, and spatial configuration are reproduced with high fidelity.

In addition, an alternative approach to constructing the detector simulation geometry has been explored, involving direct conversion from CAD to ROOT. The method requires converting the CAD's STEP[1] file into a ROOT[2]-readable format, primarily a GDML[3] file. Using the mSTS detector as a test case, employing the CAD-to-ROOT workflow, and successfully converting the mSTS geometry, the mSTS geometry is prepared by reading the GDML file and storing it in the ROOT format. Once the geometry is composed, we perform a simulation using GEANT4, an event transport engine, with typical UrQMD-generated events to assess runtime performance and compare it with the mSTS geometry, built from primitive solids.

It was observed that the event run-time increases in the case of tessellated solid-based geometry compared to primitive solid-based geometry, as discussed in **Chapter 2**, **Section 2.4**. Moreover,

[1] Standard for the Exchange of Product Model Data
[2] ROOT is a software framework for high-energy physics
[3] Geometry Description Markup Language

the different physics processes and secondary particle production have also been performed and compared against the reference geometry. Our observation from the comparison is that both geometry variants produce almost the same trend, with little to no difference. Therefore, based on this study, we conclude that tessellated solid-based geometry is an efficient and reliable method for incorporating complex detector volume structures and hardware modifications, as well as facilitating fast testing. However, for large-scale simulation data production, simplified geometry composed of primitive solids is preferable due to their lower computational overhead. Hence, it is a practical approach to employ tessellated solid-based geometry during the detector design, optimization, and validation phases, and then switch to a simplified detector geometry once the design is finalized.

Data Rates: Comparison data-simulation with mCBM Experiment

As mentioned earlier, the data acquisition will be in free-streaming mode at an interaction rate of $\mathcal{O}$(10 MHz), along with the STS detectors' requirements. Therefore, the system must be tested under real experimental conditions. For this purpose, to test the experiment under realistic conditions with a beam, small detector prototypes of all detector subsystems have been tested in the mCBM experiment at GSI, using the in-house SIS-18 accelerator facility. The SIS-18 provides a beam of various heavy nuclei in a range of 1-2 AGeV/c. The test of the entire sub-detector system, including its electronic hardware, as well as free-streaming data-taking, online reconstruction, and event-selection software, has been ongoing since 2018.

The mini-Silicon Tracking System (mSTS), a small-scale prototype of the entire STS, is currently under testing at the mCBM experiment. It hosts 3 tracking stations, built with 12 silicon microstrip sensors of different sizes along with the data readout electronics, to be commissioned in the final STS detector for its data rate capability. The data collected in 2024 were used to analyze the signal and noise rate performance for each sensor, and a comparison with the simulation presented and discussed in **Chapter 3**.

The data collection in 2024 for run Id 2984 was performed with the Ni beam at 1.93 AGeV and a Ni target of 0.4 cm thickness. The beam intensity, estimated by the BMON detector, placed upstream of the target, was $\sim$ 717 kHz. The beam interaction probability of the Ni ion beam with the Ni target of the given thickness was $\sim$10%.

Therefore, simulated data were produced with the same experimental conditions. The simulation data include Ni-Ni collision events generated with UrQMD at 1.93 AGeV/c and beam-background

events for δ-electrons, transported through the detector using the GEANT4 event transport engine. After the event transport, the next step in digitization was to process the detector response in time-based mode, setting the ENC and discriminator threshold values for each sensor to mimic the simulation conditions, as in the experiment. The time-based digitization models signal by sampling hit sources according to a Poisson distribution, consistent with the assumed interaction rate. The Rice formula determines the noise-related trigger rate and depends on the effective ENC and discriminator threshold, as well as the zero-frequency values used to generate the noise. The noise is produced at a constant rate for the entire time window during the digitization stage.

A detailed, module-by-module comparison of channel rates between data and simulation was performed by separating the measured mSTS data into off-spill periods—containing only electronic noise—and in-spill periods, which include noise, hadronic, and beam–target interactions. The off-spill data were used to benchmark the simulated noise. While for most modules the measured noise rates agree with the simulated Rice-formula noise band, some sensors show under- or overestimation, likely due to threshold dispersion or temperature-dependent variations in leakage current that shift the noise pedestal. The typical dark-rate range of 0.4 (minimum) – 1.4 (maximum) kHz per channel confirms that noise occupies only about 1% of the available bandwidth. For the physics contribution, in-spill minus off-spill data were compared with simulations that included hadronic and beam–target interactions. In this background-subtracted comparison, the agreement is excellent, as the noise contribution is negligible relative to particle-induced hits. Quantitatively, the average per-channel rate for the $n-$side is 2.23 kHz in data versus 2.01 kHz in simulation (10% deviation). In comparison, for the $p-$side it is 2.92 kHz in data versus 2.03 kHz in simulation (30% deviation). Overall, the study demonstrates that the simulation reproduces the physical hit rates with high fidelity, whereas remaining discrepancies are confined mainly to the noise modelling of a few specific modules.

Data rates: Expectations in STS @ CBM

Similarly, the data rate study for the Silicon Tracking System was conducted via simulation and discussed in **Chapter 4**. In this case, we have used the events generated by the UrQMD model for minimum-bias Au+Au collisions at the highest beam momentum (12 AGeV/c) foreseen for the CBM experiment. We have also generated the beam-background for $\delta-$electrons events transported through the detector using the GEANT4 transport engine, considering the beam-target interaction probability roughly $\sim 1\%$. Once the event transport step was completed, the subsequent digitization

of the detector response was performed in time-based mode at an UrQMD event rate of 10^7 events/s and, for beam-background, 10^9 events/s at the highest interaction rate.

During the digitization stage, we have considered two scenarios as follows,

- **First:** In this case, we applied the ENC and discriminator threshold value 1000 e and 4000 e (4σ), respectively, to all 876 silicon sensors.
- **Second:** In this case, we calculated the ENC values for each sensor to be used in the STS detector based on the characteristics of the module (sensor strip length and attached micro-cable length) and its corresponding 4σ discriminator threshold.

The data rate per channel obtained for each case was compared to determine the number of ASICs required for different uplinks.[4] Upon the comparison of the per-channel rate obtained for sensors' individual settings of ENC and discriminator threshold value, we have observed that a small fraction of ASICs count shifted from the lowest band (single uplink) to higher rate bands(two or five uplinks) compared to the global setting with ENC = 1000 e and threshold = 4000 e as shown in the Table 4.6. The difference in the highest total rate per channel observed for an individual setting and between the global setting is $\approx 9\%$ and is limited to a small number of ASICs. This suggests that the signal and noise rates expected in the STS detector remain within the designed readout bandwidth and rate capacity.

The STS detector uses three types of Front-End Boards (FEBs), denoted FEB8, distinguished by the number of uplinks: one, two, or five. FEB type is assigned based on the rate expected in that module.

Physics Performance of the STS

Ultimately, in **Chapter 5**, we discuss the physics performance of the entire STS detector, providing key performance parameters, such as acceptance, hit and tracking efficiencies, spatial hit resolution, and momentum resolution across the relevant phase space.

First, we show the STS detector efficiency vs polar acceptance, which indicates that the STS as a stand-alone detector has an efficiency $\geq 95\%$ over the range $5^\circ < \theta < 25^\circ$. Additionally, the hit reconstruction efficiency was evaluated for the entire STS detector and for each sensor in its

[4] The rate bands are $[0, 73)$, $[73, 146)$, and $[146, 367)$ kHits/s per channel, corresponding to ASICs equipped with 1, 2, and 5 uplinks, respectively, based on the nominal link bandwidth.

respective station at different threshold and dead-time settings. We have observed that the average hit reconstruction efficiency for the entire STS, with an ENC of 1000 e and dead time of 200 ns, remains $\sim$ 97.5% at a discriminator threshold value of 2000 e and drops to 94% at a threshold of 9000 e. Similarly, the hit reconstruction efficiency, with an ENC of 1000 e and a discriminator threshold of 4000 e, at a dead time of 200 ns, stays roughly 97% while it drops to a $\sim$ 95% at a dead time of 800 ns.

Following this, the track reconstruction efficiency of the STS detector was evaluated. For all particles, above $p \geq 1$ GeV/c, an efficiency of 97% is calculated, while if evaluated separately for primary and secondary particles, a calculated efficiency stays $\sim$ 98% and $\sim$ 93% respectively.

In addition, the performance of cluster characterization is studied. For particles produced in hadronic interactions (UrQMD) the typical cluster size is 2, while for all other beam-target interactions (typically EM interactions producing $\delta-$electrons), the typical cluster size is $\sim$ 4 in the first STS station and decreases to $\sim$ 3 as we move towards the STS stations located downstream. This is due to the $\delta-$electrons, which bent under the magnetic field and crossed the detector plane at a higher incident angle. Furthermore, we have also discussed the relationships between cluster size and the inclination angle, as well as between cluster charge and other factors.

Moreover, the hit space resolution of the STS is studied with hit residuals, i.e., with the difference between the Monte Carlo position of the point and the position of the reconstructed point. It yields a resolution of approximately 10μm, consistent with the 58μm pitch.

At the end of the thesis, we discuss the potential of the STS detector for particle identification applications. This would complement the Time-of-Flight (TOF) measurements with the TOF wall detector, which in the CBM experiment allows π/K separation up to about 3.0 GeV/c and K/p separation up to roughly 5.5 GeV/c. Using the measurement of $\langle dE/dx \rangle$, the STS could help separate particles with the same m/Z ratio, specifically the hydrogen family ($d(^2H), t(^3H)$), up to a momentum of 2.5 GeV/c. This is extremely useful for reconstructing hypernuclei.

In summary, the outcome of this thesis provides a baseline for the detector's key performance parameters, derived from realistic geometry and simulations that include all beam-target effects and noise. This work constitutes a key milestone for the STS, delivering its first performance evaluation within the full CBM setup.

Appendix

Appendix A

Material budget

The material budget of a detector element is usually expressed in units of radiation length X_0. For a pure element i, an approximate expression for the radiation length in mass units is given by

$$X_{0,i} \simeq \frac{716.4\, A_i}{Z_i\,(Z_i+1)\,\ln\!\left(\frac{287}{\sqrt{Z_i}}\right)} \quad [\mathrm{g/cm^2}] \tag{A.1}$$

where Z_i and A_i denote the atomic number and atomic mass of the element, respectively.

Dividing by the mass density ρ_i yields the radiation length

$$X_{0,i}^{(\mathrm{len})} = \frac{X_{0,i}}{\rho_i} = \frac{716.4\, A_i}{Z_i\,(Z_i+1)\,\ln\!\left(\frac{287}{\sqrt{Z_i}}\right)\,\rho_i} \quad [\mathrm{cm}] \tag{A.2}$$

For a compound or mixture, the radiation length is obtained as the weighted sum of the individual contributions:

$$\frac{1}{X_0^{\mathrm{mix}}} = \sum_i \frac{w_i}{X_{0,i}} \tag{A.3}$$

where w_i is the mass fraction of component i in the material. A detailed discussion of these formulas is given in **Chapter 2**.

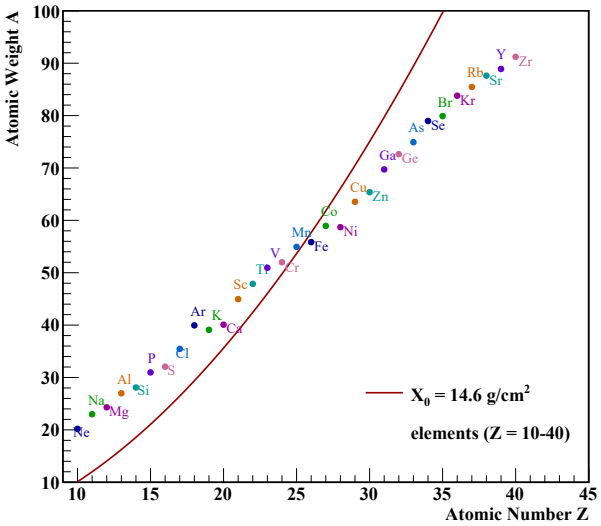

Figure A.1: Analytically finding the atomic number Z and atomic mass A, once the radiation length is known based on the Equation A.1.

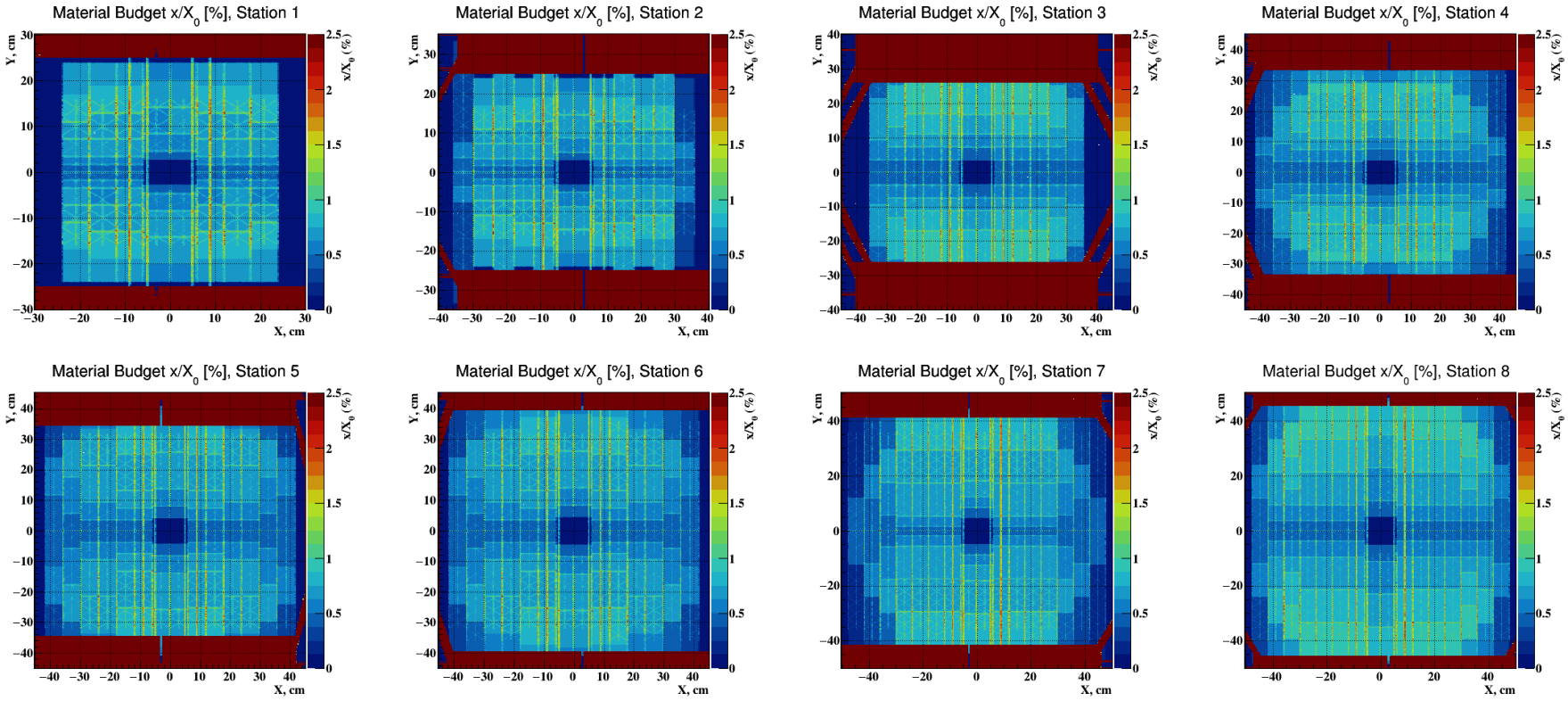

Figure A.2: Material budget histogram for all STS stations. To illustrate the active components' material budget, the Z-axis range was limited to 2.5%.

Appendix B

mSilicon Tracking System: Digi Distribution

In this section, we present the experimentally measured digis channel distribution for each silicon sensor used in the mSTS experiment (Ni-Ni collision, @ 1.93 AGeV, $\sim$ 717 kHz rates). The distribution shown in the Figure B.1 represents the In-spill - Off-spill digis and only the background as an Off-spill digis distribution.

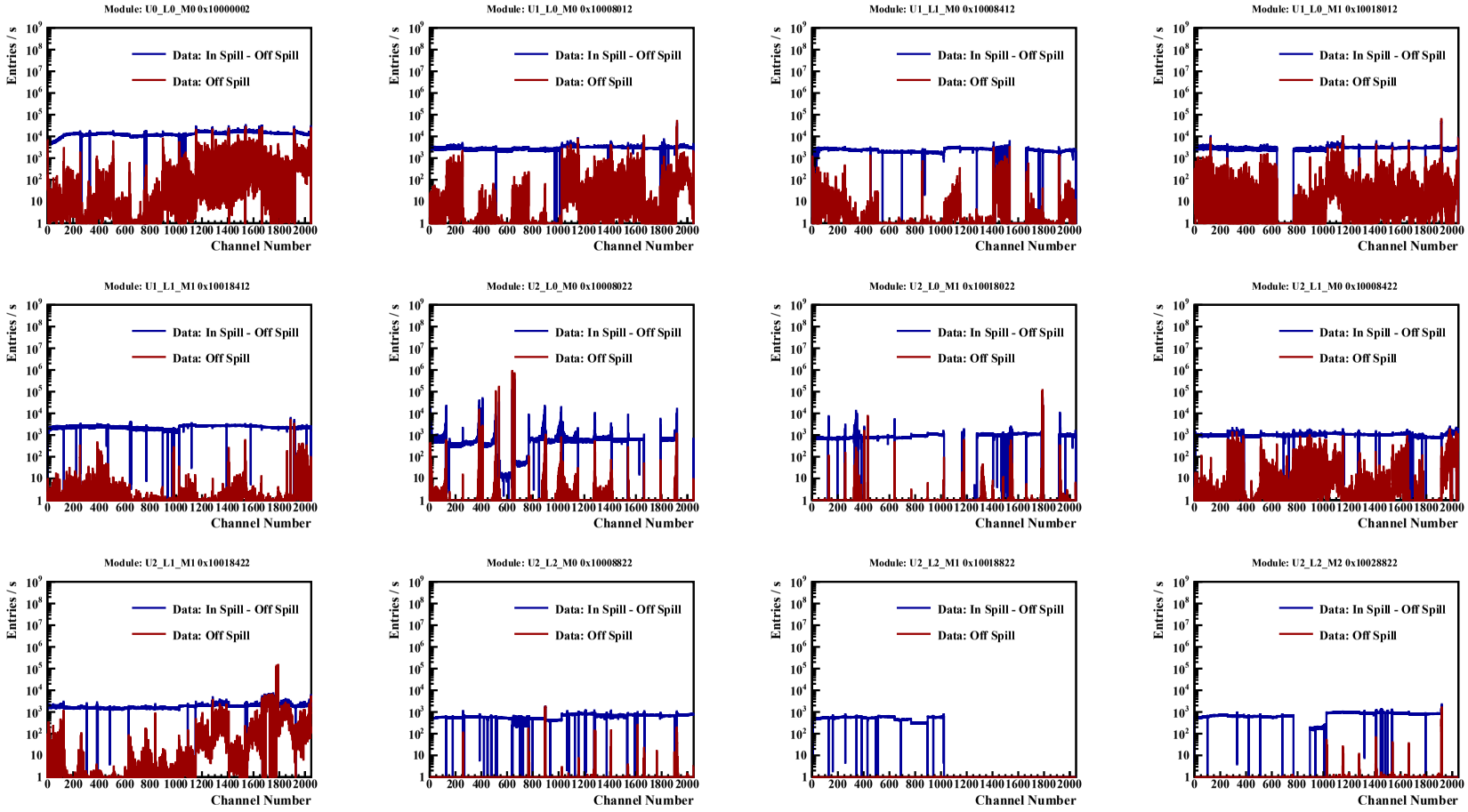

Figure B.1: Digi channel distribution together for (In-Spill-Off-spill) and for Off-Spill period for all the modules used in the mSTS experiment.

Figure B.2 shows the comparison of Off-Spill digi distribution from data and noise digis obtained through simulation.

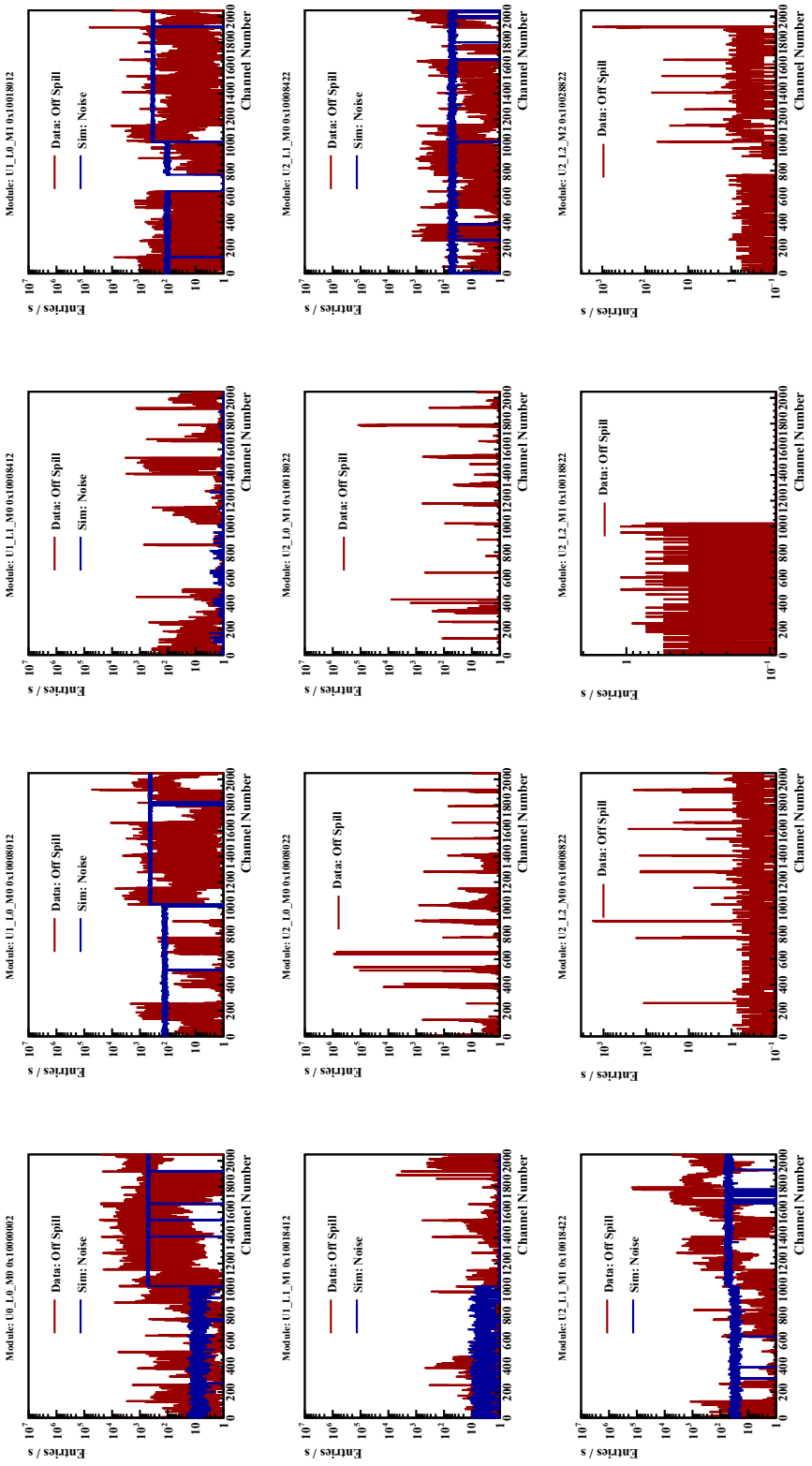

Figure B.2: Digi distribution of Off-Spill period for all the modules used in the mSTS experiment and Noise distribution obtained in the simulation when setting the ENC and threshold values used in the mSTS experiment.

Appendix C

Particle Interaction with Matter

The interaction of the beam with the target generates a variety of particle species, including photons, delta electrons, and others. These particles further interact with the detector material used in the simulation. Photon, an electromagnetic radiation, is a massless and chargeless particle that can interact with matter through various mechanisms, as outlined below:

- Photoelectric effect
- Compton scattering
- Pair production

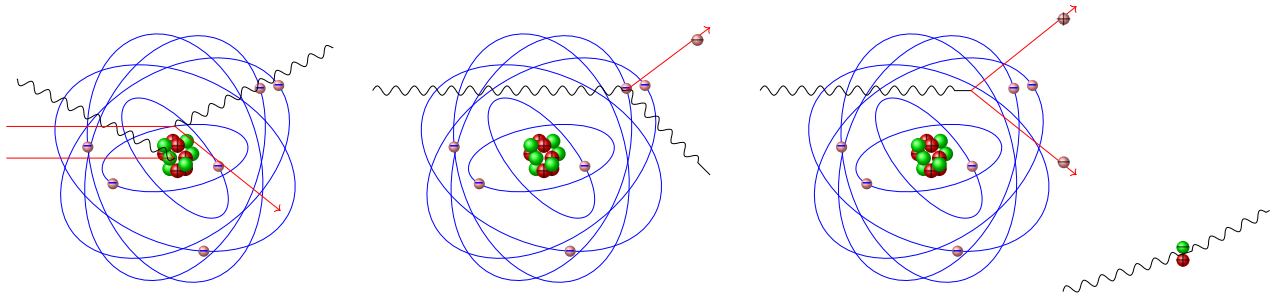

(a) Bremsstrahlung (b) Compton Scattering (c) Pair production (d) Annihilation

Figure C.1: Various Electromagnetic (EM) processes happen in matter

Figure C.1 depicts different Electromagnetic (EM) processes that happen during beam transport in GEANT4.

C.1 Photoelectric Effect

The simple and basic idea of the photoelectric effect is that when the photons impinge on the material, they are absorbed and subsequently emit electrons. The emitted electrons don't depend on light intensity but rather on its frequency. If the frequency is lower than a certain value, there is no electron emission.

$$E = \frac{hc}{\lambda} \tag{C.1}$$

Where, h = Planck constant, c = Velocity of light, λ = Wavelength

As we know, electrons are tightly bound with their respective atoms; therefore, we require such an amount of energy, which is higher than the bound energy, to get free from the atoms. This is known as a work function of the material. To have an electron emitted, we must have:

$$E \geq \phi \ , \upsilon \geq \frac{\phi}{h} \ , \lambda \leq \frac{hc}{\phi} \tag{C.2}$$

The maximum energy of the outgoing photo-electron is given by,

$$E_e = E - \phi \tag{C.3}$$

C.2 Compton Scattering

The scattering of an incident photon from a loosely bound electron or a free electron is known as Compton scattering. The following equation can be used to obtain the wavelength of the scattered photon.

$$\lambda = \lambda_0 + \frac{h}{m_e c}[1 - cos\theta] \tag{C.4}$$

where, λ and λ_0 are the wavelengths of the incident and scattered photons, respectively; m_e is the mass of an electron; and θ is the scattering angle.

C.3 Pair Production

For pair production to occur, the photon's energy must exceed the rest mass of the electron and positron, at least 1.022 MeV. The energy of the photon converts into the mass of the particle

according to the Einstein relation $E = mc^2$.

$$E_\gamma > 2m_e \tag{C.5}$$

$$\gamma + \text{nucleus} \rightarrow \text{e}^- + \text{e}^+$$

C.4 Delta Electron

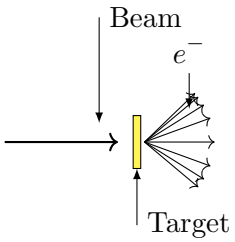

Figure C.2: Beam interaction with Au target.

Delta electrons are the secondary electrons knocked out of an atom when a beam interacts with a target.

C.4.1 Delta electrons: Theta distribution

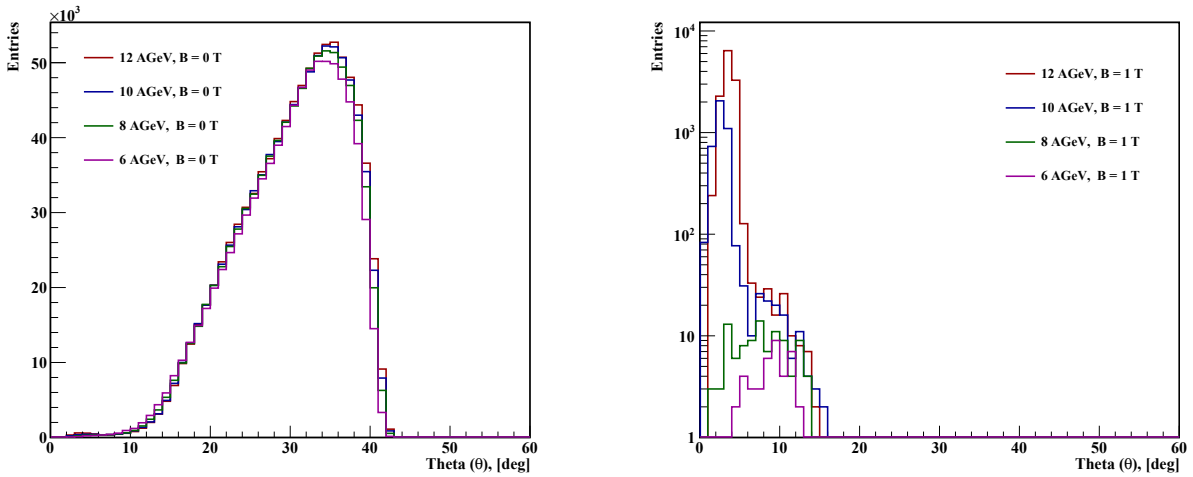

(a) Without magnetic field

(b) With magnetic field

Figure C.3: Comparison of the theta distribution of the delta electrons, with and without a magnetic field, for those MC track that has at least 1 MC point on the STS station.

Figure C.3 shows the theta distribution with and without a magnetic field at different beam energies, the MC tracks of the delta-electrons that have created at least 1 MC point in the STS station.

C.4.2 12 AGeV/c

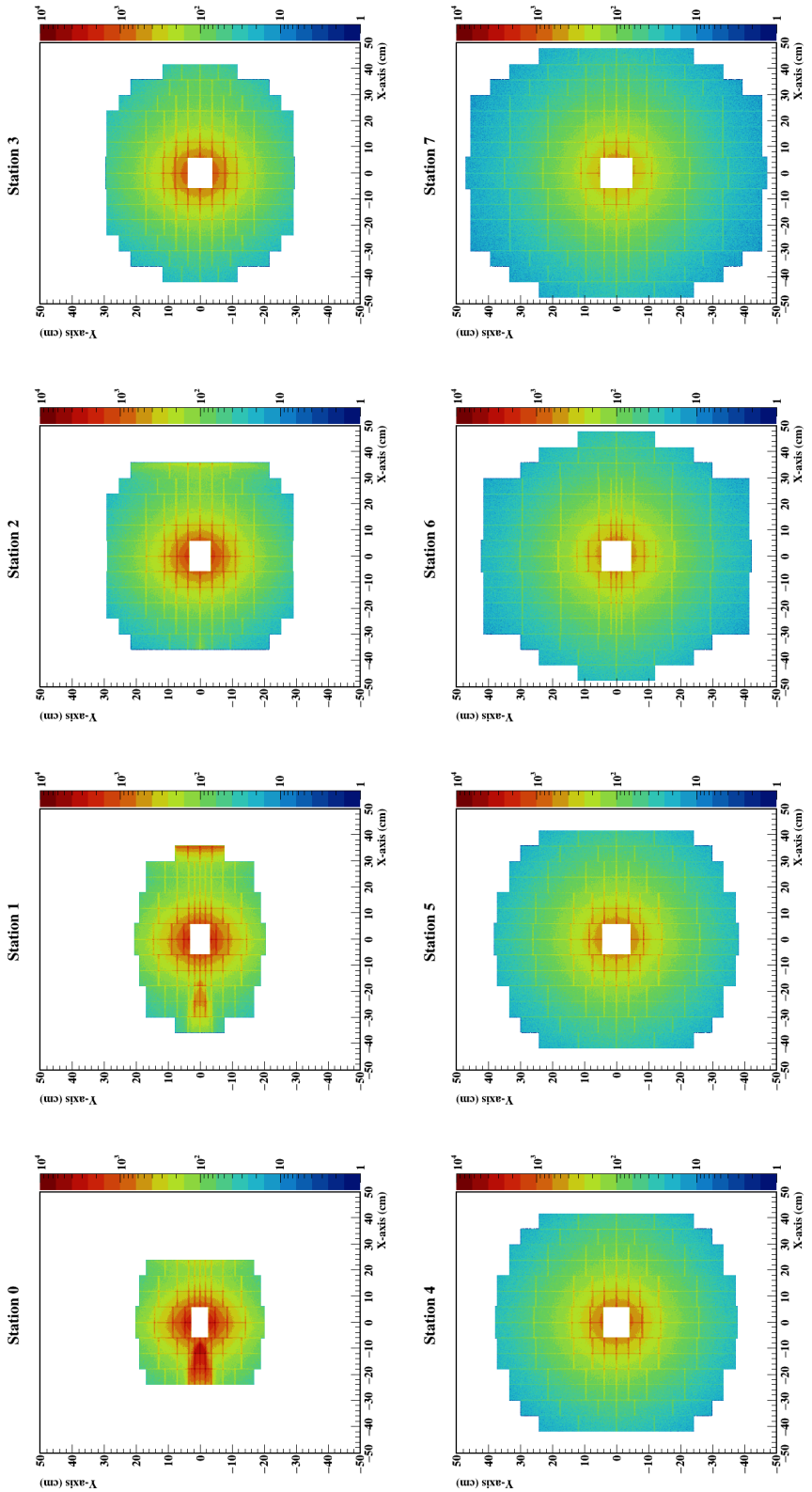

Figure C.4: Particle density distribution of UrQMD and Beam source at 12 AGeV/c at 1 T·m magnetic field.

C.4.3 10 AGeV/c

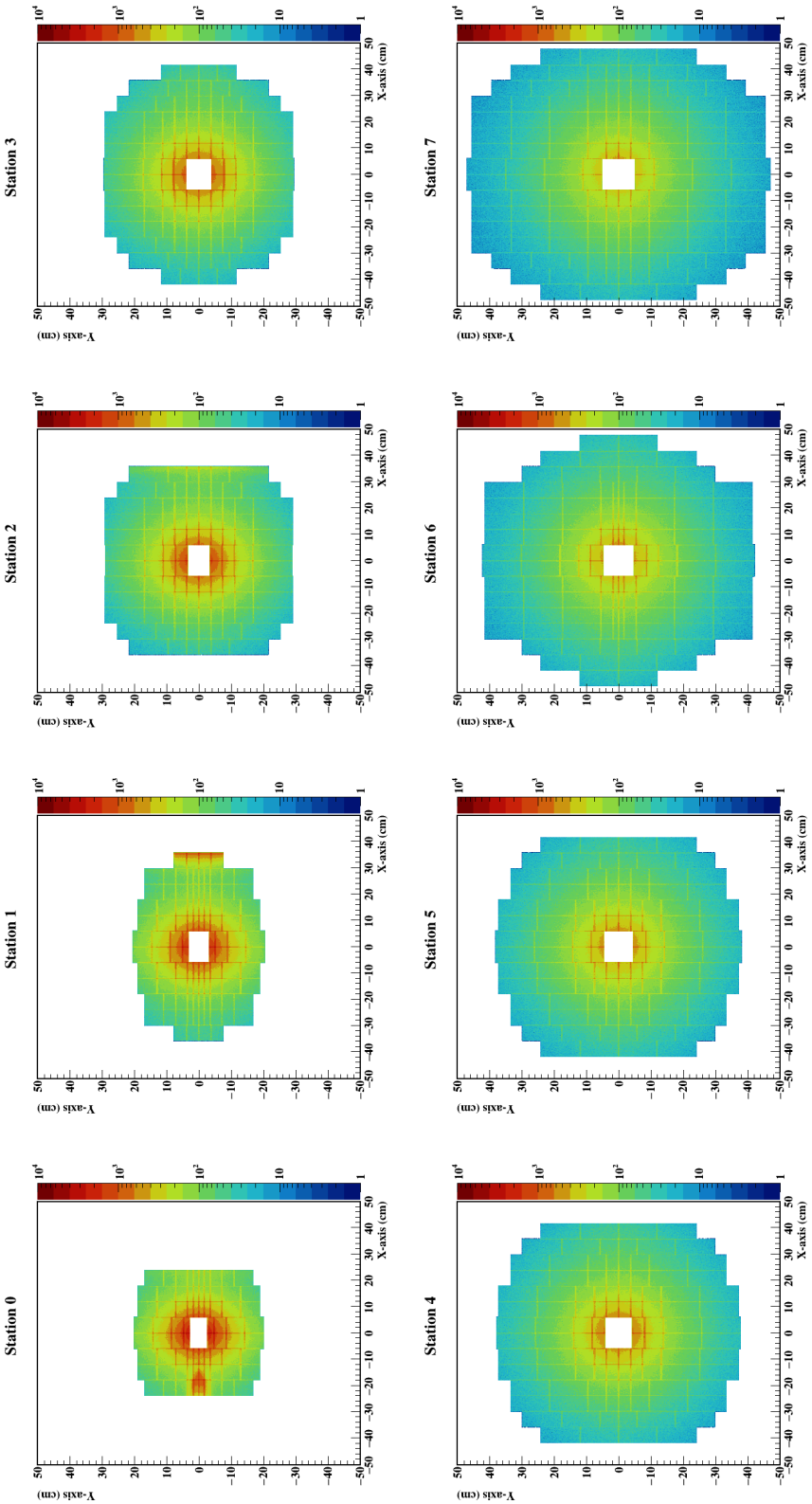

Figure C.5: Particle density distribution of UrQMD and Beam source at 10 AGeV/c at 1 T·m magnetic field.

C.4.4 8 AGeV/c

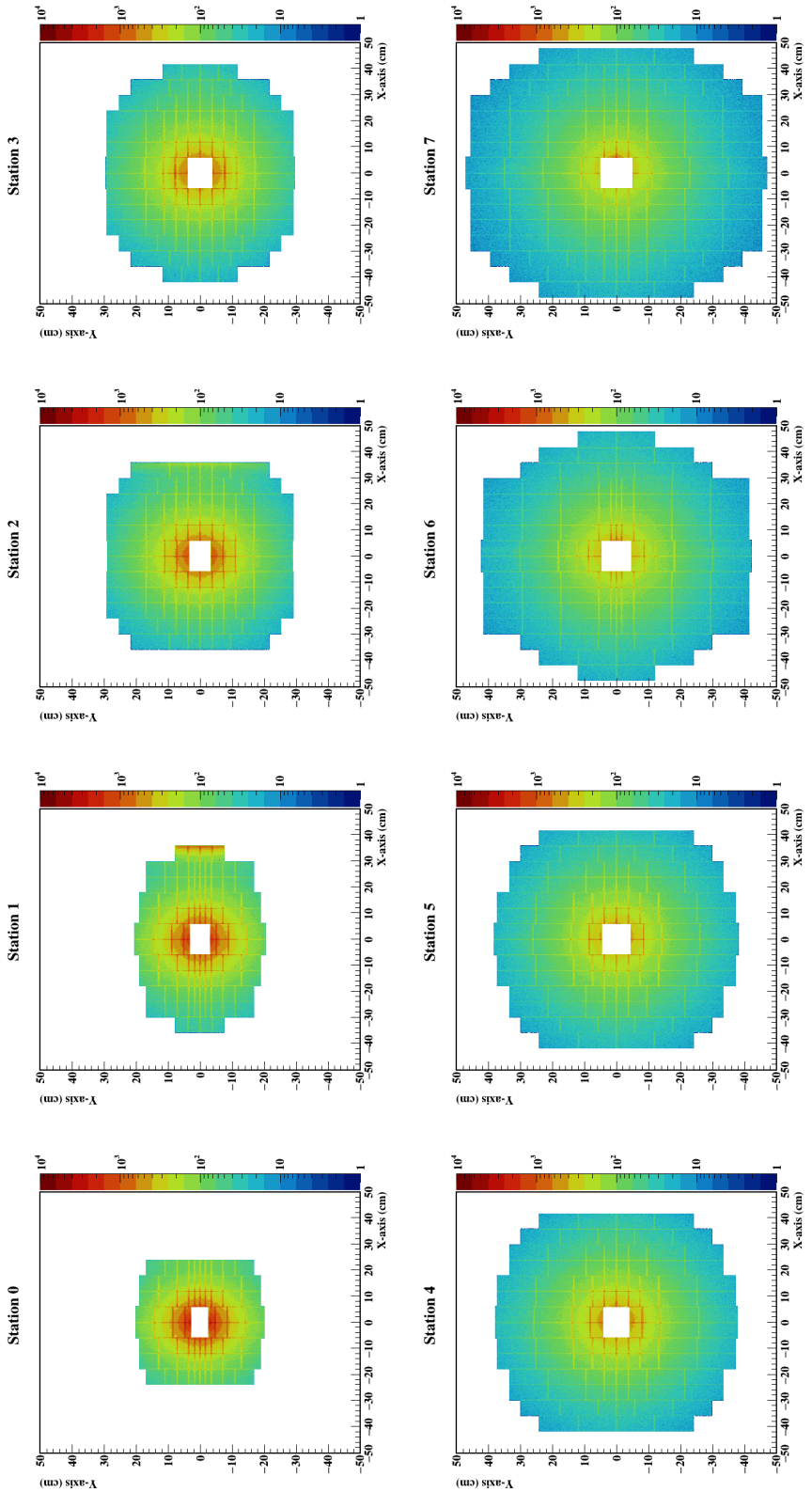

Figure C.6: Particle density distribution of UrQMD and Beam source at 8 AGeV/c at 1 T·m magnetic field.

C.5 Comparison of Geant3 and Geant4

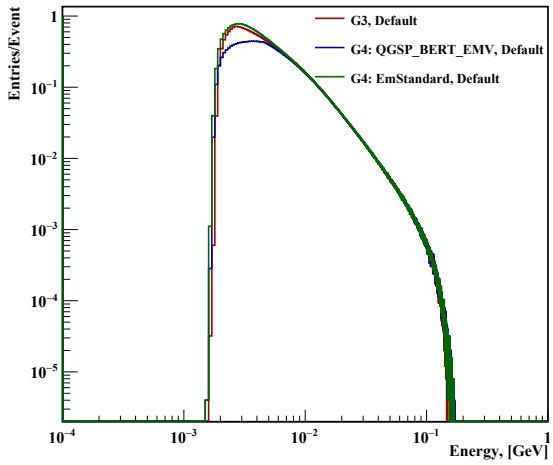

(a) Without magnetic field

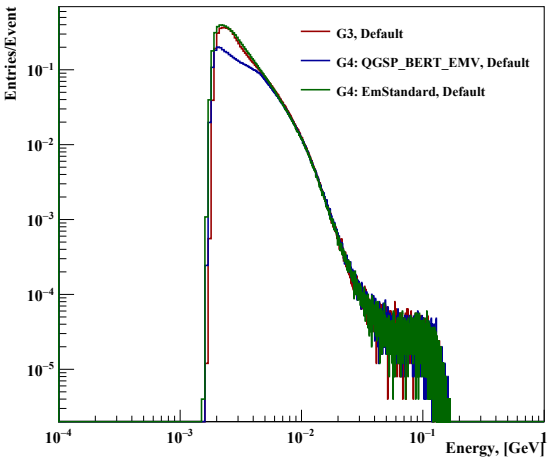

(b) Without magnetic field, at least one MC point

Figure C.7: Comparison of the energy distribution of the delta electrons, with and without a magnetic field, and GEANT3 vs GEANT4 for beam energy 12 AGeV.

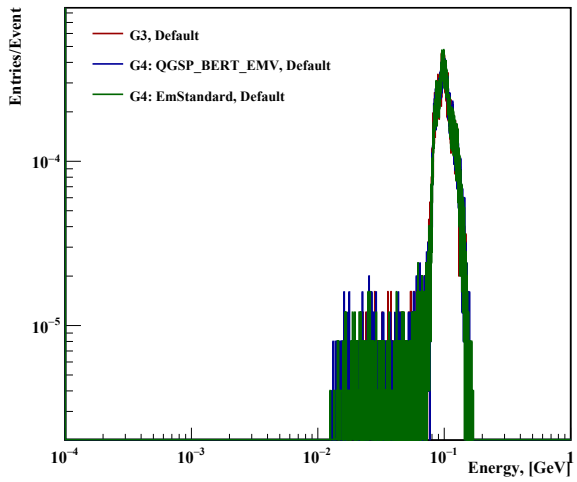

Figure C.8: With magnetic field

Figure C.7 represents the energy distribution of $\delta-$electrons originated from a target in beam-target interaction. Figure C.7a shows the energy distribution of delta-rays without a magnetic field and with the default setting[1] in CBM-ROOT. We observe that, at higher energy $\geq$ 0.006 GeV (6 MeV), in GEANT3 and GEANT4, different electromagnetic physics lists produce the same distribution. However, in GEANT4 with `EMV` physics list, there is a variation in the lower energy regime, compared to GEANT3, and in GEANT4 with `emStandard` physics list. This is because, in GEANT4, the `EMV` option is the faster EM physics list but is less optimized for lower-energy regimes. On the other hand, `emStandard` considers a more precise lower-energy regime and matches the GEANT3 spectra with less discrepancy at lower energies. Figure C.7b shows the same distribution but considering only those tracks that have created at least 1 MC point in the STS detector.

Figure C.8 illustrates the energy distribution of the delta-electrons that have been created at least

[1] In CBM-ROOT: In Geant3, a default energy cut of 1 MeV is being used. On the other hand, in GEANT4, there is a default 1 MeV cut along with a VMC range cut of 1mm, which is being used.

one MC point under the magnetic field at 12 AGeV. We observe that only delta tracks originating from a target with at least 10 MeV energy can reach the detector. Below that, the energy tracks bend under the magnetic field and go out of the acceptance.

Appendix D

STS Data rates

Expected maximum rate for each STS station via simulation at 12 AGeV/c at 10 MHz.

Data Rates (MB/s)				
Station	**Total**	**UrQMD**	**Beam**	**Noise**
0	114.778	28.31	106.57	0.202
1	67.12	22.66	62.97	0.196
2	30.84	25.62	24.82	0.245
3	23.22	21.23	3.99	0.202
4	20.08	18.12	4.67	0.199
5	18.58	16.52	3.41	0.1997
6	22.99	19.11	3.76	0.204
7	15.33	13.41	2.81	0.200

Table D.1: Maximum peak data rate for each STS detector station by setting ENC 1000 e and discriminator threshold 4000 e.

Data Rates (MB/s)				
Station	**Total**	**UrQMD**	**Beam**	**Noise**
0	126.11	30.91	117.27	0.198
1	74.098	24.62	69.65	0.20
2	32.49	27.21	26.12	0.253
3	24.46	22.35	4.181	0.200
4	20.75	18.71	4.695	0.201
5	19.22	17.09	3.366	0.204
6	22.92	19.03	3.743	0.205
7	15.582	13.61	2.83	0.206

Table D.2: Maximum peak data rate for each STS detector station by an individual sensor setting of ENC and discriminator threshold value.

The Table D.1 and Table D.2 show the expected maximum peak data rate from each source and in each STS station obtained through simulation at 10 MHz interaction rate with the highest beam energy (12AGeV/c).

The Table D.3 below shows the maximum data rate per channel for the global ENC and the discriminator threshold. In contrast, Table D.4 shows the maximum channel rate in the case of individual sensor ENC and threshold parameters.

Data Rates (MB/s)				
Station	**Total**	**UrQMD**	**Beam**	**Noise**
0	235.066	57.97	218.24	0.41
1	137.46	46.42	128.96	0.40
2	63.16	52.47	50.83	0.50
3	47.55	43.47	8.17	0.41
4	41.12	37.09	9.56	0.41
5	38.06	33.89	6.99	0.408
6	47.08	39.146	7.71	0.416
7	31.38	27.45	5.75	0.410

Table D.3: Maximum data rate (kHz) in a channel for each STS detector station by setting ENC 1000 e and discriminator threshold 4000 e.

Maximum Channel Data Rates (kHz)				
Station	**Total**	**UrQMD**	**Beam**	**Noise**
0	258.27	63.30	240.175	0.405
1	151.75	50.41	142.651	0.409
2	66.54	55.71	53.48	0.518
3	50.087	45.76	8.56	0.41
4	42.489	38.32	9.61	0.412
5	39.37	34.99	6.81	0.416
6	46.93	38.97	7.66	0.42
7	31.91	27.86	5.80	0.421

Table D.4: Maximum data rate (kHz) in a channel for each STS detector station by an individual sensor setting of ENC and discriminator threshold value.

In the following section, we present the rate distribution for each STS station, separately for each source.

D.1 Total Signal distribution at 12 AGeV/c

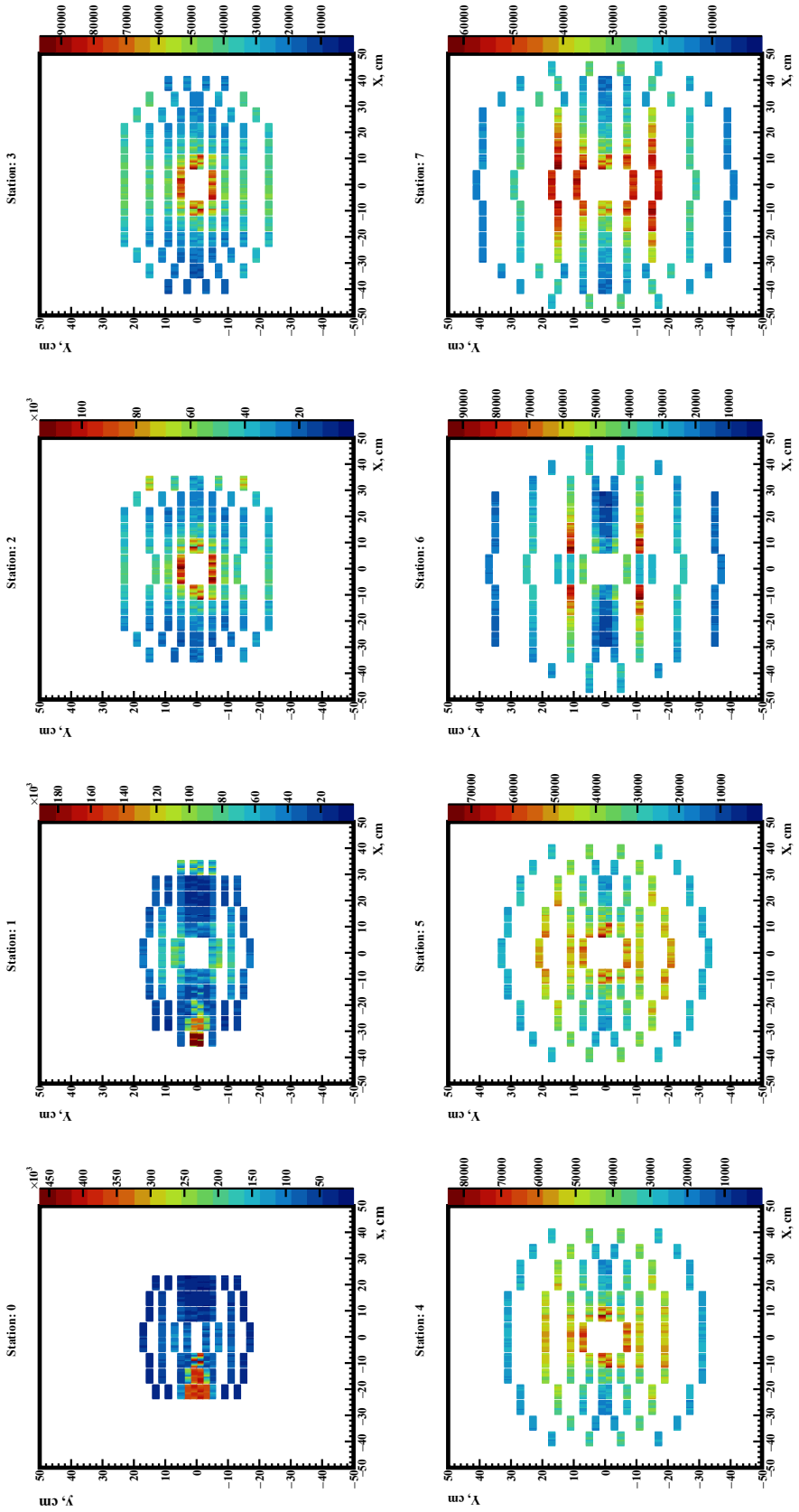

Figure D.1: Total Digi distribution of the signal registered from UrQMD, Beam, and Noise at the ENC 1000 e and discriminator threshold 4000 e. Each band represents the particular ASICs of the Sensor

D.2 UrQMD Signal distribution at 12 AGeV/c

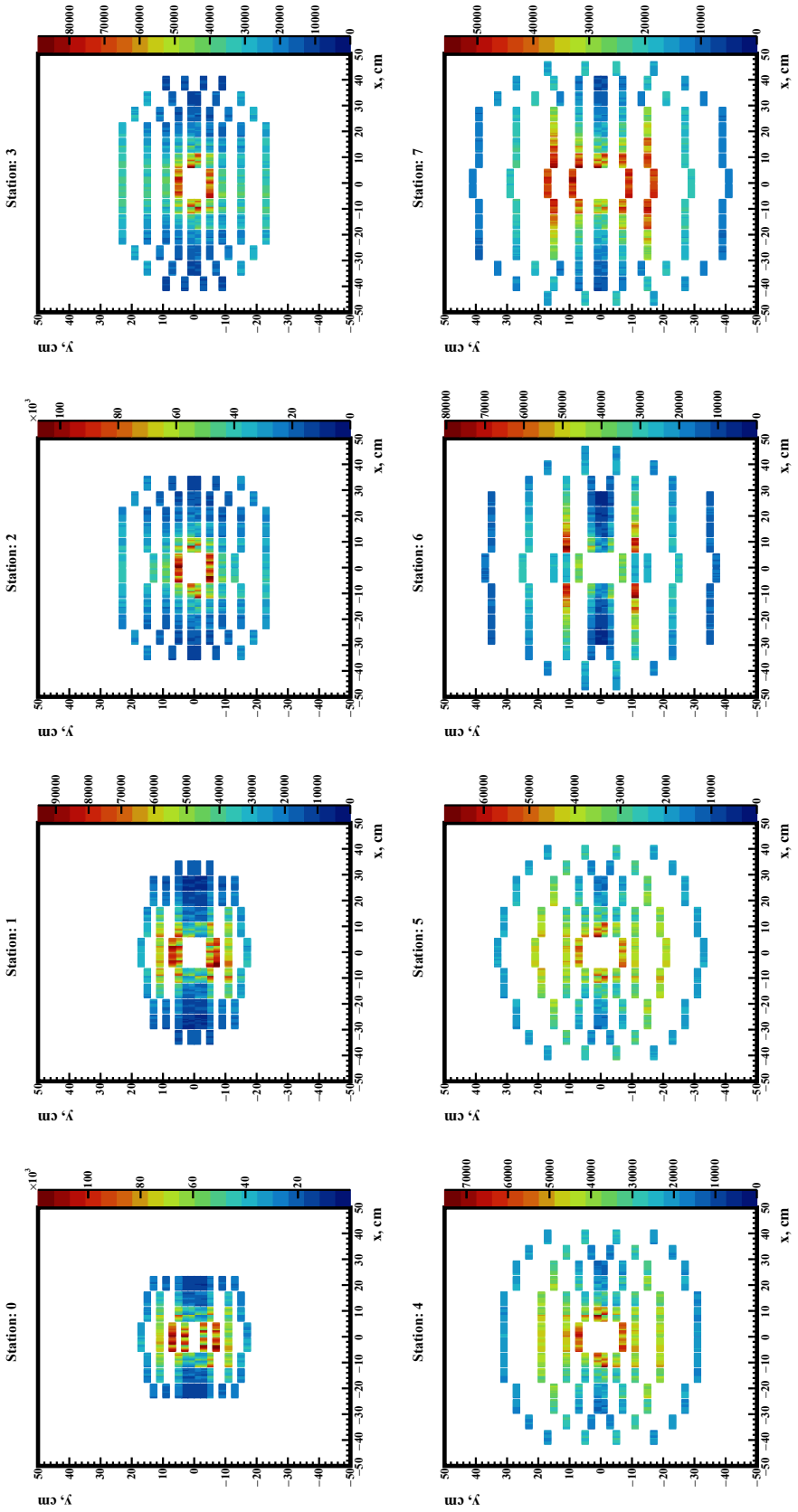

Figure D.2: Total Digi distribution of the signal registered from the UrQMD at the ENC 1000 e and discriminator threshold 4000 e. Each band represents the particular ASICs of the Sensor

D.3 Beam Signal distribution at 12 AGeV/c

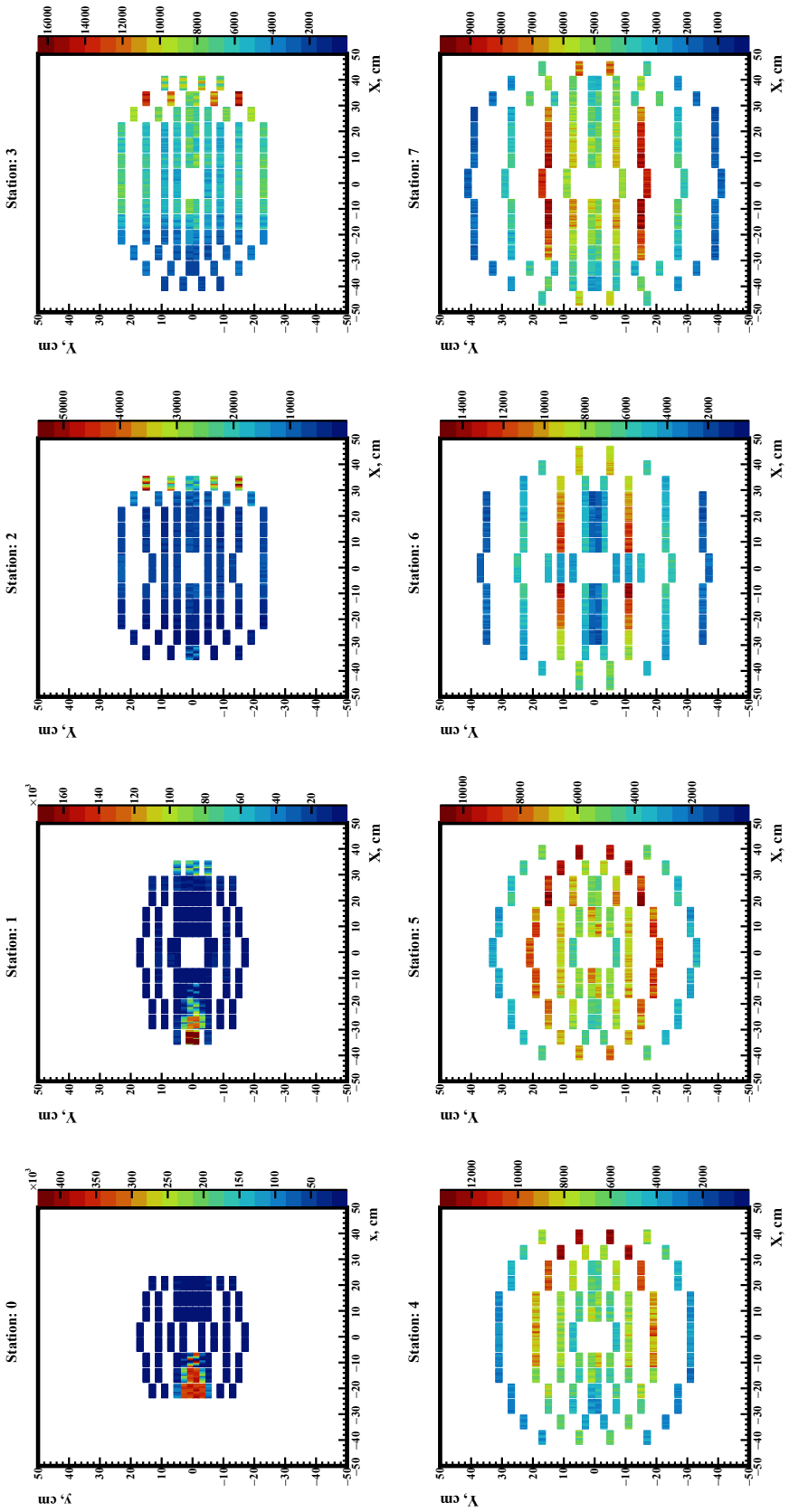

Figure D.3: Total Digi distribution of the signal registered from the Beam source($\delta-$electrons) at the ENC 1000 e and discriminator threshold 4000 e. Each band represents the particular ASICs of the Sensor

D.4 Noise Signal distribution at 12 AGeV/c

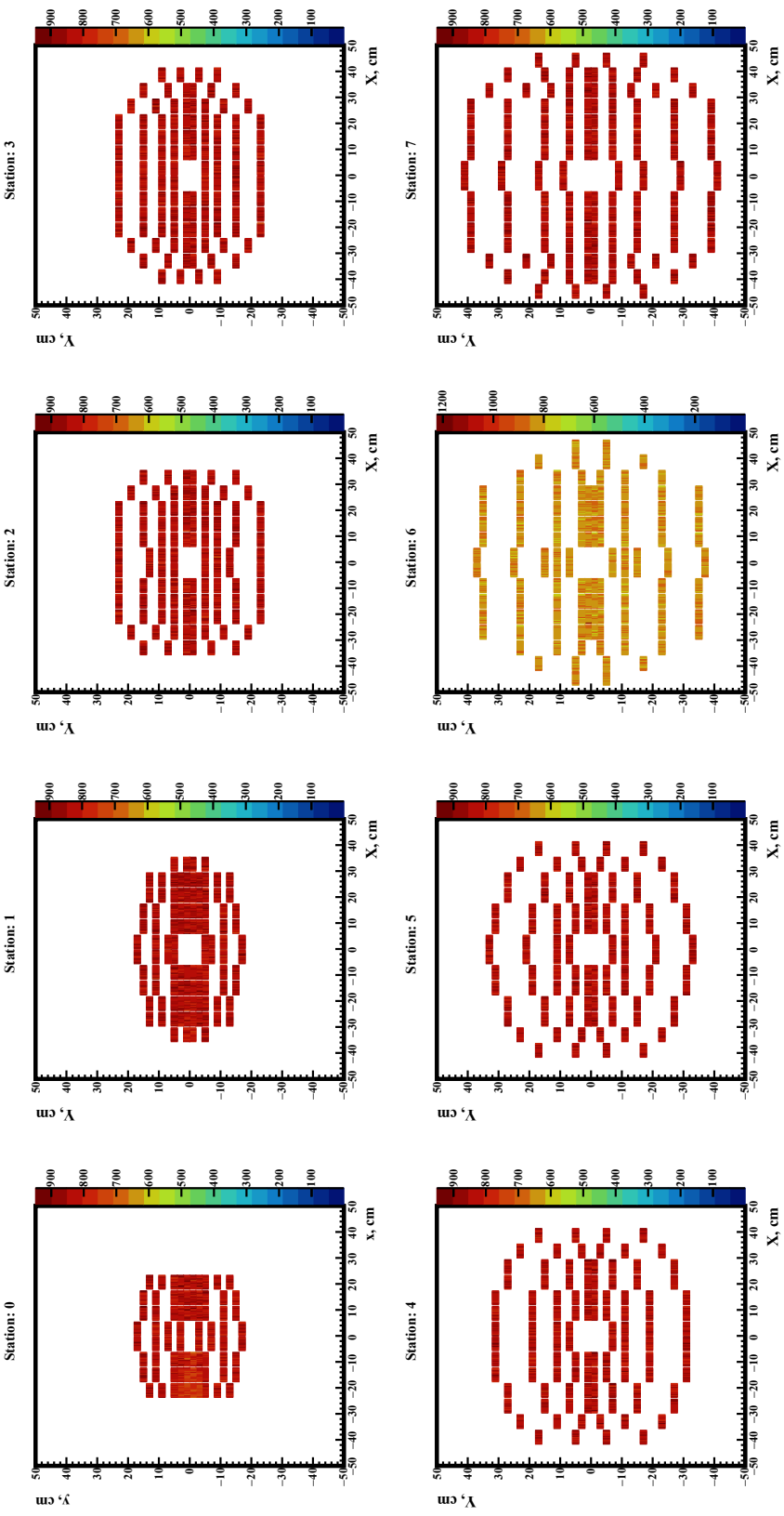

Figure D.4: Total Digi distribution of the signal registered from the Noise source at the ENC 1000 e and discriminator threshold 4000 e. Each band represents the particular ASICs of the Sensor

D.5 Total Signal distribution at 12 AGeV/c

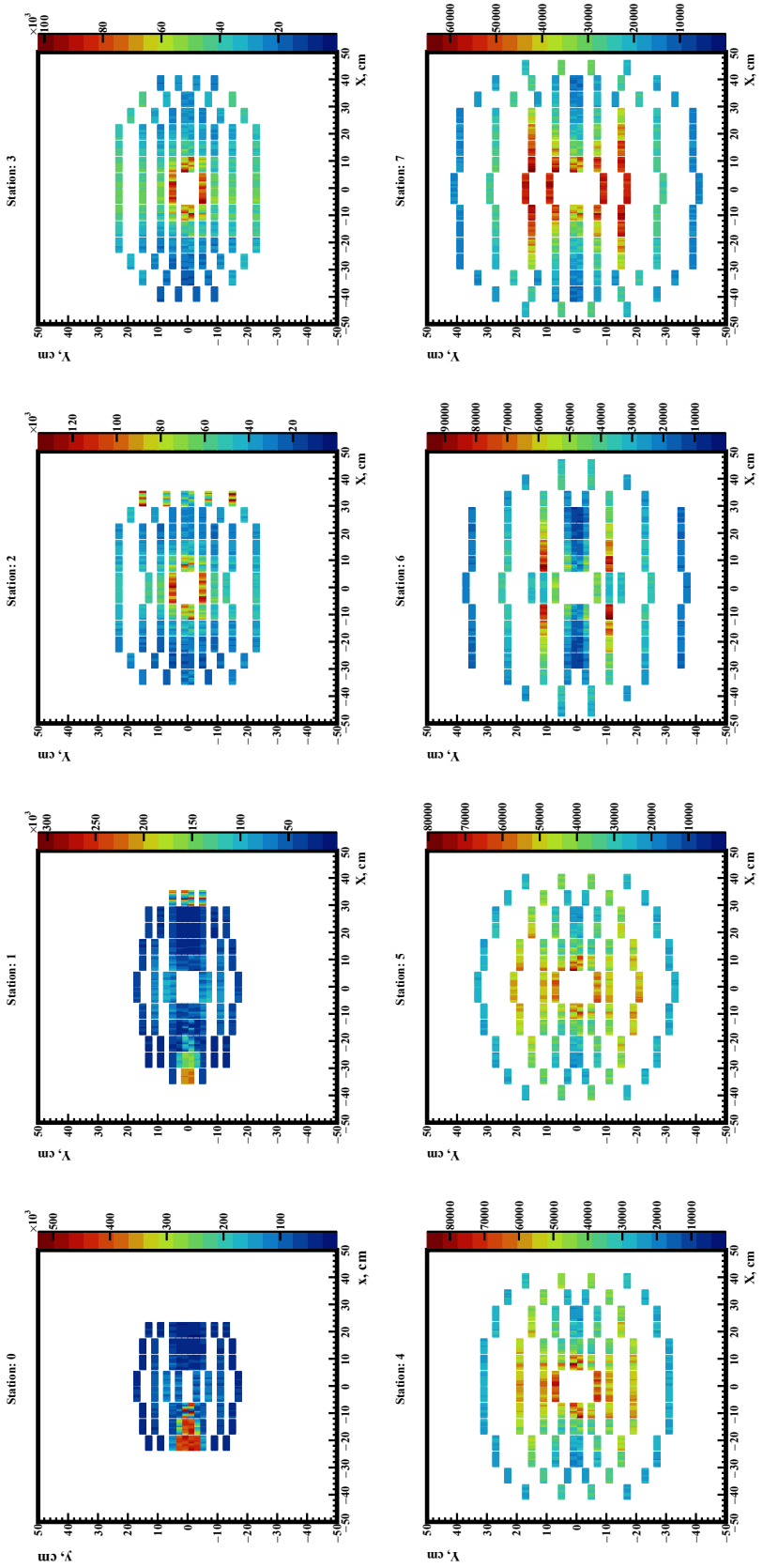

Figure D.5: Total Digi distribution of the signal registered from UrQMD, Beam, and Noise individual ENC and its corresponding (4σ) threshold value. Each band represents the particular ASICs of the Sensor

D.6 UrQMD Signal distribution at 12 AGeV/c

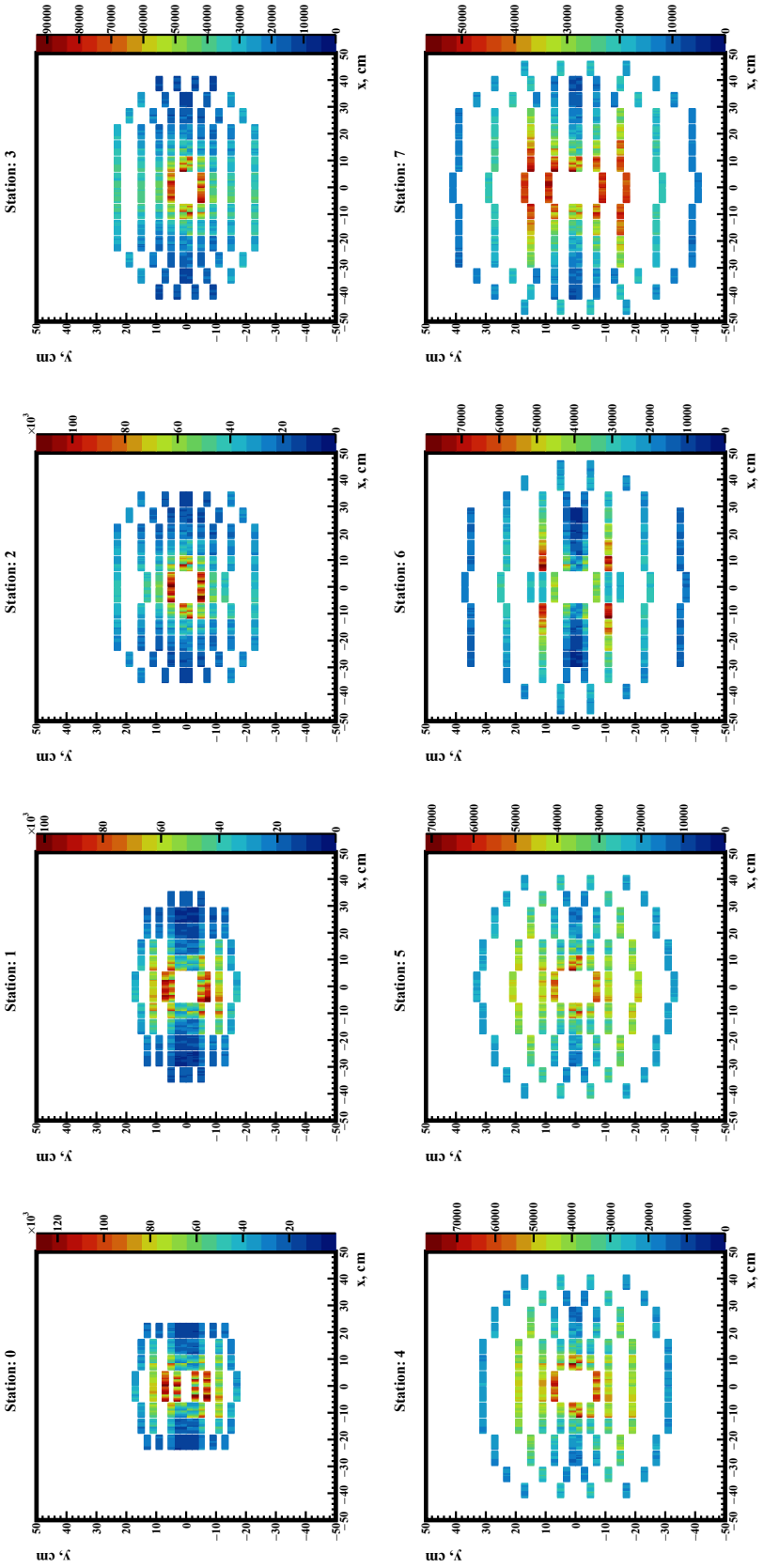

Figure D.6: Total Digi distribution of the signal registered from the UrQMD for individual ENC and its corresponding (4σ) threshold value. Each band represents the particular ASICs of the Sensor

D.7 Beam Signal distribution at 12 AGeV/c

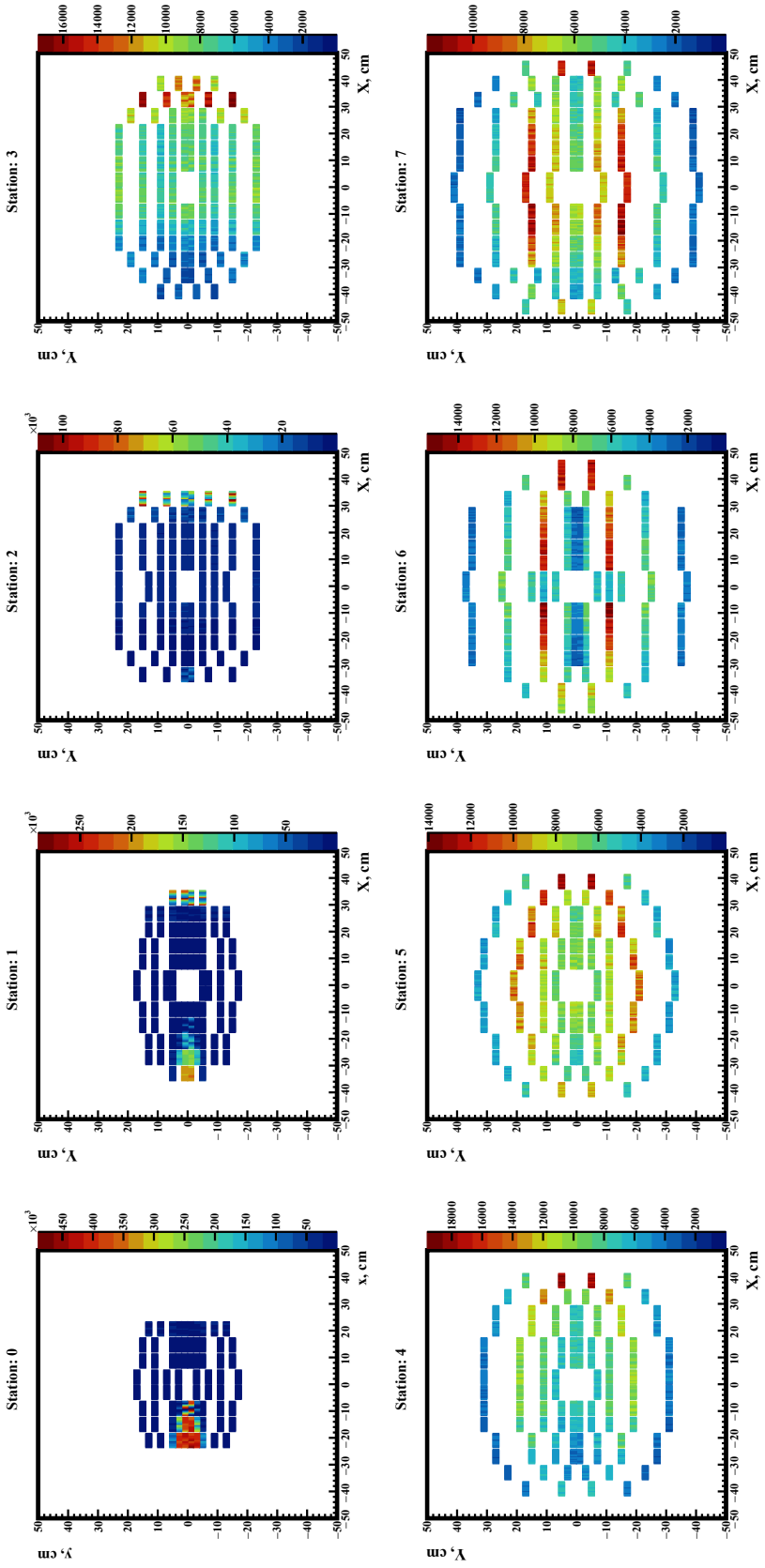

Figure D.7: Total Digi distribution of the signal registered from the Beam source($\delta-$electrons) for individual ENC and its corresponding (4σ) threshold value. Each band represents the particular ASICs of the Sensor

D.8 Noise Signal distribution at 12 AGeV/c

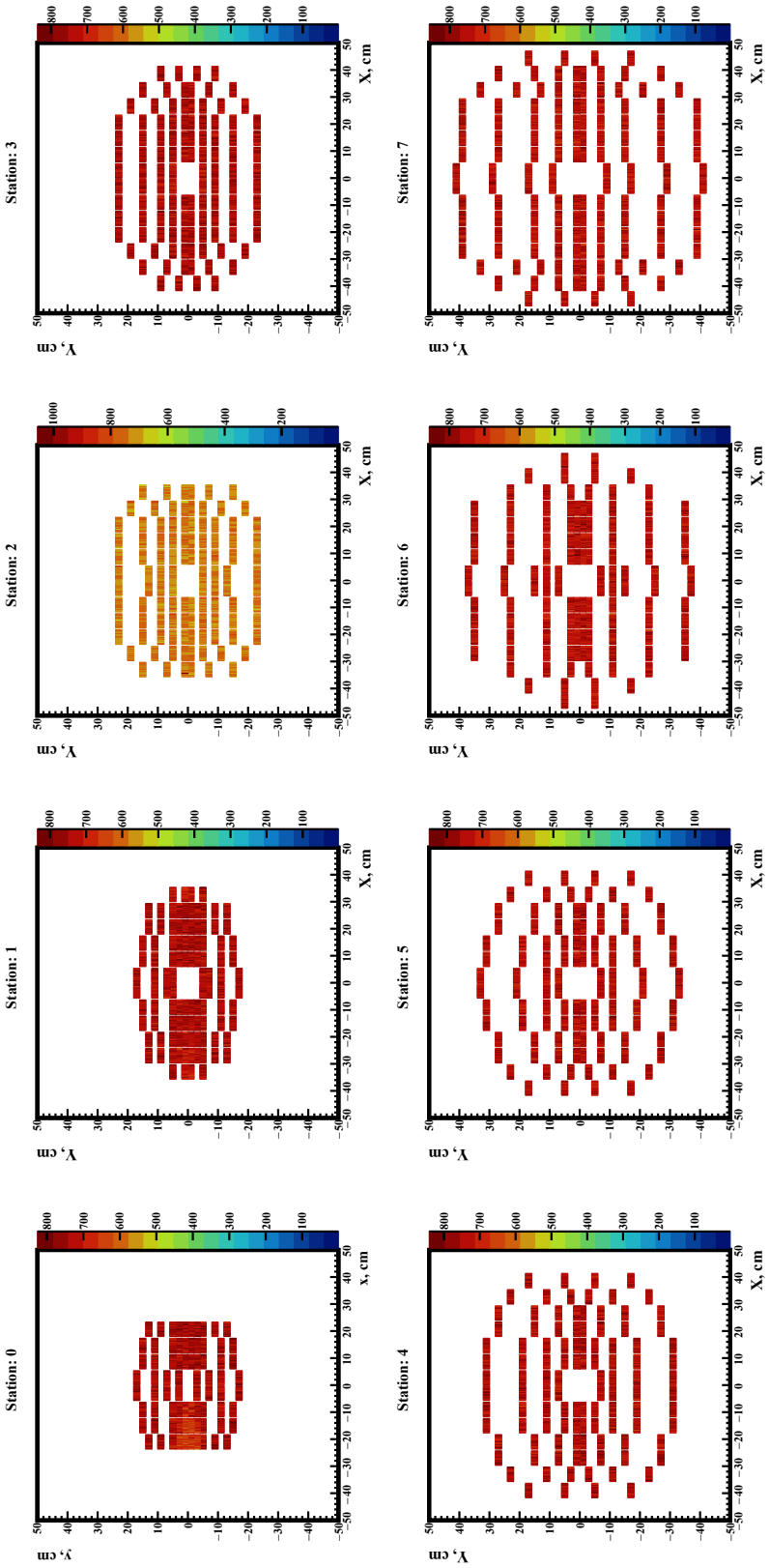

Figure D.8: Total Digi distribution of the signal registered from the Noise source for individual ENC and its corresponding (4σ) threshold value. Each band represents the particular ASICs of the Sensor

Appendix E

Charged Particle Multiplicity

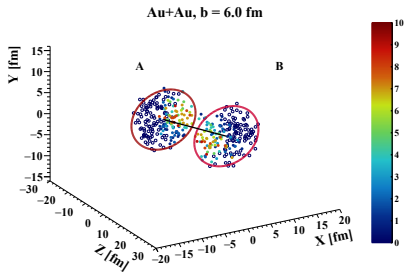

Figure E.1: Au+Au collision at 12 AGeV/c from a Glauber model at 6 fm.

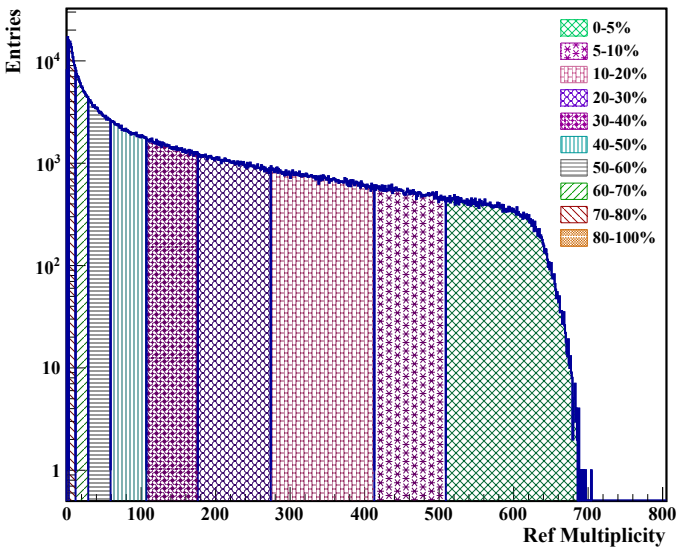

Figure E.2: Multiplicity distribution of charged particles for UrQMD model-based generated events of Au+Au interaction at 12 AGeV/c and classified into different centrality classes.

Appendix F

Detector Acceptance: Efficiency

To calculate efficiencies for individual particle species as a function of different physics observables, a loose selection criterion was applied, requiring tracks to contain at least three hits.

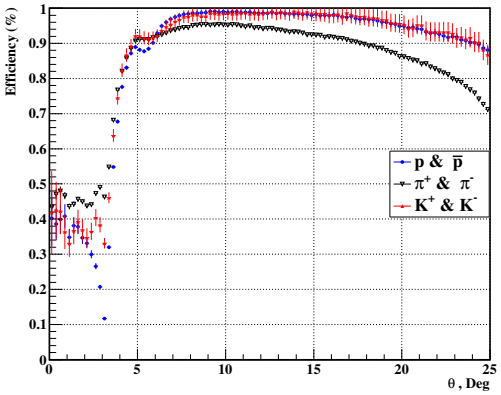

(a) Efficiency vs. θ

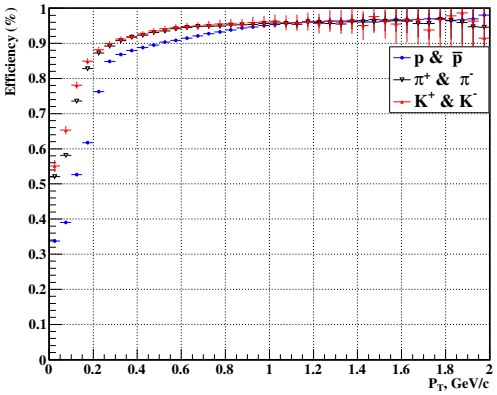

(b) Efficiency vs. p_T

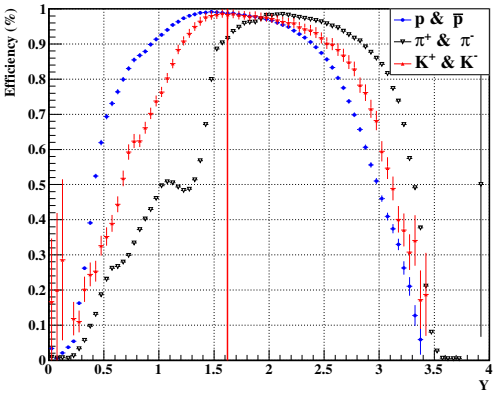

(c) Efficiency vs. Rapidity(y)

Figure F.1: Efficiency performance of the STS detector for individual particle species.

Appendix G

Hits Reconstruction Efficiency

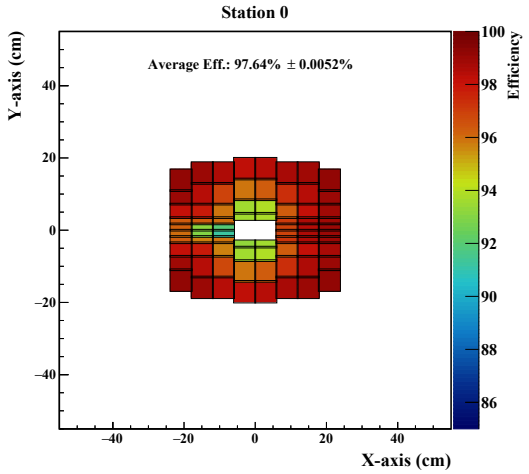

(a) UrQMD

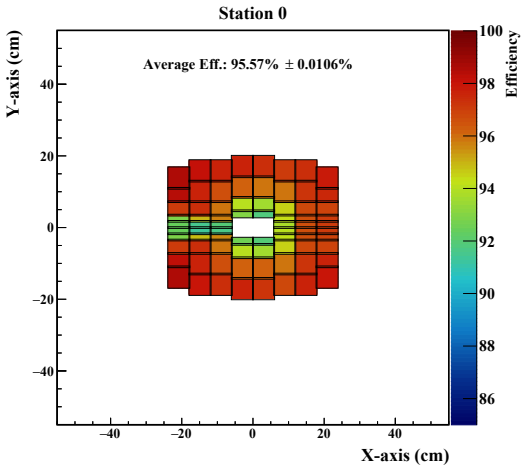

(b) Beam

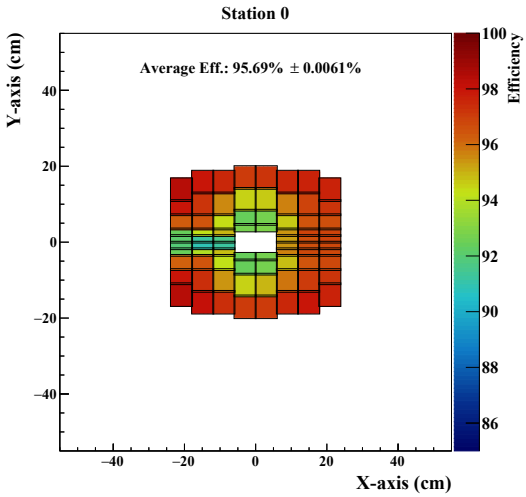

(c) UrQMD and Beam

Figure G.1: Hits reconstruction efficiency for each sensor of Station 0 of the STS detector at ENC = 1000 e, threshold = 4000 e, and dead time 200 ns, in time-based simulation at 12 AGeV/c and 10 MHz rates.

G.1 UrQMD source: Hits reconstruction Efficiency

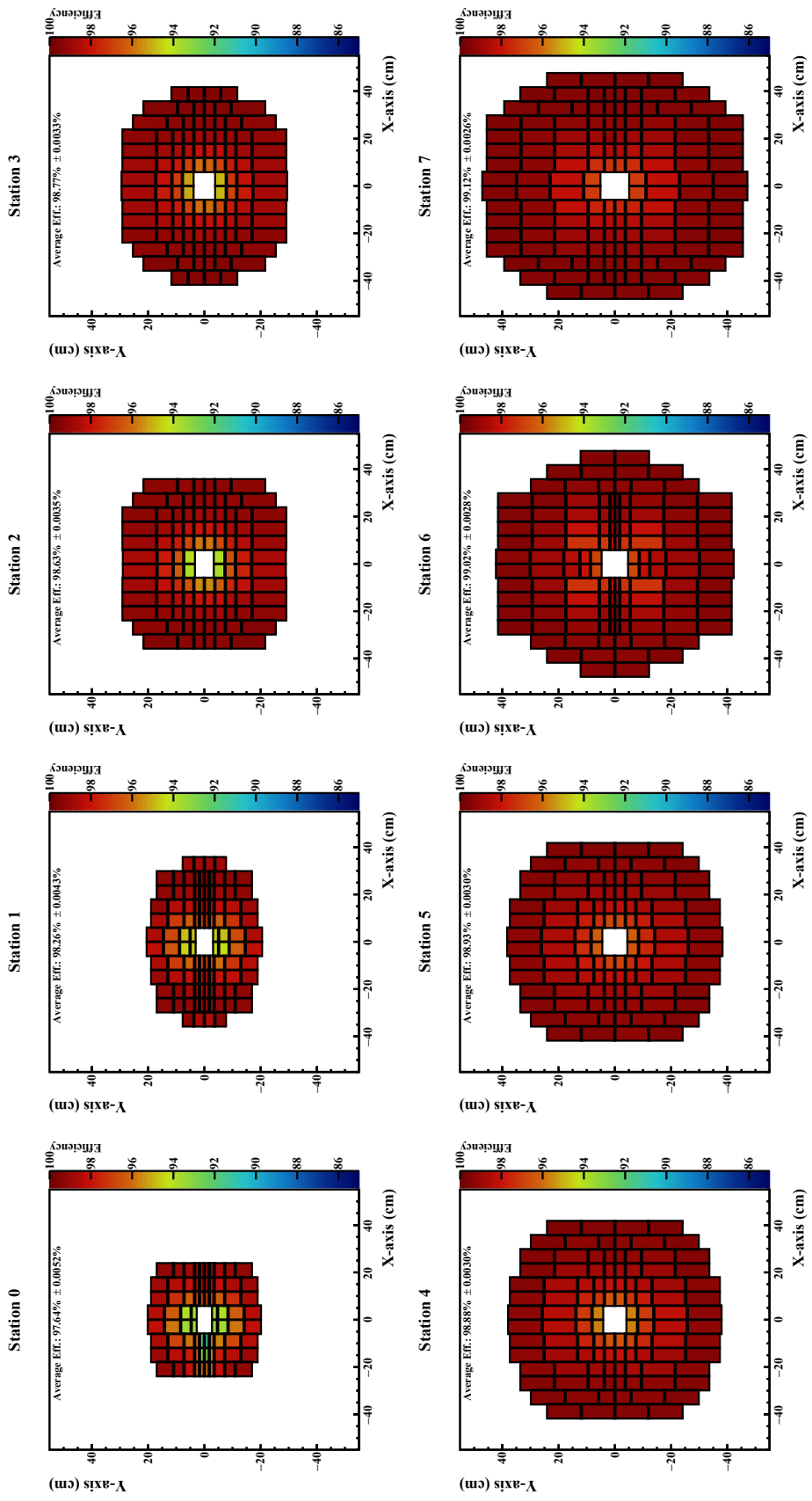

Figure G.2: Hits reconstruction efficiency of each STS station in a case of UrQMD source only

G.2 Beam source: Hits reconstruction Efficiency

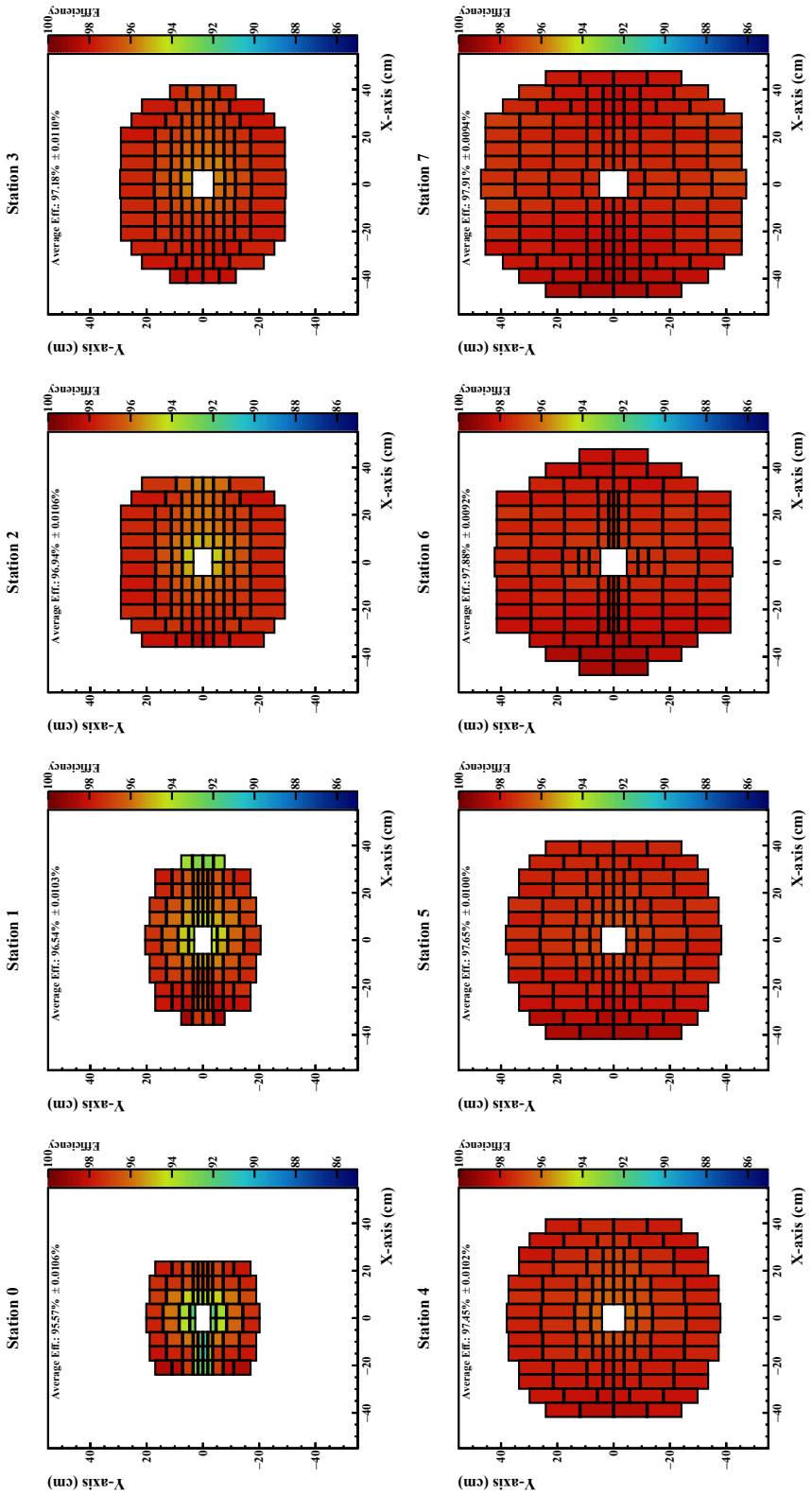

Figure G.3: Hits reconstruction efficiency of each STS station in a case of Beam source only

Appendix H

Cluster Characterization

In this section, we show the relation between cluster size and inclination angle obtained for individual sources, e.g., UrQMD, Beam, etc. Also, we discuss the correlation in cluster size for the silicon sensor, including both sides ($n-$ and $p-$sides). Further detail discussion refer to **Chapter 5**, **Section 5.3**

H.1 Cluster size vs Inclination angle

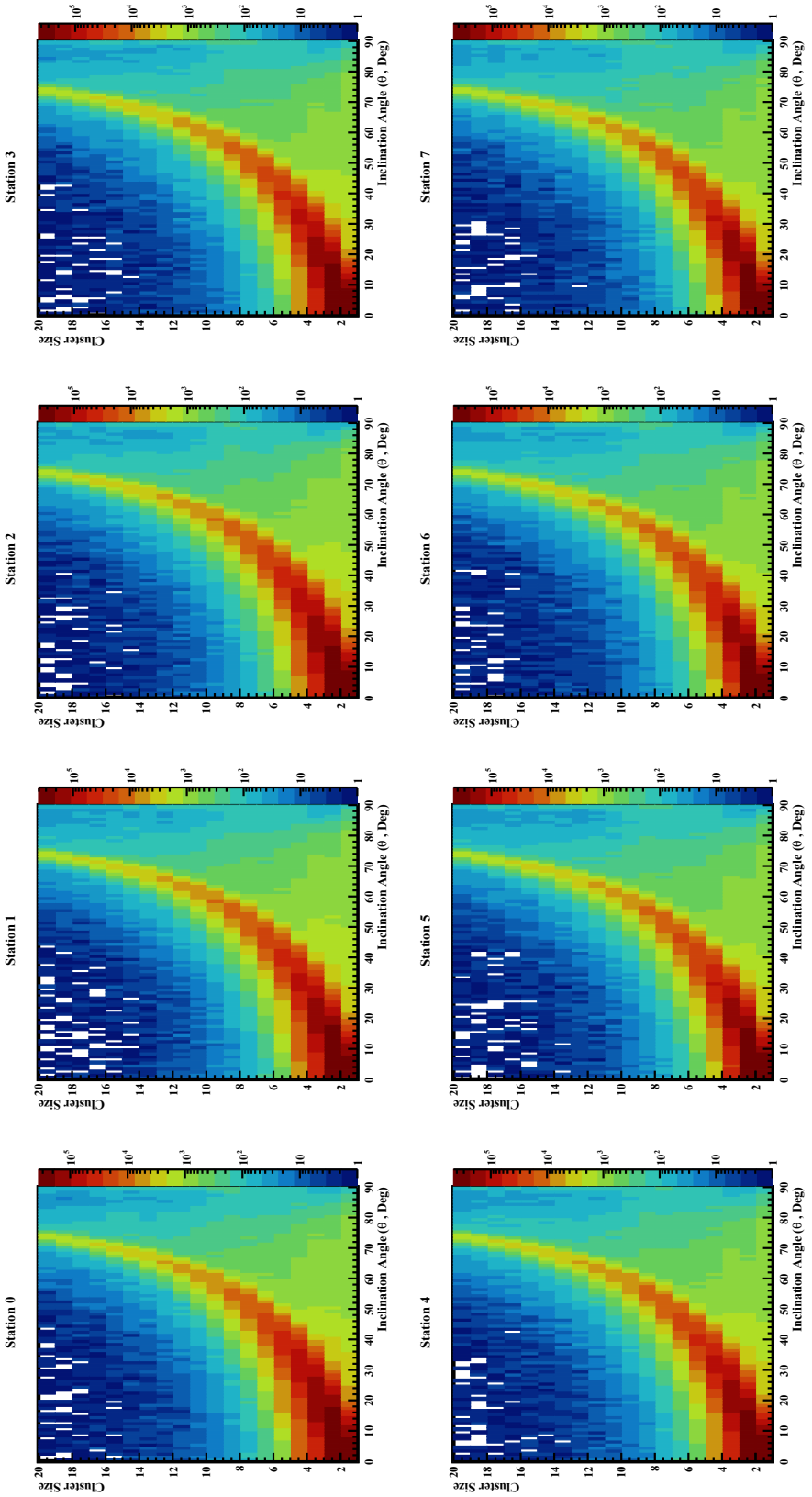

Figure H.1: Cluster size vs. Inclination angle for all particles in UrQMD events at 12 AGeV/c and 10 MHz.

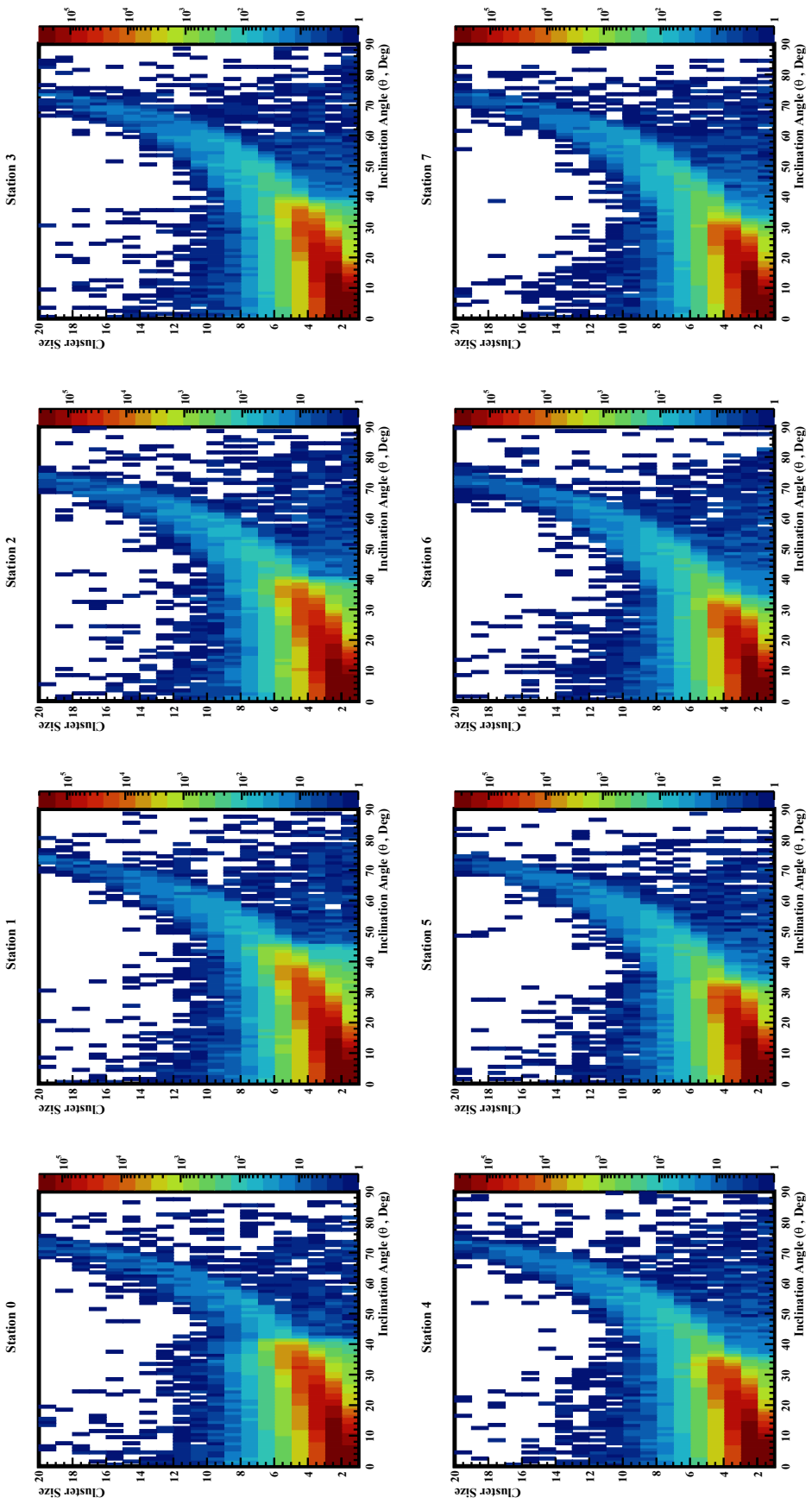

Figure H.2: Cluster size vs. Inclination angle for all particles of momentum $(p) \geq$ 1 GeV/c at 12 AGeV/c and 10 MHz.

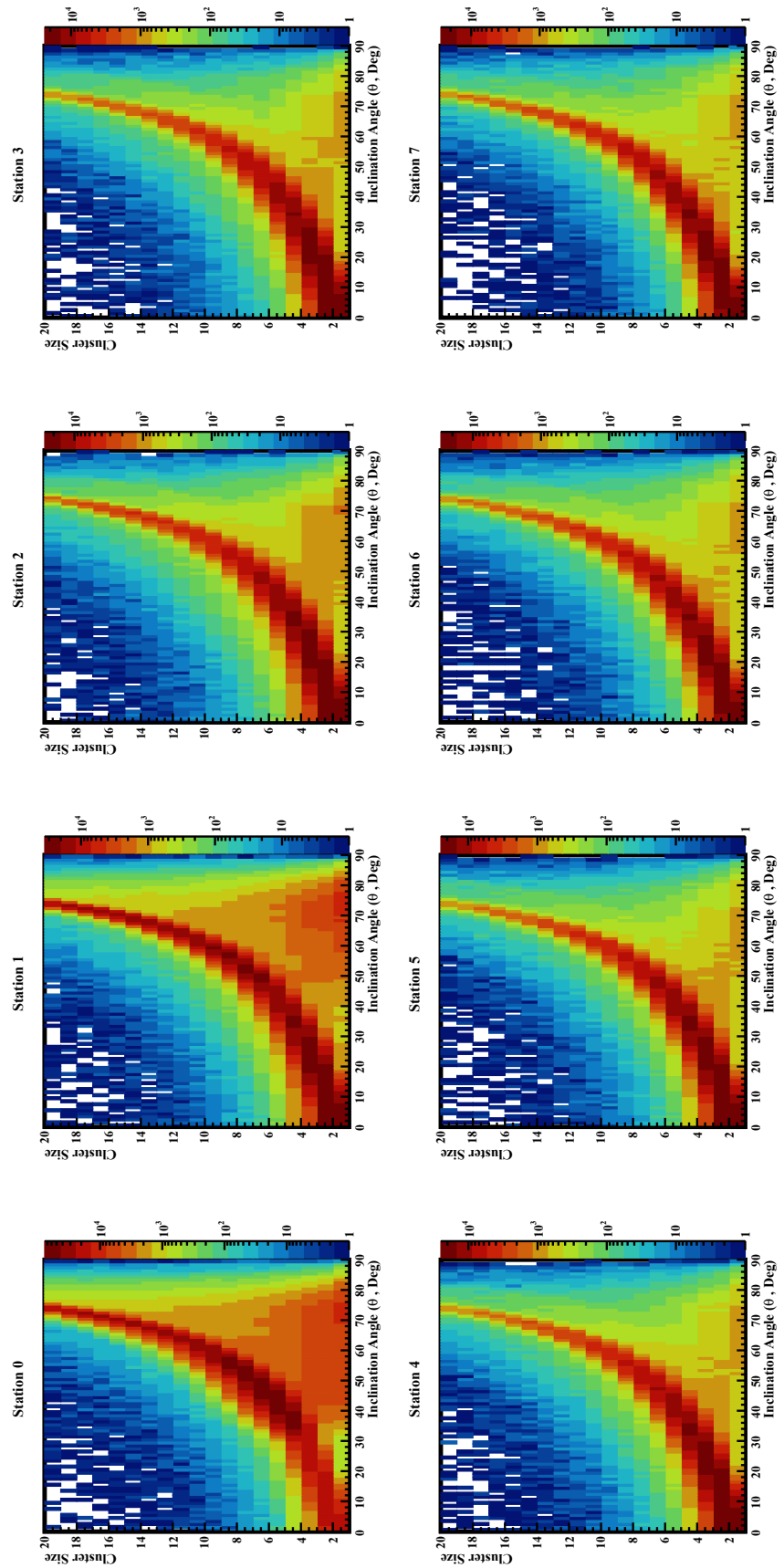

Figure H.3: Beam events ($\delta-$electrons) induced cluster size vs. Inclination angle for particles at 12 AGeV/c and 10 MHz.

H.2 Cluster size correlation

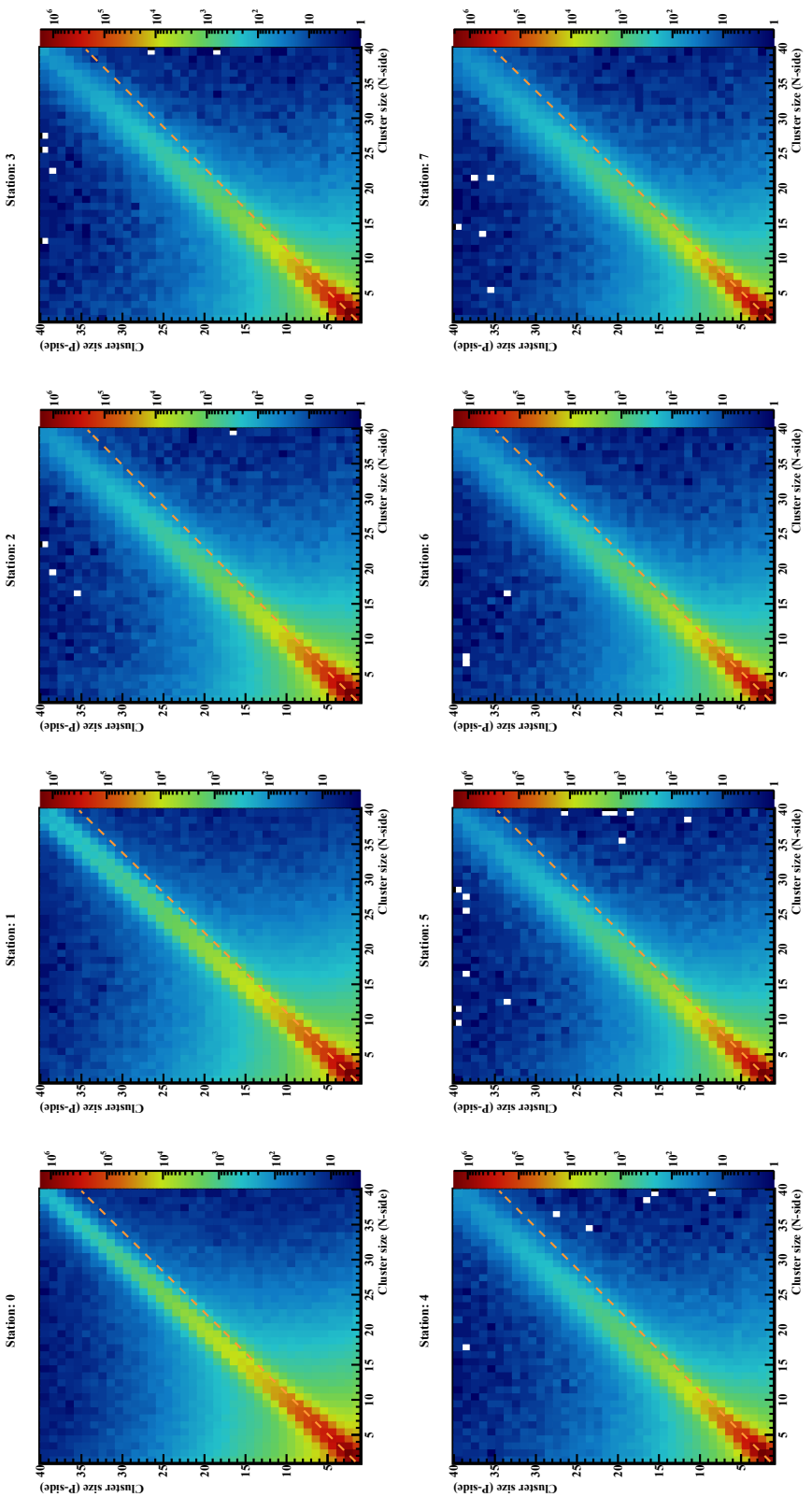

Figure H.4: Cluster size correlation for $n-$ and $p-$side of the silicon micro-strips sensor for both UrQMD and beam event sources.

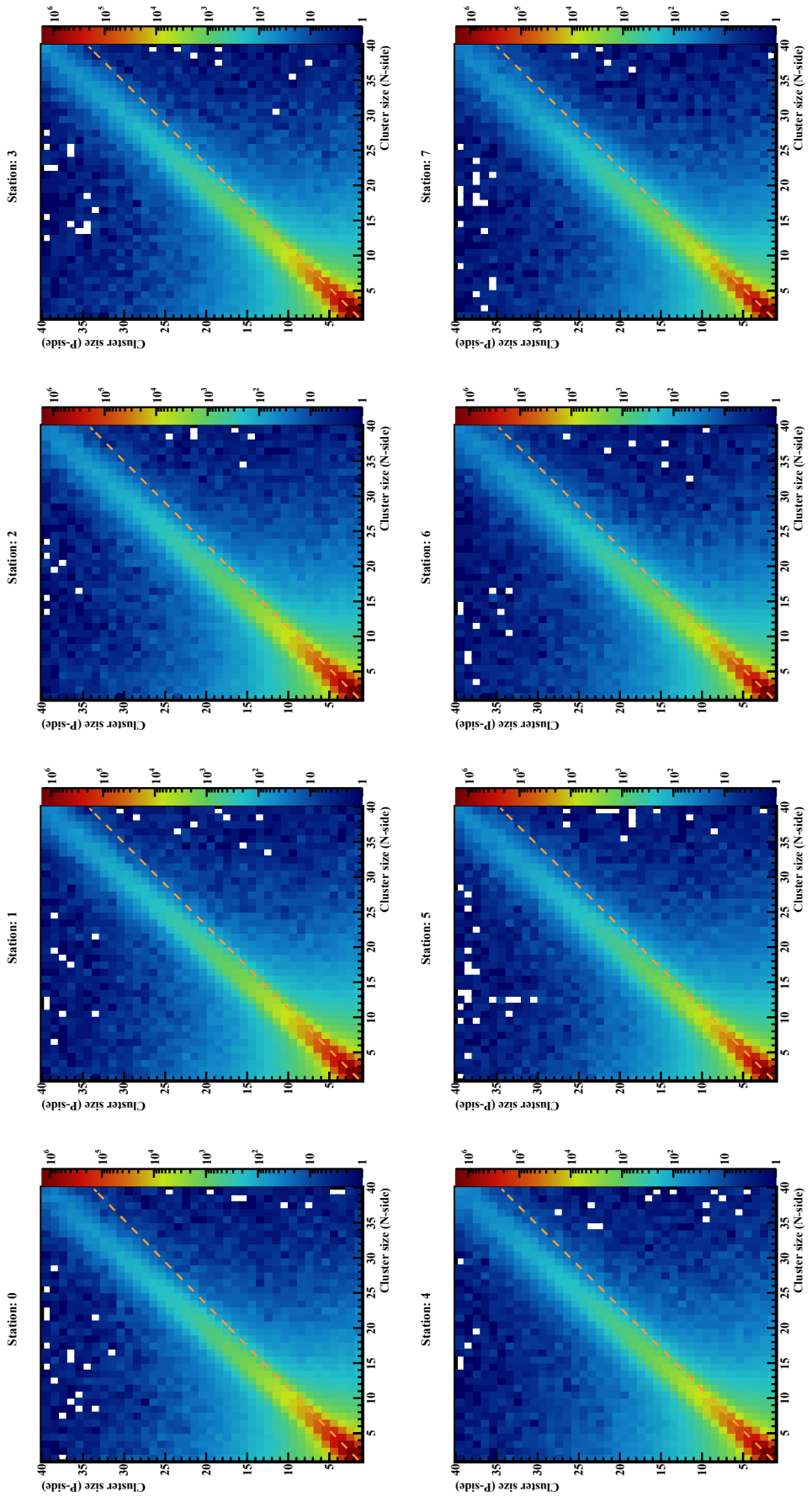

Figure H.5: Cluster size correlation for $n-$ and $p-$side of the silicon micro-strips sensor for UrQMD event sources.

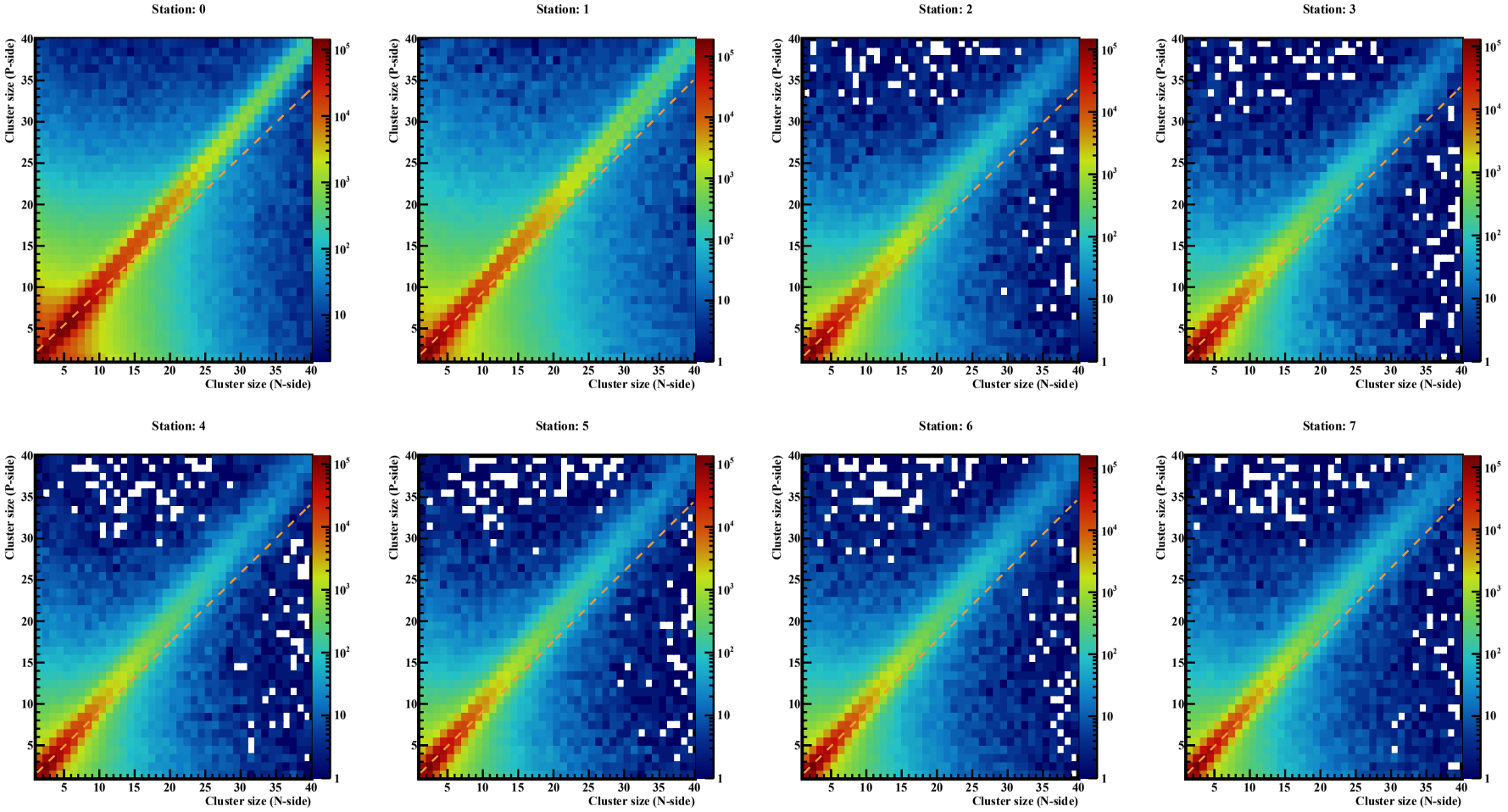

Figure H.6: Cluster size correlation for $n-$ and $p-$side of the silicon micro-strips sensor for Beam event sources.

List of Figures

List of Tables

List of Acronyms

AdepT Accelerated demonstrator of electromagnetic Particle Transport.

AIDA Advanced European Infrastructures for Detectors at Accelerators.

APPA Atomic, Plasma Physics and Applications.

ASCII American Standard Code for Information Interchange.

ASIC Application Specific Integrated Circuit.

ATLAS A Toroidal LHC Apparatus.

BM@N Baryonic Matter at Nuclotron.

BMON Beam Monitor and Start.

BVH Bounding Volume Hierarchy.

CAD Computer-Aided Design.

CATIA Computer-Aided Three-Dimensional Interactive Application.

CBM Compressed Baryonic Matter.

CEP Critical End Point.

CERN Conseil Européen pour la Recherche Nucléaire, or European Council for Nuclear Research.

CF Carbon Fibre.

CMS Compact Muon Solenoid.

CPU Central Processing Unit.

DAQ Data Acquisition.

ENC Equivalent Noise Charge.

EOS Equation of State.

FEB FEE Board.

FEE Front-End Electronics.

FEP Fluorinated Ethylene Propylene.

FLUKA FLUktuierende KAskade, or Fluctuating Cascade.

FPOB FEE Power Board.

FSD Forward Spectator Detector.

GDML Geometry Description Markup Language.

GEANT4 GEometry ANd Tracking.

GPU Graphics Processing Unit.

GRP Glass Reinforced Plastic.

GSI Gesellschaft für Schwerionenforschung - GSI Helmholtz Centre for Heavy Ion Research.

HADES High Acceptance DiElectron Spectrometer.

HL-HEP High-Luminosity High Energy Physics.

HL-LHC High-Luminosity Large Hadron Collider.

HMR High Mass Region.

HPC High-Performance Computing.

HTML Hypertext Markup Language.

IMR Intermediate Mass Region.

LHC Large Hadron Collider.

LMR Low Mass Region.

LQCD Lattice QCD.

LSZH Low Smoke Zero Halogen.

mCBM mini-Compressed Baryonic Matter Experiment.

MIP Minimum Ionising Particle.

MRADSIM Matter-RADiation interaction SIMulation.

MRPC Multi-Gap Resistive Plate Chambers.

mSTS mini-Silicon Tracking System.

MuCh Muon Chambers.

MVD Micro Vertex Detector.

MWPC Multi-Wire Proportional Counters.

NICA Nuclotron-based Ion Collider fAcility.

NUSTAR Nuclear Structure, Astrophysics and Reactions.

PA Polyamide.

PANDA AntiProton Annihilation at Darmstadt.

PC Polycarbonate.

PE Polyethylene.

PHQMD Parton-Hadron-Quantum-Molecular Dynamics.

POB Power Board.

PP Polypropylene.

PTFE Polytetrafluoroethylene.

QCD Quantum Chromodynamics.

QED Quantum Electrodynamics.

QGP Quark-gluon Plasma.

RHIC Relativistic Heavy Ion Collider.

RICH Ring Imaging Cherenkov.

ROB Read-Out Board.

ROOT Responsible Operations and Observations Technology.

RPOB Read-Out Power Board.

SIMD Single Instruction Multiple Data.

SIMT Single Instruction Multiple Thread.

SIS-100 Schwerionensynchrotron-100.

SIS-18 Schwerionensynchrotron-18.

SM Standard Model.

SMX STS/MuCh X-Y-Time-Energy Read-out.

SPS Super Proton Synchrotoron.

STEP Standard for the Exchange of Product Model Data.

STL Standard Triangle Language, Stereolithography.

STS Silicon Tracking System.

TOF Time-of-Flight.

TRD Transition Radiation Detector.

UrQMD Ultrarelativistic Quantum Molecular Dynamics.

USolid Unified Solids.

VecGeom Vectorized Geometry.

XML Extensible Markup Language.

Bibliography

[1] Carsten Burgard, Example: Standard model of physics, Published 31-12-2016. https://texample.net/tikz/examples/model-physics/

[2] ATLAS collaboration, Observation of a new particle in the search for the Standard Model Higgs boson with the ATLAS detector at the LHC, Physics Letters B Volume 716, Issue 1, 17 September 2012, Pages 1-29

[3] Giunti, Carlo et al., Fundamentals of Neutrino Physics and Astrophysics, Oxford University Press, 2007. https://doi.org/10.1093/acprof:oso/9780198508717.001.0001

[4] The KATRIN Collaboration, Direct neutrino-mass measurement based on 259 days of KATRIN data. https://doi.org/10.1126/science.adq9592

[5] M.Thomson, Modern Particle Physics, Cambridge University Press, 2013.

[6] N. Cabibbo et al., Exponential hadronic spectrum and quark liberation, Physics Letter B, 1975. https://doi.org/10.1016/0370-2693(75)90158-6

[7] M. Gazdzicki, The SPS ion program and the first LHC data, 2011. https://doi.org/10.48550/arXiv.1109.3653

[8] P. J. Reardon, BNL RHIC Group, The relativistic heavy ion collider project at Brookhaven, Nuclear Physics A, 1988. https://doi.org/10.1016/0375-9474(88)90923-2

[9] I. Zurbano Fernandez et al., High-Luminosity Large Hadron Collider (HL-LHC): Technical design report, 2020. https://doi.org/10.23731/CYRM-2020-0010

[10] W. Fu, QCD at finite temperature and density within the fRG approach: An overview, Theor. Phys. 74 097304. https://doi.org/10.1088/1572-9494/ac86be

[11] M. A. Stephanov, QCD phase diagram and the critical point, International Journal of Modern Physics A, 2005. https://doi.org/10.1142/S0217751X05027965

[12] W. Fu et al., Hyper-order baryon number fluctuations at finite temperature and density, Phys. Rev. D 104, 094047 (2021). https://doi.org/10.1103/PhysRevD.104.094047

[13] F. Gao et al., Chiral phase structure and critical end point in QCD, Physics Letter B 820, 2021. https://doi.org/10.1016/j.physletb.2021.136584

[14] W. Fu et al., Ripples of the QCD critical point, Phys. Rev. D 111, L031502. https://doi.org/10.1103/PhysRevD.111.L031502

[15] Y. Lu et al., Finite density signatures of confining and chiral dynamics in QCD thermodynamics and fluctuations of conserved charges, 2025. https://doi.org/10.48550/arXiv.2504.05099

[16] Kathryn C Meehan, The fixed-target experiment at STAR, 2016 J. Phys.: Conf. Ser. 742 012022. https://doi.org/10.1088/1742-6596/742/1/012022

[17] M. Kapishin, Heavy Ion BM@N and MPD experiments at NICA, JPS Conf. Proc. 32 (2020) 010093. https://doi.org/10.7566/JPSCP.32.010093

[18] R. Arnaldi, Future facilities: the CERN SPS, 2025 https://doi.org/10.48550/arXiv.2505.10286

[19] K. Ozawa et al., The J-PARC heavy ion project, EPJ Web of Conferences 271, 11004 (2022). https://doi.org/10.1051/epjconf/202227111004

[20] J. Cleymans et al., Comparison of Chemical Freeze-Out Criteria in Heavy-Ion Collisions, PHYSICAL REVIEW C 73, 034905 (2006). https://doi.org/10.1103/PhysRevC.73.034905

[21] A. Andronic et al., Hadron production in central nucleus–nucleus collisions at chemical freeze-out, Nuclear Physics A 772 (2006) 167–199. https://doi.org/10.1016/j.nuclphysa.2006.03.012

[22] B. Mohanty et al., Freeze-Out Parameters in Heavy-Ion Collisions at AGS, SPS, RHIC, and LHC Energies, Advances in High Energy Physics, 2015, 349013, 20 pages, 2015. https://doi.org/10.1155/2015/349013

[23] T. Galatyuk, Future facilities for high μ_B physics, Nuclear Physics A 982 (2019). https://doi.org/10.1016/j.nuclphysa.2018.11.025

[24] N. Herrmann et al., COLLECTIVE FLOW IN HEAVY-ION COLLISIONS, Annu. Rev. Nucl. Part. Sci. 1999. https://doi.org/10.1146/annurev.nucl.49.1.581

[25] S. A. Voloshin et al., Methods for analyzing anisotropic flow in relativistic nuclear collisions, Phys. Rev. C 58:1671-1678, 1998. https://arxiv.org/abs/nucl-ex/9805001 https://doi.org/10.1103/PhysRevC.58.1671

[26] Hades Collaboration, Proton, deuteron and triton flow measurements in Au+Au collisions at $\sqrt{SNN}$ = 2.4 GeV, Eur. Phys. J. A (2023). https://doi.org/10.1140/epja/s10050-023-00936-6

[27] A. Andronic et al., Excitation function of elliptic flow in Au+Au collisions and the nuclear matter equation of state, Phys. Lett. B612 (2005) . https://doi.org/10.1016/j.physletb.2005.02.060

[28] M. A. Stephanov, Non-Gaussian Fluctuations near the QCD Critical Point, PRL 102, 032301 (2009). http://dx.doi.org/10.1103/PhysRevLett.102.032301

[29] V. Koch, Hadronic Fluctuations and Correlations, 2008. https://doi.org/10.48550/arXiv.0810.2520

[30] F. Rennecke et al., QCD phase structure & equation of state: A functional perspective, 2025. https://doi.org/10.48550/arXiv.2510.11270

[31] M. S. Abdallah et al., Measurements of Proton High-Order Cumulants in $\sqrt{s}_{NN}$ = 3 GeV Au+Au Collisions and Implications for the QCD Critical Point, Physical Review Letters 128, 202303 (2022). https://doi.org/10.1103/PhysRevLett.128.202303

[32] A. Pandav, Presentation at CPOD 2024. https://conferences.lbl.gov/event/1376/contributions/8772/attachments/5163/4984/CPOD2024_PandavA_e9.pdf

[33] X. Zhang et al., UrQMD Simulations of Higher-order Cumulants in Au+Au Collisions at High Baryon Density, Chin. Phys. C 50, no.1,011003 (2026). https://doi.org/10.1088/1674-1137/ae0995

[34] J. Adamczewski-Musch et al. (HADES), Proton number fluctuations in $\sqrt{S}_{NN}$ = 2.4 GeV Au+Au collisions studied with HADES, Phys. Rev. C 102, 024914 (2020), https://doi.org/10.1103/PhysRevC.102.024914

[35] Dielectron Performance of the Compressed Baryonic Matter Experiment, Ph.D Thesis, 2025. https://www.uni-muenster.de/imperia/md/content/physik_kp/meyerahrens2025.pdf

[36] M. Urban et al., Modifications of the Rho Meson from the Virtual Pion Cloud in Hot and Dense Matter, Nucl.Phys.A 673 (2000) 357-374, https://doi.org/10.1016/S0375-9474(00)00125-1

[37] R. Rapp et al., Chiral Symmetry Restoration and Dileptons in Relativistic Heavy-Ion Collisions, Adv. Nucl. Phys. 25 (2000) 1, https://doi.org/10.48550/arXiv.hep-ph/9909229

[38] G. Agakishiev et al., First measurement of proton-induced low-momentum dielectron radiation off cold nuclear matter, Physics Letter B, 715, 2012. https://doi.org/10.1016/j.physletb.2012.08.004

[39] ALICE Collaboration, First direct access to the ρ^0 p interaction via correlation studies at the LHC, 2025. https://doi.org/10.48550/arXiv.2508.09867

[40] T. Galatyuk, https://github.com/tgalatyuk/QCD_caloric_curve

[41] Hendrik van Hees et al., Thermal dileptons as fireball thermometer and chronometer, Physics Letter B 753, 2016. http://dx.doi.org/10.1016/j.physletb.2015.12.065

[42] F. Seck et al., Thermal dileptons from coarse-grained transport as fireball probes at SIS energies, Eur. Phys. J. A 52, 131 (2016). https://doi.org/10.1140/epja/i2016-16131-1

[43] CBM Collaboration, Challenges in QCD matter physics – The scientific programme of the Compressed Baryonic Matter experiment at FAIR, 2017. https://doi.org/10.48550/arXiv.1607.01487

[44] K. Lipka et al., Determination of the charm-quark mass in the MS scheme using charm production data from deep-inelastic scattering at HERA, Physics Letter B, 718, 2012. http://dx.doi.org/10.1016/j.physletb.2012.11.010

[45] S. Bethke, Experimental Tests of Asymptotic Freedom, 2024. http://arxiv.org/abs/hep-ex/0606035v2

[46] R. Rapp et al., Heavy Quarks in the Quark-Gluon Plasma, 2018. http://arxiv.org/abs/0903.1096v2

[47] J. Steinheimer et al., Sub-threshold charm production in nuclear collisions, Phys. Rev. C 95, 014911 (2017), https://doi.org/10.1103/PhysRevC.95.014911

[48] R. L. Workman et al. Review of Particle Physics. PTEP, 2022:083C01, 2022

[49] Min He et al., Heavy-quark diffusion and hadronization in quark-gluon plasma, Phys. Rev. C 86, 014903. https://doi.org/10.1103/PhysRevC.86.014903

[50] Yu.L. Dokshitzer et al., Heavy Quark Colorimetry of QCD Matter, Phys. Lett. B 519:199-206, 2001. https://doi.org/10.1016/S0370-2693%2801%2901130-3

[51] J. Steinheimer et al., Hypernuclei, dibaryon and antinuclei production in high energy heavy ion collisions: Thermal production vs. Coalescence, Physics Letters B 714 (2012). https://doi.org/10.1016/j.physletb.2012.06.069

[52] A. Andronic et al., Production of light nuclei, hypernuclei and their antiparticles in relativistic nuclear collisions, Phys. Lett. B 697:203-207, 2011. https://doi.org/10.1016/j.physletb.2011.01.053

[53] I. Vidana, Hyperons: the strange ingredients of the nuclear equation of state, 2018. https://doi.org/10.48550/arXiv.1803.00504

[54] H. H. Gutbrod et al., FAIR Baseline Technical Report, 2006. https://inspirehep.net/literature/1621651

[55] CBM Collaboration, Technical Design Report for the CBM Online Systems – Part I, DAQ and FLES Entry Stage, 2023. https://repository.gsi.de/record/340597

[56] J. Heuser et al., Technical Design Report for the CBM, 2013. https://repository.gsi.de/record/54798

[57] Hamamatsu Photonics, https://www.hamamatsu.com/jp/en.html

[58] S. Mehta, Investigation of thermal and structural integrity of modules and ladders of the Silicon Tracking System of the CBM experiment, PhD Thesis, University of Tübingen, 2024. https://tobias-lib.ub.uni-tuebingen.de/xmlui/handle/10900/163359?show=full

[59] A. Senger Non-Ionising energy loss(NIEL) in STS cooling, STS construction meeting 2023. https://indico.gsi.de/event/18427/contibutions/75188/

[60] K.Agarwal, Ph.D thesis, Thermal Management of the Silicon Tracking System of the CBM Experiment at FAIR, 2025. http://dx.doi.org/10.15496/publikation-102494

[61] R. Brun et al., The ROOT geometry package, Nuclear Instruments and Methods in Physics Research A 502 (2003) 676–680, https://doi.org/10.1016/S0168-9002(03)00541-2

[62] J. Allison et al., Recent developments in GEANT4, Nucl. Instrum. Meth. A 835 (2016) 186-225. https://doi.org/10.1016/j.nima.2016.06.125

[63] R. Chytracek et al., Geometry Description Markup Language for Physics Simulation and Analysis Applications, IEEE Transactions on Nuclear Science 53(5):2892 - 2896 10.1109/TNS.2006.881062

[64] V. L. Highland. Some Practical Remarks on Multiple Scattering. Nucl. Instrum. Meth., 129:497, 1975. https://doi.org/10.1016/0029-554X(75)90743-0

[65] G.R. Lynch and O.I. Dahl. Approximations to multiple Coulomb scattering. Nucl. Instrum. Meth. B, 58:6–10, 1991. https://doi.org/10.1016/0168-583X(91)95671-Y

[66] R. L. Gluckstern. Uncertainties in track momentum and direction, due to multiple scattering and measurement errors. Nucl. Instrum. Meth., 24:381– 389, 1963.

[67] Z. Drasal and W. Riegler. An extension of the Gluckstern formulae for multiple scattering: Analytic expressions for track parameter resolution using optimum weights. Nucl. Instrum. Meth. A, 910:127–132, 2018.

[68] H. Kolanoski and N. Wermes, Particle Detectors fundamentals and applications, Oxford University Press, 6 2020.

[69] M. Gupta et al., Calculation of radiation length in materials, PH-EP-Tech-Note-2010-013. https://cds.cern.ch/record/1279627?ln=en

[70] Gerald R. Lynch and Orin I. Dahl, Approximations to multiple Coulomb scattering, Nuclear Instruments and Methods in Physics Research B58 (1991) 6-10 https://doi.org/10.1016/0168-583X(91)95671-Y

[71] P.A. Zyla et al. (Particle Data Group), Prog. Theor. Exp. Phys. 2020, 083C01 (2020) https://doi.org/10.1093/ptep/ptaa104

[72] M. Teklishyn et al., Minimal material, maximum coverage: Silicon Tracking System for high-occupancy conditions, Nucl. Instrum. Methods Phys. Res. A, 1080, 170714, 2025 https://doi.org/10.1016/j.nima.2025.170714

[73] J. Heuser et al., Production Readiness Review for the STS Carbon Fiber Ladders, CBM Technical Note CBM-TN-19006, 2019. https://indico.gsi.de/event/8579/contributions/37306/attachments/27063/33854/CBM-TN-19006-v1.1.pdf.

[74] Rene Brun et al., ROOT - An Object Oriented Data Analysis Framework, Nuclear Instruments and Methods in Physics Research A 389 (1997) 81-86. https://doi.org/10.1016/S0168-9002(97)00048-X

[75] C. M. Poole et al., Fast Tessellated Solid Navigation in GEANT4, IEEE Transactions on Nuclear Science, vol. 59, no. 4, pp. 1695-1701, Aug. 2012, 10.1109/TNS.2012.2197415

[76] Juergen Riegel, Werner Mayer, Yorik van Havre (2001-2017). FreeCAD (Version 0.16.6712)

[77] S. Belogurov et al. 2011 J. Phys.: Conf. Ser. 331 032035.

[78] A. Behcet Alpat et al., MRADSIM (Matter-RADiation Interactions SIMulations), https://doi.org/10.48550/arXiv.2411.11173

[79] A. Behcet Alpat et al., MRADSIM-Converter: A new software for STEP to GDML conversion, https://doi.org/10.1016/j.cpc.2023.108688

[80] The VecGeom repository. Available at: https://gitlab.cern.ch/VecGeom/VecGeom

[81] O. Singh, M. Shiroya et al. Modelling of simulation geometries using Tessellated Shapes with the Vectorized Geometry (VecGeom) package, CBM Progress Report 2023 pg. 174- 175. https://doi.org/10.15120/GSI-2024-00765

[82] The ATLAS Collaboration, ATLAS Software and Computing HL-LHC Roadmap, Tech. Rep. CERN-LHCC-2022-005, LHCC-G-182, CERN, Geneva, 2022. https://cds.cern.ch/record/2802918

[83] J. Apostolakis et al., Detector Simulation Challenges for Future Accelerator Experiments, Frontiers in Physics. 10. 913510. https://doi.org/10.3389/fphy.2022.913510

[84] S. Agostinelli et al., Geant4—a simulation toolkit, Nuclear Instruments and Methods in Physics Research A 506 (2003) 250–303. https://doi.org/10.1016/S0168-9002(03)01368-8

[85] F. Ballarini et al., The FLUKA code: Overview and new developments, EPJ Nuclear Sci. Technol. 10, 16 (2024). https://doi.org/10.1051/epjn/2024015

[86] G Amadio et al., The GeantV project: preparing the future of simulation, Journal of Physics: Conference Series 664 (2015) 072006. 10.1088/1742-6596/664/7/072006

[87] Amadio G., Ananya, A., Apostolakis, J. et al. GeantV Results from the Prototype of Concurrent Vector Particle Transport Simulation in HEP. Comput Softw Big Sci 5, 3 (2021). https://doi.org/10.1007/s41781-020-00048-6

[88] G. Amadio et al., Electromagnetic physics vectorization in the GeantV transport framework, EPJ Web of Conferences 214, 02031 (2019). https://doi.org/10.1051/epjconf/201921402031

[89] AdePT project. https://github.com/apt-sim/AdePT

[90] S. C. Tognini et al., Celeritas: GPU-accelerated particle transport for detector simulation in High Energy Physics experiments. https://arxiv.org/pdf/2203.09467

[91] S. Wenzel et al., A VecGeom navigator plugin for Geant4, EPJ Web of Conferences 245, 02024 (2020). https://doi.org/10.1051/epjconf/202024502024

[92] J. Apostolakis et al., Surface-based GPU-friendly geometry modeling for detector simulation, EPJ Web of Conferences 295, 03039 (2024). https://doi.org/10.1051/epjconf/202429503039

[93] D. Cvijetic et al., Converting Solids to VecGeom's Surface Model, CERN Summer Student Project Report, CERN EP–SFT Group, Geneva, Switzerland, August 26, 2022. https://repository.cern/records/s4jzx-a1m61/preview/VecGeom_SurfModel.pdf

[94] Stan, Eduard George et al., GPU-friendly boundary representation geometry model for simulation, CERN-STUDENTS-Note-2023-177, SFT simulation R&D group, CERN, Geneva, Switzerland. https://repository.cern/records/gt855-ete70/files/CERN_Report.pdf?download=1

[95] Sandro Wenzel et al., Accelerating navigation in the VecGeom geometry modeller 2017, J. Phys.: Conf. Ser. 898 072032. https://doi.org/10.1088/1742-6596/898/7/072032

[96] The CBM Collaboration, Technical Design Report for the CBM Online Systems – Part I DAQ and FLES Entry Stage, July 2023. https://repository.gsi.de/record/340597/files/CBM%20TDR%20Online%20Systems%20-%20Part%20I.pdf

[97] E. Lavrik et al., Optical inspection of the silicon micro-strip sensors for the CBM experiment employing artificial intelligence, Nuclear Instruments and Methods in Physics Research Section A, Volume 1021, 2022. https://doi.org/10.1016/j.nima.2021.165932

[98] S. O. Rice, Mathematical analysis of random noise," in The Bell System Technical Journal, vol. 23, no. 3, pp. 282-332, July 1944. https://doi.org/10.1002/j.1538-7305.1944.tb00874.x

[99] I. Sorokin et al., Rice formula applicability for noise rate estimation in the CBM and other experiments with self-triggered electronics: comparing the calculation to a measurement on example of the n-XYTER chip, CBM Progress Report 2011. https://repository.gsi.de/record/54080/files/GSI-2013-04802.pdf

[100] G. Giacomini, Noise Characterization of Silicon Strip Detectors Comparison of Sensors with and without Integrated JFET Source-Follower, PhD Trieste University, 2007. https://inspirehep.net/literature/1429490

[101] K. Kasinski et al., Characterization of the STS/MUCH-XYTER2, a 128-channel time and amplitude measurement IC for gas and silicon microstrip sensors, 2018. https://doi.org/10.1016/j.nima.2018.08.076

[102] A. Rodríguez et al., Functional characterization of modules for the Silicon Tracking System of the CBM experiment, Nuclear Instruments and Methods in Physics Research Section A, 1058, 2024. https://doi.org/10.1016/j.nima.2023.168813

[103] O. Maragoto, Characterization and commissioning of the front-end electronics for the Silicon Tracking System of the CBM experiment, PhD Thesis, 2023. https://repository.gsi.de/record/348003

[104] A. Rodriguez, The CBM Silicon Tracking System front-end electronics, from bare ASIC to detector characterization, commissioning and performance, 2019. https://www.uni-frankfurt.de/105807764/PhD_Thesis_ARRodriguez.pdf

[105] P. Spiller et al., The FAIR Heavy Ion Synchrotron SIS100, 2020 JINST 15 T12013. https://doi.org/10.1088/1748-0221/15/12/T12013

[106] Gerald Eigen, Detectors in High-Energy Physics Experiments Underlying Physics, Working Principles, and Realizations, 2025. https://doi.org/10.1007/978-3-031-67336-8

[107] H. Malygina, Hit reconstruction for the Silicon Tracking System of the CBM Experiment, Ph.D Thesis, 2018. https://indico.gsi.de/event/7235/contributions/32684/attachments/23549/29499/Malygina_dissertation_printed.pdf

[108] J. M. Heuser et al., Technical Design Report for the CBM Silicon Tracking System, October 2013. https://repository.gsi.de/record/54798

[109] S. A. Bass et al., Microscopic models for ultrarelativistic heavy ion collisions, Prog. Part. Nucl. Phys .41:255-369,1998. https://doi.org/10.1016/S0146-6410(98)00058-1

[110] C. Grupen et al., PARTICLE DETECTORS, Cambridge University Press, July 2023. https://doi.org/10.1017/9781009401531

[111] H. Spieler, Semiconductor Detector Systems, Oxford University Press (2005).

[112] C. Jacoboni et al., A Review of Some Charge Transport Properties of Silicon, Solid-State Electronics, 1977, Vol. 20, 1977. https://doi.org/10.1016/0038-1101(77)90054-5

[113] Lu Bai et al., Simulation of silicon strip detector for space-based cosmic ray experiments with Allpix^2, Radiat Detect Technol Methods 7, 355–363 (2023). https://doi.org/10.1007/s41605-023-00396-y

[114] I. Deppner et al., The CBM Time-of-Flight system, 2019 JINST 14 C09020. https://doi.org/10.1088/1748-0221/14/09/C09020

[115] N. Herrmann, Technical Design Report for the CBM Time-of-Flight System (TOF), GSI-2015-01999 (2014). https://repository.gsi.de/record/109024

[116] Christian Lippmann, Particle identification, Nuclear Instruments and Methods in Physics Research A 666 (2012) 148–172. https://doi.org/10.1016/j.nima.2011.03.009

[117] The ALICE Collaboration, Particle identification in ALICE: a Bayesian approach, Eur. Phys. J. Plus (2016) 131: 168, https://link.springer.com/article/10.1140/epjp/i2016-16168-5

[118] O. Derenovskaya et al., Heavy Fragments Identification Using Energy Loss Method in the STS Detector of the CBM Experiment, EPJ Web of Conferences 226, 03005 (2020). https://doi.org/10.1051/epjconf/202022603005

[119] H. Malygina et al., CBM Progress Report 2017. https://repository.gsi.de/record/209729

[120] J. Aichelin, E. Bratkovskaya et al., Parton-hadron-quantum-molecular dynamics: A novel microscopic n-body transport approach for heavy-ion collisions, dynamical cluster formation, and hypernuclei production, PHYSICAL REVIEW C 101, 044905 (2020). https://doi.org/10.1103/PhysRevC.101.044905

Acknowledgments

The work presented in this thesis is the result of the collective support, guidance, and encouragement of many individuals from both my professional and personal circles, each of whom has contributed in meaningful ways to different stages of this journey.

Before expressing my gratitude to my supervisor, I would like to extend my sincere thanks to Dr. Maksym Teklishyn, who played a pivotal role in my coming to GSI, first as a Master's student and later as a Ph.D. candidate. He was among the first to evaluate my application for a Ph.D. position in 2018/19. However, circumstances led me to begin with a Master's thesis at GSI in 2020. Whether he still recalls it or not, I remain genuinely grateful for his support at that early stage, which laid the foundation for the journey that followed.

After that, I would like to thank Dr. Evgeny Lavrik, Dr. Olga Bertini, and Dr. Anton Lymanets, with whom I completed my Master's thesis, and from whom I learned a lot about Machine learning and Image processing for identifying defects on the surface of silicon sensors and their support and guidance while working with them in the STS lab from the very beginning.

Moving forward with my Ph.D. journey, I would first like to express my thanks to my supervisor, Dr. Alberica Toia, and my mentor, Dr. Volker Friese, for their guidance and care during my time at GSI, as well as for their encouragement.

A special thanks to Dr. Florian Uhlig, who has helped me solve many software-related issues and provided guidance. Also, thankful to Dr. David Emschermann for his constant guidance in introducing me to STS geometry work when I was starting my Ph.D., and for being there whenever I needed his help. I am also sincerely grateful to Dr. Eoin Clerkin, whose help and criticism in every aspect helped me work hard to improve the STS simulation geometry. Also, I am thankful to Oleg Vasylev, Jens Thaufelder, and Patrick Dahm for their help and for being there whenever I needed help with STS/mSTS CAD geometry. I would like to extend my gratitude to Dr. Ulrich Frankenfeld, Dr. Johan Heuser, and Dr. Christian Schmidt for the fruitful discussion and their

constant guidance and support.

I have been fortunate to work in an excellent STS group, where I met wonderful colleagues such as Dr. Adrian Rodríguez, Dairon Rodríguez, and Lady Maryann. Their support, willingness to help, and the memorable moments we shared—including the unforgettable Cuban parties—made my time even more enjoyable. I would also like to express my special gratitude to Dr. Dario Ramírez for always being there for me, for our many discussions, and for his constant support throughout this journey.

A special thanks goes to Dr. Shaifali Mehta and Dr. Kshitij Agarwal, whom I have known for almost the last ten years and have been friends with. It was my pleasure to work with them in the same group. I would like to say to Shaifali that I miss those days of sharing the same office and having heated fights, but that you were still there for me whenever I needed your advice and help. Apart from this, I would like to thank you, Kshitij (Baba), for your good advice, guidance, and unwavering support. In addition, I am grateful to Meethika Narang for the many wonderful moments we shared, especially those coffee breaks at the GSI cafeteria. I fondly remember those days spent together with you three, which made my time here truly memorable.

Moreover, I would like to express my gratitude to Anurag Tiwari and Dr. Reema Chawdhury for their friendship, encouragement, and continuous support throughout my journey. I am especially thankful to Dr. Omvir Singh for his constant guidance, valuable discussions, and for always helping me whenever I faced difficulties in my work. I also extend my sincere thanks to my friends Jeniffer Steitz, Jelena Bardak, and Bellona Bles for their support and for making my time at GSI both memorable and enjoyable.

Last but certainly not least, I would like to express my deepest gratitude to my family, and especially to my wife, Dr. Twinkal Munjani, for their unwavering support, encouragement, and patience throughout my Ph.D. journey.